Lecture Notes
in Geoinformation and Cartography

LNG&C

Jukka M. Krisp
Liqiu Meng
Roland Pail
Uwe Stilla *Editors*

Earth Observation of Global Changes (EOGC)

Springer

Lecture Notes in Geoinformation and Cartography

For further volumes:
http://www.springer.com/series/7418

Jukka M. Krisp · Liqiu Meng
Roland Pail · Uwe Stilla
Editors

Earth Observation of Global Changes (EOGC)

Springer

Editors
Jukka M. Krisp
Technische Universität
München (TUM)
Munich
Germany

Roland Pail
Technische Universität
München (TUM)
Munich
Germany

Liqiu Meng
Technische Universität
München (TUM)
Munich
Germany

Uwe Stilla
Technische Universität
München (TUM)
Munich
Germany

ISSN 1863-2246 ISSN 1863-2351 (electronic)
ISBN 978-3-642-32713-1 ISBN 978-3-642-32714-8 (eBook)
DOI 10.1007/978-3-642-32714-8
Springer Heidelberg New York Dordrecht London

Library of Congress Control Number: 2012948186

Printed on acid-free paper

Springer is part of Springer Science+Business Media (www.springer.com)

Preface

This book documents the research activities related to earth observation and global changes. The contributions originate from selected presentations at the EOGC2011—3rd Earth Observation and Global Changes Conference, which was jointly organized by Technische Universität München (TUM) in Germany, Peking University (China), and University of Waterloo (Canada). The conference was related to the JURSE2011—Joint Urban Remote Sensing Event, held in the same week at TUM. The EOGC2011 was a forum for researchers dealing on earth observation and global changes with respect to the information technology. The event was cosponsored by International Society for Photogrammetry and Remote Sensing (ISPRS), International Cartographic Association (ICA), International Association of Geodesy (IAG), International Society for Digital Earth (ISDE), and the International Office of TUM. The conference gathered 66 participants from 19 countries with 31 selected presentations covering a variety of aspects concerning Remote Sensing, GIS, Cartography, and Geodesy. Two keynote speeches were given by Prof. Reiner Rummel and Prof. Markus Rothacher. We thank all the contributors for their excellent input and all the participants for making the EOGC2011 an outstanding and multidisciplinary event.

Nineteen papers from the proceedings are elaborated and now published in this book "Earth Observation of Global Changes (EOGC)" within the Springer series "Lecture Notes in Geoinformation and Cartography". As the field of study covers a wide spectrum of research topics, the editor team assures the quality of this cross-disciplinary field. The editors are Prof. Liqiu Meng for the topic Global Change and Change Detection; Dr. Jukka M. Krisp for the topic Spatial Modelling, GIS, and Geovisualization; Prof. Roland Pail for Physical Geodesy; and Prof. Uwe Stilla for the topic Photogrammetry and Remote Sensing. Our aim is to benefit the scientific community in a wide range by presenting different topics from different perspectives.

Jukka M. Krisp
Liqiu Meng
Roland Pail
Uwe Stilla

Contents

Reviewers

The production of this book would have not been possible without the professional help of our scientific review committee. We would like to thank all the following experts who have helped to review the papers published within this book.

Bamler	Richard	Technische Universität München, Germany
Brenning	Alexander	University of Waterloo, Canada
Buchroithner	Manfred	Technische Universität Dresden, Germany
Ding	Xiaoli	The Hong Kong Polytechnic University, Hong Kong, China
Eineder	Michael	German Aerospace Center (DLR), Germany
Esch	Thomas	German Aerospace Center (DLR), Germany
Gege	Peter	German Aerospace Center (DLR), Germany
He	Yuhong	University of Toronto Mississauga, Canada
Hinz	Stefan	Karlsruhe Institute of Technology, Germany
Hugentobler	Urs	Technische Universität München, Germany
Krisp	Jukka	Technische Universität München, Germany
Li	Jonathan	University of Waterloo, Canada
Melgani	Farid	University of Trento, Italy
Meng	Liqiu	Technische Universität München, Germany
Meyer	Franz Josef	University of Alaska Fairbanks, United States of America
Müller	Jürgen	Institute of Geodesy, Leibniz University of Hannover, Germany
Pail	Roland	Technische Universität München, Germany
Seitz	Florian	Technische Universität München, Germany
Smit	Julian Lloyd	University of Cape Town, South Africa
Stilla	Uwe	Technische Universität München, Germany
Tommaselli	Antonio Maria Garcia	UNESP, Brazil
Wei	Yao	Munich University of Applied Sciences, Germany
Yang	Xiaojun	Florida State University, United States of America

(continued)

(continued)

Yi	Weiyong	Technische Universität München, Germany
Zhang	Yun	University of New Brunswick, Canada
Zhou	Fuqun	Canada Centre for Remote Sensing, Canada

Contributors

Fadwa Alshawaf Institute of Photogrammetry and Remote Sensing (IPF), Karlsruhe Institute of Technology (KIT), Karlsruhe, Germany; Geodetic Institute (GIK), Karlsruhe Institute of Technology (KIT), Karlsruhe, Germany

Manuel Antón Geophysics Centre of Évora, University of Évora, Évora, Portugal; Department of Physics, University of Extremadura, Badajoz, Spain

Martin Bachmann German Aerospace Center (DLR), Wessling, Germany

Yifang Ban Division of Geoinformatics, Department of Urban Planning and Environment, Royal Institute of Technology, Stockholm, Sweden

Markus Boldt Institute of Photogrammetry and Remote Sensing (IPF), Karlsruhe Institute of Technology (KIT), Karlsruhe, Germany

Maurice Borgeaud European Space Agency, ESRIN, Frascati, Italy

Daniele Bortoli Geophysics Centre of Évora, University of Évora, Évora, Portugal; Institute of Atmospheric Sciences and Climate, Bologna, Italy

Andreas Christian Braun Institute of Photogrammetry and Remote Sensing (IPF), Karlsruhe Institute of Technology (KIT), Karlsruhe, Germany

Florian Burkert Technische Universität München (TUM), Remote Sensing Technology, Munich, Germany

Emilio Chuvieco Department of Geography, University of Alcala, Alcalá de Henares, Spain

Villaroel Constanza Department of Geography, University of Concepción, Barrio Universitario, Concepción, Chile

Maria João Costa Geophysics Centre of Évora, University of Évora, Évora, Portugal; Department of Physics, University of Évora, Évora, Portugal

Amaia de Miguel German Aerospace Center (DLR), Wessling, Germany

Frank de Morsier École Polytechnique Fédérale de Lausanne, LTS 5, Lausanne, Switzerland

Denise Dettmering Deutsches Geodätisches Forschungsinstitut (DGFI), Munich, Germany

Ana F. Domingues Geophysics Centre of Évora, University of Évora, Évora, Portugal

Sabrina Eberle German Aerospace Center (DLR), Wessling, Germany

Alata Elatawneh Institute of Forest Management (IFM), Technische Universität München (TUM), Munich, Germany

Theodor Foerster Institute for Geoinformatics, University of Muenster, Muenster, Germany

Thomas Fuhrmann Geodetic Institute (GIK), Karlsruhe Institute of Technology (KIT), Karlsruhe, Germany

Dorothy Furberg Division of Geoinformatics, Department of Urban Planning and Environment, Royal Institute of Technology, Stockholm, Sweden

Volker Gass Swiss Space Center, École Polytechnique Fédérale de Lausanne, Lausanne, Switzerland

Mario A. Gomarasca CNR-IREA, Institute for Electromagnetic Sensing of the Environment, Milan, Italy

Martin Habermeyer German Aerospace Center (DLR), Wessling, Germany

Bernhard Heck Geodetic Institute (GIK), Karlsruhe Institute of Technology (KIT), Karlsruhe, Germany

Stefan Hinz Institute of Photogrammetry and Remote Sensing (IPF), Karlsruhe Institute of Technology (KIT), Karlsruhe, Germany

Danielle Hoja Remote Sensing Technology Institute, German Aerospace Center (DLR), Wessling, Germany

Georg Kaspar Center for Digital Media, University of Muenster, Muenster, Germany

Mengistie Kindu Institute of Forest Management (IFM), Technische Universität München (TUM), Munich, Germany

Andreas Knöpfler Geodetic Institute (GIK), Karlsruhe Institute of Technology (KIT), Karlsruhe, Germany

Thomas Krauss Remote Sensing Technology Institute, German Aerospace Center (DLR), Wessling, Germany

Jukka M. Krisp Technische Universität München (TUM), Bauingenieur- und Vermessungswesen, Kartographie (LFK), Munich, Germany

Christoph Küchler RUAG Schweiz AG, Emmen, Switzerland

Pavan Kulkarni Geophysics Centre of Évora, University of Évora, Évora, Portugal

Xiaoguang Luo Geodetic Institute (GIK), Karlsruhe Institute of Technology (KIT), Karlsruhe, Germany

Christine Makasy German Aerospace Center (DLR), Wessling, Germany

Vivanco Mauricio Department of Geography, University of Concepción, Barrio Universitario, Concepción, Chile

Michael Mayer Geodetic Institute (GIK), Karlsruhe Institute of Technology (KIT), Karlsruhe, Germany

Arnulf Melzer Limnological Institute, Technische Universität München, Munich, Germany

Liqiu Meng Department of Cartography, Technische Universität München, Munich, Germany

Xiaolin Meng Department of Civil Engineering, The University of Nottingham, Nottingham, UK

Roderic Molina Geographical Information Systems International Group—GISIG, Via Piacenza 54, Genoa, Italy

Antonios Mouratidis ESA/ESRIN, Via Galileo Galilei, Frascati, Italy

Helmut Mühle German Aerospace Center (DLR), Wessling, Germany

Rupert Müller German Aerospace Center (DLR), Wessling, Germany

Roland Pail Institute of Astronomical and Physical Geodesy, Technische Universität München, Munich, Germany

Stefan Peters Department of Cartography, Technische Universität München, Munich, Germany; Technische Universität München (TUM), Bauingenieur- und Vermessungswesen, Kartographie (LFK), Munich, Germany

M. Lucrecia Pettinari Department of Geography, University of Alcala, Alcalá de Henares, Spain

Johannes Rahlf Institute of Forest Management (IFM), Technische Universität München (TUM), Munich, Germany

Adelheid Rappl Bavarian State Institute of Forestry (LWF), Freising, Germany

Peter Reinartz Remote Sensing Technology Institute, German Aerospace Center (DLR), Wessling, Germany

Albert Remke 52°North GmbH, Muenster, Germany

Sebastian Roessler Limnological Institute, Technische Universität München, Munich, Germany

Carolina Rojas Department of Geography, University of Concepción, Barrio Universitario, Concepción, Chile

Francesco Sarti ESA/ESRIN, Via Galileo Galilei, Frascati, Italy

Andreas Schenk Geodetic Institute (GIK), Karlsruhe Institute of Technology (KIT), Karlsruhe, Germany

Michael Schmidt Deutsches Geodätisches Forschungsinstitut (DGFI), Munich, Germany

Thomas Schneider Limnological Institute, Technische Universität München, Munich, Germany; Institute of Forest Management (IFM), Technische Universität München (TUM), Munich, Germany

Opazo Sergio Facultad de Ciencias, Universidad de Magallanes, Punta Arenas, Chile

Bolelang Sibolla Geomatics Division, School of Architecture, Planning and Geomatics, University of Cape Town, Cape Town, South Africa

Ana Maria Silva Geophysics Centre of Évora, University of Évora, Évora, Portugal; Department of Physics, University of Évora, Évora, Portugal

Julian Lloyd Smit Geomatics Division, School of Architecture, Planning and Geomatics, University of Cape Town, Cape Town, South Africa

Tobias Storch German Aerospace Center (DLR), Wessling, Germany

Ulrike Sturm-Hentschel Institute of Photogrammetry and Remote Sensing (IPF), Karlsruhe Institute of Technology (KIT), Karlsruhe, Germany; Institute of Regional Sciences, Karlsruhe Institute of Technology (KIT), Karlsruhe, Germany

Antje Thiele Institute of Photogrammetry and Remote Sensing (IPF), Karlsruhe Institute of Technology (KIT), Karlsruhe, Germany

Jean-Philippe Thiran École Polytechnique Fédérale de Lausanne, LTS 5, Lausanne, Switzerland

Paolo Villa CNR-IREA, Institute for Electromagnetic Sensing of the Environment, Milan, Italy

Adrian Vogel RUAG Schweiz AG, Emmen, Switzerland

Joachim Vogt Institute of Regional Sciences, Karlsruhe Institute of Technology (KIT), Karlsruhe, Germany

Yanbin Wang China University of Mining and Technology, Beijing, China

Malte Westerhaus Geodetic Institute (GIK), Karlsruhe Institute of Technology (KIT), Karlsruhe, Germany

Patrick Wolf Limnological Institute, Technische Universität München, Munich, Germany

Jiantong Zhang Department of Cartography, Technische Universität München, Munich, Germany

Yueqin Zhu Department of Cartography, Technische Universität München, Munich, Germany; China University of Mining and Technology, Beijing, China

Introduction

The general research topic "earth observation of global changes" covers many disciplines and challenges. Therefore, the contributions within this book are organized under the general headings of Physical Geodesy, Photogrammetry and Remote Sensing, Global Change and Change Detection, and Spatial Modeling, GIS and Geovisualization.

Physical Geodesy

The main tasks of Physical Geodesy are to determine the figure of the Earth, its orientation and rotational motion in inertial space, and its gravity field, as well as their temporal changes. The first issue includes the highly precise determination of positions and kinematics of the solid Earth's surface, but also the variations of the ocean surface due to ocean currents or sea level rise. The second issue deals with the highly precise determination of the Earth's rotation axis in global space and its changes due to irregular rotation motion resulting from a temporally changing moment of inertia. The gravity field defines a physical, equipotential reference surface and thus serves as zero surfaces for vertical reference frames, with respect to which small changes resulting from geophysical surface and subsurface processes can be described. Temporal gravity field variations reflect mass transport processes in our system Earth related to the global hydrological cycle, ice mass melting, ocean circulation, or atmospheric processes. Correspondingly, physical geodesy measures the Earth system processes from the deep Earth's interior up to the upper atmosphere.

In two contributions to this book, selected fields of Physical Geodesy are addressed. The first paper by PAIL reviews the huge gain of knowledge on the Earth's static and time-variable gravity field during the last decade due to dedicated satellite gravity missions such as CHAMP, GRACE, and GOCE. While GRACE has revolutionized our knowledge on global mass transport processes such as the global water cycle and ice mass melting in Greenland and Antarctica, GOCE is providing an unprecedented high-resolution picture of the static gravity field. Apart from the progress of global gravity field modelling based on these new satellite data, with emphasis on the contribution of the ESA mission GOCE, the

paper also gives insight into the impact of this improved knowledge of the global gravity field on our understanding of system Earth.

The second contribution by Zhang et al. deals with the ionized component of the upper Earth's atmosphere. Here, the free electrons and ions influence propagation of electromagnetic waves. Apart from contributing to improve the understanding of the physics of the atmosphere, it is also crucial for the processing of geodetic space techniques and remote sensing, because it influences the travel times of the primary signals. In this paper, the monitoring of the total electron content (TEC) is discussed, which is usually measured by dual-frequency GNSS. The paper investigates the optimum combination of GNSS occultation observations with information derived from low-Earth orbiting satellites, such as the altimeter satellites Envisat, Jason-1, and Jason-2 in order to enhance global vertical TEC maps. It could be shown that improvement from these additional data sources can be achieved in areas with good data coverage.

Photogrammetry and Remote Sensing

High-resolution remote sensing techniques operate in different spectral bands, from high-resolution radar satellite missions such as TerraSAR-X and TanDEM-X to optical and hyper-spectral sensors such as the RapidEye constellation or in the near-future EnMAP mission. They monitor with very high accuracy and spatial resolution the geometry of the Earth's surface, resulting in global digital terrain models with resolutions of a few meters, and also their temporal changes. Thus, they are used to derive 3-D surface deformations resulting from large Earthquakes, to monitor volcanoes, and to derive velocity fields of ice sheets and glaciers. Additionally, surface changes due to hydrology or and ice mass melting can be observed, enabling to compute volume changes and, assuming density to be known, mass balance estimates, which are important quantities to monitor natural global change processes. Remote sensing techniques provide cost-effective tools for monitoring physical quantities of components of the Earth's system. Thus they are also widely used for monitoring, mapping, and assessing of damage related to natural disaster events.

Eight contributions to this book treat techniques from Photogrammetry and Remote Sensing for a variety of applications related to different components of the earth system, e.g., monitoring of settlement changes, forests, invasive aquatic plants, and flash-flood or determination of atmospheric water vapor and ozone variation.

The contribution by De Morsier et al. describes the registration of airborne videos with reference images based on a phase-correlation approach. The task of image to image registration is frequently addressed in the literature for change detection by comparison of images taken at different time. An application named by the authors is the provision of up-to-date images for quick assessment of damaged areas after natural hazards. They show one example that their approach performs better than an approach using mutual information.

The contribution by Storch et al. gives an overview about the ground segment design of the Environmental mapping and analysis program (EnMAP) and describes the image processing chain for the intended products on different levels. The major

objectives of the first German hyperspectral satellite remote sensing mission are to measure, derive, and analyze diagnostic parameters, which describe vital processes on the Earth's surface encompassing agriculture, forestry, soil, and geological environments, as well as coastal zones and inland waters. Those geochemical, biochemical, and biophysical parameters are assimilated in physically based ecosystem models, and ultimately provide information reflecting the status and evolution of various terrestrial ecosystems.

The contribution by Sturm-Hentschel et al. focuses on the methodology for detecting and characterizing settlement changes in developing countries using very high spatial resolution (VHSR) data. In many developing countries, coastal areas show high dynamics of settlement structures, which are hardly regulated by regional planning and therefore give rise to a series of risks. Most of all, increasing settlement density and spread in areas close to the shoreline and into wetland areas appear worrying against the background of climate change and sea level rise. An approach based on both manual and segment-based (semi-)automatized building detection is described and discussed for the coastal area of Benin. Results are used to analyze the settlement process and model its further evolution by data-driven modeling.

In the contribution by Schneider et al. the potential of high-resolution satellite data for forest management planning and disaster management is investigated, driven by the fact that an increase of forest damages by natural hazards can be observed. It is emphasized that added value can be achieved by a combination of multispectral data (using the RapidEye constellation) and SAR data (TerraSAR-X). It could be shown that such a concept is appropriate to deliver relevant information for interim forest inventories, but not yet with a quality which were required for decision making. However, this situation will change with future remote sensing systems.

The contribution by Roessler et al. presents an approach to monitor invasive aquatic plants (Elodea nuttallii and Najas marina) by multiseasonal multispectral remote sensing data (RapidEye). These invasive species have been subject of multidisciplinary research for several years, as it is assumed that increasing water temperature promotes their expansion. Submerged macrophytes in freshwater lakes are used as longterm indicators for nutrient conditions. Climate change is thought to favour invasive submersed macrophytes in freshwater ecosystems and therefore to have profound influence on lake ecosystems. The information about the current state of the water body is used to produce depth-invariant combinations of spectral bands using a simple physically-based semiempirical method. In situ reflectance measurements were processed with the same method and subsequently used in a Matched Filtering spectral unmixing approach. The results show a good separation between vegetated and bare littoral areas. A reliable differentiation of plant species still requires further method development.

The contribution by Mouratidis and Sarti deals with the satellite-based monitoring of floods, which are one of the most significant natural disaster events. Remote sensing tools enable a cost-effective monitoring and mapping, but also assessment of the damages caused by floods. As selected case study regions the Balkans and several countries in East Europe are used to investigate the feasibility of SAR techniques, and their efficiency in terms of spatial and temporal resolution. Especially the latter

one turns out to be a challenge, where currently the required high repetition rate of SAR acquisitions is currently the limiting factor. Based on this analysis, the challenges and data requirements for future remote sensing missions are discussed.

The contribution by Alshawaf et al. investigates the combination of InSAR and GNSS observations to determine the atmospheric water vapor content in the troposphere, which also causes a signal delay in microwave signals. Therefore, the wet atmosphere is one of the major error sources of (interferometric) SAR applications. While with GNSS techniques the temporal variability can be estimated for a spatially sparse array, the InSAR technique provides not only point information, but also spatial water vapor variations for a whole area. The combination of these two complementary data sources has a high potential to improve spatio-temporal modeling of the wet atmosphere, and thus to compute more reliable signal delays of remote sensing systems.

The contribution by Domingues et al. investigates the seasonal variation of ozone in Portugal. Ozone plays a relevant role in controlling the chemical composition of the atmosphere, in the troposphere it is harmful to humans and plants, and it is a component of smog and an important greenhouse gas. Results were derived from spectral measurements using the terrestrial UV-Vis. Spectrometer for Atmospheric Tracers Measurements. The ground-based results are also compared with data from Ozone Monitoring Instrument (OMI) onboard Aura Satellite.

Global Change and Change Detection

Global change and change detection involves the challenging research and development questions such as how the huge amounts of sensory data and mapping data can be effectively and efficiently archived, accessed, disseminated, and integrated, what types of gradual or abrupt changes are relevant for which target groups and which applications, which methods or algorithms are available, adaptable, or still missing for the detection of the various changes. These questions are tackled by five papers in the book.

The paper from Foerster et al. is dedicated to the dissemination of large volume sensor data about global change. Based on the analysis of bottlenecks in existing approaches that are file-based, service-based, or satellite-based, the authors proposed a hybrid approach using a satellite-based system for accessing sensor data on distributed nodes and then disseminating the data in the Internet through web services. The interoperable web service interfaces allow on the one hand the providers to upload the data with appropriate metadata and on the other hand the users to directly integrate the data into their research work on global change. Two case studies with raster-based and feature-based data have been implemented using free and Open Source Software, thus proved the feasibility of the hybrid approach.

Villa et al. address in their paper a topic on harmonisation of geodata and services with a platform called HUMBOLDT in line with the European Spatial Data Infrastructure (ESDI). Two test scenarios—protected areas and maritime themes—were implemented to demonstrate the usefulness and capabilities of harmonization approach. The scenario of protected areas was designed to seamlessly transform the structure and geometry of protected areas from multiple sources at different

governance levels for the purposes of planning, management, and tourism promotion. The ocean scenario was based on a centrally running geoportal with a portrayal interface that allows users such as policy makers and scientists to view information about oil and chemical spills in three regions over European Seas and answer common queries.

The paper by Hoja et al. deals with damage assessment in the post-crisis phase, taking the Haiti Earthquake as an example. A number of (semi)automatic methods of change detection were applied to the satellite data of the capital town of Port-au-Prince and compared with manual measurements as well as the database of the Haiti Action Plan for Reconstruction. Among others, the image differencing and the Iteratively reweighted multivariate alteration detection (IR-MAD) algorithm incorporating texture information can run automatically. According to the authors, the IR-MAD algorithm could reveal a correctness of 89 %, which is at least as good as the performance of image differencing. 3-D changes in heights and volume of buildings or other objects can also be detected, but not yet verified due to hard accessibility of 3-D reference data.

Furberg and Ban reported their research work on the environmental impact assessment based on the urban land cover changes of Stockholm between 1986 and 2006. They adopted four scenes of SPOT imageries over Stockholm as test data, transformed them into seven land cover categories. Depending on factors such as proportion and condition of green areas, proximity of these areas to intense urban land use, proportion of urban areas in their immediate vicinity, and the noise level, an environmental impact index reflecting the urban growth is derived. The index scores of the individual analysis units can then be measured and ranked. The authors found out the varying changes from the center to the north and east of the Stockholm area. These findings are intended to serve as decision support for ecological urban planners.

The paper by Rojas et al. is focused on the identification of representative land cover and land use scenarios in the metropolitan area of Concepción in Chile before and after the recent earthquake. Based on a temporal analysis of satellite image classifications, they revealed and evaluated the significant land use and land cover changes. Maps were also used for the verification of their study. According to the authors, it was most difficult to identify the beach class which may be mixed either with the open lands or with the cliff due to its low spectral contrast. The recognition of wetlands and forests areas also proved rather complex. A wetland is per definition a humid land belted by water, but it can contain vegetation which may be recognized as grasslands. The detection accuracy of forests, on the other hand, depends very much on the presence and the growing phase of the trees.

Spatial Modelling, GIS and Geovisualization

As this book covers a very wide range of topics the last part includes four papers covering different ground. Therefore, this part of the book is summarized under the general topic of spatial modeling, Geographic Information Systems (GIS), and Geovisualization. Spatial modelling and GIS go hand in hand in the research papers, with GIS used as a sophisticated tool to model real world spatial relations. More

particular, the papers include investigations on a spatial GIS-based model on fire occurrences, a study on the average global fire rates. Additionally, the process of geovisualization is extended with a directed kernel density method suggesting one way how to deal with dynamic densities in a visual way. Furthermore, the achievements of how GNSS can contribute to a spatial model dealing with structural monitoring are examined in one case study.

On a general level, the paper by Sibolla and Smit explores the level of integration that can be achieved between fire modeling, as a division of environmental modelling and GIS. It focused the role of GIS in predictive fire modelling and fire management. A model developed for the important aspects of fires, like fire behaviour and fire spread is investigated. Within the paper, they develop a detailed grid-based model and suggest to extent this toward a GIS-based decision support tool.

The paper from Krisp et al. is focused on the visualization of dynamic points. The authors suggest to apply a directed kernel, based on the movement direction of each point to calculate and visualize the density. Using this method has the advantage to show the hot spot densities and indicate the movement direction of each hot spot. The paper uses a case study of a crowd of people approaching the Munich soccer stadium, and shows how particular dense parts of the crowd are moving.

The paper from Pettinari and Chuvieco investigates the correlation between the global average fire density (AFD) and variables such as lightning discharges and population density. The analysis of the association between the global average fire density and its causative agents show diverse results depending of the fuel types present. In particular, their findings show a positive correlation between the fire density and lightning with the highest coefficient values corresponding to shrubs and grasses on the tropical dry and temperate wet climates.

The contribution by Meng investigates the recent achievements in Global Navigation Satellite Systems (GNSS)-based bridge structural health monitoring (SHM) research and development. Within this paper, the author introduces the concepts of integrated monitoring and processing for the formation of a regional geo-hazard early warning system. The architecture of such a system is presented with the findings drawn from analyzing real-life monitoring data sets. The author proposes a setup to integrate the monitoring sensors installed on the slender structures such as long suspension bridges with GNSS continuously operational reference stations (CORSs) for geo-hazard monitoring and early warning purposes.

Part I
Physical Geodesy

Global Gravity Field Models and Their Use in Earth System Research

Roland Pail

Abstract The launch of dedicated gravity satellite missions such as CHAMP, GRACE and GOCE has revolutionized our knowledge of the Earth's gravity field. Since the gravity field reflects mass distribution and mass transport through the complex system Earth, a precise knowledge of the global gravity field and its temporal variations is important for many areas of Earth system research, such as solid Earth geophysics, oceanography, hydrology, glaciology, atmospheric and climate research. In this paper the progress of global gravity field modelling based on satellite data is reviewed, with special emphasis on first results of the ESA mission GOCE, where the new observation type of satellite gradiometry enables to derive high-resolution static gravity field models. Additionally, first combined satellite-only gravity field models based on GRACE and GOCE, making benefit of the individual strengths of these two missions, are addressed, and the application of these gradually improving gravity field models in several fields of geoscientific research is discussed.

1 Introduction

The Earth's gravity field reflects the mass distribution and its transport in the Earth's interior and on its surface. In 2000, the era of dedicated satellite gravity missions began with the launch of CHAMP (CHAllanging Minisatellte Payload; Reigber et al. 2002), followed by the launches of GRACE (Gravity Recovery And

R. Pail (✉)
Institute of Astronomical and Physical Geodesy, Technische Universität München, München, Germany
e-mail: pail@bv.tum.de

J. M. Krisp et al. (eds.), *Earth Observation of Global Changes (EOGC)*, Lecture Notes in Geoinformation and Cartography, DOI: 10.1007/978-3-642-32714-8_1,

Climate Experiment; Tapley et al. 2007) in 2002, and GOCE (Gravity field and steady-state Ocean Circulation Explorer; Drinkwater et al. 2003) in 2009. Based on data of these missions, global Earth's gravity field models with homogeneous accuracy and increasingly high spatial resolution could be derived.

The Earth's gravitational potential V is usually parameterized in terms of coefficients of a spherical harmonic series expansion in spherical coordinates (with radius r, co-latitude ϑ, longitude λ):

$$V(r,\vartheta,\lambda) = \frac{GM}{R}\sum_{n=0}^{N_{\max}}\left(\frac{R}{r}\right)^{n+1}\sum_{m=0}^{n}\bar{P}_{nm}(\cos\vartheta)[\bar{C}_{nm}\cos(m\lambda)+\bar{S}_{nm}\sin(m\lambda)] \quad (1)$$

$\bar{P}_{nm}$ where G is the gravitational constant, M the mass of the Earth, R the mean Earth radius, $\bar{P}_{nm}$ the fully normalized Legendre polynomials of degree n and order m, and$\{\bar{C}_{nm};\bar{S}_{nm}\}$ the corresponding coefficients to be estimated.

Satellite gravity missions measure derived quantities of the gravitational potential V, depending on their specific measurement concept. Since they are the only measurement technique which can directly observe mass changes on a global scale, they are a unique observational system for monitoring mass redistribution in the Earth system.

The high-resolution static gravity field, represented by the geoid, serves as a unique physical reference surface. It is not only used in geodesy to define height systems, but also in a variety of geoscientific disciplines. Since it represents the surface of an ideal ocean at rest, in oceanography it is compared with the actual ocean surface, which can be derived by satellite altimetry. Thus, the so-called mean dynamic topography (MDT) can be computed, from which geostrophic ocean surface currents can be derived. These ocean currents are, beside the atmosphere, the second largest mechanism for global heat transport through the Earth system. High-resolution static gravity field models also provide boundary values for geophysical models of lithospheric structures and dynamic processes in the Earth's mantle and crust.

Temporal gravity variations, as they can be derived from the GRACE mission, are a direct measure of mass variations and thus are able to monitor mass transport processes in land hydrology, cryosphere, ocean, and atmosphere. Thus, the determination of the gravity field can contribute to derive ice and water mass balance. Non-gravimetric methods are based on the observation of the individual contributors to mass balance. As an example, in the case of land hydrology these are precipitation P, evapo-transpiration ET and surface run-off R.

$$P - ET - R = \Delta S \quad (2)$$

These individual components are difficult to observe homogeneously on a global scale and therefore are only inaccurately known, leading to large error margins also for the resulting mass balance equation. The unique quality of gravity field measurements is the fact that they directly measure the right-hand side of the mass balance Eq. (2), i.e., storage changes ΔS representing the sum of all

contributors to mass balance. Of course, also global gravity field estimates suffer from several error sources, such as the separability of different sources composing the gravity field signal, errors in geophysical background models, and limitations in spatial and temporal resolution. In spite of this fact, gravimetric methods offer the possibility of closing the Earth mass budget comprising the effect of various interacting processes within the Earth system. With a global view of mass transport, they provide a unique framework in which the results from other Earth observation missions monitoring certain Earth's subsystems can be related to each other, and they are an important contributor to the monitoring of several Essential Climate Variables (ECVs; Liebig et al. 2007).

In the present paper, a brief review of important results of a decade of gravity field observation from space is given in Sect. 2, and the achievable performance is evaluated. Based on the continuously improving accuracy and spatial resolution of these models, in Sect. 3 the added value of combined global gravity field models derived from GRACE, GOCE and complementary gravity data is evaluated, and potential applications in Earth science are discussed in Sect. 4. Finally, Sect. 5 provides the main conclusions and an outlook to future research activities.

2 Satellite Gravity Missions: Status and Results

2.1 CHAMP

After a series of satellite laser ranging (SLR) missions, from which the very long-wavelength component of the Earth's gravity field could be and is still derived by orbit analysis, a new era of gravity field determination from space began with the launch of the first dedicated gravity field mission CHAMP in 2000 into a low Earth orbit (450 km altitude). CHAMP was equipped with a space-borne GPS receiver enabling continuous 3D tracking of the satellite using the GPS constellation. This so-called high-low satellite-to-satellite tracking constellation (SST-hl) provided a completely new opportunity to determine the long wavelength static gravity field with unprecedented accuracy. In addition, CHAMP was the first satellite being equipped with an accelerometer dedicated to observe the non-gravitational accelerations acting on the satellite, like air drag, solar radiation pressure and Earth albedo. For the first time a homogeneous global gravity field model could be derived from a single satellite. Several static models have been computed, which outperformed all previous satellite-only solutions in the long wavelengths (up to degree and order 70) at least by a factor of ten (e.g., Reigber et al. 2002; Gerlach et al. 2003). Today, CHAMP-only gravity field solutions up to degree 100 are available.

The magenta curve in Fig. 1 shows the performance of the model AIUB-CHAMP03S (Prange et al. 2011) in terms of the degree error median

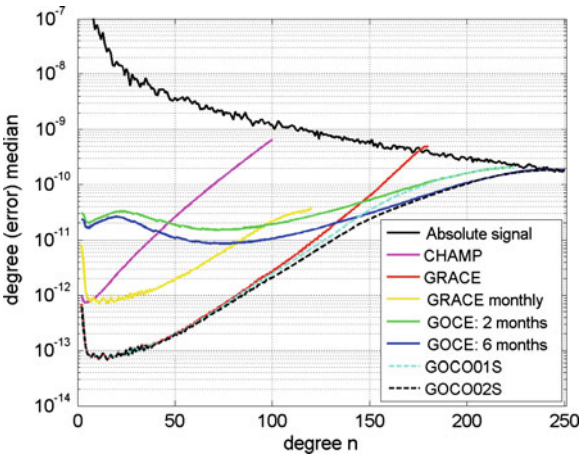

Fig. 1 Degree error medians of several global gravity field models

$$\sigma_n = median_m\left\{\sigma_{\bar{C}_{nm}}; \sigma_{\bar{S}_{nm}}\right\}, \tag{3}$$

where $\left\{\sigma_{\bar{C}_{nm}}; \sigma_{\bar{S}_{nm}}\right\}$ denote the formal coefficient error estimates of the gravity field model. It represents the error per harmonic degree n and thus per spatial (half) wavelength λ, according to $\lambda = 20{,}000\ \text{km}/n$.

As a reference, the absolute gravity field signal is displayed as black curve. Evidently, a signal-to-noise ratio of one is reached at a degree of about $n = 100$.

After 10 years of successful operation and decreasing orbit altitude, the CHAMP mission passed away on 19 September 2010.

2.2 GRACE

In 2002 the along-track satellite formation mission GRACE was launched into a near polar low Earth orbit (500 km altitude). Apart from high-low satellite-to-satellite tracking by the GPS constellation for each individual satellite, the key element is a K-band microwave ranging system observing the distance variation between the two satellites with micrometer accuracy. This type of mission is called a low–low satellite-to-satellite tracking constellation (SST-ll). In addition, for observing the non-gravitational accelerations again an accelerometer has been located in the centre of mass of each satellite. The GRACE mission has two main goals: (1) the determination of the static field up to medium wavelengths (degrees 100–150) with unprecedented accuracy, and (2) the determination of the long wavelength time variations of the gravity field. The most recent static models derived purely from GRACE data resolve the global gravity field up to degree 180, e.g., GGM03S (Tapley et al. 2007), EIGEN-5S (Förste et al. 2008), AIUB-GRACE02s (Jäggi et al. 2009), and ITG-Grace2010S (Mayer-Gürr et al. 2010). The red curve in Fig. 1 shows the performance of one of the best currently available

GRACE models ITG-Grace2010S, resolved up to degree/order 180. Compared to CHAMP, the superior measurement principle of SST-ll results in a significantly better performance in the low to medium wavelength range as well as a higher spatial resolution.

The GRACE mission opened the possibility to derive the non-tidal, temporal variations in the gravity field from space by solving for monthly gravity field models. The analysis of monthly fields allows to monitor the continental water storage variations, and to estimate the mass balance of ice sheets. Monthly solutions are routinely provided by the research institutions GFZ, CSR, JPL, and ITG (University of Bonn). Additionally, GRGS provides 10 days interval solutions (Bruinsma et al. 2010a). Even daily solutions based on a Kalman filter approach are computed by ITG (Kurtenbach et al. 2009). Regional solutions, independent of spherical harmonic fields and obtained using alternative approaches, have been computed by the Ohio State University (Han et al. 2005) and the NASA Goddard Space Flight Center (Lemoine et al. 2007). The yellow curve in Fig. 1 shows the achieved accuracy of a typical monthly GRACE solution.

Spectacular science results have been achieved by the analysis of GRACE data. As an example for cryospheric applications, the mass loss of the Greenland ice sheet has been observed to be in the order of 100–200 gigatons per year (e.g., Wouters et al. 2008; Velicogna 2009), and a significant negative trend of the integral Antarctic ice mass since 2002 was observed by GRACE-based studies (Horwath and Dietrich 2009). Figure 2 shows mass balance estimates for Greenland and Antarctica applying different methods, as they have been collected by Allison et al. (2009). Although they almost unambiguously show ice mass loss, the absolute value differs considerably, and still large uncertainties persist. This is not only due to methodological differences. In the case of the GRACE results, the main error sources are the separability of the gravity signal of ice from other gravity field contributors, such as glacial isostatic adjustment (GIA) in reaction to ice load changes, errors of other geophysical background models (atmosphere, ocean) applied during the GRACE processing, as well as the restricted spatial and temporal resolution leading to aliasing effects.

GRACE is also able to monitor the global hydrological cycle, both, concerning inter-annual variations and emerging trends of continental water storage. As an example, based on GRACE data the ground water depletion in Northern India could be detected (Tiwari et al. 2009), thus monitoring the loss of non-renewable drinking water resources from space. Nowadays, GRACE data are already assimilated into hydrological models or are used for their calibration (Werth et al. 2009a).

Since GRACE takes measurements only in one direction (along-track), the resulting error structure is highly anisotropic, which is one reason for the typical striping pattern of monthly gravity field solutions. The necessary filtering applying different methods (Werth et al. 2009b) limits the achievable spatial resolution of these monthly temporal GRACE solutions to 400–500 km. With sophisticated filter strategies spatial resolutions even down to 300 km seem to be possible.

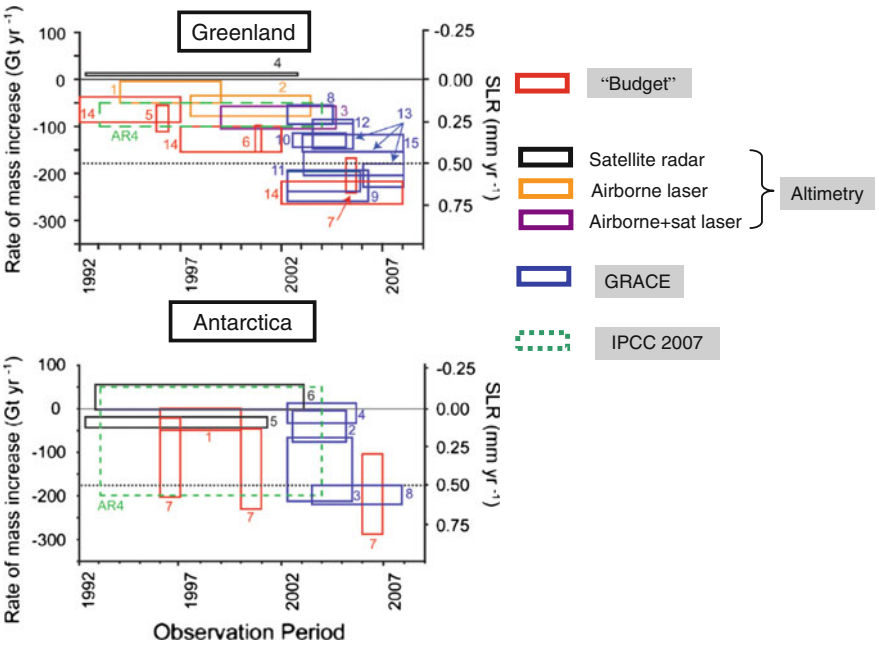

Fig. 2 Ice mass trends for Greenland (*top*) and Antarctica (*bottom*) derived by different methods indicated by colors; the graphics show the rate of mass increase/loss and the resulting sea level rise (SLR); from: Allison et al. (2009), modified

After 9 years of successful and almost continuous operation, battery problems might force the future mission scenario to hibernation phases, in order to monitor as a minimum mass variation trends until 2014/15. A GRACE follow-on mission is foreseen to be launched in August 2017.

2.3 GOCE

The GOCE satellite was successfully launched on 17 March 2009, and started its operational phase in September 2009. GOCE is based on a sensor fusion concept: SST-hl using GPS orbit information, as it is done for the CHAMP mission, plus on-board satellite gravity gradiometry (SGG). This completely new measurement concept is based on the observation of gravitational gradients (representing second order derivatives of the Earth's gravitational potential) in space with accelerometers over short baselines from a platform flying in drag-free mode, i.e. by in-situ compensating the non-gravitational forces. By measuring these gravity gradients, it is the first mission that observes direct functionals of the Earth gravity field from space, and not only the indirect influence of the gravity field on the spacecraft orbits. Further, whereas the GRACE observables (ranges and range rates between the two GRACE satellites) are sensitive in the along-track direction only, the full

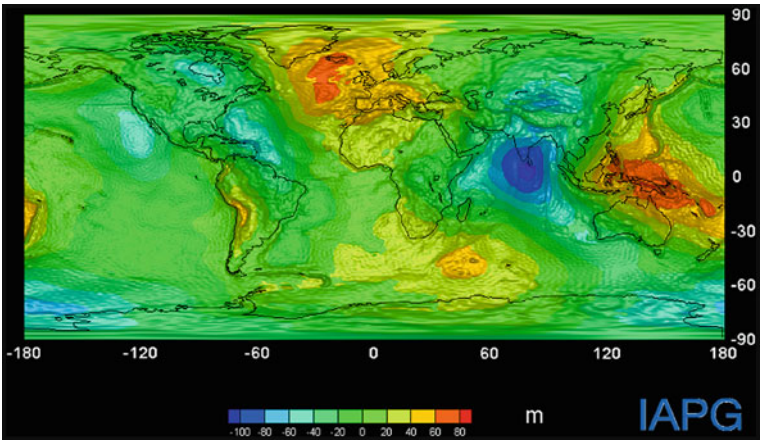

Fig. 3 Time-wise earth gravity field model GO_CONS_CGF_2_TIM_R1 derived from 71 days of GOCE data, expressed in geoid heights [m]

gravitational tensor is measured in-situ by the GOCE gradiometer, thus providing 3D information of the Earth's gravity field with an isotropic error structure.

The GOCE mission is designed to resolve the medium to short wavelengths of the static gravity field (up to a maximum degree and order of 240–250). This higher resolution compared to GRACE is not only possible due to the different observation type of gravity gradients, which is more sensitive to detail structures of the gravity field, but also due to an extremely low satellite altitude of about 255 km, which is achievable only due to the active drag compensation. In contrast, the SST-ll observation technique applied by GRACE is superior in the low to medium wavelengths of the gravity field spectrum.

First GOCE gravity field models based on about 71 days of GOCE data (November 2009 to January 2010) have been computed in the frame of the ESA project "High-Level Processing Facility" (Rummel et al. 2004) by applying 3 independent and complementary processing strategies, the direct (Bruinsma et al. 2010b), time-wise (Pail et al. 2010a), and space-wise (Migliaccio et al. 2010) method, and have been made publicly available in July 2010. An overview of the processing strategies and an evaluation and validation of the results can be found in Pail et al. (2011). Figure 3 shows the gravity field solution of the time-wise method GO_CONS_CGF_2_TIM_R1, which is a pure GOCE solution without any gravity field prior information, in terms of geoid heights.

The green curve in Fig. 1 shows the corresponding formal error estimates of this gravity field model, resolved up to degree/order 224, in terms of degree error medians. GOCE starts to become superior over GRACE approximately at degree $n = 150$. Below, GRACE shows a better performance due to its SST-ll concept and the larger data volume. Generally, the independently obtained results of GRACE and GOCE show a striking consistency in the low to medium degrees,

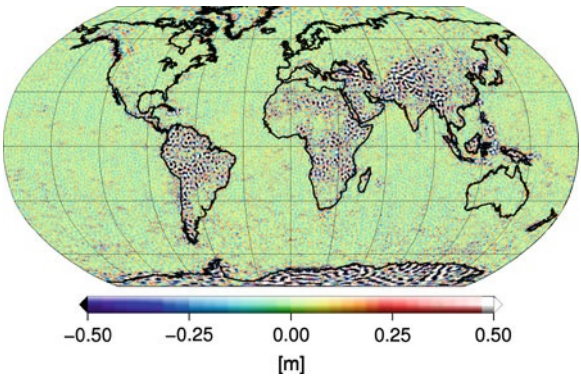

Fig. 4 Geoid height differences between GOCE model GO_CONS_CGF_2_TIM_R1 and combined gravity field model EIGEN-5C up to degree/order 200

demonstrating that both missions are reasonably calibrated, and no major systematic errors are inherent in the gravity field models derived from them.

A comparison of this solution against the combined gravity field model EIGEN-5C (Förste et al. 2008), which includes GRACE, terrestrial gravity field and satellite altimetry data, reveals interesting and promising features. Figure 4 shows geoid height differences between GOCE and EIGEN-5C, resolved up to degree/order 200. They show a high consistency (small differences) for Europe, Northern Asia, North America, and the open ocean areas.

However, in regions where currently available terrestrial gravity field data are known to be poor, such as South America, Africa, Asia or Antarctica, significant differences show up, demonstating the impact of only 2 months of GOCE data for the gravity field knowledge in these regions.

The release 2 of a time-wise GOCE-only gravity field solution GO_CONS _CGF_2_TIM_R2 based on the data period November 2009 to July 2010 (effectively 6 months after reduction of data gaps and calibration phases) has become publicly available in February 2011. The blue curve in Fig. 1 shows the significant improvement compared to the previous 2 months solution (green curve). As it has to be expected, due to the increase of the data amount by a factor of about 3, the improvement is in the order of $\sqrt{3}$ over a wide spectral range. The cross-over with the GRACE performance has now been decreased from 150 to about 135.

It can be shown that this factor of $\sqrt{3}$ is not only present in the formal errors, but is a real improvement of the gravity field accuracy. For this purpose, gravity anomaly deviations of the 2 months solution GO_CONS_CGF_2_TIM_R1 (top) and the release 2 model GO_CONS_CGF_2_TIM_R2 (bottom) from EIGEN-5C have been computed (Fig. 5), clearly showing the noise reduction over the open oceans and regions with high-quality terrestrial gravity field data incorporated in EIGEN-5C.

Originally, the nominal GOCE mission end was scheduled for April 2011. However, it was decided by ESA to extend the mission until December 2012. Recalling the improvement when including a larger data amount as shown in Figs. 1 and 5, this leaves a very promising perspective. In order to evaluate the impact of GOCE on the global knowledge of the Earth's gravity field and thus on

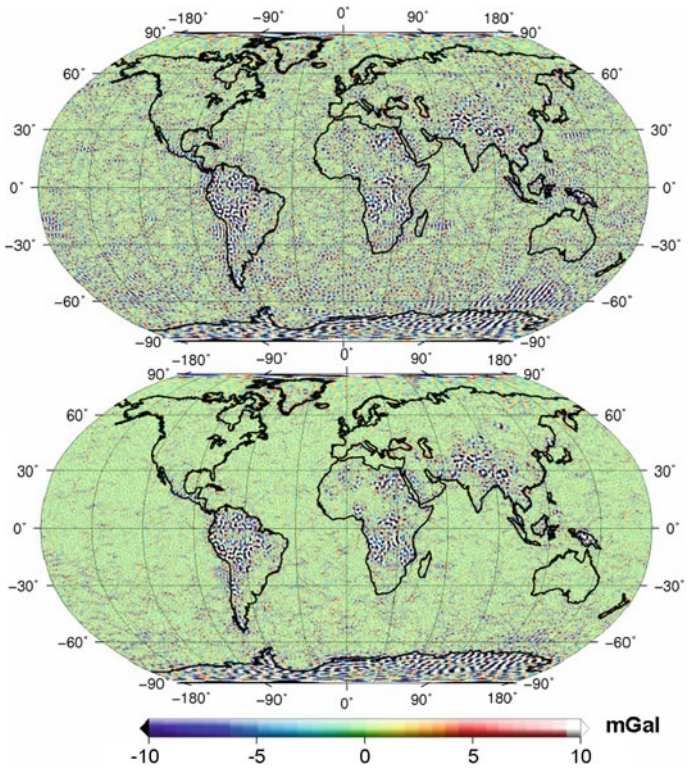

Fig. 5 Gravity anomaly deviations from EIGEN-5C up to degree/order 200: (*top*) GOCE 2 months solution GO_CONS_CGF_2_TIM_R1; (*bottom*) GOCE 6 months solution GO_CONS_CGF_2_TIM_R2

many applications in Earth sciences, Fig. 6 shows cumulative geoid height errors (left) and gravity anomaly errors (right) in dependence of the harmonic degree (spatial resolution). The red and blue curves show the performance of the 2 months and the 6 months solutions, respectively, while the black curve represents a performance prediction assuming a successful GOCE mission (at the present altitude) until end of 2012. The results are 3 cm geoid height error and 1 mGal gravity anomaly error at degree/order 200 (= 100 km half wavelength).

3 Combined Satellite-Only Gravity Field Models

It was discussed in Sect. 2 and shown in Fig. 1 that the GRACE mission shows a better performance than GOCE in the low to medium degrees up to 130–150 due to the SST-ll concept, while beyond GOCE starts to become superior because of SGG. Thus, a consistent combination of these two missions makes optimal benefit of the individual strengths of these two satellite missions. A first satellite-only

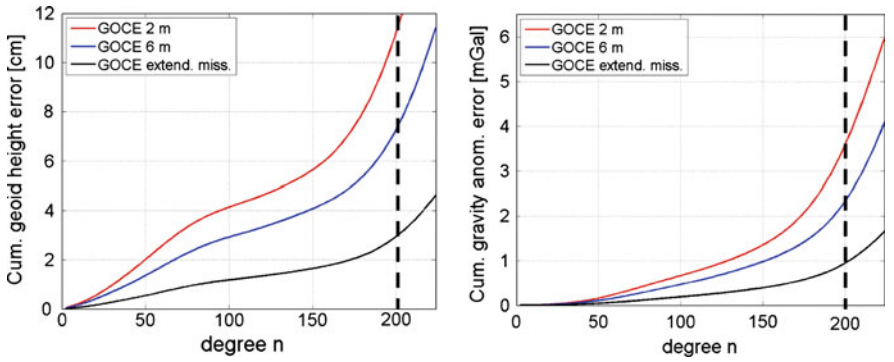

Fig. 6 Cumulative geoid height errors in [cm] (*left*) and cumulative gravity anomaly errors in [mGal] (*right*) for GOCE solutions based on a different amount of data

combined model GOCO01S (Pail et al. 2010b) was computed by addition of normal equations of these two satellite missions, plus some additional constraints to improve the signal-to-noise ratio in the high degrees.

GOCO stands for "Gravity observation combination" and is a joint project intivitative by the Institute of Astronomical and Physical Geodesy, TU München, the Institute of Theoretical and Satellite Geodesy, Graz University of Technology, the Institute of Geodesy and Geoinformation, University of Bonn, the Astronomical Institute, University of Bern, and the Space Research Institute, Austrian Academy of Sciences (www.goco.eu). The main objective is to derive combined global gravity field models from complementary data sources such as the satellite gravity missions GOCE, GRACE and CHAMP, terrestrial gravity field and satellite altimetry data, and SLR.

For GOCO01S, concerning GOCE a slightly improved version of the GOCE normal equations of the time-wise solution based on approximately 2 months of data was used. The improvement is mainly related to a better treatment of some minor data problems of one of the gradiometer components in the South of Australia. Additionally, GRACE normal equations of ITG-Grace2010S (Mayer-Gürr et al. 2010) up to degree/order 180, which are based on GRACE data covering the time span from August 2002 to August 2009, have been used for the combination.

The processing methodology is described in Pail et al. (2010b). Since the lower degrees are well-determined by GRACE, no gravity field information derived from GOCE orbits was included. Figure 7 shows the performance of the individual components and the final model in terms of degree error medians.

The magenta curve represents an unregularized solution which is solely based on 2 months of GOCE gradiometry, while the red curve is related to the GRACE-only solution. The combination solution GOCO01S is displayed as blue dashed curve. As a reference, the GOCE-only model GO_CONS_GCF_2_TIM_R1 is displayed in green color. In addition to SGG, it is based on kinematic GOCE precise science orbits in the low degrees.

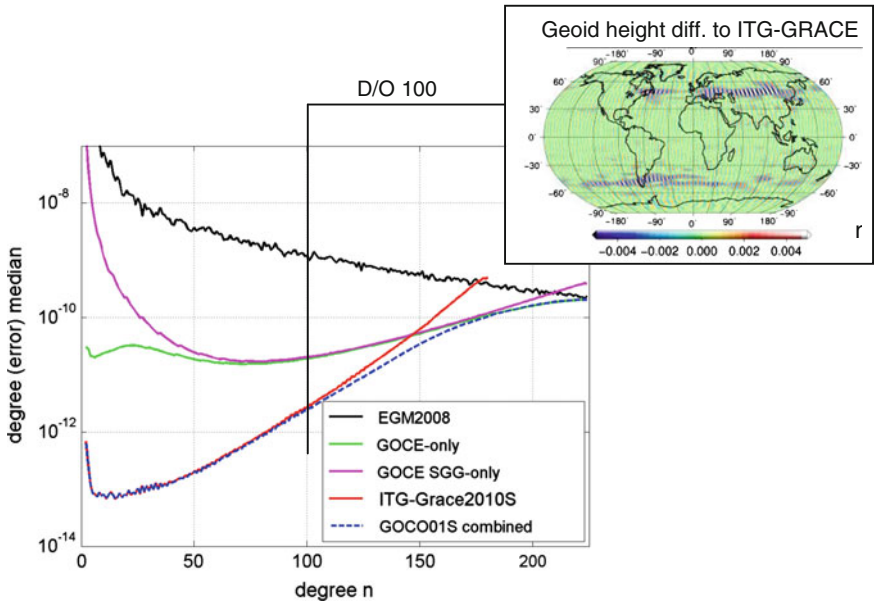

Fig. 7 Degree error medians of the GOCE component (*magenta*), the GRACE component (*red*), and the combined GOCO01S solution (*blue dashed*). As a reference, the GOCE-only SST + SGG solution GO_CONS_GCF_2_TIM_R1 (*green*), and the absolute gravity field signal based on EGM2008 (*black*) are displayed. *Upper right* geoid height differences between GOCO01S and ITG-Grace2010S up to degree/order 100

Analyzing the satellite-only combination model GOCO01S, evidently GOCE starts to contribute already below degree/order 100, shown by the divergent error curves (red vs. blue). In order to illustrate this contribution more lucidly, geoid height differences between GOCO01S and the pure GRACE component ITG-Grace2010S up to degree 100 are visualized in the upper right, revealing patters which are typical for GRACE errors. Thus, it can be concluded that by inclusion of only 2 months of GOCE data the 7 years GRACE solution could be improved by a few millimetres already at degree/order 100.

In June 2011, also a second release of a combined satellite-only model, GOCO02S, was processed. It is based on 8 months of GOCE data (November 2009 to July 2010) and the ITG-Grace2010S model. Additionally, normal equations of 12 months of GOCE GPS-SST, 8 years of CHAMP GPS-SST and 5 years of SLR to 5 satellites have been included. Table 1 summarizes the main features and data used for GOCO01S and GOCO02S.

The performance of GOCO02S is shown as dashed black curve in Fig. 1. Still, the main contributors to this solution are GOCE (dark blue curve) and GRACE (red curve), while the contributions by the additional componenents included in this solution are only very minor. SLR has been adopted in order to stabilize the estimates of the very low degrees. The performance in the high degrees is

Table 1 Main features and data sets used for the combined gravity field models GOCO01S and GOCO02S. Also given is the maximum degree/order (d/o) of resolution and the number of observations contained in the individual normal equations

Data set	GOCO01S d/o 224	GOCO02S d/o 250	GOCO02S #obs. [mio.]
ITG-Grace2010S	d/o 180 7 years	d/o 180 7 years	85
GOCE gradiometry	d/o 224 2 months	d/o 250 8 months	57
GOCE GPS-SST (high-low tracking)	–	d/o 110 12 months	72
CHAMP GPS-SST (high-low tracking)	–	d/o 120 8 years	63
SLR	–	d/o 5 5 years/5 sats.	2
Constraints	d/o 170–224 (Kaula)	d/o 180–250 (Kaula)	–
SUM			280

dominated by the GOCE contributions, and thus is very similar as shown in Fig. 5 for the GOCE-only model.

4 Earth Science Applications

As discussed in Sect. 1, one of the main geoscientific applications of high-resolution static satellite gravity field solutions is oceanography. In order to show the impact of the new GOCE models in this field of application, the mean dynamic topography (MDT), which is defined as the difference of the mean sea surface h and the geoid N,

$$H = h - N \tag{4}$$

has been computed for the region of the Antarctic Circumpolar Current (ACC) on a regular grid of $0.5^\circ \times 0.5^\circ$ using a mean sea surface (DGFI-2010) derived from 17.5 years of data of several altimeter missions (ERS-1, ERS-2, ENVISAT, TOPEX/Poseidon, Jason-1, and Jason-2), and a geoid model. The strategy of the MDT computation and the filtering of the mean sea surface is described in Albertella et al. (2010).

Figure 8 shows the resulting MDT using either the GRACE-only model ITG-Grace2010S or the combined model GOCO01S for computing the geoid. The top row shows the MDT for selected spectral ranges (degrees 90–120, 120–150, and 150–180) when using ITG-Grace2010S.

In addition to oceanographic signals, striping patterns related to GRACE errors are visible in all three spectral windows, but grow in amplitude with increasing degrees. In contrast, when using the GOCO01S model and thus additionally

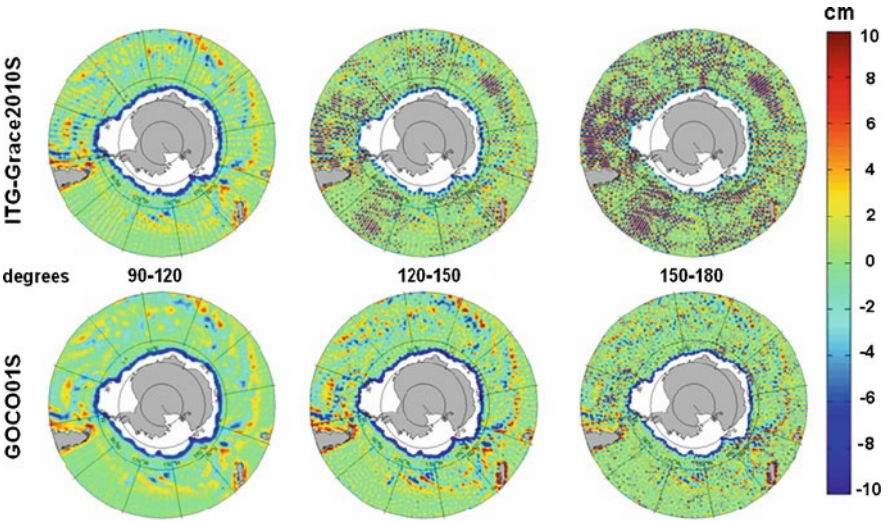

Fig. 8 Mean dynamic topography derived from multi-year and multi-mission satellite altimetry data, and two global geoid models (*top row* ITG-Grace2010S; *bottom row* GOCO01S), analyzed in different spectral windows: (*left*) degrees 90–120; (*centre*) degrees 120–150; (*right*) degrees 150–180

2 months of GOCE data, these error structures almost vanish, and the oceanographic signal becomes more prominently visible. Especially in the spectral window of degrees 150–180 the great contribution by the additional high-resolution information of GOCE is evident.

Applying a simplified form of the Navier-Stokes equation assuming geostrophic conditions, ocean surface velocities can be derived as horizontal derivatives of the mean dynamic topography H:

$$\begin{aligned} 2\,\omega\,\sin\,\varphi\,v &= -g\,\frac{\partial H}{\partial x} \\ 2\,\omega\,\sin\,\varphi\,u &= g\,\frac{\partial H}{\partial y} \end{aligned} \tag{5}$$

u and v are the geostrophic velocities in North and East direction, respectively, ω is the Earth's rotation rate, and g is mean gravity. Please note that the North component of the velocity u is obtained by the derivative of the dynamic topography in East direction, and the East component v by the derivative in North direction. Descriptively this means, that the surface currents flow along the isolines of the MDT.

Figure 9 shows the geostrophic surface velocities $\sqrt{u^2+v^2}$ of the Antarctic Circumpolar Current (ACC) derived from the MDT (cf. Fig. 8), resolved up to degree/order 180, when using for the geoid either the GRACE-only model ITG-Grace2010S, GOCO01S, or GOCO02S. Since geostrophic velocities are first order

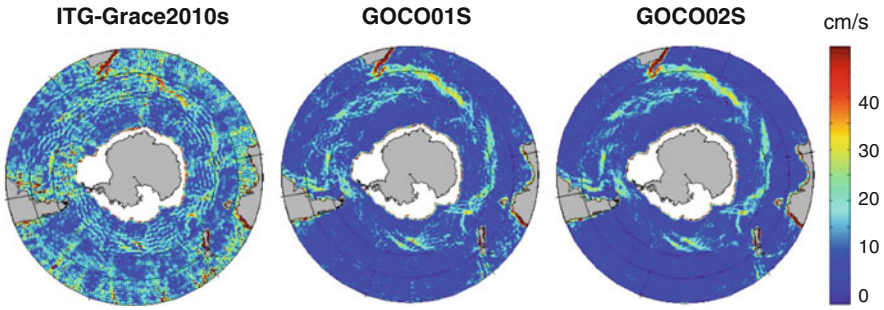

Fig. 9 Geostrophic ocean surface velocities [cm/s] of the Antarctic circumpolar current derived from geodetic MDT using different global geoid models, resolved up to degree/order 180

derivatives of the MDT, they are particularly sensitive to high degree signals. Similarly to Fig. 8, also here there are huge numerical artefacts in the solution of the GRACE-only model, while the actual ocean currents are already clearly visible in GOCO01S. The second release GOCO02S shows further improvement and reduction of noise. Consequently, for the first time it has become possible to derive ocean currents with high accuracy and spatial resolution from satellite data.

Another example where the impact of GOCE for the estimation of geostrophic velocities becomes also visible is the Gulf current (Fig. 10). Again, significant improvements when using GOCE data is evident. These results are compared to velocities which have been measured *in-situ* by drifters. The latter dataset has been compiled in the frame of the project Drifter Data Assembly Center (DAC), a segment of the Global Drifter program coordinated by NOAA and AOML (Lumpkin and Garraffo 2005). The total ocean velocity signal in this area has an rms amplitude of 17.10 cm/s. The differences of the velocities derived by using the ITG-Grace2010S model from this drifter measured velocities is 9.46 cm/s. This value could be significantly reduced to 5.86 cm/s when using the combined GOCO02S model.

It should be emphasized that for this type of studies it is crucial to use a pure satellite-only gravity model, which is independent of terrestrial gravity field and satellite altimetry data. Since the mean sea surface is derived from satellite altimetry data, it is important that the geoid model, which is subtracted from the mean sea surface in order to derive the MDT, does not include altimetry data as well.

As another field of application for high-resolution static gravity models, current studies investigate the impact on GOCE for modelling subduction zones and dynamic processes of the lithosphere. For this geophysical application, combination models from satellite gravity, terrestrial gravity data, and gravity anomalies derived from satellite altimetry, are computed (Fecher et al. 2011), in order to further extend the spatial resolution to substantially higher degrees than for satellite-only models.

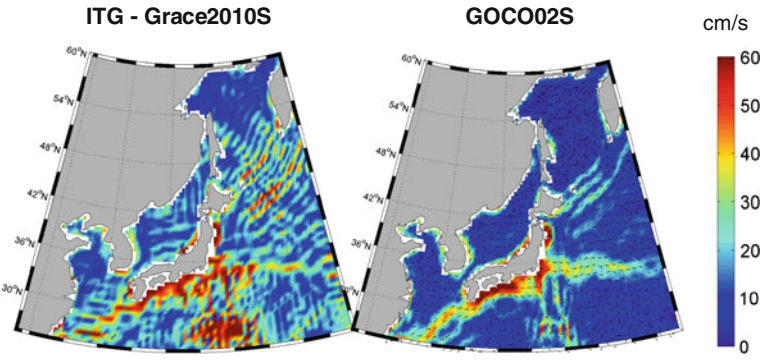

Fig. 10 Geostrophic ocean surface velocities [cm/s] of the Gulf current derived from geodetic MDT using ITG-Grace2010S (*left*) and GOCO02S (*right*), resolved up to degree/order 180

Therefore, as part of the GOCO project initiative several numerical studies to solve full normal equation systems up to degree/order 600 in a rigorous sense have been performed (Fecher et al. 2010). In the near future, rigorous combination solutions complete to degree/order 720 are envisaged. Since the storing and solution of a full equation system of degree/order 600 requires a working memory of about 1 Terabyte, tailored processing strategies on supercomputers have to be applied.

5 Conclusions and Outlook

In this paper an overview of the status of global gravity field modelling using data from dedicated satellite gravity field missions CHAMP, GRACE and GOCE is given, and exemplarily selected geoscientific applications and their impact on Earth system research are discussed.

Spectacular results could be obtained from static and, in particular, time-variable GRACE gravity fields, from which the long-wavelength component of global mass transport processes could be derived for the very first time in a consistent way. The new observation type of GOCE gradiometry allows to achieve a higher spatial resolution of the static gravity field, and thus a more refined picture of small scale processes in oceanography and solid Earth geophysics.

In this paper the progress of GOCE gravity field processing is reviewed, concentrating on those activities the author is responsible. Compared to the first GOCE-only solution GO_CONS_GCF_2_TIM_R1, recent GOCE solutions including a larger amount of GOCE data show improvements according to the statistical $\sqrt{N}$ rule of uncorrelated observations. This is a strong indicator that there are no significant systematic errors in these solutions, and that the stochastic models, which are applied to form the metric of the normal equation systems of the individual components, are correct and meaningful.

Additionally, the first consistent combination models of satellite gravity field data, GOCO01S and GOCO02S, have been addressed, and their impact on an important oceanographic application, namely the derivation of the mean dynamic topography and ocean surface currents, is discussed.

It is important to emphasize that for the computation of the gravity field models discussed in this paper no external gravity field information is used, neither as reference model, nor for constraining the solution. Thus they are GOCE-only/satellite-only in a rigorous sense. Due to this independence of external gravity field information (especially terrestrial gravity field data and satellite altimetry) they can be used for an *independent* comparison and combination with terrestrial gravity data and altimetric gravity anomalies, and for assimiliation into ocean models (using a high-resolution geoid which is independent of altimetry).

For geophysical applications GOCE gradiometry provides as a new observation type, which will enable an improved modelling of lithospheric structures (Hosse et al. 2011). A comparison of the new GOCE models with previously existing gravity field models shows, that substantial improvement of our gravity field knowledge could be achieved especially in regions with interesting geophysical features, such as the Andes and Himalaya area, or the East African rift zone.

Future activities of global gravity field modelling will include the incorporation of gradually increasing amounts of GOCE data for the computation of GOCE-only and satellite-only combined models. Recently, a new pre-processing method for GOCE gravity gradients related to an improved angular rate reconstruction could be derived (Stummer et al. 2011), which has been implemented in the official ESA Level 1b processor, so that reprocessed gradients with an improved performance particularly in the long to medium wavelengths will shortly be available, and thus will further improve satellite-only gravity field models.

In parallel, also the inclusion of terrestrial gravity anomalies and satellite altimetry by combination on normal equation level, and rigorously solving very large normal equations for 500,000 unknown gravity field parameters, is currently under investigation.

The application of these gradually improving static and time-variable gravity field models in several geoscientific fields will demonstrate their valuable contribution to Earth system research.

Acknowledgments The author acknowledges the European Space Agency for the provision of the GOCE data. Parts of the work described in this manuscript are financed through European Space Agency contract no. 18308/04/NL/MM.

References

Albertella A, Wang X, Rummel R (2010) Filtering of altimetric sea surface heights with a global approach. In: Mertikas SP (ed) Gravity, geoid and earth observation, IAG symposia, vol. 135. Springer, Berlin, pp 247–252

Allison I, Alley RB, Fricker HA, Thonmas RH, Warner RC (2009) Ice sheet mass balance and sea level. Antarct Sci 21:413–426. doi:10.1017/S0954102009990137

Bruinsma SL, Lemoine J-M, Biancale R, Valès N (2010a) CNES/GRGS 10-day gravity field models (release 2) and their evaluation. Adv Space Res 45:587–601. doi:10.1016/j.asr.2009.10.012

Bruinsma SL, Marty JC, Balmina G, Biancale R, Förste C, Abrikosov O, Neumeyer H (2010b) GOCE gravity field recovery by means of the direct numerical method. In: Lacoste-Francis H (ed) Proceedings of the ESA living planet symposium (28 June–2 July 2010, Bergen, Norway), ESA publication SP-686, The Netherlands, ISBN (online) 978-92-9221-250-6, ESA/ESTEC

Drinkwater MR, Floberghagen R, Haagmans R, Muzi D, Popescu A (2003) GOCE: ESA's first earth explorer core mission. In: Beutler G et al (ed) Earth gravity field from space—from sensors to earth science, space sciences series of ISSI, vol 18. Kluwer Academic Publishers, Dordrecht, The Netherlands, pp 419–432, ISBN: 1-4020-1408-2

Fecher T, Pail R, Gruber T (2010) Global gravity field determination from terrestrial data. Poster presented at the American geophysical union fall meeting, San Francisco

Fecher T, Pail R, Gruber T (2011) Global gravity field determination by combining GOCE and complementary data. In: Ouwehand L et al. (ed) In: Proceedings of the 4th international GOCE user workshop, ESA Publication SP-696, ESA/ESTEC, Noordwijk, The Netherlands, ISBN (Online) 978-92-9092-260-5, ISSN 1609-042X

Förste C, Flechtner F, Schmidt R, Stubenvoll R, Rothacher M, Kusche J, Neumayer KH, Biancale R, Lemoine JM, Barthelmes F, Bruinsma S, König R, Meyer U (2008) EIGEN-GL05C—a new global combined high-resolution GRACE-based gravity field model of the GFZ-GRGS cooperation. Geophys Res Abstr 10, EGU2008-A-03426, SRef-ID: 1607–7962/gra/EGU2008-A-03426

Gerlach C, Földvary L, Svehla D, Gruber T, Wermuth M, Sneeuw N, Frommknecht B, Oberndorfer H, Peters T, Rothacher M, Rummel R (2003) A CHAMP-only gravity field model from kinematic orbits using the energy integral. Geophys Res Lett 30:20. doi:10.1029/2003/GL018025

Han SC, Shum CK, Jekeli C, Alsdorf D (2005) Improved estimation of terrestrial water storage changes from GRACE. Geophys Res Lett 32(6):L07302

Horwath M, Dietrich R (2009) Signal and error in mass change inferences from GRACE: the case of Antarctica. Geophys J Int 177(3):849–864. doi:10.1111/j.1365-246X.2009.04139.x

Hosse M, Pail R, Horwath M, Mahatsente R, Götze H, Jahr T, Jentzsch M, Gutknecht BD, Köther N, Lücke O, Sharma R, Zeumann S (2011) Integrated modeling of satellite gravity data of active plate margins—bridging the gap between geodesy and geophysics. Poster presented at the AGU fall meeting, San Francisco

Jäggi A, Beutler G, Meyer U, Prange L, Dache R, Mervart L (2009) AIUB-GRACE02S—status of GRACE gravity field recovery using the celestial mechanics approach. Presented at the IAG scientific assembly, 31 Aug–4 Sept 2009, Buenos Aires, Argentina

Kurtenbach E, Mayer-Gürr T, Eicker A (2009) Deriving daily snapshots of the earth's gravity field from GRACE L1B data using Kalman filtering. Geophys Res Lett 36:L17102

Lemoine FG, Luthke SB, Rowlands DD, Chinn DS, Klosko SM, Cox CM (2007) The use of mascons to resolve time-variable gravity from GRACE. In: Rizos C, Tregoning P (eds) Dynamic planet—monitoring and understanding a dynamic planet with geodetic and oceanographic tools, Springer, Berlin, pp 231–236

Liebig V, Herland E-A, Briggs S, Grass H (2007) The changing earth—new scientific challenges for ESA's living planet programme. ESA SP-1304, European Space Agency, Noordwijk, The Netherlands

Lumpkin R, Garraffo Z (2005) Evaluating the decomposition of tropical atlantic drifter observations. J Atmos Oceanic Technol I 22:1403–1415

Mayer-Gürr T, Kurtenbach E, Eicker A (2010) ITG-Grace2010 gravity field model. http://www.igg.uni-bonn.de/apmg/index.php?id=itg-grace2010

Migliaccio F, Reguzzoni M, Sansó F, Tscherning CC, Veicherts M (2010) GOCE data analysis: the space-wise approach and the first space-wise gravity field model. In: Lacoste-Francis H (ed) Proceedings of the ESA living planet symposium (28 June–2 July 2010, Bergen, Norway), ESA Publication SP-686, ISBN (Online) 978-92-9221-250-6, ESA/ESTEC, The Netherlands

Pail R, Goiginger H, Mayrhofer R, Schuh W-D, Brockmann JM, Krasbutter I, Höck E, Fecher T (2010a) Global gravity field model derived from orbit and gradiometry data applying the time-wise method. In: Lacoste-Francis H (ed) Proceedings of the ESA living planet symposium (28 June–2 July 2010, Bergen, Norway), ESA Publication SP-686, ISBN (Online) 978-92-9221-250-6, ESA/ESTEC, The Netherlands

Pail R, Goiginger H, Schuh W-D, Höck E, Brockmann JM, Fecher T, Gruber T, Mayer-Gürr T, Kusche J, Jäggi A, Rieser D (2010b) Combined satellite gravity field model GOCO01S derived from GOCE and GRACE. Geophys Res Lett 37:L20314. doi:10.1029/2010GL044906

Pail R, Bruinsma S, Migliaccio F, Förste C, Goiginger H, Schuh W-D, Höck E, Reguzzoni M, Brockmann JM, Abrikosov O, Veicherts M, Fecher T, Mayrhofer R, Krasbutter I, Sansó F, Tscherning CC (2011) First GOCE gravity field models derived by three different approaches. J Geodesy 85(11):819–843. doi:10.1007/s00190-011-0467-x

Prange L (2011) Global gravitiy field determination using the GPS measurements made onboard the low earth orbiting satellite CHAMP. Geodätisch-geophysikalische Arbeiten in der Schweiz, vol 81, Dissertation, Universität Bern

Reigber C, Balmino G, Schwintzer P, Biancale R, Bode A, Lemoine JM, Koenig R, Loyer S, Neumayer H, Marty JC, Barthelmes F, Perossanz F (2002) A high quality global gravity field model from CHAMP GPS tracking data and accelerometry (EIGEN-1S). Geophys Res Lett 29(14):1692. doi: 10.1029/2002GL015064

Rummel R, Gruber T, Koop R (2004) High level processing facility for GOCE: products and processing strategy. In: Lacoste H (ed) Proceedings of the 2nd international GOCE user workshop "GOCE, the geoid and oceanography", ESA SP-569, ESA, ISBN (Print) 92-9092-880-8, ISSN 1609-042X

Stummer C, Fecher T, Pail R (2011) Alternative method for angular rate determination within the GOCE gradiometer processing. J Geodesy 85(9):585–596. doi:10.1007/s00190-011-0461-3

Tapley B, Ries J, Bettadpur S, Chambers D, Cheng M, Condi F, Poole S (2007) The GGM03 mean earth gravity model from GRACE. Eos Transactions, AGU vol 88 (52), Fall meeting supplement, Abstract G42A-03

Tiwari VM, Wahr J, Swenson S (2009) Dwindling groundwater resources in northern India from satellite gravity observations. Geophys Res Lett 36:L18401. doi:10.1029/2009GL039401

Velicogna I (2009) Increasing rates of ice mass loss from the Greenland and Antarctic ice sheets revealed by GRACE. Geophys Res Lett 36:L19503. doi:10.1029/2009GL040222

Werth S, Güntner A, Petrovic S, Schmidt R (2009a) Integration of GRACE mass variations into a global hydrological model. Earth Planet Sci Lett 277:166–173. doi:10.1016/j.epsl.2008.10.021

Werth S, Güntner A, Schmidt R, Kusche J (2009b) Evaluation of GRACE filter tools from a hydrological perspective. Geophys J Int 179(3):1499–1515. doi:10.1111/j.1365-246X.2009.04355.x

Wouters B, Chambers D, Schrama EJO (2008) GRACE observes small-scale mass loss in Greenland. Geophys Res Lett 35:L20501. doi:10.1029/2008GL034816

Enhanced TEC Maps Based on Different Space-Geodetic Observations

Jiantong Zhang, Michael Schmidt, Denise Dettmering, Liqiu Meng, Yueqin Zhu and Yanbin Wang

Abstract The ionosphere is defined as part of the upper earth's atmosphere, where the density of free electrons and ions is high enough to influence the propagation of electromagnetic radio frequency waves. The ionisation process is primarily depending on the Sun's activity and varies strongly with time, as well as with geographical location. The knowledge of the electron density is the critical point for many applications in positioning and navigation. During the last decade, dual-frequency Global Navigation Satellite Systems (GNSS), in particular the Global Positioning System (GPS) have become a promising tool for monitoring the Total Electron Content (TEC), i.e. the integral of the electron density along the ray-path between the transmitting satellite and the receiver. Hence, geometry-free GNSS measurements provide information on the electron density, which depends on spatial position and time, i.e. four-dimensional (4-D). At present the International GNSS Service (IGS) provides time-dependent vertical TEC (VTEC) maps based on more than 100 permanent ground stations; however, these stations are mainly located on the continents and provide less accurate results over the oceans. New space-based observation techniques, especially various Low-Earth-Orbiting (LEO) satellite missions such as *FORMOSAT-3/COSMIC* and *CHAMP*, as well as dual-frequency radar altimetry missions such as *Jason-1*, *Jason-2* and *Envisat*, can also contribute ionospheric evaluation on a global scale. The former get the TEC values from GPS-LEO occultation observations, whereas the latter provide VTEC observations from the on-board double-frequency radar altimeter. In order to enhance the IGS VTEC maps, i.e. balancing the insufficient GNSS coverage

J. Zhang (✉) · L. Meng · Y. Zhu
Department of Cartography, Technische Universität München, Munich, Germany
e-mail: jt.zhang@bv.tum.de

M. Schmidt · D. Dettmering
Deutsches Geodätisches Forschungsinstitut (DGFI), Munich, Germany

Y. Zhu · Y. Wang
China University of Mining and Technology, Beijing, China

J. M. Krisp et al. (eds.), *Earth Observation of Global Changes (EOGC)*,
Lecture Notes in Geoinformation and Cartography, DOI: 10.1007/978-3-642-32714-8_2,

over the sea, efficient and inexpensive occultation observations and altimetry measurements can be collected and utilized. In this way the IGS VTEC products can benefit from additional data sources. In this paper, we combine both occultation and altimetry measurements to enhance the IGS VTEC maps. Our model consists of a given reference part (background model) computed from the IGS VTEC products, and also of an unknown correction term. In contrary to the traditional spherical harmonic approach, we use a global multi-dimensional B-spline approach for modelling the unknown correction term. We rely on normalized endpoint-interpolating B-splines for modelling the latitude- and the time-dependency and trigonometric B-splines for the dependency on the longitude. Several constraints, e.g. for the poles, for meridian, have to be considered carefully. Since B-splines are localizing functions, i.e. they are characterized by a compact support, data gaps can be handled appropriately. The unknown series coefficients of our multi-dimensional B-spline expansion are calculable from the LEO and the altimetry measurements applying parameter estimation. The relative weighting between the different data sources, the prior information, and the constraints will be performed by Variance Component Estimation (VCE). We compare the enhanced VTEC maps between the combined approach, which is based on VCE, and a second approach using *FORMOSAT-3/COSMIC* and *Jason-1* data only within selected periods. It will be shown that an improvement from the additional data sources is visible in the areas with good data coverage. In regions with limited amount of observations the background model values from IGS will be conserved.

1 Introduction

The knowledge of electron density is the critical point in correcting electromagnetic measurements for ionospheric disturbances. Dual-frequency Global Navigation Satellite Systems (GNSS) and other observation techniques can be used to determine the Slant Total Electron Content (STEC) or the VTEC, i.e. TEC along the vertical. Many approaches can be used to produce ionosphere maps from data of the permanent GPS ground stations. IGS, for example, has more than 100 permanent GPS stations, and it provides global TEC map with a temporal of 2 h (Hernández-Pajares et al. 1999). However, the distribution of the IGS stations is rather heterogeneous, only few stations are located in the oceanic regions; but also on some continents such as Africa the GPS network is rather coarse-meshed. The space-borne GPS receivers flying on Low-Earth-Orbiting (LEO) satellites, such as the *FORMOSAT-3/COSMIC* satellites, *CHAMP* and *GRACE*, provide additional measurements for calculating VTEC maps on a global scale. Moreover, altimetry measurements, e.g. from *Jason-1*, *Jason-2* and *Envisat* also provide information for the VTEC maps, especially over the oceans. To combine both data sources on the basis of existing IGS VTEC maps, the enhanced VTEC map benefits from all data sources.

In our approach we decompose the VTEC model into two parts, namely (1) a global background model part, which is from the IGS VTEC products and (2) a correction part. The latter is modelled as a series expansion in terms of

localizing base functions. The occultation and altimetry measurements are utilized to calculate the unknown series coefficients by applying parameter estimation procedures.

In this contribution, we choose a multi-dimensional B-splines approach for modelling VTEC. To be more specific, we use so-called endpoint-interpolating quadratic B-splines for representing the data along latitude and time, as well as trigonometric B-splines along the longitude. We apply our method to *FORMOSAT-3/COSMIC* and *Jason-1* measurements and obtain enhanced VTEC maps from the IGS VTEC maps. Due to the localisation feature of the B-spline base functions the combined model can handle data gaps appropriately (Schmidt et al. 2011); furthermore the evaluations show the advantages of a multi sensor analysis.

2 Related Work and Fundamentals

2.1 Related Work

The IGS Ionosphere Working Group started to develop global ionospheric TEC products in 1998. It delivers global VTEC maps from different research groups with a temporal spacing of 2 h or less. Todorova et al. (2008) combined GNSS and altimetry data to produce VTEC maps. The approach is based on a spherical harmonic expansion and shows the potential for increasing the accuracy of TEC maps with manually setting weights for both data sources.

Spherical harmonic models can be appropriately used for global VTEC maps. For regional applications or in case of data gaps, localizing base functions are more qualified. Jekeli (2005) gives a review on different types of splines and their applications. Schmidt (2007) presented a B-spline approach to estimate the electron density regionally from GNSS observations; herein the International Reference Ionosphere (IRI) was used as background model; Zeilhofer et al. (2009) extended this approach to the 4-D case. Furthermore, Dettmering et al. (2011) introduced the combination of different space-geodetic observation techniques for regional ionosphere modelling. Schmidt et al. (2011) introduced trigonometric B-splines for global VTEC modeling and showed its advantages for unevenly distributed input data for simulated data sets. Here we use this approach on real data for estimating the VTEC model coefficients from different space-geodetic observation techniques.

2.2 Related Fundamentals

Schumaker and Traas (1991) developed spherical splines by combining so-called endpoint interpolating polynomial B-splines with trigonometric B-splines. Both

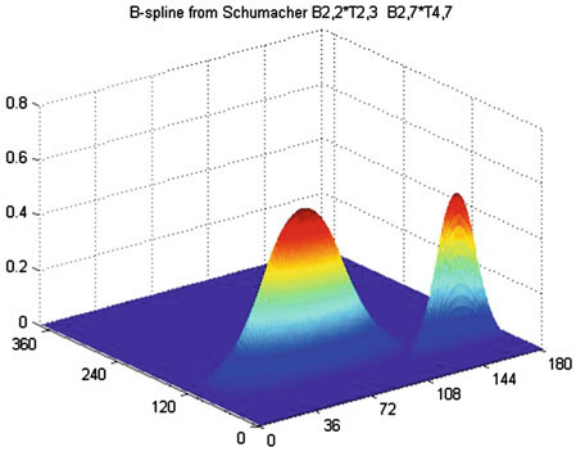

Fig. 1 Products of B-splines $N^2_{2,2} \times T^3_{2,3}$ and $N^2_{2,7} \times T^3_{4,7}$

types of B-splines are compactly supported, i.e. the values are different from zero only in a finite range within the specific interval $I = [V_{\min}, V_{\max}]$. The normalized quadratic endpoint interpolating B-splines of order m are defined recursively at a sequence of non-decreasing knots $t^j_0, t^j_1, \ldots t^j_{m_j+2}$ with $k = 0, \ldots m_j - 1$ and $m = 1, \cdots, d$, with $m_j = 2^j + m$ as shown in the Eqs. (1) and (2):

$$N^m_{j,k}(x) = \frac{x - t^j_k}{t^j_{k+m} - t^j_k} N^{m-1}_{j,k}(x) + \frac{t^j_{k+m+1} - x}{t^j_{k+m+1} - t^j_{k+1}} N^{m-1}_{j,k+1}(x) \tag{1}$$

with the initial values

$$N^0_{j,k}(x) = \left\{ \begin{array}{ll} 1 & for \quad t^j_k \leq x < t^j_{k+1} \\ 0 & else \end{array} \right\} \tag{2}$$

In case of global modelling by means of the spherical B-splines a globally defined function f is restricted to $f(0, \varphi, t) = f(2\pi, \varphi, t)$. Thus, the normalized periodic trigonometric B-splines can be used. These splines can be calculated via a recurrence relation. Suppose for the knots w.r.t. the longitude the inequalities $\cdots < \lambda^j_l < \lambda^j_{l+1} < \cdots$ the definition equation of the trigonometric B-splines reads

$$T^m_{j,l}(\lambda) = \frac{\sin \frac{\lambda^j - \lambda^j_l}{2}}{\sin \frac{\lambda^j_{l+m-1} - \lambda^j}{2}} T^{m-1}_l(\lambda) + \frac{\sin \frac{\lambda^j_{l+m} - \lambda^j}{2}}{\sin \frac{\lambda^j_{l+m} - \lambda^j_{l+1}}{2}} T^{m-1}_{l+1}(\lambda) \tag{3}$$

with $T^1_{j,l}(\lambda) = \{^{1,\ \lambda_l \leq \lambda < \lambda_{l+1}}_{0,\ otherwise}, l = 0, \cdots, L_j - 1 \quad with \quad L_j = 3 \cdot 2^j$; the level value J defines the number of distinct knot points, m is the order of the splines.

Figure 1 visualizes the product of selected N^2_J and T^3_J base functions; these products are also known as tensor products. Note, the higher the level value J is

chosen the sharper is the peak and the finer are the structures which can be modelled.

The study which is introduced in the next section uses simplified gradations of positioning and orientation errors. More specifically, a distinction will only be made between erroneous and error-free positioning and/or orientation.

3 Global Enhanced VTEC Model

3.1 Enhanced Global VTEC Approach for Single Data Source

In analogy to the enhanced model presented by Schmidt (2007), *VTEC* can be decomposed into the background model $VTEC_{ref}(p,t)$ and a correction term $\Delta VTEC(p,t)$ for the observation on location p at time t

$$VTEC(p,t) = VTEC_{ref}(p,t) + \Delta VTEC(p,t) \tag{4}$$

Schmidt discussed different approaches to model the correction term $\Delta VTEC(p,t)$ in Eq. (4) (Schmidt et al. 2007); with some modifications the model can be extended to a global approach (Schmidt et al. 2011). Here we assume that $\Delta VTEC(p,t)$ is represented by the series expansion

$$\Delta VTEC(p,t) = \sum_{k_1=0}^{M_{J_1}-1} \sum_{k_2=0}^{M_{J_2}-1} \sum_{k_3=0}^{M_{J_3}-1} d_{k_1,k_2,k_3}^{J_1,J_2,J_3} \phi_{k_1}^{J_1}(\varphi) T_{k_2}^{J_2}(\lambda) \phi_{k_3}^{J_3}(t) \tag{5}$$

wherein p means the observation site with latitude φ and longitude λ; t means the time; $\phi_k^J(t) = N_{J,k}^2(t)$ are the normalized quadratic B-splines as defined in Eq. (1) with $m = d = 2$, $T_k^J(\lambda) = T_{J,k}^3(\lambda)$ the periodic trigonometric B-splines according to Eq. (3) with $m = 3$.

Considering the time dependency, we divide the observation period $[t_s, t_e]$ into L subintervals $\Delta t = \frac{t_e - t_s}{L}$, i.e. $L = 6$ in our test. The correction term $\Delta VTEC$ is the difference between the background model and the real measurements considering the measurement error e. Under this assumption we establish the Gauss-Markov model from Eq. (5)

$$y + e = Ad \text{ with } D(y) = \sigma_y^2 P_y^{-1} \tag{6}$$

On the left side of Eq. (6) we introduce the $n \times 1$observation vector $y = [y_1, y_2, \ldots y_n]'$and the $n \times 1$ vector $e = [e_1, e_2, \ldots e_n]'$ of the measurement errors. Furthermore, $d = [d_{0,0,0}^{J_1,J_2,J_3}, \ldots, d_{m_{J_1-1},m_{J_2-1},m_{J_1-1}}^{J_1,J_2,J_3}]'$ means the $u \times 1$ vector of the unknown scaling coefficients, whereas the $n \times u$ coefficient matrix A collects the spatio-temporal tensor product B-spline functions

$$A = \begin{bmatrix} a_{0,0,0}^{J_1,J_2,J_3}(\varphi_1,\lambda_1,t_1) & \cdots & a_{m_{J1}-1,m_{J2}-1,m_{J3}-1}^{J_1,J_2,J_3}(\varphi_1,\lambda_1,t_1) \\ \vdots & \ddots & \vdots \\ a_{0,0,0}^{J_1,J_2,J_3}(\varphi_n,\lambda_n,t_n) & \cdots & a_{m_{J1}-1,m_{J2}-1,m_{J3}-1}^{J_1,J_2,J_3}(\varphi_n,\lambda_n,t_n) \end{bmatrix} \tag{7}$$

Herein $a_{0,0,0}^{J_1,J_2,J_3}$is the product of $\phi_0^{J_1}(\varphi_1)T_0^{J_2}(\lambda_1)\phi_0^{J_3}(t_1)$.

In order to evaluate the unknowns $d$additional constraints have to be considered (Schumaker and Traas 1991)

$$H \times d = w \tag{8}$$

whereas H and w means an $r \times u$ given matrix and an $[r \times 1]$given vector of the constraints for Eq. (6) with $u = I \cdot J \cdot K$ with $I = m_{J_1-1}$; $J = m_{J_2-1}$; $K = m_{J_3-1}$. Consequently, the number of constraints depends on the selected levels J_1, J_2 and J_3 for the B-splines.

From Eqs. (6) and (8) a Gauss-Markov model with constraints is defined. Assuming the constraints in Eq (8) as an additional observation equation including a $r \times 1$ error vector v this model can be rewritten as

$$\begin{cases} Ad = y + e \\ Hd = w + v \end{cases} \text{ with } D\left(\begin{bmatrix} y \\ w \end{bmatrix}\right) = \sigma^2 \begin{bmatrix} P^{-1} & 0 \\ 0 & cI \end{bmatrix} \tag{9}$$

wherein c with $c > 0$ is the weight factor for constraints. With the $r \times r$ unit matrix I we set equal weights for pseudo measurements 0. The least squares estimator is given by Koch (1999) and reads

$$\hat{d} = (A'PA + H'H/c)^{-1}(A'Py + H'w/c) \tag{10}$$

So the correction term for a new given location and time can be estimated by estimator $\hat{d}$ in Eq. (9):

$$y_{new} = \Delta\widehat{VTEC}(p_{new}, t_{new}) = (A_{new}) \cdot \hat{d} \tag{11}$$

3.2 Hypotheses Global VTEC Model Based on Multi Observation

Measurements from different platforms, i.e. different satellite missions, have their own characteristics and accuracy levels. Moreover, several studies have shown that altimetry such as the *Jason-1* mission overestimate VTEC by about 3-4 TECU compared to the values delivered by GNSS (Brunini et al. 2005). Considering different ionosphere measurements at the same time, a proper weighting scheme should be chosen in order to account for the accuracy level of each data source i, so the new observation equations for each measurement techniques reads

$$A_i \cdot d = y_i + e_i \text{ with } i \in \{1, \ldots, m\} \tag{12}$$

with

$$D\left(\begin{bmatrix} y_1 \\ \vdots \\ y_i \\ \vdots \\ y_m \end{bmatrix}\right) = \begin{bmatrix} \sigma_1^2 P_1^{-1} & \cdots & 0 & \cdots & 0 \\ \vdots & \ddots & \vdots & \vdots & \vdots \\ 0 & \cdots & \sigma_i^2 P_i^{-1} & \cdots & 0 \\ \vdots & \cdots & \vdots & \vdots & \vdots \\ 0 & \cdots & 0 & \cdots & \sigma_m^2 P_m^{-1} \end{bmatrix}$$

here in, m indicates the number of different measurement types; A_i and d are the same as in Eq. (6), y_i is the observation vector for the ith type of measurement. The covariance factors σ_i^2 are unknown parameters since the relative weighting P_i of different kinds of observations is usually unknown. The selection of weights for different type of measurements is the most important step for this model; however, it is difficult to choose the weights although Todorova et al. (2008) manually set the weights in order to generate the TEC map from multiple data sources and get positive results.

An alternative approach is to choose these different weights automatically, e.g. by VCE (Koch and Kusche 2002), it estimates the variance factors iteratively. Moreover, the ratio of these weights can be used as regularization parameters (Arsenin and Krianev 1992). In the framework of Bayesian inference prior information for the unknown parameters is introduced, in this way we may add a new type of observation equation supposing the expectation vector and the corresponding covariance matrix of the unknown coefficient vector are given according to

$$d = \mu + e_\mu \tag{13}$$

with

$$D(d|\sigma_\mu^2) = \sigma_\mu^2 \cdot P_\mu^{-1}$$

here in, the $u \times 1$ vector μ is the prior information on the unknown parameters, and P_μ is the corresponding given $u \times u$ weight matrix. In addition to the groups of measurements (*FORMOSAT-3/COSMIC*, *Jason-1*), the constraints are also treated as one observation group just like the prior information which are necessary to account for areas and epochs without measurements, furthermore, it assumes the constraint has also error vector v. So the extended Gauss-Markov model is

$$\begin{bmatrix} A_1 \\ A_2 \\ H \\ I \end{bmatrix} \cdot d = \begin{bmatrix} y_1 \\ y_2 \\ w \\ \mu \end{bmatrix} + \begin{bmatrix} e_1 \\ e_2 \\ v \\ e_\mu \end{bmatrix} \tag{14}$$

with

$$D\left(\begin{bmatrix} y_1 \\ y_2 \\ w \\ \mu \end{bmatrix}\right) = \begin{bmatrix} \sigma_1^2 P_1^{-1} & 0 & 0 & 0 \\ 0 & \sigma_2^2 P_2^{-1} & 0 & 0 \\ 0 & 0 & \sigma_w^2 P_w^{-1} & 0 \\ 0 & 0 & 0 & \sigma_\mu^2 P_\mu^{-1} \end{bmatrix}$$

herein, H and w are already defined in Eq. (9); A_1 and A_2 are related to the *FORMOSAT-3/COSMIC* data and the altimetry *Jason-1* observations, respectively. Note that we set $m = 2$, since we just have *FORMOSAT-3/COSMIC* and *Jason-1* in our test. Then, the estimation $\hat{d}$ of the unknown parameter vector d follows from the normal equations:

$$\begin{aligned} &\left(\frac{1}{\sigma_1^2} A_1^{'} P_1 A_1 + \frac{1}{\sigma_2^2} A_2^{'} P_2 A_2 + \frac{1}{\sigma_w^2} A_w^{'} P_w A_w + \frac{1}{\sigma_\mu^2} P_\mu\right) \hat{d} \\ &\quad = \frac{1}{\sigma_1^2} A_1^{'} P_1 y_1 + \frac{1}{\sigma_2^2} A_2^{'} P_2 y_2 + \frac{1}{\sigma_w^2} A_w^{'} P_w y_w + \frac{1}{\sigma_\mu^2} P_\mu \mu \end{aligned} \tag{15}$$

The variance σ_i^2 can be estimated iteratively using different strategies, refer to Koch and Kusche (2002) for more detail. Analogously to Eq. (12), the reconstruction of $\Delta\widehat{VTEC}$ can be estimated by the estimator $\hat{d}$ from Eq. (15) for any point p within the observation period $[t_s, t_e]$.

4 Numerical Comparisons

4.1 Data Sets

In our investigation, we choose the measurements from *FORMOSAT-3/COSMIC* and *Jason-1* as our test data sets. The occultation measurements have a homogeneous distribution over the sphere comparing to the altimetry observations. We choose 1 day with maximum number of measurements as test data set in order to reach a high model resolution which requires enough observations to estimate the unknown parameters, i.e. the B-spline coefficients of high level J. Figure 2 shows the input measurements on July 24th, 2006.

To get the input difference data between the measurements and the background model $\Delta\widehat{VTEC}$ has been calculated for both observation types w.r.t. IGS VTEC. Figure 3 shows these differences for 24 h: the mean value for the difference from *FORMOSAT-3/COSMIC* is around −2.53 TECU; on the contrary, the corresponding value for *Jason-1* is +2.55 TECU.

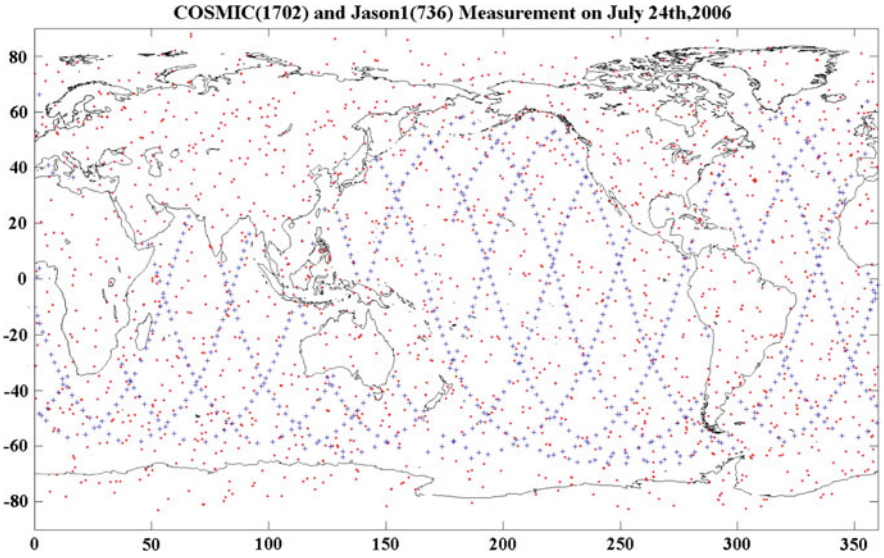

Fig. 2 Distribution of *FORMOSAT-3/COSMIC* and *Jason-1* measurements

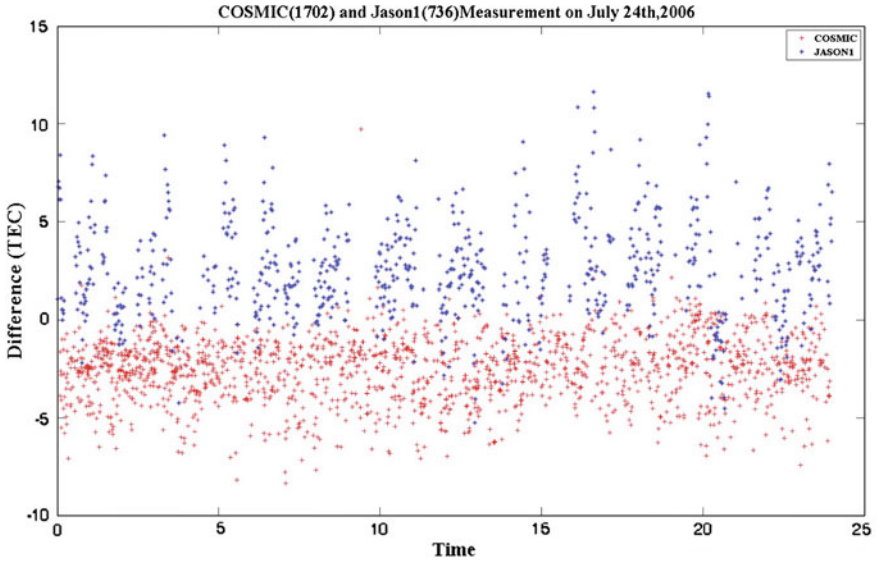

Fig. 3 *VTEC* differences between two types of measurements comparing to IGS model

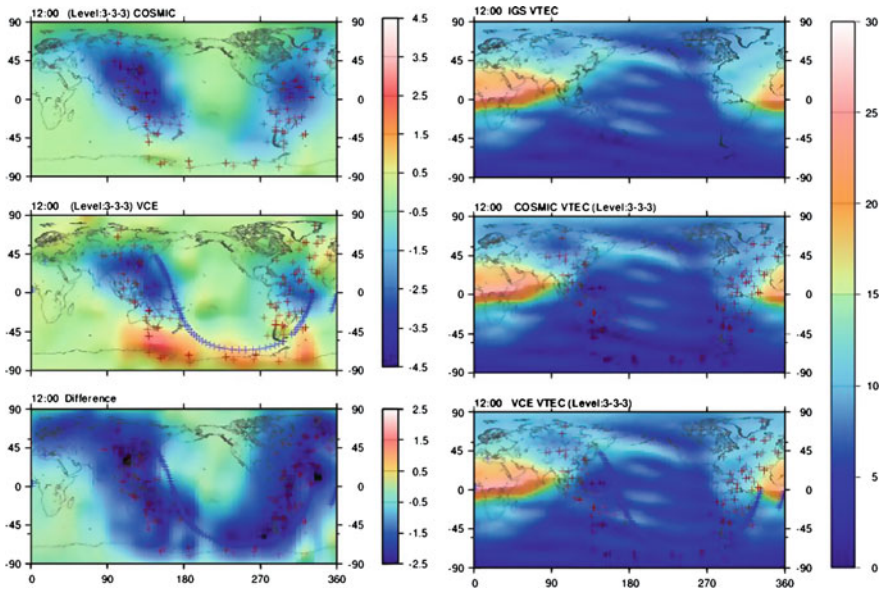

Fig. 4 *VTEC* corrections (*left side*) and reconstructions (*right side*) from both approaches

4.2 Results and Discussion

We compute the correction term as well as the reconstructed VTEC maps by Eqs. (13) and (5) respectively. In this test, we set $J_1 = 3$, $J_2 = 3$ and $J_3 = 3$ for Eq. (5), let $K_1 = M_{J_1} - 1$, $K_2 = M_{J_2} - 1$, $K_3 = M_{J_3} - 1$ i.e. it has $K_1 = 24$, $K_2 = 10$, $K_3 = 10$ local functions for longitude, latitude and time respectively; thus we have 2,400 unknowns. In order to estimate the bias of both data sources, two more unknowns are added, that means the model has 2,402 unknowns.

The correction value at a specific time depends on the location and VTEC intensity of the input measurements. Figure 4 (a–f) shows the map of the correction terms from each approach at 12:00 UT. First row left (4a), COSMIC corrections only; first row right (4d), IGS VTEC; second row left (4b), VCE approach; second row right (4e), IGS + COSMIC corrections; last row left (4c), differences between COSMIC and VCE solution; last row right (4f), IGS + VCE corrections. The unit is in TECU, and the COSMIC data is indicated with red '+', whereas the *Jason-1* data is indicated with blue '+'. Obviously, the result of the combined approach in Fig. 4b shows the modifications w.r.t the *FORMOSAT-3/COSMIC* approach, especially in the areas with altimetry measurements.

The difference of the correction term from both approaches has been calculated using Eq. (16), revealing values between (−2.5 and 0.5) TECU, see Fig. 4c:

$$\Delta d = \Delta\widehat{VTEC}_{\text{cosmic}} - \Delta\widehat{VTEC}_{VCE} \tag{16}$$

Table 1 Standard deviations and offsets in the test

	FORMOSAT-3/COSMIC		*Jason-1*		Constraints	Prior information
	Input	Result	Input	Result		
σ_i	1.67	0.82	2.55	1.95	0.04	1.88
λ_i	1		0.18		420.25	0.19
Bias	−2.18		2.71		–	–

To reconstruct the VTEC maps, we choose a regular grid with $\Delta\lambda = 5°$, $\Delta\varphi = 2.5°$ and $\Delta t = 2\,\text{h}$.

The proposed integrated global model in Eq. (14) has the ability to revise the background model in Eq. (4). No matter with only one data source (Fig. 4a) or with two data sources (Fig. 4b), it generates the modifications from the real measurements, and it shows less influence from the data gaps, i.e. the area without input data. The result in Fig. 4b presents the benefit from altimetry data especially along the satellite ground track. The difference between two approaches in Fig. 4c also shows that most modifications are located along the orbit.

In the VCE approach, the variance has been estimated iteratively till its convergence. Table 1 shows the computed variances and biases. The variance of the constraints is the smallest because the constraint as observation is assumed to be ideal measurements which have better precision that the real measurements from *FORMOSAT3/COSMIC* and *Jason-1* in Eq. (14). As shown in Table 1, *FORMOSAT-3/COSMIC* has more stable measurements than *Jason-1*, and the bias from the estimated results is also correct comparing to the mean value in the test data sets. The standard deviation of *FORMOSAT-3/COSMIC* decreases from 1.67 to 0.82, whereas the standard deviation of *Jason-1* drops from 2.55 to 1.95, so this also verifies the efficient combination of both data sources, as shown in Table 1. In order to estimate the relative weighting of different data source, we rearrange the Eq. (15) by multiplying σ_1^2 on both side

$$\begin{aligned}&(\lambda_1 A_1^{'} P_1 A_1 + \lambda_2 A_2^{'} P_2 A_2 + \lambda_3 A_w^{'} P_w A_w + \lambda_4 P_\mu)\hat{d} \\ &\quad = \lambda_1 A_1^{'} P_1 y_{_1} + \lambda_2 A_2^{'} P_2 y_2 + \lambda_3 A_w^{'} P_w y_w + \lambda_4 P_\mu \mu\end{aligned} \tag{17}$$

with the regularization parameters $\lambda_1 = 1$; $\lambda_2 = \frac{\sigma_1^2}{\sigma_2^2}$; $\lambda_3 = \frac{\sigma_1^2}{\sigma_w^2}$; $\lambda_4 = \frac{\sigma_1^2}{\sigma_\mu^2}$.

In Table 1, comparing to *FORMOSAT-3/COSMIC*, *Jason-1* has lower influence because the distribution is limited by its ground track, which has unbalanced temporal distribution. The prior information I in Eq. (14) has also small influence in the computation, which indicates that the prior knowledge is not the decisive factor in this model. Comparing to the real measurements and prior information, the constraint H in Eq. (14) has strong influence in the model, because it has the ability to make sure that the results fulfill all constraints in Eq. (8).

The standard deviation σ_i is according to the Eq. (18), which can be calculated by:

$$\sigma_i = \sqrt{\frac{\hat{e}_i P_i \hat{e}_i}{r_i}} \tag{18}$$

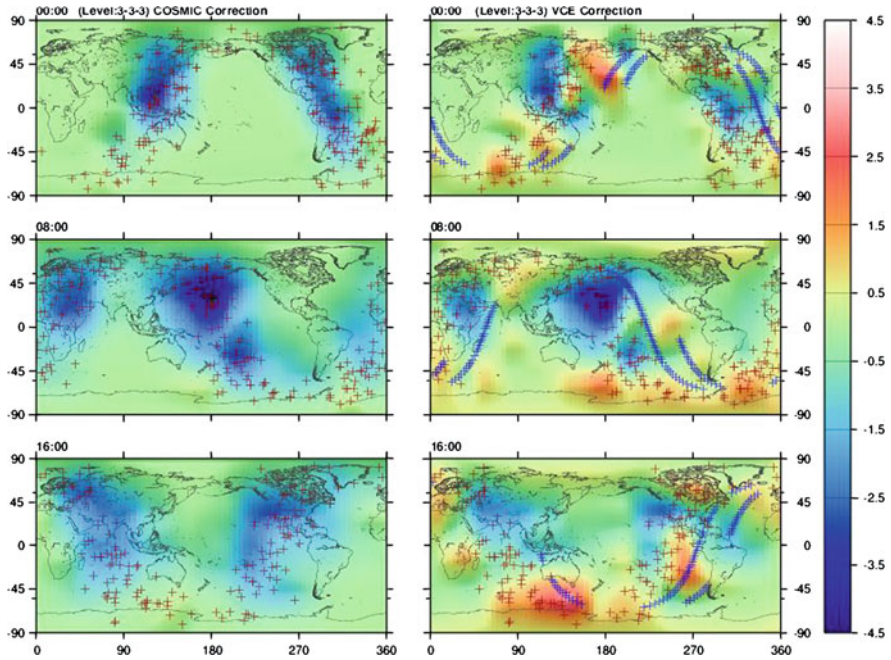

Fig. 5 Corrections term for both approaches (in TECU)

with $\hat{e}_i = \hat{y}_i - y_i$; P_i is the same as in Eq. (14), r_i is the partial redundancies, Koch and Kusche (2002) calculated the redundancy

$$r_i = n_i - tr\left(\frac{1}{\sigma_i^2} A_i^{'} P_i A_i N^{-1}\right) \tag{19}$$

and

$$r_\mu = n_\mu - tr\left(\frac{1}{\sigma_\mu^2} P_\mu N^{-1}\right)$$

for different observation types i and prior information respectively.

The enhanced *VTEC* maps can be reconstructed for a given position and time within the observation period. Figure 5 only shows part of the reconstructed VTEC maps at 8 h interval from both approaches, whereas Fig. 6 shows the enhanced *VTEC* maps in the same epoch as Fig. 5.

Usually the proposed model with a higher resolution provides better approximation of the VTEC maps. However, it requires more measurements to estimate the unknown parameters, for instance, if it choose $J_1 = 3$, $J_2 = 4$, $J_3 = 3$ in Eq. (5) respectively, i.e. $K_1 = 24$, $K_2 = 18$, $K_3 = 10$, that means it has 4,320 unknowns. Whereas it needs 17,280 unknowns if it selects $J_1 = 4, J_2 = 5, J_3 = 3$, so it is reasonable in near future if more data sources if new satellite missions can provide such amount of data with homogeneous global distribution.

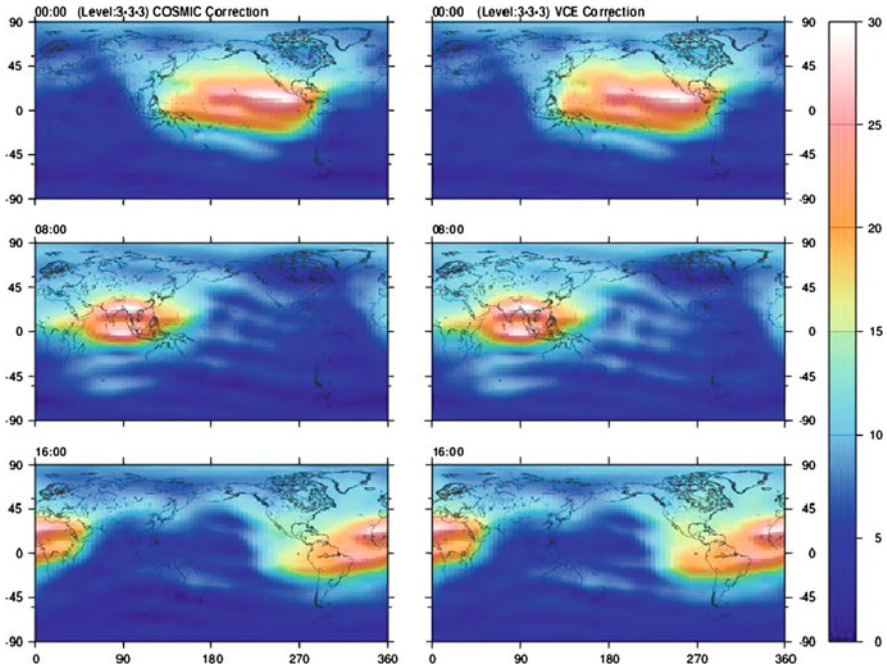

Fig. 6 Enhanced VTEC maps based on IGS VTEC (in TECU)

5 Conclusion

In this paper, we present an efficient fusion approach for combining two different data sources to generate enhanced VTEC maps by global B-splines model; moreover, using more than two different data sources is also possible in our approach. The model is separated into a background part (IGS VTEC map) and a correction part whose unknown coefficients are estimated based on measurements from LEO osculations and altimetry.

In the numerical test, we use the *FORMOSAT-3/COSMIC* as well as *Jason-1* observations for one selected day to test the approach. For the combination of both data types, variance component estimation is applied. Both data types show systematic offsets of about 2 TECU with respect to GPS (with different sign). The *FORMOSAT-3/COSMIC* data in our test has stronger regularization ability than *Jason-1*. The enhanced VTEC maps show an enhancement about ± 3 TECU. In the maps showing the deviation (Fig. 4b) i.e. the enhancement about the additional data source can be clearly seen.

The results in this paper are only based on one specific day. To get a more robust assessment, a longer time period is necessary in order to check the influence of different ionospheric conditions and different data coverage through more/other measurements. Although the enhancement is obviously in the correction map, additional validation procedures are necessary, for instance, the cross-validation or validation from other independent data source, and it's our future work.

References

Arsenin VY, Krianev AV (1992) Generalized maximum likelihood method and its application for solving ill-posed problems. In: Tikhonov A (ed) Ill-posed problems in natural sciences. TVP Science Publishers, Moscow, pp 3–12

Brunini C, Meza A, Bosch W (2005) Temporal and spatial variability of the bias between TOPEX- and GPS-derived total electron content. J Geodesy 79:175–188

Dettmering D, Schmidt M, Heinkelmann R, Seitz M (2011) Combination of different space-geodetic observations for regional ionosphere modeling. J Geodesy 85(12):989–998. DOI:10.1007/s00190-010-0423-1

Hernández-Pajares M, Juan JM, Sanz J, Orus R, Garcia-Rigo A, Feltens J, Komjathy A, Schaer SC, Krankowski A (1999) The IGS VTEC map: a reliable source of ionospheric information since 1998. J Geodesy 83:263–275

Jekeli C (2005) Spline representations of functions on a sphere for geopotential modeling. Technical report no. 475, Ohio state university, Ohio

Koch KR (1999) Parameter estimation and hypothesis testing in linear models. Springer, Berlin

Koch KR, Kusche J (2002) Regularization of geopotential determination from satellite data by variance components. J Geodesy 76:259–268. doi:10.1007/s00190-002-0245-x

Schmidt M (2007) Wavelet modelling in support of IRI. Adv Space Res 39(5):932–940

Schmidt M, Bilitza D, Shum CK, Zeilhofer C (2007) Regional 4-D modelling of the ionospheric electron content. Adv Space Res 42:782–790

Schmidt M, Dettmering D, Mößmer M, Wang Y, Zhang J (2011) Comparison of spherical harmonic and B-spline model for VTEC. Radio Sci 46:RSOD11. doi:10.1029/2010RS004609

Schumaker LL, Traas C (1991) Fitting scattered data on sphere like surface using tensor products of trigonometric and polynomial splines. Numerische Mathematik 60(1):133–144. DOI:10.1007/BF01385718

Todorova S, Hobiger T, Schuh H (2008) Using the global navigation satellite system and satellite altimetry for combined global ionosphere maps. Adv Space Res 42(4):727–736

Zeilhofer C, Schmidt M, Bilitza D, Shum CK (2009) Regional 4-D modelling of the ionospheric electron density from satellite data and IRI. Adv Space Res 43:1669–1675

Part II
Photogrammetry and Remote Sensing

Robust Phase-Correlation Based Registration of Airborne Videos Using Motion Estimation

Frank de Morsier, Maurice Borgeaud, Christoph Küchler, Adrian Vogel, Volker Gass and Jean-Philippe Thiran

Abstract This paper presents an algorithm for near-real time registration of airborne video sequences with reference images from a different sensor type. Phase-correlation using Fourier-Melin Invariant (FMI) descriptors allow to retrieve the rigid transformation parameters in a fast and non-iterative way. The robustness to multi-sources images is obtained by an enhanced image representation based on the gradient norm and by the extrapolation of registration parameters by motion estimation between frames. A phase-correlation score, indicator of the registration quality, is introduced to regulate between frame-to-reference image registration and extrapolation from previous frames only. Our Robust Phase-Correlation based registration algorithm using Motion Estimation (RPCME) is compared with a Mutual Information (MI) algorithm for the registration of two different panchromatic airborne videos with Geoeye reference images. The RPCME algorithm registered most of the frames accurately, retrieving much better orientation than MI. It shows robustness and good accuracy to multisource images with the advantage of being a direct (non-iterative) method.

F. de Morsier (✉) · J.-P. Thiran
École Polytechnique Fédérale de Lausanne, LTS 5, Lausanne, Switzerland
e-mail: frank.demorsier@epfl.ch

M. Borgeaud
European Space Agency, ESRIN, Frascati, Italy

C. Küchler · A. Vogel
RUAG Schweiz AG, Emmen, Switzerland

V. Gass
Swiss Space Center, École Polytechnique Fédérale de Lausanne, Lausanne, Switzerland

J. M. Krisp et al. (eds.), *Earth Observation of Global Changes (EOGC)*,
Lecture Notes in Geoinformation and Cartography, DOI: 10.1007/978-3-642-32714-8_3,

1 Introduction

In the management of natural hazards, the quick assessment of the damaged areas is essential to help the coordination of the rescue teams. An airborne vehicle (like Unmanned Aerial Vehicle) equipped with an optical sensor could be launched quickly after the disaster and provide up-to-date images allowing a comparison with the reference images available from any source (space or airborne sensors). The analysis and fusion of remote sensing images requires an accurate registration, i.e. finding the parameters of a transformation that matches each pixel of the images to the physical reality. Thus, the comparison between airborne video frames and reference images requires a registration robust to the differences in sensor sensitivity, weather and light conditions, lens distortions, view angles as well as temporal changes on the ground. A near-real time registration onboard could allow for live damage detection and let the airplane dynamically focus on damaged areas.

The general problem of registration has been extensively investigated in the literature for remote sensing (e.g. fusion of multi-temporal or multimodal images), medical imaging (e.g. fusion of CT and MRI images) and computer vision (Zitova and Flusser 2003). Two main categories of registration can be separated: affine registration (preserving straight lines) and non-affine registration (where local distortions are allowed). In this wide range of methods, focus has been set on affine registration methods which are potentially faster for near-real time scenarios and accurate enough once perspective and lens distortions are corrected.

In the particular case of airborne video registration, the registration of a frame with a reference image can be helped by the previous frames. The motion between consecutive frames can be easily retrieved using standard registration techniques, since they are extremely redundant. In Cannata et al. (2000), a Kalman filter allows for an online registration based on a certain number of previous frames. In Shastry et al. (2005), airborne video registration for traffic-flow monitoring is done using fixed features and helicopter movements are removed from inter-frame registration. In Wu and Luo (2008), a prediction model of the camera movement allows to remove outliers in feature points matching by taking advantage of the relationships among consecutive video frames. A global optimization problem involving frame-to-reference and frame-to-frame constraints can be minimized to get the registration parameters (Kumar et al. 2000, Hirvonen et al. 2001).

However the appearance between the frame and the reference image is often dissimilar from temporal changes and different sensor sensitivity. A more robust representation of the images is needed in order to see these methods working with images from different sources. In Hirvonen et al. (2001), Oriented energy image pyramids are used to register video frames having a different appearance than the reference image. However in this case the registration is obtained by solving a minimization problem which does not guarantee the method to be fast.

This paper motivated by the mentioned limitations aims at presenting a fast registration method for airborne video platforms having a potential for near-real

time registration and being robust to video having strong differences with the available reference image. The phase-correlation (PC), a non-iterative method, allows to retrieve the affine rigid transformation parameters between two images (rotation, scaling and translation) with low computational complexity (Kuglin and Hines 1975). The PC is sensitive to images differences, therefore robustness to changes and multi-sources images is obtained by an enhanced image representation and by the extrapolation of registration parameters using the inter-frame motion.

2 Methodology

This section introduces the methodology for the robust registration of airborne video frames with a reference image having a different appearance. Two different pixel-based approaches for registering images with a subpixel accuracy are presented: Mutual Information and Phase-Correlation. Both are evaluated and compared for the registration of different airborne videos in Sect. 3.

2.1 Mutual Information Registration

The Mutual Information registration algorithm (MI) is a standard registration approach based on image intensities and not on local image features. This registration method is introduced here for comparisons with our proposed algorithm based on phase-correlation (see Sect. 2.2). Mutual information measures the amount of information that one variable contains about the other, i.e. it expresses the probability that the pixels are reflecting the same physical reality in both images. It is really often used in multi-source/multimodal registration because handling well non-linear transformations (no *a priori* on intensity relationship). Therefore we selected this pixel-based method for comparison with our phase-correlation based algorithm. Analogous to the Kullback–Leibler expression, the mutual information is defined as follows:

$$\mathrm{MI} = \sum_{I_1, I_2} \mathrm{p}(I_1, I_2') \log \frac{\mathrm{p}(I_1, I_2')}{\mathrm{p}(I_1) p(I_2')} \tag{1}$$

with I_2' being the image after affine transformations, $p(I_1)$ the marginal distribution of I_1 and $p(I_1, I_2')$ the joint probability distribution. These probabilities can be computed from their normalized joint histogram. The registration is based on maximizing the mutual information between the image I_1 and the transformed image I_2'. The implementation has been realized using the HPV interpolation and the Powell's Direction set method, for more details see Lu et al. (2008).

2.2 Phase-Correlation Registration

The phase-correlation (PC) exploits the Fourier shift properties. An image $I_1(x, y)$ translated of (x_0, y_0) becomes $I_2(x; y) = I_1(x - x_0; y - y_0)$ and can be expressed in the Fourier domain as: $\hat{I}_2(\eta, \xi) = e^{-j2\pi(\eta x_0 + \xi y_0)} \cdot \hat{I}_1(\eta, \xi)$. The normalized cross power spectrum $R(\eta, \xi)$ between these two images is a phase change in the Fourier domain.

$$R(\eta, \xi) = \frac{\hat{I}_1 \cdot \hat{I}_2^*}{\left|\hat{I}_1 \cdot \hat{I}_2^*\right|} = e^{-j2\pi(\eta x_0 + \xi y_0)} \tag{2}$$

with $\hat{I}^*$ the complex conjugate of $\hat{I}_2$.

The phase-correlation $PC(x, y)$, being the inverse Fourier transform of $R(\eta; \xi)$, is ideally a delta function shifted from the center of $(x_0, y_0) : PC(x, y) = \hat{R}(x, y) = \delta(x + x_0, y + y_0)$. Therefore the localization of the PC maximum peak yields to the horizontal and vertical shifts existing between the two images.

Using the same properties, one can retrieve rotation and scaling differences using the Fourier-Melin Invariant descriptors (FMI) of the images. The FMI of an image corresponds to its Fourier transform magnitude mapped in the log-polar space. The magnitude of the Fourier transform is invariant to shifts and the log-polar space maps rotation and scaling into horizontal and vertical shifts (Gibson et al. 2001).

For subpixel displacements between the images, the delta function of the PC is spread over a small neighborhood, corresponding to a Dirichlet kernel (Foroosh et al. 2002). The zero-padding of the normalized cross power spectrum $R(\eta, \xi)$, as suggested by (Marcel et al. 1997), involves the inverse Fourier transform of a large matrix. A computationally costless approach for subpixel accuracy is the interpolation of the peak position using its neighborhood pixels values (Gibson et al. 2001). Let the maximum peak subpixel position be $PC(x_0 + \Delta x; y_0 + \Delta y)$:

$$\Delta x = \frac{PC(x_0 + 1, y_0) - PC(x_0 - 1, y_0)}{PC(x_0, y_0) + PC(x_0 + 1, y_0) + PC(x_0 - 1, y_0)} \tag{3}$$

$$\Delta y = \frac{PC(x_0, y_0 + 1) - PC(x_0, y_0 - 1)}{PC(x_0, y_0) + PC(x_0, y_0 + 1) + PC(x_0, y_0 - 1)} \tag{4}$$

In real situations, the PC result is noisy from image non-rigid distortions and temporal differences, and can result in a wrong location of the maximum peak. However a concentration of high-values are present in the neighborhood of the real peak location. Therefore the peak localization is improved by low-pass filtering the PC with a Gaussian kernel (standard deviation of the Gaussian low-pass filter set to 2 pixels for all the experiments with a PC size of 1,024 × 1,024 pixels). A PC result is presented in Fig. 1 before and after low-pass filtering.

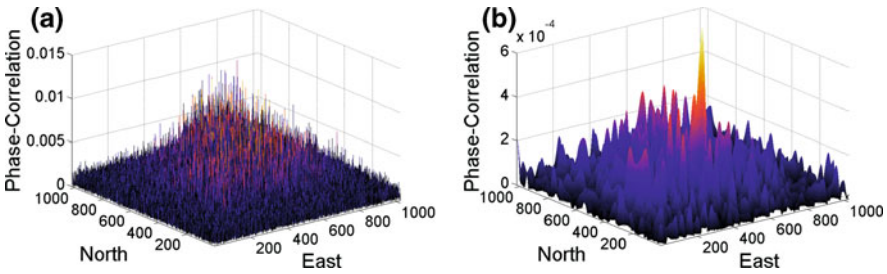

Fig. 1 Phase-correlation result before **a** and after **b** low-pass filtering. The maximum peak corresponding to the translation between two images is more accurate after smoothing

2.3 Robust Image Representation

The differences in illumination from the sunlight, weather conditions and sensors sensitivity disturb the registration process. These changes are mainly concentrated in the low frequencies of the image and can be attenuated by using a high-frequency image representation. The gradient representation ∇I was used by Argyriou and Vlachos (2004) with the vertical derivative mapped to the imaginary part. We assessed that this representation was sensitive to changes between the images and preferred to use the more robust Euclidian norm of the gradient: $G(x;y) = |\nabla I| = \sqrt{(\partial_x I)^2 + (\partial_y I)^2}$.

The gradient norm representation introduces artifacts in the FMI descriptor, because of the edges cutted at the image boundaries. This introduces high frequency values in the Fourier magnitude which are alterating the FMI descriptor and would result in registering the frame of the images. However these artifacts can be attenuated by applying a Tukey window on the gradient representation (Vandewalle et al. 2006). The Tukey window is a truncated Gaussian letting unchanged the central part of the image and attenuating only the borders.

The log-polar transformation, applied on the Fourier transform magnitude of the gradient norm image, maps the low frequencies into an important part of the log-polar image. These low frequencies gives not much information on orientation and are too distorted to be useful for scaling. Reddy and Chatterji (1996) suggested to use a high-pass filter before the log-polar mapping to discard low frequencies.

2.4 Registration Extrapolation from Inter-Frame Motion

The consecutive frames of a video sequence are highly redundant and extremely similar. The important overlapping part between two consecutive frames allows the estimation of motion parameters between them. The motion between consecutive frames can be efficiently represented by a rigid transformation (rotation,

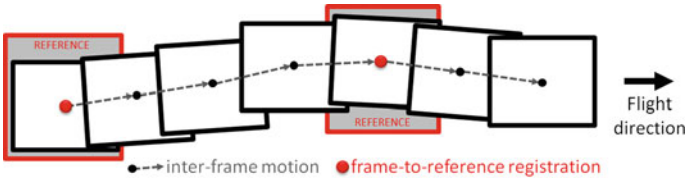

Fig. 2 Schematic representation of frame-to-frame and frame-to-reference registrations

scaling and shifts). Therefore PC can be used between video frames to estimate the inter-frame motion parameters. This is often used for video blocks motion in video compression applications (Argyriou and Vlachos 2004), however here we consider the entire image and not several blocks. The motion between video frames allows to extrapolate the parameters of previous frame-to-reference image registrations. Therefore the registration between a video frame and the reference image gets an accurate initialization from the extrapolated registration parameters of the previous frame. If important changes occured between a frame and the reference image the registration between them could rely only on the extrapolated registration parameters. The next section present a PC score allowing to decide whether the registration parameters should only be extrapolated or not (Fig. 2).

2.5 A Phase-Correlation Score for Registration Quality Assessment

The algorithm works at two levels: inter-frame registration (motion estimation between consecutive video frames) and frame-to-reference registration (registration of a video frame with a reference image). The inter-frame registration is used to initialize the frame-to-reference image registration. The maximum peak search in the PC plane is restricted to a certain window, avoiding to get extreme values corresponding to incoherent parameters. The search window is defined by the maximum angle, scaling and translation values estimated possible between two consecutive frames.

The introduction of a PC score at the frame-to-reference translation level allows to regulate the registration. The PC score is derived from the normalized PC peak power. The peak can be spread over several pixels around the maximum (Dirichlet kernel), as seen in Sect. 2.2 therefore the PC score is defined as

$$score = \frac{\sum_{i=-1}^{1} \sum_{j=-1,|j|\neq|i|}^{1} PC(x_0+i, y_0+j)^2}{\sum_{i=1}^{N} \sum_{j=1}^{M} PC(i,j)^2} \tag{5}$$

The score reflects directly the quality of the registration. In case of a low score, under a user-defined limit, the frame-to-reference parameters are discarded and

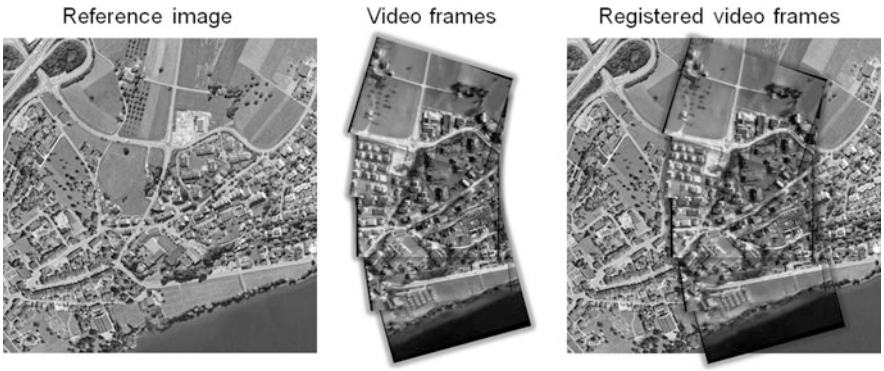

Fig. 3 Reference image (*left*), video n°2 frames (*middle*) and overlay of the registration (*right*)

only the initial parameters, obtained by extrapolation from the previous frame, are used for registration.

3 Experimental Setup

Performances of our Robust Phase-Correlation algorithm using Motion Estimation (RPCME) have been assessed and compared in an experimental setup made of two airborne videos and airborne reference images from GeoEye at high-resolution ($\sim$50 cm). One reference image and the corresponding video frames registered are represented and overlayed in Fig. 3.

The airborne videos were taken at constant altitude with a fixed field of view. They have an angle of view close-to-vertical and have been corrected for perspective distortion (some residual distortions are remaining in video n°2 from inaccurate angle of view information). The video camera has a single panchromatic band ranging up to near-infrared wavelengths with a resolution of 567×720 pixels resulting in pixels with a resolution around 50 cm and a monochrome depth of 8 bits. The sensitivity to near-infrared gives an appearance not similar to the Geoeye products, which is important to assess the robustness of our algorithm to different sources.

The video n°1 is a straight flight over agricultural fields and roads with a cloud partially covering frames 20–50. The video n°2 is a right-turning flight over urban and agricultural areas with important urban changes between frame 15–25: (Fig. 3).

The RPCME algorithm is compared with the Mutual Information maximization algorithm (MI), having an important robustness to multi-sources images (Lu et al. 2008).

Both RPCME and MI have the same initializations from registration parameters extrapolated using the inter-frame motion estimated by phase-correlation. Therefore, only the frame-to-reference registration changes between the two algorithms

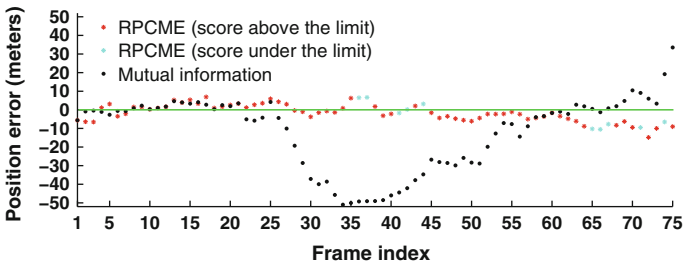

Fig. 4 Video n°1 registration results: position of the registered frames with RPCME and MI

and the image representation (pixel intensities for MI). The MI algorithm always perform a frame-to-reference registration since the regulation is done using the PC score.

The registration positions and orientations are compared with a flight track obtained from coarse GPS flight positions. Hence the position accuracy assessment can only be done on the across-track position.

4 Experimental Results

In Fig. 4, the position of the registered frames from video n°1 are compared relatively to the flight track. RPCME is extremely robust to the cloud partial occlusion between frames 25 and 50 compared to the MI algorithm. The frames having a PC score lower than the score limit, can be observed in light blue dots. Already between the frames 25 and 35 the RPCME is more accurate than MI, without resorting to regulation (score above the score limit). This robustness is obtained from the gradient norm representation of the images. In Fig. 5, the influence of the score regulation on the position error can be well observed. The score regulation avoids the position error to increase when the cloud is present by stopping the frame-to-reference registration.

The position accuracy in video n°2 is equivalent for both algorithms, except the position error increasing for the RPCME algorithm from frame 15–20 (Fig. 6). Some perspective distortions that could not be corrected between these frames led to inaccurate registration positions. The errors common to both algorithms observed between frames 20–40 are due to the flight track interpolation (Figs. 6 and 7).

Concerning the orientation accuracy, the RPCME algorithm is more accurate along the flight than MI (Fig. 8). After the frame 20 the MI algorithm cannot get back the correct orientation and propagates an orientation error through the frames. It is important to notice that the reference orientation can be locally less accurate, since derived from the interpolated flight track. The end of the flight is over agricultural land having less distinct structures causing trouble to the algorithms to

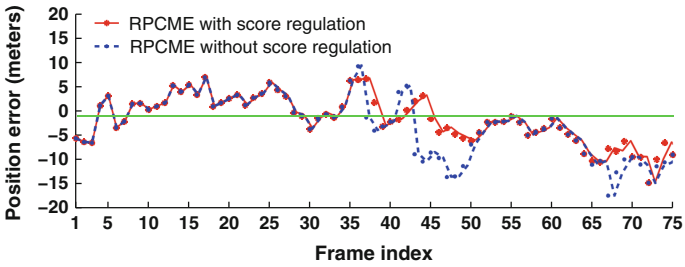

Fig. 5 Video n°1 registration results: RPCME position errors with and without score regulation

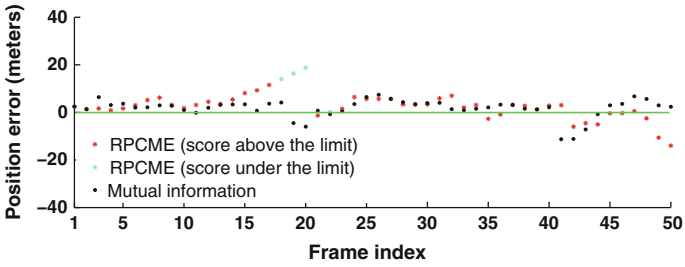

Fig. 6 Video n°2 registration results: position of the registered frames with RPCME and MI

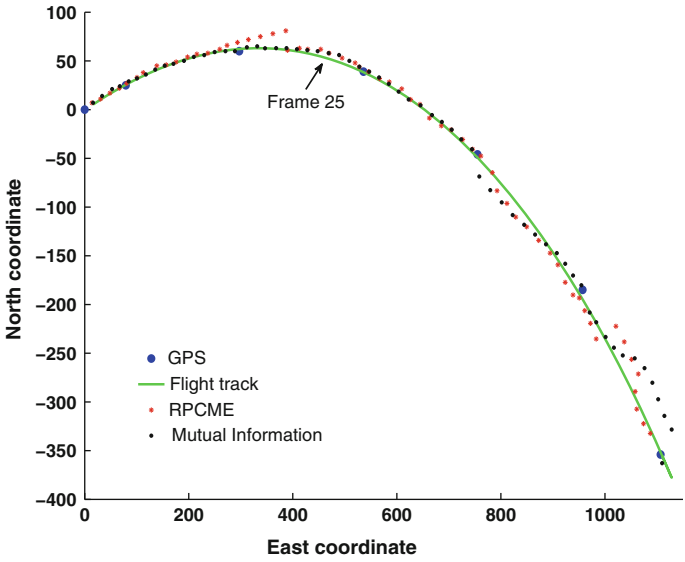

Fig. 7 Video n°2 registration results: 2D view of the position of the registered frames

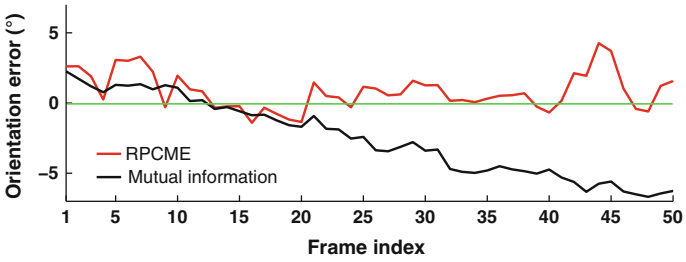

Fig. 8 Video n°2 registration results: orientation errors of the registered frames

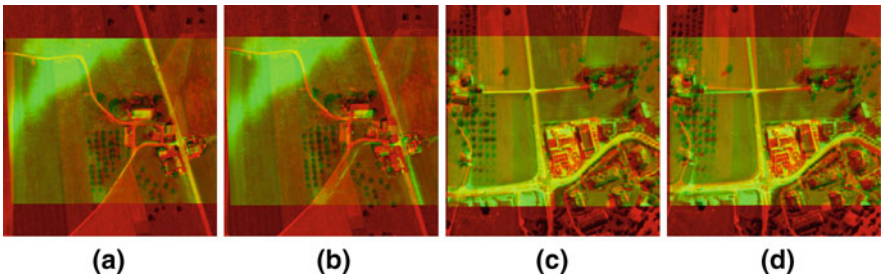

Fig. 9 Video n°1 frame 26: registration results for **a** RPCME, **b** MI. Video n°2 frame 25: registration results for **c** RPCME, **d** MI

get an accurate position and orientation. A visual assessment of the accuracy between RPCME and MI on Red-Green overlays is presented in Fig. 9.

The main limitation are still coming from the presence of structures in the data. Our RPCME method is pixel-based but exploit the gradient norm of the images which keeps only structure in the data. This is a tradeoff between multisource robustness and the required amount of distinct features in the images.

In terms of computation time, RPCME is performing more than five time faster than MI. RPCME requires 8 FFT + 4 FFT^{-1} + 2 rotations + 4 log-polar interpolations. This shows the potential for implementing this algorithm in hardware for near-real time registration. The RPCME algorithm shows accurate position for most of the registered frames and is very accurate on frame orientation compared to the MI algorithm.

5 Conclusion

We have presented how Phase-Correlation (PC) can be used for the registration of airborne video frames with a reference image from a different sensor in the presence of temporal changes. The robustness is obtained from an enhanced image representation based on the gradient norm, from a low-pass filtering of the phase-

correlation and from the extrapolation of the registration parameters between video frames to initialize or replace the video-to-reference registration when not reliable (indicated by a low Phase-Correlation score).

Globally, the Robust Phase-Correlation registration using Motion Estimation (RPCME) algorithm shows robustness and good accuracy to multi-sources images with the advantage of being a fast, non-iterative method. This combination of rapidity and robustness can be particularly interesting for the registration of videos from unmanned aerial vehicles (UAV), allowing some further on-board post processing of the images. It would be particularly interesting to test the algorithm on more airborne videos having higher groundtruth accuracy for a better assessment.

Further perspectives are on the automatic tuning of the score threshold limit, based on the images content and the extension to other types of image modalities.

Acknowledgments Thanks to the EPFL Swiss Space Center and RUAG Schweiz AG for supporting this research project.

References

Argyriou V, Vlachos T (2004) Using gradient correlation for subpixel motion estimation of video sequences. In: Proceedings of IEEE international conference on acoustics, speech, and signal processing, Citeseer, pp 329–332

Cannata RW, Shah M, Blask SG, Van Workum JA (2000) Autonomous video registration using sensor model parameter adjustments. In: Proceedings of the 29th applied imagery pattern recognition workshop, pp 215–222

Foroosh H, Zerubia J, Berthod M (2002) Extension of phase correlation to subpixel registration. IEEE Trans Image Process 11(3):188–200

Gibson S, Kreinovich V, Longpre L, Penn B, Starks S (2001) Intelligent mining in image databases, with applications to satellite imaging and to web search. In: Data mining and computational intelligence, pp 309–336

Hirvonen D, Matei B, Wildes R, Hsu S (2001) Video to reference image alignment in the presence of sparse features and appearance change. In: Proceedings of the 2001 IEEE computer society conference on computer vision and pattern recognition, vol 2. pp 366–373

Kuglin C, Hines D (1975) The phase correlation image alignment method. In: IEEE 1975 conference on cybernetics and society, pp 163–165

Kumar R, Samarasekera S, Hsu S, Hanna K (2000) Registration of highly-oblique and zoomed in aerial video to reference imagery. In: International conference on pattern recognition, pp 303–307

Lu X, Zhang S, Su H, Chen Y (2008) Mutual information-based multimodal image registration using a novel joint histogram estimation. Comput Med Imaging Graph 32(3):202–209

Marcel B, Briot M, Murrieta R (1997) Estimation of translation and rotation by fourier transform. Traitement du Signal 14(2):135–149

Reddy BS, Chatterji BN (1996) An FFT-based technique for translation, rotation, and scale-invariant image registration. IEEE Trans Image Process 5(8):1266–1271

Shastry A, Schowengerdt R, Res G, Bangalore I (2005) Airborne video registration and traffic-flow parameter estimation. IEEE Trans Intell Transp Syst 6(4):391–405

Vandewalle P, Susstrunk S, Vetterli M (2006) A frequency domain approach to registration of aliased images with application to superresolution. EURASIP J Appl Signal Process, Hindawi Publishing Corporation, pp 233–233

Wu Y, Luo X (2008) A robust method for airborne video registration using prediction model. In: International conference on computer science and information technology, ICCSIT'08, pp 518–523

Zitova B, Flusser J (2003) Image registration methods: a survey. Image Vis Comput 21(11): 977–1000

EnMAP Ground Segment Design: An Overview and its Hyperspectral Image Processing Chain

Tobias Storch, Martin Bachmann, Sabrina Eberle, Martin Habermeyer, Christine Makasy, Amaia de Miguel, Helmut Mühle and Rupert Müller

Abstract EnMAP (Environmental Mapping and Analysis Program; www.enmap.org) is the first German hyperspectral remote sensing satellite mission. This chapter focuses on the challenges on the design of the ground segment as a whole and in particular of its image processing chain. In the context of the system response time we investigate the ability of tilting the satellite which allows for frequent revisits and enables meaningful downstream change detection activities on a global scale. In the context of comparable and high-quality controlled products we investigate in detail the processing steps to radiometrically calibrate, spectrally characterize, geometrically and atmospherically correct the data. The status corresponds to the baseline for the production activities of the ground segment, namely only minor changes are expected. The launch is planned for 2016. The establishment and operation of the ground segment is under responsibility of the Earth Observation Center (EOC) and the German Space Operations Center (GSOC) at the German Aerospace Center (DLR).

1 Introduction

The establishment and operation of the ground segment for the future hyperspectral satellite mission EnMAP (Environmental Mapping and Analysis Program; www.enmap.org) is under responsibility of the Earth Observation Center (EOC) and the German Space Operations Center (GSOC) at the German Aerospace Center (DLR). In July 2010, the ground segment has completed its design phase by

T. Storch (✉) · M. Bachmann · S. Eberle · M. Habermeyer
C. Makasy · A. de Miguel · H. Mühle · R. Müller
German Aerospace Center (DLR), Wessling, Germany
e-mail: tobias.storch@dlr.de

J. M. Krisp et al. (eds.), *Earth Observation of Global Changes (EOGC)*,
Lecture Notes in Geoinformation and Cartography, DOI: 10.1007/978-3-642-32714-8_4,

successfully passing the critical design review. Now, it is in the production phase. The launch is planned for 2016. The EnMAP mission is the first German space-borne optical Earth observing mission (Stuffler et al. 2007).

The EnMAP satellite will be operated on a sun-synchronous orbit at 653 km altitude with a local time of descending node set to 11:00 h ± 18 min to observe any location on the globe under defined illumination conditions featuring a global revisit capability of 21 days under a quasi-nadir observation, namely with an across-track tilt of at most 5°. The satellite has an across-track tilt capability of 30° enabling a revisit time of four days (Stuffler et al. 2009). These revisit times hold in particular for equatorial regions, whereas, e.g. Munich, Germany, (48°N) can be revisited approximately every 2.5 days and for regions at the polar circles (66.5°) it is even approximately every 1.5 days. Beside for Munich, Germany, (48°N) Fig. 1 (top) illustrates the footprints of all potential acquisitions with an off-nadir angle of at most 30° for Mogadishu, Somalia, (2°N) and for Tromsø, Norway, (69.5°N) within one month. If quasi-nadir observations are considered only, the potential acquisitions decrease from 9 to 1 for Mogadishu, from 12 to 2 for Munich, and from 26 to 4 for Tromsø. Figure 1 (top) illustrates acquisitions of approximately 1,000 km length and it thereby also reveals that the footprints are different depending on the tilt necessary to hit the target area. This effect increases from the equatorial to the Polar Regions. Such frequent revisits allow for significant change detection activities on a global scale. Furthermore, the orbit allows acquiring areas between 82°N and 82°S under nadir conditions and between 85.5°N and 85.5°S utilizing the across-track tilt capability of 30°. There may be performance degradations for some smaller areas such as parts of Polar Regions or parts of regions affected by the South Atlantic Anomaly. For a ground track passing Munich Fig. 1 (bottom) illustrates the area which can be imaged utilizing an across-track tilt of 0° (corresponding to a field of view of ∼30 km), at most 5° (corresponding to a field of view of ∼150 km), and at most 30° (corresponding to a field of view of ∼800 km) (Heiden et al. 2010). An acquisition of 90 km length is highlighted.

The major objectives of the EnMAP mission are to measure, derive, and analyze diagnostic parameters, which describe vital processes on the Earth's surface encompassing agriculture, forestry, soil and geological environments, as well as coastal zones and inland waters. Those geochemical, biochemical, and biophysical parameters are assimilated in physically based ecosystem models, and ultimately provide information reflecting the status and evolution of various terrestrial ecosystems. Based on these quantitative measurements remote sensing standard products can be substantially improved and new user-driven information products will be generated, which could so far only be produced in the frame of scientific airborne hyperspectral campaigns. During the five years of mission operations EnMAP will provide information about the status of different ecosystems and their response to natural or man-made changes of the environment, which will be evaluated by an international user community of science and industry coordinated by the German Research Centre for Geosciences (GFZ) as the mission principal

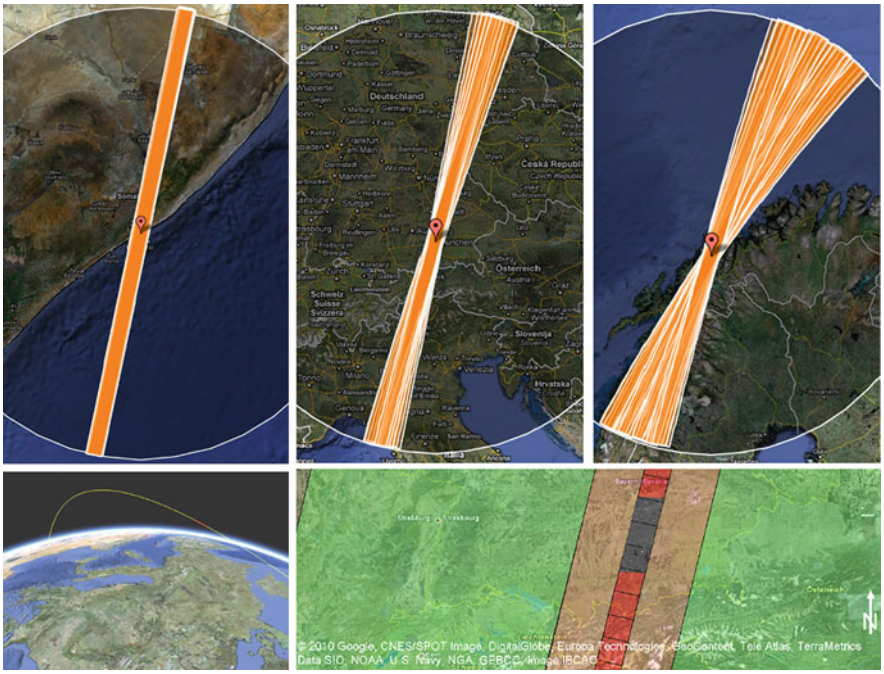

Fig. 1 *Top Left*: Potential acquisitions for Mogadishu, Somalia, (2°N) with an off-nadir angle of at most 30° and within one month. *Top Middle*: Potential acquisitions for Munich, Germany, (48°N) with an off-nadir angle of at most 30° and within one month. *Top Right*: Potential acquisitions for Tromsø, Norway, (69.5°N) with an off-nadir angle of at most 30° and within one month. *Bottom Left*: Orbit, where the satellite positions are marked red when the highlighted area illustrated at *bottom right* was imaged. *Bottom Right*: Map of Munich and southern Germany, where the area visible: (1) under nadir conditions is marked *red*, (2) within ±5° off-nadir angle is marked *red* and *orange*, (3) within ±30° off-nadir angle is marked *red*, *orange*, and *green*. The grid illustrate tiles of size 30 × 30 km^2

investigator. To meet these objectives a team of value adders and scientific partners jointly investigate the mission characteristics (Kaufmann et al. 2009).

The project management is led by the Space Agency of the German Aerospace Center (Rossner et al. 2009). The space segment consisting of instrument and bus will be established by Kayser-Threde GmbH (KT) and Orbitale Hochtechnologie Bremen-System AG (OHB System), respectively.

This chapter describes the EnMAP mission and focuses at first on the ground segment as a whole with its relations to the space and user segment and second on the image processing chain of the ground segment which includes geometric and atmospheric corrections as well as quality indicators. These indicators serve also as input for the quality assessment of higher-level products such as change detection maps, in particular of time series of products derived from hyperspectral data (Van der Meer and De Jong 2006).

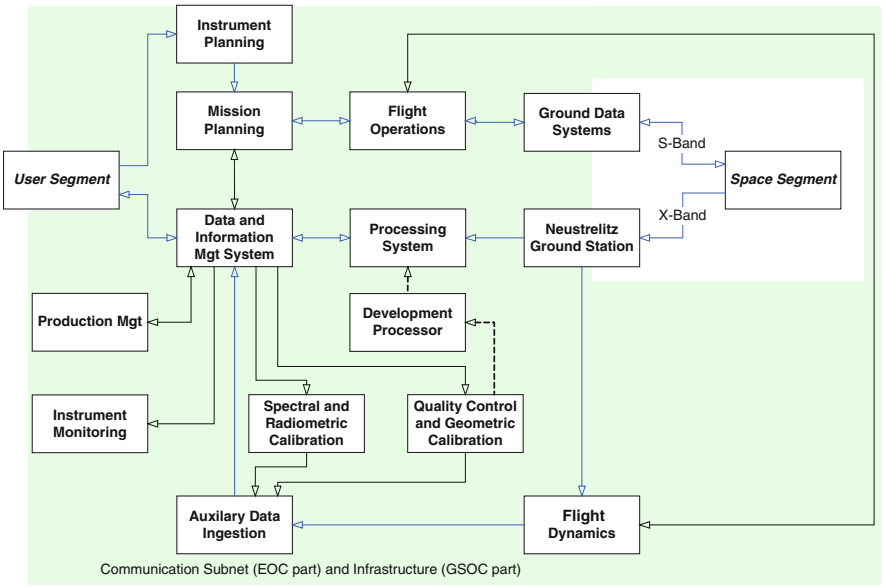

Fig. 2 Schematic illustration of ground segment

2 Ground Segment

The EnMAP ground segment is—beside its management part containing project managers, engineers, and product assurance—organized in three systems covering all aspects relevant to assure successful mission operations (Storch et al. 2010). The Mission Operation System, responsible for controlling and commanding satellite and instrument, is operated by the German Space Operations Center (GSOC) with its multi-mission control center in Oberpfaffenhofen, Germany, and its main S-band telemetry- and telecommand ground station in Weilheim, Germany. The Payload Ground System, responsible for data reception, data processing, and data archiving, as well as providing a web-interface to the EnMAP user community, is operated by the German Remote Sensing Data Center (DFD) with its multi-mission infrastructures located in Oberpfaffenhofen, Germany, and Neustrelitz, Germany, where also the main X-band payload data ground station is located. The Processor, Calibration, and Quality Control System, responsible for developing the hyperspectral processing system capable of generating high quality calibrated EnMAP data products at several processing levels, calibrating the sensor and validating the products, is operated by the Remote Sensing Technology Institute (MF) supporting the mission with its expertise and dedicated elements located in Oberpfaffenhofen, Germany, and Berlin, Germany. These three systems are further separated into 15 subsystems as illustrated in Fig. 2 (Müller et al. 2009).

Let us consider a routine scenario in the context of one of the major technical budgets of the ground segment which is—beside the product quality—the system response time. The system response time is defined as the maximal duration between the observation request put by a user and the delivery of the corresponding products to the user. The corresponding schematic workflow is marked blue in Fig. 2 starting and ending at the user segment. We subdivide the workflow when the scheduling of the observation requests is performed. Figure 3 illustrates the typical workflow for two observation requests (to be acquired within the same orbit, but not excluding each other) and corresponding up- and downlinks ending with the planning of the Timeline. Figure 4 illustrates the typical workflow beginning with the planning of the Timeline. Here, typical means that nominal operations are carried out and the segment is not in contingency operations. We do not consider the budgets concerning network throughput and network outage times here. All subsystems with exception of these for satellite control and commanding are designed such that network outage times of at least one week do not lead to loss of data (rolling archive with appropriate sizing). Thus, even longer outage times result in at most partial losses of "overflow" data. The network for satellite control and commanding is identified to be critical and therefore in particular redundant and leads to specific contingency operations.

Let us go into the details of Fig. 3. The S- and X-band ground stations communicate their availabilities (shown in blue) once a week for at least two weeks in the future. Based on this information and the observation requests submitted by a user, a planning of the subsequent Timeline is performed six hours before each S-band contact. The user can put her/his observation request in the time between the acceptance of her/his proposal (observation request #1) and at least 7 h before the S-band contact (observation request #2), where the corresponding acquisition has to be commanded. Since at least every 12 h an S-band contact is foreseen and the commanded Timeline covers up to 12 h, the user has to put her/his observation request at least 19 h before the (potential) acquisition. (The typical user is not informed about planned S-band contacts.)

Let us go into the details of Fig. 4. However, within the Timeline the two observation requests under consideration and subsequent S- and X-band contacts are scheduled (shown in blue). (Of course, the ground stations are informed about the planned S- and X-band contacts as well.) Data budgets detail that the planned S- and X-band contacts with a total duration of at least 30 min (for each band) each day are sufficient. Telecommands representing this Timeline are sent to the satellite and its telemetry is received via S-band. The loss of an S-band contact and link budgets are not considered here. At the computed moment of time the acquisition is performed. The orbit and attitude data covering an acquisition are received via X-band in the next contact whereas this cannot be assured for all channels of an image. But after 24 h the whole mass memory is dumped once (and the dump is performed by the "first in first out" principle). The loss of an X-band contact and link budgets are not considered here. At most 24 h after X-band downlinks the corresponding orbit and attitude products are generated and long-term archived. When these products and all channels of an image are available—

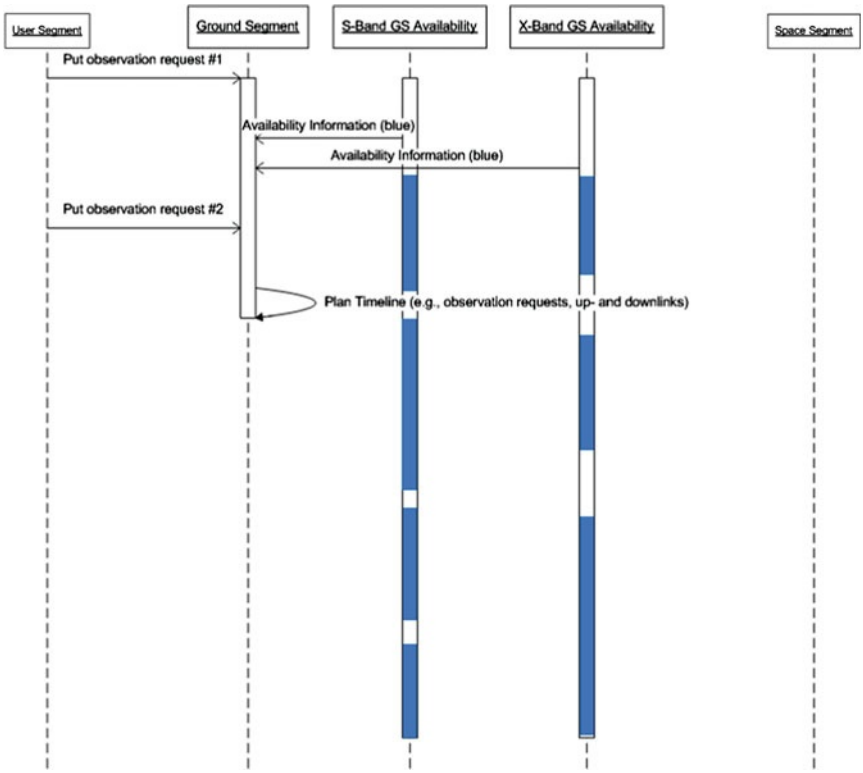

Fig. 3 Overview put observation request to planning of timeline

the calibration tables are already archived—, the archive products (Level 0) will be created. This is done in at most six days. The specific duration depends on the processors load due to the generation of products to be delivered (Level 1, Level 2). In at most four days the products to be delivered (Level 1, Level 2) are generated based on the archive products (Level 0) (Habermeyer et al. 2010).

We observe, that in particular the following subsystems are directly involved in image processing and the provision of auxiliary data (Storch et al. 2009):

- Communication Subnet (EOC part) and Infrastructure (GSOC part) connecting all subsystems via network.
- Data and Information Management System is a multi-mission facility which combines distributed archiving and dissemination of data products internally and also to the user segment through an online interface.
- Processing System generates archive products as well as spectral, radiometric, geometric, and/or atmospheric corrected hyperspectral images on an operational basis.

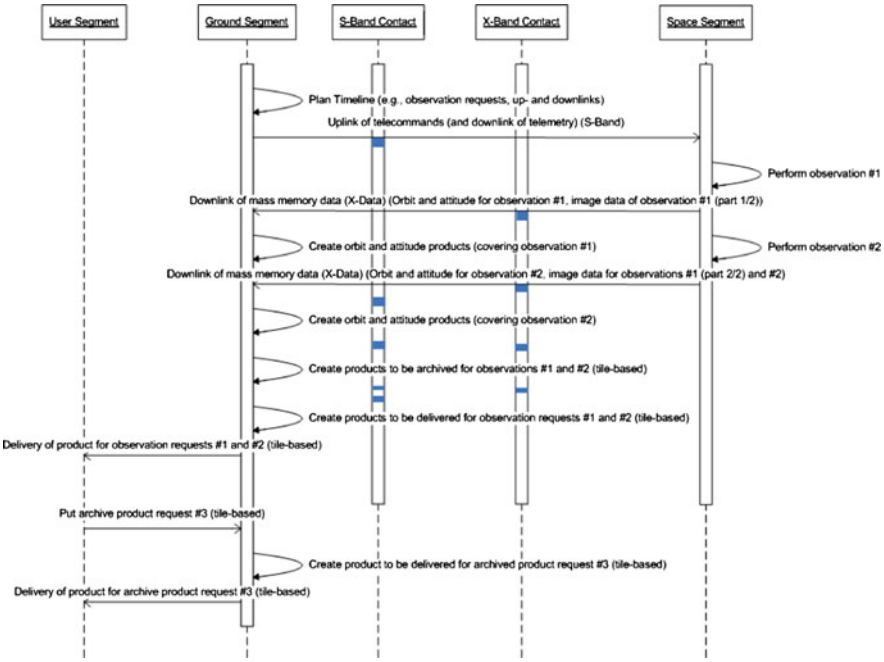

Fig. 4 Overview planning of timeline to delivery of products

- Auxiliary Data Ingestion collects all supplemental information for hyperspectral image generation such as spectral, radiometric, and geometric calibration and reference tables as well as orbit and attitude products.
- Spectral and Radiometric Calibration generates calibration and reference tables based on dark current measurements, measurements of internal sources such as lamps and Light-Emitting Diodes (LED), and Sun measurements for spectral and radiometric characterization and calibration.
- Quality Control and Ground Calibration generates geometric calibration and reference tables based on different on-ground measurements. Additionally the accuracy of all types of hyperspectral images is assessed to detect calibration or processing errors and quality information are added to the EnMAP products.
- Flight Dynamics comprises orbit and attitude determination as well as orbit prediction based on relevant on-board measurements such as data from the Global Positioning System and on-ground measurements such as ranging and angle tracking. Another aspect is the manoeuvre planning on a regular basis.
- Development Processor is used as a platform under versioning control for the development of the processing chain to be ingested in the Processing System (see above). It is described in detail in the next section.

3 Hyperspectral Image Processing Chain

The hyperspectral imager (HSI) will be realized as a pushbroom imaging spectrometer. Its data acquisition over the broad spectral range from 420 to 2,450 nm will be performed by a 2-dimensional CMOS (Complementary Metal Oxide Semiconductor) detector array for VNIR (visible and near infrared) with approximately 96 spectral channels, i.e. 6.5 nm spectral resolution, and by a 2-dimensional MCT (Mercury Cadmium Telluride) detector array for SWIR (shortwave infrared) with approximately 136 spectral channels, i.e. 10 nm spectral resolution, each with an analogue-to-digital converter resolution of 14 bits. The across direction of the arrays is used for the spatial resolution and the along direction for the spectral resolution. The ground pixel size will remain constant over the whole mission lifetime at certain latitude, e.g. 30 × 30 m^2 at nadir at 48° northern latitude. In this context a geographical accuracy of 100 m will be achieved for the image products which will be improved to 30 m with respect to a used reference image, if it exists, by ground processing. The sensors' 1,000 valid pixels in spatial across direction results in a swath width of 30 km (Mogulsky et al. 2009). An overlapping range from 900 to 1,000 nm between the VNIR and SWIR spectral channels will enable the processing chain to improve the atmospheric correction by resolving the water absorption band around 950 nm with sufficient signal to noise performance which is, e.g. 500 at 495 nm and 150 at 2,200 nm. The data acquisition of the two spectrometers is realized with the method of in-field separation utilizing two entrance slits. This leads to a time separation of approximately 88 ms between the VNIR and SWIR channels and means that the SWIR instrument scans the same area on-ground about 20 lines delayed with respect to the VNIR instrument (a small latitude dependent offset will be noticed in across direction due to the Earth rotation). Therefore an increased effort in geometric processing is necessary in order to be better than the required co-registration accuracy of 0.2 pixel size. Based on the advanced spectrometer design keystone and smile effects can be neglected, but will be recognized in the processing chain (Müller et al. 2010).

Figure 5 shows an overview of the image processing chain (de Miguel et al. 2010). The **Level 0 (L0) Product** is always generated for long-term archiving in Data Information and Management System. It is only used for internal purposes and will not be available for external users. The following products will be generated on user request:

- **Level 1 (L1) Product**: it is radiometrically calibrated, spectrally characterized, geometrically characterized, quality controlled and annotated with preliminary pixel classification (usability mask). The auxiliary information (e.g. position and pointing values, interior orientation parameters, gain and offset) necessary for further processing is attached, but not applied
- **Level 2geo (L2geo) Product**: it is derived from the L1 product and geometrically corrected (correction of sensor, satellite motion and terrain related distortions) and re-sampled to a specified grid (orthorectified). Auxiliary data for further processing are attached, but not applied.

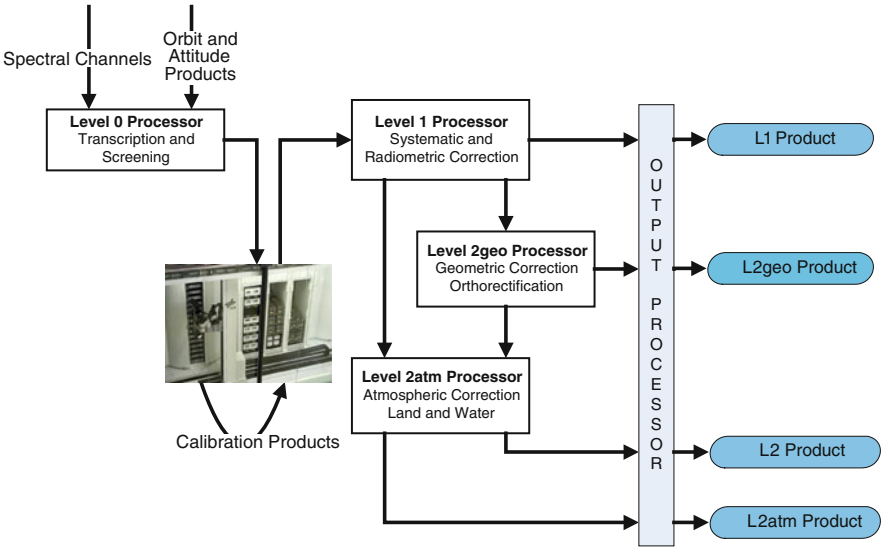

Fig. 5 Schematic illustration of image processing chain

- **Level 2atm (L2atm) Product**: it is derived from the L1 product, atmospherically corrected and the data converted to ground surface reflectance values. Auxiliary data for further processing are attached, but not applied.
- **Level 2 (L2) Product**: it is derived from the Level 2geo product, atmospherically corrected and the data converted to ground surface reflectance values.

As product format for Level 1 and Level 2 the user can choose an image format of BSQ, BIL, BIP, JPEG2000, and GeoTIFF and the metadata format is always Extensible Markup Language (XML). A product report in portable document format (PDF) is appended to the product.

3.1 Level 0 Processor

Level 0 Processing for Earth and calibration data takes

1. collects the information from the different data streams,
2. screens the image and housekeeping (HK) data quality which includes unpacking and, if necessary, decompression of the data,
3. extracts, evaluates, and transcripts the available metadata to the XML format,
4. extracts and evaluates the calibration values which includes the separation of dark current measurements at the start and end of each datatake,
5. tiles the Earth datatake into parts of size 1,024 $\times$ 1,024 pixels as illustrated in Fig. 1 (bottom right), where the first and last 12 pixels of each line are also dark current measurements,

6. generates quick looks of Earth data takes in Joint Photographic Experts Group (JPEG) format which includes the execution of parts of the Level 1, Level 2geo, and Level 2atm Processors particularly for specific channels,
7. generates dead, suspicious, land-water, and cloud-haze masks for Earth datatakes,
8. annotates the tiles of Earth datatakes with data quality and search information, and
9. archives the raw data product.

The evaluations performed include in particular checks, if temperatures, voltages, currents, and pixel values are stable or in specified ranges and that the HK data are consistent.

3.2 Level 1 Processor

Level 1 Processing corrects the hyperspectral image data for known systematic effects. It also converts the system corrected image data to physical at-sensor radiance values based on the current valid calibration values and dark current information. The correction includes

1. flagging and screening of dead pixels based on corresponding calibration tables,
2. flagging of saturated (hot) and no-response (cold) pixels including removal of dark current measurements at the start and end of each line,
3. correction for non-linearities based on Look-Up-Tables (LUT),
4. correction for dark signal based on corresponding measurements at the start and the end of the datatake,
5. correction for stray light for the spectral and spatial direction,
6. correction for response non-uniformity (RNU),
7. gain matching for the VNIR detector since the low or high gain is automatically selected, namely low gain values have to be multiplied by gain matching coefficient to high gain values,
8. spectral referencing, where channels are assigned with wavelength information, namely with the center wavelength and the full width at half maximum (FWHM),
9. radiometric referencing since the data are finally stored in integer values with 16 bits and not as floating values used in the previous steps, and
10. annotation of data quality information in the form of reports or masks.

3.3 Level 2geo Processor

Level 2geo Processing applies the method of Direct Georeferencing (DG) to convert imagery into map-accurate forms by removing sensor, satellite motion, and terrain related geometric distortions from raw imagery. In particular for

change detection application this is one of the key issues to accurately overlay the image data with existing data sets or maps, namely for multi-source data integration or fusion. The physical method of DG is based on a Line-of-Sight (LoS) model, which extensively utilizes on-board measurements from Star Tracker Systems (STS), Inertial Measurement Units (IMU), Global Navigation Systems (GNS) as well as the geometric sensor characterization by laboratory and/or in-flight calibration. Also effects such as terrain displacements, speed of light, light refraction by the Earth's atmosphere, and Earth's rotation are considered. To achieve a co-registration accuracy of 0.2 pixels between the two spectrometers not only the absolute geometric error but also the relative geometric error during 88 ms is considered. While the pixels are registered concerning time by Level 0 and Level 1 processing, the pixels are registered concerning geometry by Level 2geo processing. The 4-step process of orthorectification consists of:

1. Direct Georeferencing Model
    a. Synchronization of attitude and position/velocity measurements with time tagged image lines using appropriate interpolation,
    b. Establishment of the LoS vector using the sensor's internal geometry, payload assembly geometry and time dependent satellite motion during image acquisition,
    c. Setting up the collinearity equation to relate locations of image pixels with an earth reference coordinate frame.
2. Digital Elevation Model (DEM) Intersection Model
    a. Projection of the DEM to the coordinate frame specified in the DG model,
    b. Interpolation of the DEM to generate a dense grid of height values appropriate for the orthorectification task,
    c. Connection of the DEM and LoS vector by an iterative procedure in order to retrieve object point coordinates for each image pixel.
3. Map Projection Model
    a. Transformation of the object points to a map projection like global systems, such as Universal Transverse Mercator (UTM) projection with World Geodetic System 1984 (WGS84) datum, or local system, such as the European Lambert Azimuthal Equal Area (LAEA) with European Terrestrial Reference System 1989 (ETRS89) datum. The projection can be chosen by the user.
4. Resampling Model
    a. Provision of different resampling techniques such as Nearest Neighbor, Bilinear, and Cubic Convolution, appropriate for processing. The resampling technique can be chosen by the user.

The geometric accuracy of the orthoimages derived by DG making use of the ORTHO code can be improved using Ground Control Point (GCP) information to

refine the parameter sets of the LoS model from approximately three Ground Sampling Distances (GSD) to one GSD. Image-to-image matching algorithms such as Intensity based Image Matching and Shaded DEM Matching permit the automatic extraction of GCP provided that existing orthoimages of superior geometric quality as global or local reference images are supplied.

Data quality information, like the Root Mean Square Error (RMSE) and residual plots, where Independent Control Points (ICP) serve as input, are annotated.

3.4 Level 2atm Processor

The Level 2atm Processing performs atmospheric corrections of the images employing separate algorithms for land and water applications. Scenes may also be processed in both modes, e.g. for coastal areas or inland lakes that may contain a large percentage of land and water pixels. The mode of correction "land and water", "land only", or "water only" can be chosen by the user.

In case of atmospheric correction over land, the Level 2atm Processor will make use of the ATCOR (atmospheric correction) code which takes into consideration flat and rugged terrain, and includes haze/cirrus detection and removal algorithms. Output products will be the ground reflectance cube, aerosol optical thickness and atmospheric water vapor maps, and land, water, haze, cloud and snow maps. Therefore, the six atmospheric functions path radiance, direct and diffuse transmittance ground-to-sensor, direct and diffuse solar flux and spherical albedo are considered. Aerosol type and optical thickness is automatically determined over land. Columnar water vapor is calculated using channels around 940 and 1,130 nm and appropriate reference or window channels around 880, 1,020 nm and 1,080, 1,240 nm, respectively. An optional combined atmospheric and topographic processing is possible for scenes with accurate geometric correction (geometric accuracy better than one GSD) where no artifacts caused by the inaccurate registered DEM and orthorectified image are present can be chosen by the user.

In case of atmospheric correction over water, the Level 2atm Processor converts the top-of-atmosphere radiance imagery into water bulk reflectance values in the visible interval. The processing includes: Sun glitter map generation by identification of specular reflection, namely sun glint, on water bodies, correction of water mask, cirrus detection and correction for all water pixels not covered with clouds and not affected by sun glitter, adjacency correction, retrieval of aerosol optical thickness, and atmospheric correction for all water pixels not covered with clouds and not affected by sun glint. Only the channels in the spectral region 420 to 900 nm are processed.

Data quality information, like land-water and haze-cloud-snow probabilities based on spectral criteria as well as the aerosol optical thickness separated for land and water, are annotated.

3.5 Quality Control Activities

With the advent of operational remote sensing services there is an increasing demand in highly reliable, well documented and standardized data products (Bachmann et al. 2010). In order to achieve this goal, operational data quality control (QC) and validation activities are essential. This comprises the documented quantitive assessment of geometric, radiometric, and spectral properties of data products (see also previous sections) to be provided to the user. By this process the valid function of the sensor and processing chain is investigated and thus ensured. In order to distinguish an anomalous from a nominal state of the instrument and processor, the uncertainty budgets related to the spectral, radiometric and geometric data product properties must be known. Therefore this data uncertainty analysis is also included within QC. This is one part of the operational processing chain in order to investigate the specific quality of a data product ordered by the user such as QC flag image (per-pixel quality measure) and the related metadata, but also contributions to the overall quality flag are generated. On a regular basis an additional interactive QC analysis will be carried out such as quantification of the signal to noise ratio and modular transfer function. This is necessary since certain properties can not be analysed in a fully automated way and these information will be provided to the user community.

4 Conclusions

This chapter illustrated that the design of the ground segment for the first German optical Earth observing spaceborne mission EnMAP (Environmental Mapping and Analysis Program; www.enmap.org) and in particular of its hyperspectral image processing chain is predestinated to allow for meaningful downstream change detection activities on a global scale. Therefore, especially the system response time in combination with the frequent revisits and the comparable radiometrically calibrated, spectrally characterized, geometrically and atmospherically corrected products annotated with quality information were discussed. Activities planned to extend these considerations are the processing of simulated datatakes with a focus on its adequacy for downstream change detection purposes. Furthermore, it is planned to consider also if the system response time could be reduced and if sun glint correction could be supported. The status corresponds to the baseline for the production activities of the ground segment, namely only minor changes are expected. The establishment and operation of the ground segment is under responsibility of the Earth Observation Center (EOC) and the German Space Operations Center (GSOC) at the German Aerospace Center (DLR).

Acknowledgments Supported by the DLR Space Administration with funds of the German Federal Ministry of Economic Affairs and Technology on the basis of a decision by the German Bundestag (50 EE 0850).

References

Bachmann M, Habermeyer M, Müller A, Müller R, Schneider M, Storch T (2010) Operational quality control for hyperspectral data. In: Hyperspectral workshop 2010. Frascati, Italy

de Miguel A, Bachmann M, Makasy C, Müller A, Müller R, Neumann A, Palubinskas G, Richter R, Schneider M, Storch T, Walzel T, Wang X, Heege T, Kiselev V (2010) Processing and calibration activities of the future hyperspectral satellite mission EnMAP. In: Hyperspectral workshop 2010. Frascati, Italy

Habermeyer M, Storch T, Eberle S, Makasy C, Maslin S, de Miguel A, Mißling K-D, Mühle H, Müller R, Engelbrecht S, Gredel J, Heiden U (2010) Ground segment design of the EnMAP hyperspectral satellite mission. In: Hyperspectral Workshop 2010. Frascati, Italy

Heiden U, Gredel J, Pinnel N, Mühle H, Pengler I, Reissig K, Dietrich D, Heinen T, Storch T, Eberle S, Kaufmann H (2010) The user interface of the EnMAP satellite mission. In: IGRASS 2010. Honolulu, Hawaii, USA

Kaufmann H, Segl K, Guanter L, Chabrillat S, Hofer S, Bach H, Hostert P, Müller A, Chlebek C (2009) Review of EnMAP scientific potential and preparation phase. In: EARSeL SIG-IS workshop. Tel Aviv, Israel

Mogulsky V, Hofer S, Sang B, Schubert J, Stuffler T, Müller A, Chlebek C, Kaufmann H (2009) EnMAP hyperspectral imaging sensor on-board calibration approach. In: EARSeL SIG-IS workshop. Tel Aviv, Israel

Müller A, Braun A, Mühle H, Müller R, Kaufmann H, Storch T, Heiden U, Gredel J, von Bargen A (2009) Designing the ground segment of EnMAP: elements, organisation, and challenges. In: EARSeL SIG-IS workshop Tel Aviv, Israel

Müller R, Bachmann M, Makasy C, de Miguel A, Müller A, Neumann A, Palubinskas G, Richter R, Schneider M, Storch T, Walzel T Kaufmann H, Guanter L, Segel K, Heege T, Kiselev V (2010) The processing chain and Cal/Val operations of the future hyperspectral satellite mission EnMAP. In: 2010 IEEE aerospace conference. Big Sky, Montana, USA

Rossner G, Schaadt P, Chlebek C, von Bargen A (2009) EnMAP—Germany's hyperspectral Earth observation mission: outline and objectives of the EnMAP mission. In: EARSeL SIG-IS workshop. Tel Aviv, Israel

Storch T, de Miguel A, Palubinskas G, Müller R, Richter R, Müller A, Guanter L, Segl K, Kaufmann H (2009) Processing chain for the future hyperspectral mission. In: EARSeL SIG-IS workshop. Tel Aviv, Israel

Storch T, Eberle S, Makasy C, Maslin S, de Miguel A, Mißling K-D, Mühle H, Müller R, Engelbrecht S, Gredel J, Müller A (2010) On the design of the ground segment for the future hyperspectral satellite mission EnMAP. In: 2010 IEEE aerospace conference. Big Sky, Montana, USA

Stuffler T, Kaufmann C, Hofer S, Förster K-P, Schreier G, Mueller A, Eckardt A, Bach H, Penné B, Benz U, Haydn R (2007) The EnMAP hyperspectral imager—an advanced optical payload for future applications in Earth observation programmes. Acta Astronaut 61(1–6):115–120

Stuffler T, Hofer S, Leipold M, Förster K-P, Sang B, Schubert J, Penné B, Kaufmann H, Müller A, Chlebek C (2009) EnMAP—space segment—instrument and mission parameters. In: EARSeL SIG-IS workshop. Tel Aviv, Israel

Van der Meer FD, De Jong SM (eds) (2006) Imaging spectrometry—basic principles and prospective applications. Springer, The Netherlands

Detecting and Characterizing Settlement Changes in Developing Countries Using VHSR Data: Case of the Coastal Area of Benin

Ulrike Sturm-Hentschel, Andreas Christian Braun, Stefan Hinz and Joachim Vogt

Abstract In many developing countries, coastal areas show high dynamics of settlement structures, which are hardly regulated by regional planning and therefore give rise to a series of risks. Most of all, increasing settlement density and spread in areas close to the shoreline and into wetland areas appear worrying against the background of climate change and sea level rise. In our study area, the coastal zone of Benin, settlements are spreading into agricultural areas as well as near-natural zones, towards the lagoon and are threatened by coastal erosion. To enable regional planners to take these threats into account, process monitoring respectively modelling based on remote sensing data is needed. Due to very small land use structures and the necessity of detecting individual buildings, very high spatial resolution (VHSR) data has to be used. However, like in other developing countries, VHSR data availability is poor. Furthermore, process analysis and modelling based on approaches for industrialized countries are not feasible due to strong differences in the appearance of villages respectively suburban areas in Benin. Individual buildings are sometimes even difficult to detect by eye, nonetheless, to achieve large-scale information, automation is indispensable. We exemplify these issues for the coastal area of Benin by an approach based on both

U. Sturm-Hentschel (✉) · A. C. Braun (✉) · S. Hinz
Karlsruhe Institute of Technology (KIT), Institute of Photogrammetry and Remote Sensing, Karlsruhe, Germany
e-mail: ulrike.sturmhentschel@yahoo.de

A. C. Braun
e-mail: andreas.ch.braun@kit.edu

U. Sturm-Hentschel · J. Vogt
Karlsruhe Institute of Technology (KIT), Institute of Regional Sciences, Karlsruhe, Germany

J. M. Krisp et al. (eds.), *Earth Observation of Global Changes (EOGC)*, Lecture Notes in Geoinformation and Cartography, DOI: 10.1007/978-3-642-32714-8_5,

manual and segment-based (semi-)automatized building detection. We use the results to analyze the settlement process and model its further evolution by data driven modelling.

1 Introduction

In developing countries, there is a great need to detect spatial processes like changes in the settlement structure. Remote sensing can be used to describe the spatial extents of these processes. The derived information can consequently be used for simulation or modelling and can serve as decision base for further planning. We exemplify these issues for the coastal area of Benin in Western Africa. Like most coastal zones worldwide (Department of Economic and Social Affairs (DESA) 2007), it is the most densely populated area of the country (Institut national de la statistique de l'analyse economique (INSAE) 2004) and yet migration destination (e.g. Doevenspeck 2005; Teka 2010). Very high settlement dynamics, characterized by high building activities within and around settlements together with land seizure of formerly near-natural areas as well as agricultural areas characterize this process. Our study area is close to the administrative and economical capital, Cotonou. Several studies deal with processes in the coastal region (e.g. Domingo 2007; Teka 2010). However, unlike for other areas of the country (Doevenspeck 2005; Judex 2008), migration processes and their implications have been barely analyzed in their spatial extension for this area.

The combination of inordinate settlement processes referred to as urban sprawl by Zhang (2004) according to Bhatta (2010), and land seizure in areas near to the shore line and into wetland areas give cause for serious concern. These processes need to be detected, analyzed and monitored in order to enable regional planners to face these challenges. Remote sensing and GIS are indispensable methods for accomplishing these tasks.

There are two objectives of this study: Firstly, we want to provide a methodology needed to detect and describe vectored processes of change in the settlement structure of a village in the coastal area of Benin based on remote sensing data. A reliable detection and description of these processes is an indispensable requirement to analyze and model them. Here, we want to refine our methodology presented in Sturm-Hentschel et al. (2011). Secondly, we will make an initial attempt to model further settlement growth based on the multi-temporal building detection.

In the study area, building densification and spread can be observed. They need to be spatially determined and quantified. To detect urban sprawl synoptically, in many studies the area of impervious surface is analyzed (Epstein et al. 2002; Jat et al. 2008). Yet, in developing countries, even in urban areas, dwellings are often the only impervious objects–open soil and vegetation are found in between dwellings. Hence, an approach based on detecting impervious surface is not

adequate. Pesaresi et al. (2009) present studies working with texture. Due to similar sizes and structures of buildings and fields—those approaches fail in our study area. Since buildings and fields are partially mixed, the very first step is to detect individual dwellings in order to analyze the process. Automatic extraction of objects like roads and buildings in natural environments is one of the challenging issues in photogrammetry and computer vision. Many approaches published on the detection of individual dwellings are based on computing features that take into account pixels neighbourhoods. The extended morphological profiles used herein are one type of these features, however many alternatives exist (e.g. features based on wavelets, local intensity gradients, empirical mode decomposition). Some of these approaches yield quite promising results. However, many approaches consider small subsets of images that exclusively show the urbanized area. The number of available classes in such subsets is limited. Thus, there are few classes buildings can be confused with. In contrast to that, our approach is based on entire images that consist of urbanized, vegetated and agricultural area. Outside the urbanized area, many open soil segments are found that are very similar to roof segments from urbanized areas. Therefore, the problem of confusion between these roof segments and open soils arises. Thus, approaches focused on detecting dwellings in scenes that exclusively show urbanized areas can not be applied directly. An approach needs to be developed that is able to detect dwellings within the multitude of classes present in datasets that consist of urbanized, vegetated and agricultural areas. The interested reader may be referred to e.g. Hinz (2008) for getting more detailed information about current issues and challenges of automatic object extraction. It must be noticed, however, that almost all approaches on automatic object extraction rely on quasi-perfect data in terms of resolution, overlap, revisit time etc. But, like in many developing countries, data availability is poor in our case. Therefore, the situation changes dramatically. For the area where we implemented our approach, only the scan of a grey-scale aerial image from 1995, a Quick Bird scene taken in 2002 and a RGB aerial image of 2007 were available. The heterogeneity of both the appearance of houses as well as the data available makes multi-temporal process identification a challenging task. Thus, different strategies on data interpretation need to be employed. Furthermore, the limited number of points in time renders process modelling an even bigger challenge–both issues will be tackled in our report.

Our approach is based on manual detection in order to achieve a high level of accuracy and certainty for smaller areas and on (semi-)automatized detection to provide means to gather information for larger areas. Classification results will be presented for both approaches and a comparison will be given. The manual results serve furthermore as reference for quality assessment of the automatized detection as well as for process analysis and modelling.

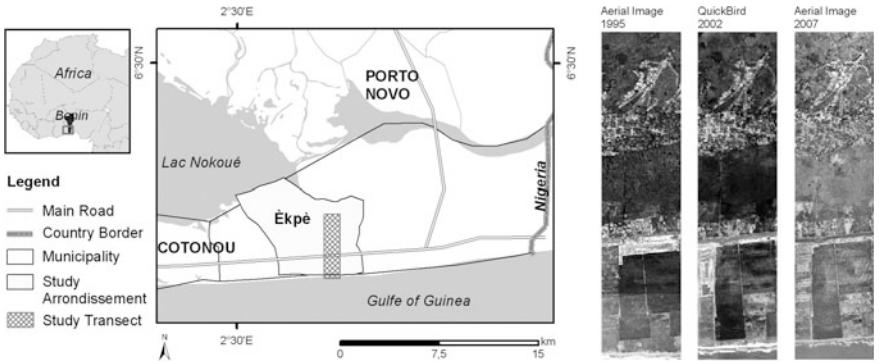

Fig. 1 Study area

2 Study Area

Our study area is situated in the coastal zone of Benin in Western Africa, situated at the Gulf of Guinea. The coastal area is geomorphologically a graded shore line with numerous recent and ancient lagoons that follow coast parallel structures in approximate west-east direction. Sandy ground and marsh alternate. The littoral is situated in the zone of tropical-summer humid climate (Weller 2002) and is characterized by two rainy seasons (April to July and October to November; Adam and Boko 1993).

Both rainy seasons implicate flooding, especially of the (ancient) lagoons. The study area represents one of the most densely populated areas of Benin (Institut national de la statistique de l'analyse economique (INSAE) 2004). It has shown very high settlement dynamics during the past years (Sturm et al. 2007; Vogt et al. 2007).

We chose the district Èkpè as our study area, a growing suburban region east of Cotonou, the administrative and economical capital. We apply our approach on a north–south transect (1,200 m × 4,850 m), which cuts several land use units. The northern and southern parts are characterized by dry sandy ground and are used apart from settlements (village of Djéffa in the north) mainly for agriculture in the north and plantations in the south. The middle part is characterized by an ancient lagoon, today marshland. The south bound is faced by the Gulf of Guinea and threatened by coastal erosion.

3 Data Base

We worked on a multi-sensorial time series using the scan of a gray-scale aerial image (March 1995, scale 1:30,000), QuickBird data (December 2002) and a color aerial image (March 2007, scale 1:20,000), see Fig. 1. The ground sampling

distance (GSD) of the gray-scale aerial image scans of 1995 is about 0.30 m, of the color aerial image of 2007 about 1.3 m; the used pan sharpened QuickBird bands of 2002 have a spatial resolution of 0.6 m. The aerial images of 1995 and 2007 are georectified based on the pan sharpened QuickBird dataset of 2002 and resampled to its GSD of 0.6 m. As one can see, our study represents an example of poor and heterogeneous data availability typical for least developed countries as mentioned above.

4 Methods

We base our approach on detecting individual buildings. The data situation, which is typical for developing countries, is not optimal for automatic detection: Dwellings in the study area show diverse shapes and sizes as well as manifold roof colors due to diverse roof materials such as new metal, corroded metal, asbestos or organic materials. Furthermore, the roofs seem to fuse with the surrounding surface: bright roofs with bright sand, darker roofs with dry vegetation. In order to have a certain and accurate base for modelling as well as for assessment, we choose to firstly classify dwellings manually, before we make an automatic attempt. The main reason for working towards an automatic building detection is to provide methods for analyzing the entire coastal area of Benin. After detecting individual buildings, we compute grid-based density estimation and analyze the density change over time. The settlement outlines we detect by a support vector approach. Based on these detected outlines, we model the change in time with a data-driven geometrical modelling approach.

4.1 Manual Building Detection

To analyze and quantify the change in the settlement structure in the coastal area of Benin we need to detect buildings. Due to the diverse shapes and manifold colors of the dwellings, we accomplish this task by manual classification at first. Buildings were digitized on-screen at a scale of 1:1,000, using the ArcGIS software. The obtained digitalization serves on the one hand as input for process analysis and on the other hand as data base for quality assessment of the automated building detection. Manual detection of dwellings assures reliable and high detection rates. However, it is very time consuming and consequently not a feasible solution for regions much larger than the study area. Thus, developing automatic detection methods is a crucial prerequisite in analyzing the entire coastal area.

4.2 Semi-Automatized Building Detection (User Defined Features)

As VHSR coverage of Benin is very heterogeneous–within the area of Èkpè, we already had to use three different sensors–a least common denominator needs to be found. Therefore, we exploit the only information present in all images–spectral intensity and geometry. Another reason for refraining to use the spectral information is that the spectral signature of dwellings is also very heterogeneous. Due to the limited spectral information, the shape of dwellings is the most important feature to detect buildings. Therefore, we segment our data, using the region growing algorithm (see Baatz and Schäpe 2000), implemented in the used eCognition Developer 8 software. As training and control areas we use such segments that overlap to at least 50 % with manually detected buildings.

In Sturm-Hentschel et al. (2011), we had only used the Bayes quadratic discriminant classifier (QDA) to classify buildings. Yet, we experienced that apart from the QDA, the Parzen classifier (based on Kernel density estimation) and the Fisher classifier (Linear discriminant analyses) produced the most accurate results for the test area used in Sturm-Hentschel et al. (2011a). For mathematical foundations see Duda et al. (2001). As the building detection needed for process analysis is a hard task, relying on a single classifier may not be the best option. We therefore tried to enhanced our approach by not only using one of the tested classifiers but now combine the results from the QDA, Parzen and Fisher classifiers by ensemble classification (Briem et al. 2002). Ensemble classification (*E*) attempts to integrate classification results by various single classifiers to a joint decision in order to yield higher accuracy rates. Various methods have been proposed (e.g. fuzzy majority voting, bagging, product combiner; see Briem et al. 2002 and Gomah et al. 2010). For our data, a very simple method yielded the best results: In the Pattern Recognition Toolbox (PR Tools) for Matlab, the decision values of each single classifier are scaled to [0,1]. Then, the product combiner multiplies the decision values of the single classifiers to a new vote. While this method is very simple, in preliminary tests it outperformed fuzzy majority voting and bagging on our data. Additionally to the ensemble classification (*E*) (see above), we tested and compared knowledge based classification (*KB*) and the newly integrated Optimal Box prototype (*OB*)–both in the eCogonition Developer 8 software. The latter classification approaches are based on samples (house vs. non-house segments) as well. The *KB* approach uses samples indirectly through analyzing the histograms of a variety of features, choosing proper features and adjusting the membership functions. *OB* generates membership functions automatically by searching the best separating features based upon sample training (Definiens 2009). Unfortunately, further information about the separation method can not be found in Definiens documentation.

Table 1 represents the chosen features. Within the *KB* approach, one set of features with their respective membership function was used for all dates. During training the histograms of all dates were compared synchronously. For *E* and *OB*,

Table 1 Used features for classification ("⊙": used; "-": not used) (*-intensity of pixels in segment)

	Ensemble classification (E)	Knowledge based classification (KB)	Optimal box classification (OB)		
	For all points in time	For all points in time	1995	2002	2007
Features based on spectral information:					
Mean*	⊙	–	⊙	–	–
Median*	⊙	–	–	–	–
Variance*	⊙	–	–	–	–
Minimum*	⊙	–	–	–	–
Maximum*	⊙	–	–	–	–
Value of segment after mean-shift	⊙	–	–	–	–
Max*-min*	⊙	–	–	–	–
No of grey values in segment	⊙	–	–	–	–
Features based on geometrical/shape information:					
Area (A)	⊙	⊙	⊙	⊙	⊙
Shape index	–	⊙	⊙	–	⊙
Lenght/width	–	–	⊙	⊙	⊙
Length (L)	–	⊙	⊙	⊙	⊙
Length of bounding box	⊙	–	–	–	–
Width	–	⊙	⊙	⊙	⊙
Width of bounding box	⊙	–	–	–	–
Equivalence diameter	–	–	⊙	–	⊙
L/4*((A)^(1/2))	⊙	–	⊙	–	⊙
L/A	⊙	⊙	⊙	⊙	⊙
Borderlength	⊙	–	⊙	–	⊙
Length of longest edge (polygon)	–	–	–	⊙	–
Extent	–	–	–	⊙	⊙
Radius of largest enclosed ellipse	–	–	–	–	⊙
Density	–	–	–	–	⊙
Asymmetry	–	–	–	–	⊙
Compactness	–	⊙	–	–	–
Number of edge pixels in segment (after canny operator)(n)	⊙	–	–	–	–
n/A	⊙	–	–	–	–

training was realized for the 2002-data. The used features and respective membership functions were afterwards transferred to the 1995- and 2007-data. For *OB*, these results were additionally compared to the outcomes of training with the 1995 data and 2007 data respectively.

In Sturm-Hentschel et al. (2011), we had developed and evaluated our first approach on a small subset of the images (in the north of the transect; village of Djéffa). There, automatic detection provided reasonable results. Both spread and densification could be assessed in general terms. Now we use the developed methods on the entire transect. Due to the heterogeneity of our data, a lack of robustness of the classification methods has to be feared.

4.3 Automatized Building Detection (Morphological Features)

The features used for semi-automatized detection were defined based on a user's appraisal, e.g. the size of the bounding box was computed and used since we considered it to be relevant for distinguishing buildings from background. However, human recognition on features adequacy for the classification process may be limited. Thus, it may be helpful to compute extra features for classification with an automatized algorithm which aims to introduce contextual information. Therefore, a second approach for automatized detection is employed. This approach is based on morphological profiles. Morphological profiles have been proposed by Benediktsson et al. (2005) mainly for the analysis of VHR data in urban datasets. The key idea is to extract features describing the spatial context of pixels to have a classification based on spectral and spatial features. The simplest method to complete this task would be to compute e.g. a median filtering applied to each channel. However, median filters are not shape-preserving, objects are simply blurred. Although they introduce spatial context into classification, the performance of classification could decrease since major objects are mixed up with minor objects. In contrast to that, it would be desirable to introduce spatial operations which completely preserve major objects and completely delete minor objects. This task is completed by morphological profiles. They apply the two key morphological operators (opening and closing) to the image channels and combine them to erosion and dilation operators. For this task, they use a structuring element (e.g. a disk) of a certain size. A structure is preserved if it completely fits into the structuring element; otherwise it is merged to the next bigger structure in which it is contained. Note that openings isolate bright objects while closings isolate dark objects in the image. Since an operation based on only one structuring element is hardly sufficient to cover the diversity of urban datasets, a whole series of structuring elements with different sizes is employed. Therefore, to an image *Im*, a whole series of closings *Cl* and opening *Op*, are computed based on structuring elements λ with different sizes (i.e. $\lambda 1,\ldots,\lambda n$). The resulting morphological profile would then be:

$$MP = \{Cl\lambda n, \ldots, Cl\lambda 3, Cl\lambda 2, Cl\lambda 1, Im, Op\lambda 1, Op\lambda 2, Op\lambda 3, \ldots, Op\lambda n\}.$$

Hence, a whole series of new features is computed which introduce the spatial context of an object in a certain neighbourhood around each pixel defined by structuring elements. These features preserve objects considered as major objects w.r.t. the current filter size while deleting smaller objects. From there, a shape preserving spectral-spatial classification is made possible. After computing the morphological profile, classification will be performed using support vector machines (SVMs, Vapnik 1992) since they have proven to be capable classifiers for spectral-spatial classification based on morphological profiles. An example is found in Tan and Du (2010).

4.4 Detecting the Settlement Outlines

As the goal of this study was to describe the change in settlement structures, merely detecting dwellings was only the first step. One approach to detect urban sprawl relies on the detection of the settlement boundary. To do this automatically, we use support vector domain description (SVDD)–which is usually used for classification. SVDD (Tax and Duin 1999) is designed to find enclosing boundary lines around data. In order to find a well-generalized boundary, it cuts off outliers–which would be single buildings far outside the settlements in our case.

4.5 Grid-Based Density Analysis

Settlement changes are not only characterized by sprawl of buildings but also by densification. On the results of the building detection, we perform grid based quantitative change detection. We aim to identify the areas of altered settlement structure. To achieve this goal we perform a grid based density analysis. We compute a grid with a size of 50 × 50 pixels (30 × 30 m^2). For each of the three points in time (1995, 2002, and 2007) we obtain an estimate for building (area) density for each year using the manual results. From these, we assess the change in settlement density by subtracting these density results from one another, estimating the densification during the periods 1995–2002, 2002–2007 and the entire period 1995–2007.

4.6 Data-Driven Modelling of Urban Sprawl

After detecting dwellings and the settlement boundary for the three points in time, we attempt to model the settlement spread. Yet, as mentioned above, the available data is very much constrained, so that we refrain from modelling density changes. Given only three points in time, modelling of processes is a hard task. Besides that, appropriate socioeconomic background is not fully explored up to now, like a lot of other information about driving and restricting factors. Nonetheless, a rough image of the dynamics is possible by a data driven, geometrical modelling, which presumes homogeneous spatial conditions. We take the normal of the boundary line in 1995 as a nucleus for our model. From there, we draw lines passing each point of the boundary outlines in 2007 (see Fig. 2). We calculate the distance d from the intersections of the lines with the boundary of 1995 and 2007. We divide this distance by the number of years (12) that passed between the points in time. Then, we interpolate starting from the 2007 line for 5 years along the direction of d. As a result, we obtained a large number of interpolation points. From these, we calculate a smooth prediction outline using the SVDD again.

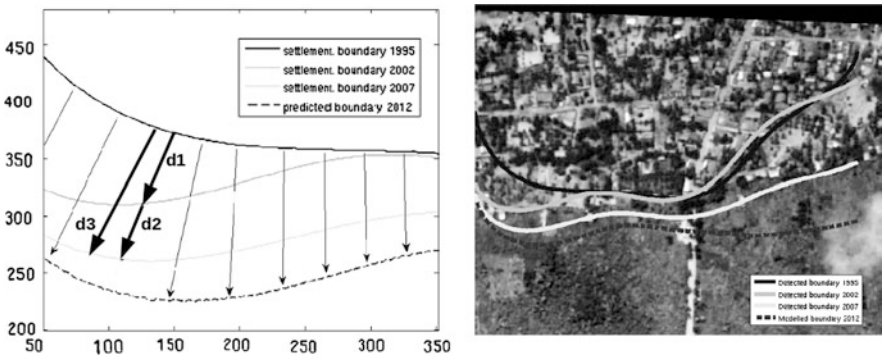

Fig. 2 Data driven modelling approach (*left* geometrical concept; *right* result, using the derived dwellings)

The result thus represents a geometrically motivated prediction for the year 2012. The blue, cyan and yellow lines represent the settlement boundaries, mentioned above, while the dashed red line represents the boundary of the data driven model for 2012 (5 years prognosis).

Of course, this is only to prognosticate the situation which would result assuming no spatial or temporal change in the urban sprawl–an assumption that is certainly incomplete.

5 Results

5.1 Comparison of Manual and Automatized Building Detection and the Resulting Settlement Outlines

Figure 3 shows (a) the manually, (b) and (c) semi-automatically detected dwellings with user defined information and (d) automatically detected dwellings with morphological information for the three points in time as grey-white dots and the respective settlement outline of the settlements produced with SVDD as a broad white line. Comparing the results, it becomes obvious, that the semi-automatic approaches based on user defined information classify too many segments of vegetated areas in the centre and the south of the scene falsely as buildings. The main reason for the high amount of false-positives is caused by confusion between open soil, vegetation and buildings of similar shape. For instance, segments in between the plantations in the south show building-like forms because of the patchiness of the plantations. The automatized approach based on morphological information also shows too many false positives, although to a smaller extent than the first semi-automatized approach. Obviously, many areas that either represent open soil within the settlement are classified as dwellings. On the other hand, it

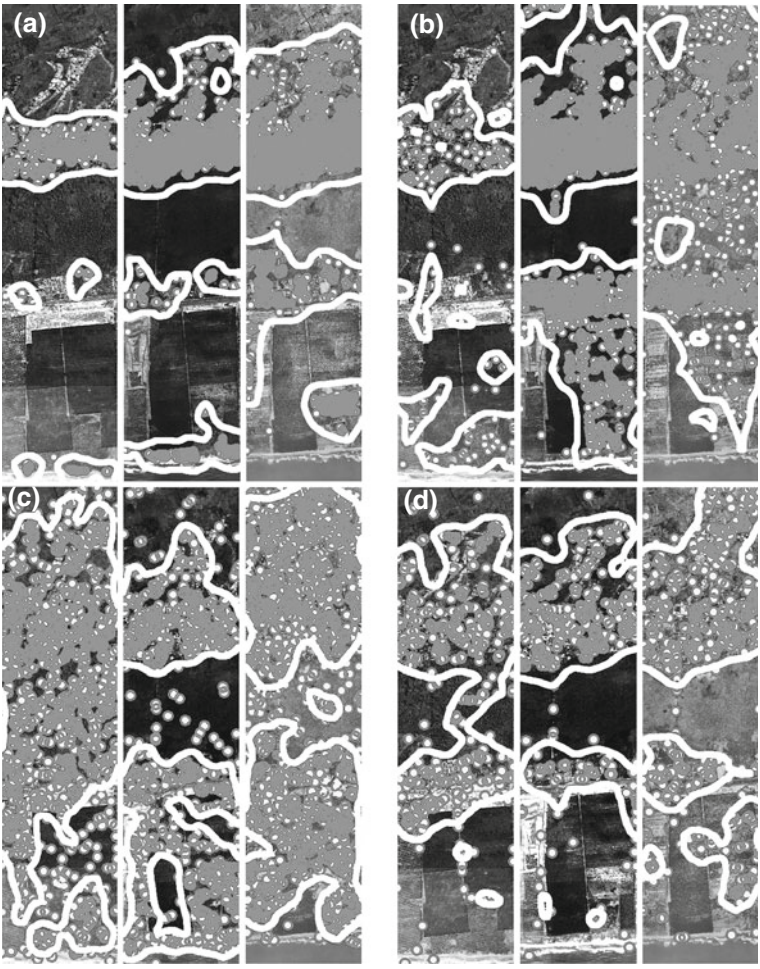

Fig. 3 Example of detected dwellings (*grey circles*) and boundaries (*white lines*) **a** manually. **b** by ensemble classification. **c** by knowledge based classification. **d** by automatized classification using morphological profiles (*left* 1995, *centre* 2002, *right* 2007)

should be noted that the major part of false positives by the *E* and *MP* approaches are found within settlements. From there, both approaches can give hints of human settlement activities although they may not perfectly allow for a building detection yet.

In respect of the spatial processes, the manual results show clearly an augmentation of dwellings and a spread of the settlements. The northern area, still left open in 1995, is being more and more populated in the following points in time. Dwellings are being erected in between the small fields. The boundaries of the areas north and south of the ancient laguna (in the middle of the images) come very close to this area; in fact, a number of houses is already situated within the

wetland. This indicates that there might be a threat of wetland vegetation (brush up to forest) being cut down when open spaces for new dwellings become scarce, or areas used for agriculture are being altered. In the south, dislocation of buildings can be noticed, caused by coastal erosion (Vogt et al. 2007). The northward spread of settlements of the village in the upper part and increase in size of the settlement patches in the centre can be observed in the automatized detection results as well, however, they are to a large extent disguised by the false-positives.

At this point, it can be concluded that the promising result for the Djéffa subset (Sturm-Hentschel et al. 2011) can not be enhanced and applied so far to the entire transect. Although morphological information has helped to reduce false positives automatized approaches still lack robustness. For this reason, density analysis and modelling have been computed on the manual results exclusively.

5.2 Quantitative Quality Assessment

Quantitative quality assessment was realized by using pixel-based measures. As control areas we used such segments that overlapped at least 50 % with manually digitized buildings.

The ensemble classification (*E*) based on user-defined features produced results that were quantitatively not satisfying (Table 2). High OAC values are yielded; however, one has to keep in mind that the major part of segments relates to non-building segments. Therefore, the non-building class vastly biases the OAC. One important performance measure for our task is the true-positive rate which is only moderate for all three points in time. For our task, performance measures which rely on a combination of completeness and correctness should be taken into account. F-Score and Youden's Index are such measures. Both are unsatisfying for the classification results. From there, although the ensemble-classification may give a first overall impression of the process, it should not be used for quantitative analyses or further processing (input for modelling). For every date, the knowledge based (*KB*) approach showed better results than the Optimal Box (*OB*) approach (Table 2). Further improvements might be necessary for that prototype, developed by Definiens. The *OB* does not even provide the best possible result: For 2007 e.g. 2002-*OB*-training transferred to the 2007-data provided a better result than training on the 2007-data itself. Altogether, Fig. 3 and all PPV values for *KB* and *OB* in Table 2 show that too many segments are wrongly classified as building. Concerning the SVM classification based on morphological profiles (*MP*), similar conclusions as for *E* can be drawn. While the OAC may seem convincing, F-Score and Youden's Index certainly are not. However, it can be stated that the results produced with morphological profiles are higher than the ones produced with user-defined features. This indicates that the relevant features for separation of buildings and non-building may be produced by automated algorithms and should be taken into account.

Table 2 Quality assessment (OAC = overall accuracy; FS = F-score; YI = Youden′s index; TPR = true positive rate; TNR = true negative rate; PPV = positive predictive value; NPV = negative predictive value)

	OAC	FS	YI	TPR	TNR	PPV	NPV
E 1995	0.98	0.26	0.38	0.39	0.99	0.19	0.95
KB 1995	0.88	0.03	0.55	0.68	0.88	0.02	0.99
OB 1995(*tr.*'02)	0.77	0.02	0.59	0.82	0.77	0.01	0.99
OB 1995	0.80	0.02	0.68	0.88	0.80	0.01	0.99
MP 1995	0.92	0.06	0.88	0.96	0.92	0.03	0.99
E 2002	0.98	0.26	0.38	0.39	0.99	0.19	0.99
KB 2002	0.93	0.13	0.74	0.81	0.93	0.07	0.99
OB 2002	0.87	0.08	0.87	0.99	0.87	0.04	0.99
MP 2002	0.94	0.16	0.85	0.91	0.94	0.08	0.99
E 2007	0.98	0.17	0.15	0.16	0.99	0.18	0.99
KB 2007	0.82	0.09	0.63	0.81	0.82	0.05	0.99
OB 2007(*tr.*'02)	0.67	0.06	0.62	0.95	0.67	0.03	0.99
OB 2007	0.61	0.05	0.58	0.98	0.60	0.03	0.99
MP 2007	0.90	0.17	0.80	0.89	0.90	0.09	0.99

5.3 Density Analysis

The settlement density and the density changes between the respective points in time are shown in Fig. 4. The images in Fig. 4a show spatially heterogeneous distributions of the dwellings. White indicates "no area covered by dwellings". Bright values show low settlement density, while dark values indicate higher settlement density. The highest density reaches 30 % areal coverage of a grid cell (black). The density change maps (Fig. 4b) reveal heterogeneous densification tendencies. Orange areas represent an increasing density, while blue ones represent a decrease.

As can be seen, the village in the north of the scene has become denser in the center and significantly increased in size between 1995 and 2007. The northern part of the village has not been very densely settled–an indicator of settlement sprawl. The same accounts for the settlement spread in the centre of the scene. The settlement at the shoreline in the south has been dislocated northwards between 1995 and 2002 as well as between 2002 and 2007, which is due to transgression of the shore line towards the north caused by coastal erosion.

5.4 Modelling the Settlement Spread

Figure 5 shows the geometrically modelled settlement spread and its prevision for 2012. Note that the settlement spread is stronger in some areas than in others (spatial anisotropy). In some areas, the urban sprawl accelerated between the two periods 1995–2002 and 2002–2007, while in others, it slowed down (temporal anisotropy).

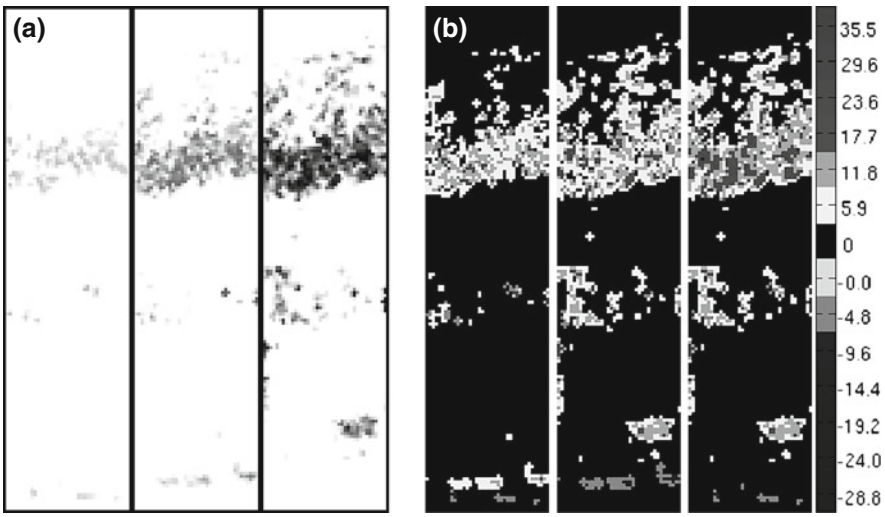

Fig. 4 **a** settlement density (*left* in 1995; *middle* in 2002; *right* in 2007) and **b** density change (*left* 1995–2002; *middle* 2002–2007; *right* 1995–2007)

If this prognosis is correct, the southbound land seizure caused by the northern settlement would implicate a severe loss of wetland vegetation. The most notable change would be a strong settlement spread towards the north of the scene, implicating a loss of agricultural areas as already observed in 2007. Furthermore, the settlements in the centre and the south east of the scene could significantly increase in size. The wetland area in the centre could decrease in size through settlement spread from the north and the south. However, these results can not be considered a reliable prognosis by themselves. While we believe that settlements will spread further into the agricultural areas in north of the scene, it is questionable to which extent people will settle in the wetlands in the future. At the shore line, no prediction line is found, since the model is not built for settlement dislocation.

We reckon that this prognosis should be used only as additional input data for a process oriented modelling as it can be derived quite easily from the classification results directly. A next step towards a process oriented modelling would be the integration of densification into the model.

6 Discussion

It could be shown, that the results perceived by manual detection serve well for further settlement analysis. While the (semi-)automization delivered for the village of Djéffa in the north of the transect good results (quality 91–97 %; detection 94–98 %; Sturm-Hentschel et al. 2011a), it did not perform well for the entire transect. Therefore, we refrained from using the detection results for an analysis

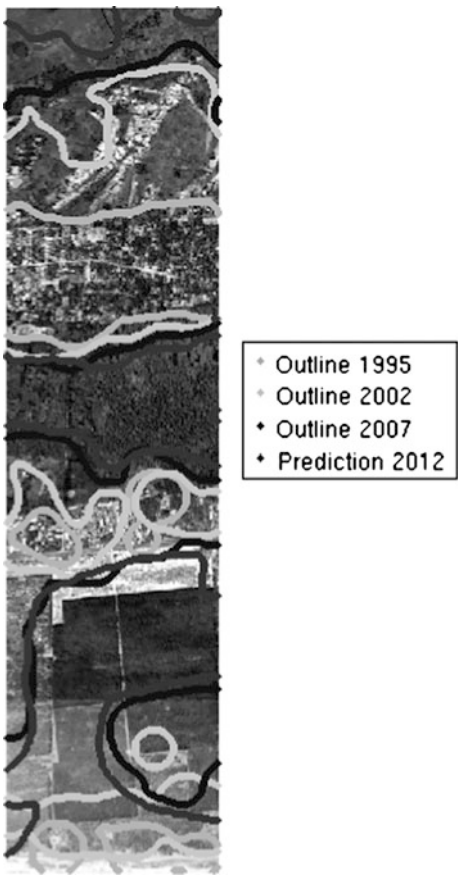

Fig. 5 Data-driven modelling of the settlement spread

of density change and modelling of settlement spread. Many segments that show open soil are fused with buildings or rooftops show different shading. Therefore, the segmentation is strongly affected by both over- and under-segmentation (Fig. 6).

As we use geometrical features besides intensity for building detection, a good segmentation is a crucial prerequisite for reliable detection. As mentioned above, we trained our classifier on the scene of 2002 only and used it for the other scenes as well. Of course, this approach has a number of limitations. Nonetheless, to train one classifier on each scene would not fulfil all the requirement of efficient transferability to other scenes taken in the coastal area.

The results for modelling the settlement spread we presented here are the outcome of a strictly data-driven geometrical approach. Data-driven modeling does not account of the factors that cause the change. They are merely represented implicitly by the boundaries detected. However, we do not have the necessary data (like e.g. land tenure, settlement behaviour and its drivers, digital terrain model, vegetation) to develop a modelling approach based on the processes themselves. It needs to be questioned whether urban sprawl will continue to follow the

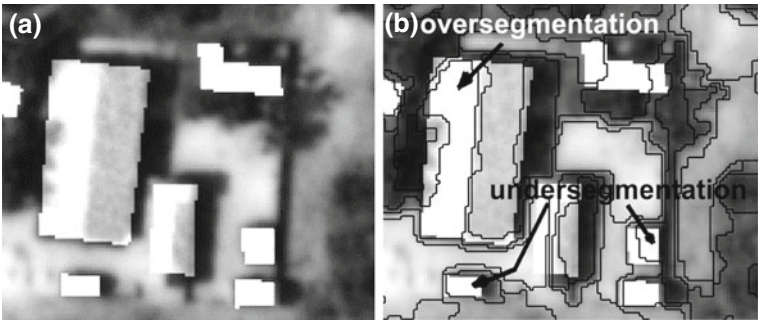

Fig. 6 **a** Image with manually digitized references and **b** segmentation result, showing over- and under segmentation (*white* digitized building reference; *black lines* segment borders)

tendency of 1995–2007. Which factors favor densification, which ones favor spread? Especially the spread into wetland area is difficult to estimate. Regarding informal conversations with settlers, financial causes seem to force people to settle into these risky areas. Yet, in order to understand these processes better, driving factors are being studied up to date.

Until now, automatized detection of dwellings is not achieved yet. Both, user-defined and morphological information is useful to describe the general tendencies (i.e. the centroid of settlements etc.). However, both approaches produce too many false-positives to be helpful in a quantitative assessment of urban sprawl. Since up-to-date classification methods were used, the second crucial point besides segmentation seems to be the features. Both types of features used are seemingly not fully able to achieve separation of buildings and background. More work has to be undertaken to find suitable features therefore. On the other hand, we believe that automatized building detection based on morphological profiles can help to capture the general tendencies of urban sprawl. This is particularly true for tasks that require a coarse image to be made available quickly. One has to keep in mind that the high precision of manual classification depends on time-consuming processing and could only be achieved by various field trips that created the users ground knowledge. One important aspect to keep in mind when considering the results of both automatized approaches–based on user-defined and based on morphological features–is the semantically different nature of the features used. The user-defined features aim to characterize the dwellings themselves (e.g. their size, length, width etc.). In contrast to that, morphological features aim to pronounce the relationship between dwellings and their spatial context.

7 Conclusion and Outlook

Semi-automatic and automatic building detection in data such as ours has not achieved the accuracy and reliability of manual classification so far. Using morphological profiles to describe the context around the individual building has admittedly reduces

false positives. Nonetheless, the performance is still unsatisfying for quantitative tasks. Since the approach based on user defined features includes features of the buildings and the morphological features are focussed on the surroundings of the buildings, an attempt to combine both could be beneficial. For manual classification, human cognition using indicators such as shadow helps to identify a dwelling even if part of it fuses with the surroundings. Therefore, manual detection seems still indispensable for analyses that require reliable results, when working on a data base like ours which is typical for many areas in developing countries.

Anyway, an enhancement of the automatized approach is needed in order to at least estimate settlement processes for larger areas. Therefore, concerning the automation of process analyses much more research efforts need to be made. Since any kind of automatized approach will work on segments, an adequate segmentation result is needed. For instance, if a dwelling is split up by over-segmentation or merged with an adjacent tree by under-segmentation, any kind of feature which aims to describe dwellings size or outline will deteriorate its performance. A poor segmentation result will therefore be the first step of error propagation that impoverishes the performance of the final result. As shown above, the segmentation result achieved up to now is far from being sufficient due to the special characteristics of villages in Benin (irregular building shapes, large areas covered with open soils or man made materials, lack of impervious surface etc.). Concerning segmentation of dwellings in relatively noisy images as presented in this study, approaches by (Ohliger et al. 2010) concerning region-based active contours might be one option to be tested.

For this study, we applied a straightforward and simple approach, detecting buildings in each scene separately. In the future, we will focus more research efforts on automization to be able to perform quantitative analyses based not only on manual but also automatized results. Crucial prerequisites hereby will be an enhanced segmentation result, more descriptive features for buildings and background and a fusion approach for user-defined and morphological features.

Regarding settlement modelling, the results of the data-driven approach should be used only as additional input data for a process oriented modelling as they can be derived from the classification results directly. Further socio-economic studies can contribute to a more processes oriented modelling.

References

Adam KS, Boko M (1993) Le Bénin. Les Editions du Flamboyant, Cotonou

Baatz M, Schäpe A (2000) Multiresolution segmenation—an optimization approach for high quality multi-scale image segmentation. In: Strobl XJ, Blaschke T, Griesebner G (eds) Angewandte geographische informationsverarbeitung. Wichmann-Verlag, Heidelberg, pp 12–23

Benediktsson JA, Palmason JA, Sveinsson JR (2005) Classification of hyperspectral data from urban areas based on extended morphological profiles. IEEE Trans Geosci Remote Sens 43(3):480–491

Bhatta B (2010) Analysis of urban growth and sprawl from remote sensing data. Springer, Heidelberg

Briem GJ, Benediktsson JA, Sveinsson JR (2002) Multiple classifiers applied to multisource remote sensing data. IEEE Trans Geosci Remote Sens 40(10):2291–2299

Definiens (2009) eCognition developer 8 reference book. Document Version 1.2.0, Definiens AG, München

Department of Economic and Social Affairs (DESA) (2007) Indicators of sustainable development: guidelines and methodologies, 3rd edn—Full set of methodology sheets, http://www.un.org/esa/sustdev/natlinfo/indicators/methodology_sheets.pdf. (Accessed 22 Nov 2011)

Doevenspeck M (2005) Migration im ländlichen Benin—Sozialgeographische Untersuchungen an einer afrikanischen Frontier. Studien zur Geographischen Entwicklungsforschung 30, Saarbrücken: Verlag für Entwicklungspolitik

Domingo E (2007) La région urbaine du littoral au Bénin: dynamiques urbanisantes et environnement, une géographie de l'aménagement du territoire. Université de Lomé

Duda RO, Hart PE, Stork DG (2001) Pattern recognition, 2nd edn. Wiley, New York

Epstein J, Payne K, Kramer E (2002) Techniques for mapping suburban sprawl. Photogram Eng Remote Sens 68(9):913–918

Gomah M, Trinder J, Shaker A, Hamed M, Elsagheer A (2010) Integrating multiple classifiers with fuzzy majority voting for improved land cover classification. In: Paparoditis N, Pierrot-Deseiligny M, Mallet C, Tournaire O (eds) IAPRS 38(3A):pp 7–12

Hinz S (2008) Automatic object extraction for change detection and GIS update. International archives of photogrammetry, remote sensing and spatial geoinformation sciences 37(B4):277–284

Institut national de la statistique de l'analyse economique (INSAE) (ed) (2004) Troisième Recensement Général de la Population et de l′Habitation de Février 2002. Cotonou: Direction des Etudes Démographiques

Jat MK, Garg PK, Khare D (2008) Modelling of urban growth using spatial analysis techniques: a case of Ajmer city (India). Int J Remote Sens 29(2):543–567

Judex M (2008) Modellierung der Landnutzungsdynamik in Zentralbenin mit dem XULU-Framework. Dissertation, University of Bonn, Bonn

Ohliger K, Edeler T, Hussmann S, Condurache AP, Mertins A (2010) A novel approach of initialising region-based active contours in noisy images by means of higher order statistics and dissimilarity. In: Proceedings IEEE 2010 International Conference on Mechatronics and Automation (ICMA) pp 477–482

Pesaresi M, Ehrlich D, Gamba P, Herold M (2009) A methodology to quantify built-up structures from optical VHR imagery. In: Global mapping of human settlement: experience, datasets and prospects, Taylor and Francis, New York, pp 27–59

Sturm U, Teka O, Vogt J, Bähr H-P, Buttschardt T (2007) Analyse von Prozessen im Küstenraum Benins–Grundlage für planerische Steuerung. In: Gönnert G, Pflüger B, Bremer JA (eds) Geographie der Meere und Küsten, Coastline Reports 9, pp 185–195

Sturm-Hentschel U, Braun AC, Hinz S, Vogt J (2011) Settlement process studies in developing countries using diverse remote sensing data types. In: Victoria Lenz-Wiedeman, Georg Bareth (eds). In: Proceedings of the ISPRS WG VII/5 Workshop, 18.-19.11.2010, Cologne, pp 131–142

Tan K, Du P (2010) Classification of hyperspectral image based on morphological profiles and multi-kernel SVM. 2010 2nd Workshop on hyperspectral image and signal pro-cessing: evolution in remote sensing (WHISPERS) pp 1–4

Tax DMJ, Duin RPW (1999) Support vector domain description. Pattern Recogn Lett 20(11–13): 1191–1199

Teka O (2010) Methode zur Analyse von raumrelevanten Prozessen in Entwicklungsländern: Das Beispiel des Küstenraums von Benin. Dissertation, Karlsruhe Institute of Technology

Vapnik V, Boser B, Guyon I (1992) A training algorithm for optimal margin classifiers. In: COLT'92 proceedings of the fifth annual workshop on computational learning theory pp 144–152

Vogt J, Sturm U, Teka O, Bähr H-P, Sinsin B (2007) Résultats Préliminaires de l′Analyse Evolutive de la Zone Côtière du Bénin: Cas Spécifiques des Arrondissements de Avlékété et de Sèmè. In: Actes du 1er colloque de l'UAC des Sciences, Cultures et Technologies, Géographie, pp 419–428

Weller U (2002) Land evaluation and land use planning for Southern Benin (WestAfrica)–BENSOTER. Hohenheimer bodenkundliche Hefte 67. Universität Hohenheim

Zhang B (2004) Study on urban growth management in China. Xinhua Press, Beijing

Parameter Determination by RapidEye and TerraSAR-X Data: A Step Toward a Remote Sensing Based Inventory, Monitoring and Fast Reaction System on Forest Enterprise Level

Thomas Schneider, Alata Elatawneh, Johannes Rahlf, Mengistie Kindu, Adelheid Rappl, Antje Thiele, Markus Boldt and Stefan Hinz

Abstract State forest administrations in Central Europe have to adapt to future climatic and socioeconomic conditions. This results in new demands for up-to-date and precise forest information—especially with regard to the increase of forest damages by natural hazards. Remote Sensing techniques are appropriated for delivering information in support of such tasks. We present details of a research project that focuses on the demonstration of the potential of satellite data for forest management planning and disaster management. Integrated in the over-all concept of a decision support system (DSS) for the forest–wood chain (Entscheidungs-Unterstützungs-System Forst-Holz, EUS-FH), the frame conditions for a 'Remote Sensing based Inventory and Monitoring System' for the forest-wood chain are developed. Particular focus is on investigations towards synergistic and complementary use of the two German satellite systems RapidEye and Terra SAR-X. The comparison is done on base of the accuracy of parameter derivation with each of the systems. The results deliver a couple of arguments for combined multispectral and SAR data use for monitoring and fast response situations in case of sudden calamities. But it reveals as well that the references against the results should be compared and, at the end, which represents the data layers to be updated, do not always fit from both, the semantic meaning e.g., the definition of 'forest' to

T. Schneider (✉) · A. Elatawneh · J. Rahlf · M. Kindu
Institute of Forest Management (IFM), Technische Universität München (TUM), Munich, Germany
e-mail: Tomi.Schneider@tum.de

A. Rappl
Bavarian State Institute of Forestry (LWF), Freising, Germany

A. Thiele · M. Boldt · S. Hinz
Karlsruhe Institute of Technology (KIT), Institute of Photogrammetry and Remote Sensing (IPF), Karlsruhe, Germany

J. M. Krisp et al. (eds.), *Earth Observation of Global Changes (EOGC)*, Lecture Notes in Geoinformation and Cartography, DOI: 10.1007/978-3-642-32714-8_6,

cartographic differences, and the representation of object categories. Harmonisation of definitions and categories to be mapped is needed.

1 Introduction

Worldwide forest resources are affected by global change phenomena. In connection, Central Europe state forest administrations have to adapt to future climatic and socio-economic conditions. The Bavarian forest sector is faced with a situation where climate change effects seem to destabilize forest ecosystems, the socio-economic demands on the ressource "forest" are continuously increasing and budgets for managing forests are cut. Significant biotic and abiotic calamity frequency increases are attributed to climate change. More than 30 % of the annual workload of a forest enterprise in Bavaria is in response to such unpredictable events. The different functions of a forest are more and more understood as social benefits and claimed by the society in the sense of stakeholder rights. In addition, national and international reporting duties are to be fulfilled by the owners and/or governmental bodies. To cope with all these diverse tasks a decision support system (DSS) (Entscheidungs-Unterstützungs-System Forst-Holz, EUS-FH) was designed for the forest-wood chain. An assessment study performed to figure out the needs of forest practitioners in forest management resulted in a list of parameters. The highest relevance was assigned to the parameters forest area, gaps, forest border length, forest changes, tree species groups, stand/tree height, and forest densities. These parameters should be updated timely for a sound decision support system (Felbermeier et al. 2010).

Amongst others, a major trigger of the activities toward such a DSS is the improved quality of the new class of high-resolution satellite imagery. Hence, current research and development deals with the opportunities of a 'Remote Sensing based Inventory and Monitoring System' for the Bavarian forests. The concept is based on the idea of integrating existing data offered by official sources such as: the Bavarian Surveying and Geoinformation Administration (LVG), the Bavarian State Forest Administration and others along, with remote sensing data as the most actual information layer. The geodatabases provide the 'a-priori' information used for restricting the solutions of the image analysis process and the results are used to update these databases. The system should be able to steer management operations and especially to support management decisions at the strategical/tactical level of a forest enterprise. At the final stage, the information system should contribute to facilitate the diverse national and international reporting duties as well.

This general approach became possible due the improved capabilities of the new generation of high-resolution and fast-revisiting remote sensing satellite systems (e.g., RapidEye, WorldView-2, TerraSAR-X, Cosmo-SkyMed soon ESA's Sentinels). The presented research is funded by the Federal Ministry of Economics and Technology, within a program of the Space Agency of the German

Aerospace Center (DLR). The program aims to promote the synergistic use of optical and radar satellite data with special emphasis to the new German systems RapidEye (RE) and TerraSAR-X (TS-X). Taking into consideration the high revisit frequency and the large area covering capability of RE, an annual update of the forest databases for whole Bavaria is likely possible. The clouds and daytime independent operation ability of the TS-X system should help, especially in the calamity case to identify the affected areas. Such a fast response capability should allow starting preventive measures within a short time and such reducing the following damages and economic losses. Apart from these basic expectations, the determination accuracy of forest parameters with each of the systems is in the focus of the project. From multi-seasonal RE data, an improvement of tree species differentiation is expected. While the prospect of high spatial resolution TS-X data is an improvement in structure parameter determination such as heights, canopy roughness, border and gaps or even single tree detection. Within the present project stage, the under development system components should demonstrate the continuous data flow required for the future operational system.

2 Previous Work

Forest mapping by remote sensing is done from the global to the local scale. Systems, mapping scale and aims are different. Remote sensing as an operational tool is established on the global and the local scale. On global scale, particular parameters like the forest coverage and the derived variables such as: biomass, LAI, CO_2-sinks and radiation budget, etc. are of high interest. The target is either the small scale documentation of forested areas or the derivation of input variables for models; the scale is of 1:250.000 and less.

On local scale, very high resolution (VHR) systems are required. The data usage is primarily for orientation (orthophoto) and in support of management actions. Aerial photographs and since a couple of years LIDAR (Light Detection and Ranging) are the most frequently used systems, followed by Quick Bird type satellite data. Mapping scales in the range of 1:10.000 and larger are targeted.

In between, at the regional to continental level with typical mapping scales of 1:25.000–1:250.000, the implementation of remote sensing methods in operational applications is still missed, at least in Germany. The concept of the 3rd National Federal Forest Inventory 2011/12 for Germany is not considering remote sensing data as information source. Nevertheless, there are a couple of studies demonstrating the potential of using the high resolution data type, e.g., for continental mapping purposes (FIRS, Corine) but for national inventories (2nd National Forest Inventory of Germany) or FAO's AfriCover concept.

This section provides an overview on forest related information extraction concepts and methods. First, a brief overview about standard Bavarian State forest inventory concept is given, followed by optical and microwave based mapping methods.

2.1 Bavarian State Forest Inventory Concept

The Bavarian State forest administration inventory concept is based on a permanent regular sample point grid net. The inventories should provide an overview over the area managed by an enterprise. The envisaged update frequency is of about 10 years, an expansion up to 12–15 years is not a singularity. Each inventory point represents a forest area of 2–4 ha. The sample point area is differentiating an inner circle of 31,25 m^2, a mid-circle of 125 m^2 and an outer circle of 500 m^2. Inside the inner circle all trees with a diameter breast height (dbh) <11 cm are registered, in the mid circle trees with dbh between 11–29 cm and in the outer circle all trees with dbh >29 cm. At least the parameter tree species, dbh, tree height, crown closure, timber stock, stand structure are measured or registered and the regeneration is estimated (Anonymous 2001; Knoke et al. 2012)

Typically, one year after an inventory the forest operations for the next period are planned. For forest planning, orthophotos are used for steering the ground survey. The produced management maps display the established new stand borders, forest operations planned for the next period, forest functions and special treatment areas as well as single trees like standards, seed trees, clearing rests. Tree species share per stand, age, condition, etc., are mentioned in the tabular records and associated comments. Interim inventories for forest status assessment, wildlife damages, vegetation status assessments, etc., are performed supplementary.

2.2 Forest Mapping by Very High Resolution Systems

Traditionally, in Bavarian forest, aerial photographs are used in support of inventories, for management planning and monitoring. In most cases, aerial photographs are visually interpreted, in special cases by using 3D analyser for a map output (Rall and Martin 2002; Heurich 2006). In practice, orthophotos are mostly used for orientation and direct decision support in the field. Since a couple of years digital analytical work stations are used to extract forest relevant parameter for special cases like inventory and monitoring of Natura 2000 plots. As well as, for forest status assessment and mountain forest monitoring (Seitz et al. 2011; Waser et al. 2008). The LVG is covering the whole area of Bavaria with digital aerial photographs every three years.

Since about two decades, LIDAR systems are in the focus of forest research. LIDAR is the most accurate system in tree height and crown size determination. As full waveform system, a tomography like insight into forest canopies is possible, delivering information on the vertical structure of forests (Heurich 2006, Reitberger et al. 2008a, b). Recent research presented solutions for single tree identification even when crowns are interlaced (Reitberger et al., 2009). The 1 m, 2 m and 5 m grid digital terrain model (DTM) for Bavaria is based on LIDAR data. An update of that data base is not planned at present.

In the concept of the EUS-FH DSS, digital aerial photographs are used for base inventories of the Bavarian forests. Forest heights are derived by difference between the (VHR) LIDAR DTM and a digital surface model calculated from the digital aerial photographs of the LVG. VHR satellite data of the QuickBird type are not considered presently for forest parameter extraction by the Bavarian state forest administration.

2.3 Mapping by High Resolution Optical Systems

In general, high resolution optical systems means, the 5–30 m ground resolution category (e.g., Landsat type systems). The aims of forest related evaluations at this interim scale might be structured into: classification of forest cover (area), estimates of forest structure (tree species composition, age, height, etc.), forest change detection and forest growth simulations (management tool).

The trend in data analysis is toward parameters assessment. While typical classification results are strongly dependent on input data, classification method and operator experience, parameters may vary in accuracy of determination but the information is comparable. Further, a forest description on base of parameter is in line with forest management data and such facilitate modeling approaches like simulations of forest growth Pretzsch (2002) or calamity distribution dynamics (Kautz et al. 2011).

The pixel sizes of the high resolution category data type do not allow single tree detection and have always to be treated as mixed pixels. Fehlert (1984) by computer simulation and Kenneweg et al. (1991) by empirical experiments proved that in the range of the RapidEye ground resolution of 6,5 m a pixel wise classification must fail because of the mixed pixel problem. Object oriented analysis methods bypass this problem by using pixel aggregations as base objects for categorization (deKok et al. 1999; Schneider et al. 2000, Tiede et al. 2006, Eckert 2006). Already deKok et al. (1999) postulated, that for a monitoring system under Bavarian State Forest conditions it may be sufficient to rely on high resolution data to detect changes. Precondition is an established data and comparison base. Eckert (2006) demonstrated for a test site in Argentina with forests of similar complex structure like the ones we have to deal with in Mid-Europe, that high resolution data of different origin (Aster, Landsat) are appropriated to extract forest parameters with an acceptable accuracy for regional surveys. In Scandinavian countries, in Canada, etc. with extensive forest management systems the usage of high resolution data is standard.

In the present study, high resolution optical data are provided by Rapid Eye. The data are limited on the visible (VIS) and Near Infrared (NIR) spectral range, but firstly offer the option of multi-seasonal evaluations with a space operating system. The option of repeated observations under slightly changing appearances over the objects of interest is expected to bring advances in tree species identification and parameter determination.

2.4 Mapping by Microwave Systems

Synthetic Aperture Radar (SAR) remote sensing is an active imaging method based on microwave signals, which is—in contrast to optical remote sensing—independent of sun-illumination. Furthermore, the amplitude of the received signals is nearly free from atmospheric clutter (clouds, fog, etc.), so that SAR facilitates mapping tasks also under worse weather conditions. The high resolution of the new SAR satellite sensor generation (up to 1 m ground sampling distance) and the possibility of obtaining repeat and single-pass interferometric SAR (InSAR) data from multiple images make this data attractive for the extraction of both radiometric and geometric/structural parameters. Hence, SAR data are commonly used for purposes of classification, elevation extraction, and change detection.

Approaches of classifying forest areas using SAR data utilizing the possibilities of SAR polarimetry are given in Sato and Koike (2003) and Lee et al. (2005). The combination of SAR image data with optical or hyperspectral image data and Lidar data are investigated in Volden et al. (1998), Zhang et al. (2008), Hilbert et al. (2010), and Ackermann et al. (2010). Other evaluations detecting forest areas treat the analysis of SAR texture (Kourgli and Belhadj-Aissa 2009). In Kirscht and Rinke (1998), a method of reconstructing the 2.5 dimensional structure of elevated objects (e.g., buildings and vegetation like trees and forest) is described by utilizing their radar shadow length in airborne SAR image data.

Lemp and Koch (2009), analyzed forest areas by using TerraSAR-X image data. They focused on the problem of separating forest from grassland, which show similar backscatter intensity and statistics dependent on surface roughness, incidence angle and look direction. Furthermore, they state that an interferometric evaluation is impossible since the TerraSAR-X data show high decorrelation in forest areas. Therefore, a combined analysis of multi-frequency data (e.g., L-band and X-band images) is recommended. This problem of InSAR and PolInSAR phase decorrelation in repeat-pass datasets was also stated by Koch (2010), whereby for example, single-pass interferometry, facilitated by the TanDEM-X mission, could solve this problem.

In De Zan et al. (2009) multi-baseline InSAR data of this new TanDEM-X mission were simulated to show the high potential for height extraction. Already with few interferograms promising results of extracting height profiles in vegetated areas were achieved. One further method extracting tree and forest heights is provided by SAR tomography, for example by using airborne data (Reigber and Moreira 2000) or an upcoming satellite mission (Cloude and Papathanassiou 2008).

In this study, we use first high resolution repeat-pass TerraSAR-X data alone.

3 Parameter Extraction from RE and TS-X Data

To consider various growth conditions the study covers different growth regions of Bavaria (Fig. 1).

Fig. 1 Test site locations across the growth zones of Bavaria

The focus of the paper is on image analysis. The aim is to show which kind of forest parameters are extractable from the electro-optical RE data and the microwave TS-X data respectively and which accuracies are retrievable with each of the systems (complementarities). Due to the fact that data take opportunities for the first observation period 2009 fit neither the time frames nor the areas, the present paper highlights solely examples demonstrating the approach. Accordingly, the image analysis starts by independently processing the multi-spectral and radar data.

Due to the high geometric and orbital accuracy and resolution of the data, the prospect in our case is an improvement in forest structure parameter determination like heights, canopy roughness, border and gaps or, in special cases, even single tree detection. Improvements in tree species identification are expected by the multi-seasonal imaging option of RE. The key in this case are the changes due to phenology. The expectations are toward fingerprint like profiles of tree species types.

The presented results have to be seen as the entrance step for tree species differentiation. Solely the assessment of the first set of the above listed parameters is addressed. Examples are shown for the assessment of the parameter forest area, border length, gaps and forest tree groups ‘coniferous’, ‘broadleaved’ and ‘mixed’ as well as for forest height estimations and change detection options. These parameters are controlled by the pixel size and may be considered as ‘stable’ or ‘static’, at least over the period of one season.

Table 1 Geodata provided by Bavarian State authorities used for verification

Geodata	Date	Producer
ATKIS-Basis-DLM (Amtlich-Topographisch Kartographisches Informations System, official topographic-cartographic information system)	2009	LVG
TN (Tatsächliche Nutzung, land use data)	2010	LVG
FÜK (Forstliche Übersichtskarte, forest overview map)	2009	LWF

3.1 Hypotheses

Hypothesis 1: Forest management relevant parameters are derivable from RapidEye and TeraSAR-X data. The hypothesis is tested on base of multi-seasonal RapidEye and TerraSAR-X data from up to five test sites in different growth regions of Bavaria.

Hypothesis 2: The combination of both data sets improves the forest determination. Each of the sensors has specific advantages in parameter extraction. The hypothesis is tested by combining parameter derivable exclusively from each of the sensors in a synergistic manner.

Hypothesis 3: The complementarities of the two sensor concepts facilitate fast reactions in the disaster case. The hypothesis is tested in the frame of change detection studies by comparing the potential of detecting structural changes with both systems.

3.2 Data

3.2.1 Geodata

Geodata are provided by the Bavarian State Institute of Forestry (LWF), the Bavarian Surveying and Geoinformation Administration (LVG), and the Traunsteiner Stadtwald community forest administration. The data layers used for first verification purposes are listed in Table 1.

The ATKIS-Basis-DLM is a digitized land cover model based on the Bavarian topographic map 1:25.000 with an accuracy of $\pm$ 3 m (Katzur and Franke 2007). It has the same information about land cover use as the map TN, which is based on cadastral data and digital orthophotos. FÜK is a product of the LWF and shows the property pattern of state, private and municipal forests of Bavaria.

3.2.2 RapidEye Data

The RapidEye satellite constellation consists of five satellites carrying on-board the push broom sensor Jena Spaceborne Scanner JSS 56. Each sensor is capable of collecting image data in five distinct bands of the electromagnetic spectrum: Blue

Table 2 RE images of the five test sites for five different phenological stages

Test site\phenology	2nd	3rd	4th	5th	1st
Traunstein er Stadtwald	17.05.2009	29.07.2009 01.08.2009	07.09.2009	23.09.2009[a]	11.05.2010
Bayerischer Wald	23.05.2009	01.08.2009 15.08.2009	01.09.2009	27.09.2009	
Freisinger Forst	20.05.2009	27.07.2009		22.09.2009[a]	22.04.2010
Oberammergau	20.05.2009	27.07.2009		20.10.2009[a]	29.04.2010
Iphofen/Steigerwald	17.06.2009		24.08.2009	23.09.2009[a]	19.04.2010

[a] images with large cloud coverage

(440–-510 nm), Green (520–590 nm), Red 630–680 nm), Red-Edge (690–730 nm) and Near-Infrared (760–880 nm). The dynamic range is covering 12 Bit, the ground sampling distance 6,5 m, resampled to 5 m pixels. At 75 km swath width, this constellation offers large area coverage and a frequent revisit interval of 2–5 days.

Radiometric and geometric corrected level 3A data were ordered to cover each test site at least five times across the vegetation period from spring to autumn. The delivered data sets for the 2009 vegetation period are listed in Table 2. The second vegetation period to be analysed was planned for 2011.

3.2.3 TerraSAR-X Data

SAR data were provided by the German TerraSAR-X satellite system. Due to the daylight independence and the nearly all-weather capability of radar systems the acquisition chance depends more on system workload than on weather conditions. The test site specific image parameters are summarized in Table 3.

Hence, we focused first on the recording of repeat-pass images to allow InSAR analysis and second on a temporal overlap with the RapidEye acquisitions to support the fusion purpose. The SAR images are recorded in Spotlight Mode, in HH polarization, with a wavelength of 31 mm (X-Band). The incidence angle θ varies between 27 and 49 degree and the geometric slant range resolution is about 1.2 m. In addition to the 15 images of 2010, for change detection purpose, new acquisitions in 2011 and 2012 are planned.

3.3 Methods and Results

3.3.1 Pre-processing of RapidEye Data

The multi-seasonal image analysis to be performed with the RE datasets requires a precise georectification as well as an atmospheric correction at the highest possible level. The accuracy of the geometric correction of the images was checked, and most of the images were spatially matched together in each test site. However,

Table 3 Summary of test site specific TerraSAR-X image parameters

	First acquisition	Repeat-pass interval	θ	Orbit
Traunstein Stadtwald	20.05.2010	11 days (2 img.)	30°	Ascending
Bayerischer Wald	23.05.2010	11/22 days (4 img.)	42°/48°	De-/ascending
Freisinger Forst	30.05.2010	11 days (2 img.)	49°	Ascending
Oberammergau	02.06.2010	11 days (3 img.)	27°/33°	De-/ascending
Iphofen/Steigerwald	16.06.2010	11 days (4 img.)	33°	Ascending

some of the images that did not match were corrected by applying specific amount of shift in both direction (easting and northing). The final achieved RMSE is below 0.8 pixel. The atmospheric correction was applied for all images in each test site, by using ATCOR 3, implemented in PCI Geomatica 10.3.

3.3.2 Processing of RapidEye Data

To extract forest parameters from RE data an object-oriented analysis technique was employed using eCognition Developer 8 program of the Trimble Company (Baatz and Schäpe 2000, Schneider et al. 2000). Two levels of segmentation were created, the upper level to delineate the forest areas and the lower level to extract the tree species groups. For the upper level of segmentation, scale parameter of 60 was chosen, while for the shape and compactness parameters 0.3 and 0.2 respectively. For the lower level, the parameters were set to 15 for scale, 0.2 for shape and 0.6 for compactness. In addition, layer weights were set to 5 for the NIR, 3 for the red edge, green and blue bands, and 1 for the red band.

The second step is the classification of the created objects. The set of features for classification was selected by the help of the feature space optimization tool implemented in eCognition. The first step of the hierarchical classification rule set was to separate the urban areas and the water bodies, by analyzing the NDVI and NIR layers in the upper level. Then the forest areas were classified as described in the following subsection. Afterwards, the lower level was segmented and classified into deciduous, coniferous and mixed forest stands.

3.3.3 Parameter Extraction from RapidEye Data

Forest Boundaries (border length and area): Due to the different land use and ownership of Bavarian landscape, the task to delineate the forest boundaries is of great importance. Within the study we tried thatfore to figure out which phenological stage is best suited for a forest boundary determination and, second, which is the improvement by a multi-seasonal analysis. Forest masks were created for each study area from each mono-temporal dataset, as well as from the combination of all the images multi-seasonal analysis. For the extraction of the forest areas in the mono-temporal analysis the layer of brightness, NDVI and the ratios Blue/Green were selected. While in the multi-seasonal analysis the brightness and the ratios Green/Blue were used.

Table 4 Error matrix of the RE multi-seasonal forest mask calculated with different GIS-layers of different administrations in Bavaria

Error matrix	Overall accuracy (%)	KHAT
ATKIS-Basis-DLM	94.69	0.89
TN	94.38	0.88
FÜK	91.35	0.82

Table 5 Overall accuracy of mono and multi-seasonal RE data takes evaluations for each parameter, subset Freising test site

Parameters	Overall accuracy			
	Mono-temporal seasons			Multi-temporal (%)
	22.04.2010 (%)	20.05.2009 (%)	27.07.2009 (%)	
Forest area	95.15	90.86	94.56	94.69
Gaps	98.82	97.92	98.48	99.11
Group of tree species	67.87	66.11	69.71	67.13

The first attempt to verify the evaluation success on base of the forest management maps was not successful. Forest management maps are produced to support production, are restricted on enterprise areas and differ in content, accuracy and actuality. Nevertheless, with regard to a future operational phase the result assessment should be performed on basis of official map sources. Maps with forest area layers are produced by different authorities. The maps finally used for these comparisons are listed in Table 4.

The result of the error matrix between ATKIS-Basis-DLM, TN and FÜK illustrate that the overall accuracy of ATKIS-Basis-DLM is the best, quite close followed by TN. Fig. 2 shows the comparison of RE forest masks [a, b, c] of different vegetation stages. The combined or multi-seasonal evaluation [d] delivered the most accurate forest mask [f]. A visual example of the fitting of the produced RE masks with the ATKIS-layer is shown in examples [e, f].

Extraction of Gaps: There are two forest gap types to be considered. Permanent unstocked areas e.g., wood storage and short term gaps due to clearance but calamities (storm throw, bark beetle attack, etc.). Especially the detection of the last category of gaps is of great importance for the DSS. The rule-sets developed for forest area determination have been expanded for a gap assignment rule (…surrounded by…). The evaluation of gap mapping success proved to be difficult. In general, there are no records on temporary gaps after clearings or disasters. Identification and delineation of gaps is such producing a new information layer. The results of the comparison against the ATKIS-Basis-DLM are displayed in Table 5.

Classification of Forest Types: The mono-temporal and multi-seasonal classification of the lower level of segmentation used the layers of Near-Infrared (NIR) and NDVI for the separation between the coniferous and deciduous tree stands. After first iteration, many objects were still unclassified due to the existence of the mixed stands in the area. Visually, most of these objects were identified as mixed

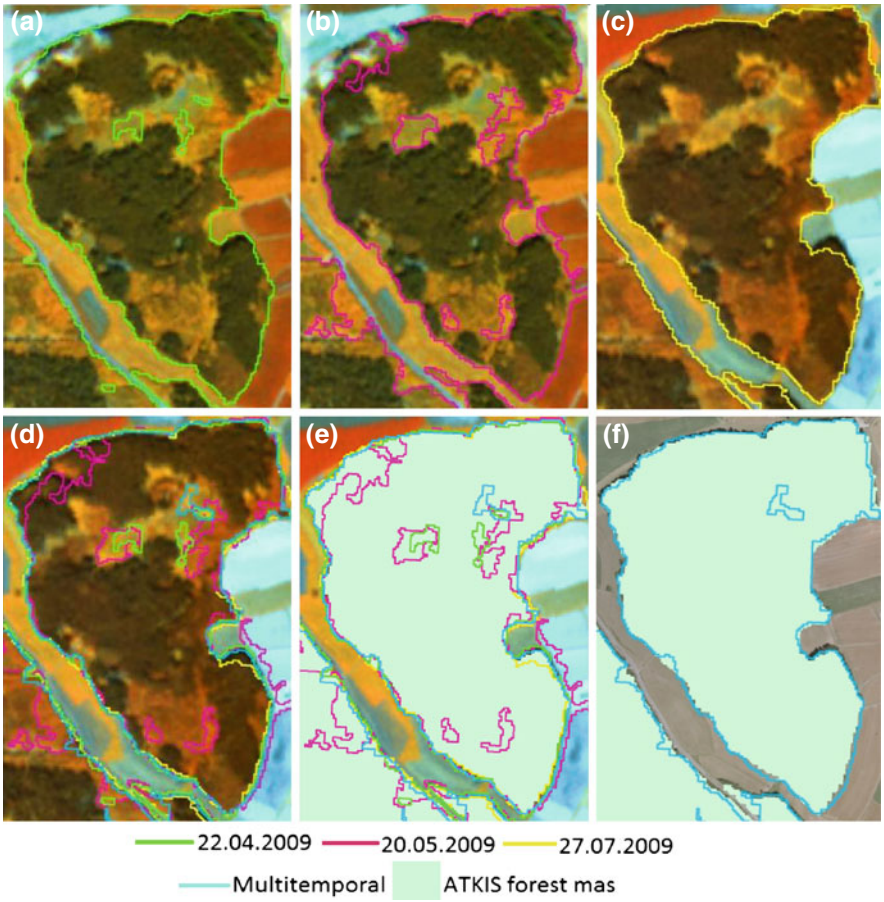

Fig. 2 Result of forest boundary extraction using RE image overlaid with mono and multi temporal extracted boundaries: forest boundaries from the images with date 22.04.2010 (**a**), 20.05.2009 (**b**), 27.07.2009 (**c**), RE image form 27.07.2009 overlaid with mono and multi temporal (**d**), RE image form 27.07.2009 overlaid with mono and multi temporal forest mask and ATKIS-Layer (**e**), orthophoto overlaid with multi temporal boundaries and ATKIS-Layer (**f**)

forest or shaded areas. Eventually the shaded areas in the forest were classified by using the NDVI layer value into mixed forest and streets in the forests that was later on excluded from the forest area Fig. 3a.

As post classification step, the forest type classifications were grouped within the state forest stands borders in GIS. Whereas, the classification result was tabulated within the state forest stands borders using 'tabulate area' function in zonal tool in Spatial Analyst Tools of ArcMap environment. The result was a detailed description for each stand. Figure 3b shows the percentage of the deciduous and coniferous trees within each stand.

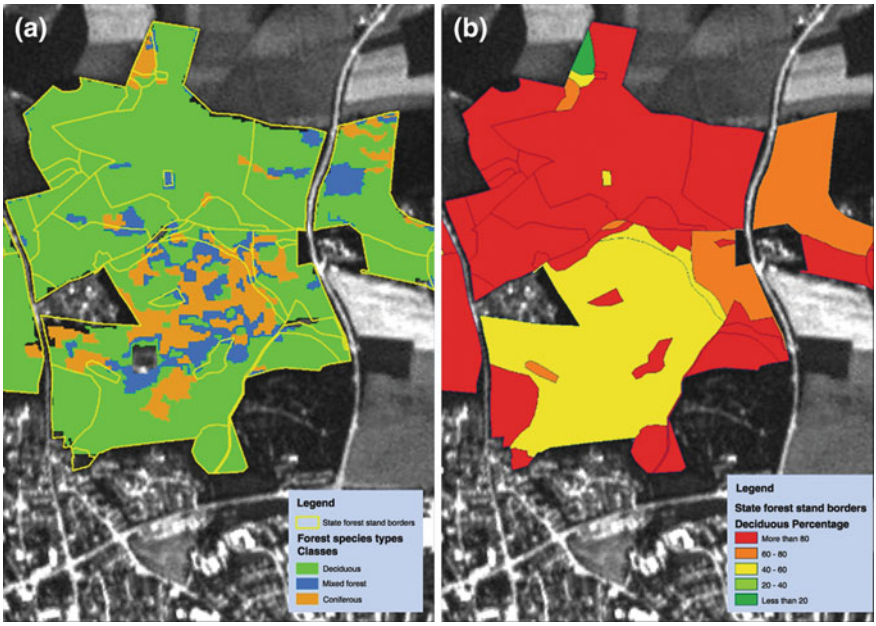

Fig. 3 Multi-temporal classification for the main tree species groups (**a**), and Forest stands with the percentage of deciduous trees in each stand according to the forest management records (**b**). Freising test site

The different group of tree species; coniferous, deciduous and mixed forest tree groups were classified and compared with the ATKIS-Basis-DLM in an error matrix.

3.3.4 Evaluation of Parameter Extraction Success

According to the results of the official GIS-layer assessment, the ATKIS-Basis-DLM forest layer was chosen for verifying the performance of the mono- to multi-seasonal forest mask and the accuracy of the parameter extraction (Table 4). For this task an error matrix (Lillesand et al. 2004) was generated with a point raster for the entire study area in Freising, with a point spacing of 50 m (total points 15928) (Straub et al. 2008). Table 5 gives an overview about the accuracy of the parameter determination for each mono and the multi temporal dataset.

The overall accuracy for the parameter forest area shows the highest agreement with the ATKIS-Basis-DLM forest layer for the image from the 22.04.2010 (Table 5). The generated multi-seasonal mask and the mask from the 27.07.2009 data show quite similar agreements. Only the mask from the 20.05.2009 data set shows a 4 % lower agreement. These results demonstrate that even a mono-temporal forest mask may be sufficient for forest non-forest delineation.

The overall accuracy in Table 5 for all images shows a good result of gap detection, especially the multi temporal dataset has an accuracy of 99.11 % with the gaps of the ATKIS-Basis-DLM. Again, the multi temporal layer includes all different vegetation spectral patterns, hence a more precise detection of the gaps is possible.

First results of group of tree species classification have an overall accuracy between 66.11 % and 69.71 %. The KHAT index (Congalton 1991) of the error matrix has a value between 0.44 and 0.50. Several factors have an influence on the classification for example different vegetation stages of the trees, training areas, quality of the images and especially the verification data. Therefore, a better result will be expected, if the comparison is done by inventory data.

3.3.5 TerraSAR-X Data Evaluation

In comparison to optical data analysis, our SAR image analysis takes advantage of the higher geometric resolution of the imagery and focuses in particular on structural parameters. In the following subsection, the geocoding procedure is described—the most important step for fusion and assessment. Subsequently, several approaches of automatic extraction of forest parameters are described and first results are shown.

3.3.6 Preprocessing of TerraSAR-X Data

The side looking SAR imaging principle leads to a projection of the recorded intensity values in slant range geometry. For this reason, the image position of an object is characterized, on one hand, by the azimuth position parallel to the flight track and, on the other hand, by the range position representing the distance between SAR sensor and object on ground. Due to this cylindrical geometry, the SAR signature of objects is different to optical images, which are generally taken in central perspective and/or parallel projection. Consequently, the appearance of elevated objects is very different; a displacement towards the sensor's nadir axis in SAR images and reversed in optical data (Thiele et al. 2006). Therefore, the requested fusion of the multi-sensor data, the assessment with GIS data, and the fusion of satellite images taken from ascending and descending orbits require a step of geocoding to achieve SAR information in world coordinate system. The correct geocoding, also called orthorectification, of a pixel in a SAR image can be determined based on the sensor carrier navigation data and the known distance between sensor and corresponding ground points. And hence, a good Digital Surface Model (DSM) including all elevated objects is required. Effects due to even small deviations of the navigation data from the true sensor position and missing height information in the elevation data are discussed in Thiele et al. (2006).

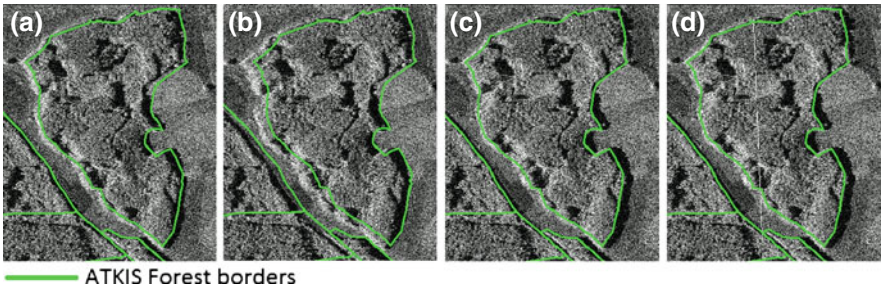

Fig. 4 Result of geocoding using mean terrain height from SAR header (**a**), SRTM heights (**b**), DGM5 (**c**), and DGM2 (**d**). Freising test area, subset

For this study, height models of different quality level are available, the "scene average height" extracted from the TSX metadata, SRTM data, a DGM5 and a DGM2 of the LVG. Additionally, high quality navigation data are delivered by DLR. The different results of geocoding overlaid with GIS information are shown in Fig. 4. As can be seen, the orthorectification results are reasonably good. For our purpose a high level of precision is requested, which can be better achieved by the use of the DGM5 and DGM2.

3.3.7 Processing of TerraSAR-X Data

For the subsequent parameter extraction depending on the workflow, slant range as well as ground range images are used. Radiometry based steps are done in slant range geometry to avoid interpolation effects, high level steps and assessment steps are accomplished in ground range geometry.

3.3.8 Parameter Extraction from TerraSAR-X Data

Extraction of Forest Boundaries: The signature of forest in the SAR images is characterized by rather high average magnitude values, which is mainly caused by volume scattering. Furthermore, side-looking geometry of the SAR system and the height of the trees lead to the layover (l) phenomenon appearing at objects facing towards the sensor and the shadow (s) phenomenon on object parts hidden for the sensor.

For automatic segmentation and classification of forest areas, we select two information layers, the magnitude and the local coefficient of variation (CoV). The CoV layer exploits SAR image statistics, which is dominated by the speckle effect—a multiplicative noise well known for all coherent imaging systems. In detail, the CoV is the ratio of standard deviation and mean intensity in a local neighbourhood $<I>$(Eq. 1).

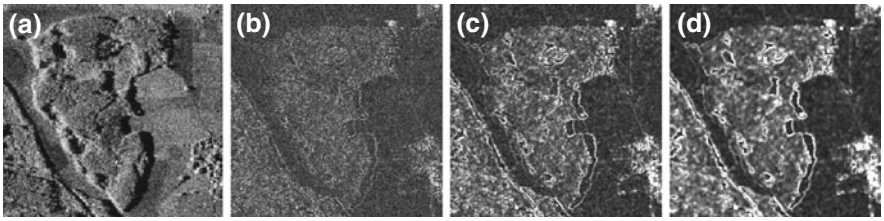

Fig. 5 Input layers of forest boundary extraction in a subset of the Freising test area: magnitude layer (**a**), CoV layer with window size 5 × 5 pixel (**b**), 9 × 9 pixel (**c**), and 13 × 13 pixel (**d**)

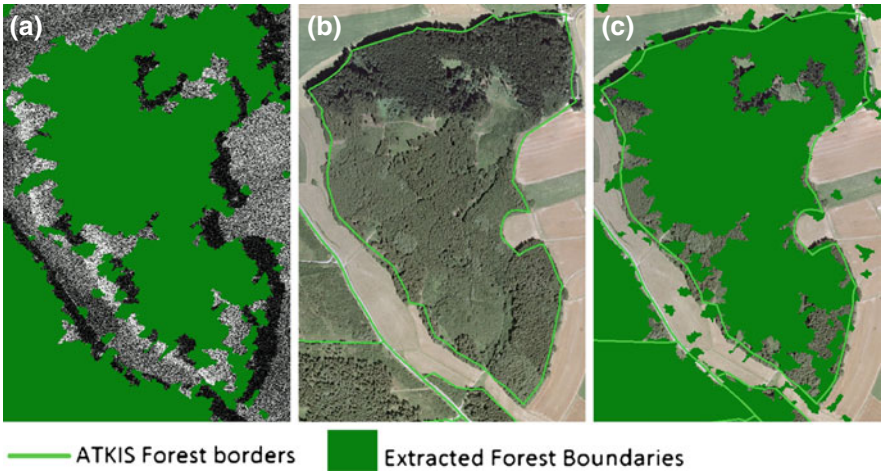

Fig. 6 Result of forest boundary extraction of a subset of the Freising test area: SAR magnitude image overlaid with extracted boundaries (**a**), orthophoto overlaid with ATKIS layer (**b**), and orthophoto overlaid with extracted boundaries and ATKIS layer (**c**)

$$CoV = \frac{\sigma}{\langle I \rangle} \tag{1}$$

The local CoV is a good feature to distinguish between homogeneous and heterogeneous areas in SAR images with respect to the chosen window size (local neighbourhood). Different window sizes (see Fig. 5) are tested to differentiate between homogeneous vegetation (e.g., fields and grassland) and heterogeneous forest areas.

The results are given in Fig. 6 showing an overlay of orthophoto and GIS layer. The visual assessment shows a good overlap between SAR boundaries and ATKIS layer. Differences are visible in the level of detail, in the classification of enclosed grassland, and the misclassification of some Agricultural land. An improvement is expected by decreasing segmentation level, which is currently limited by image size.

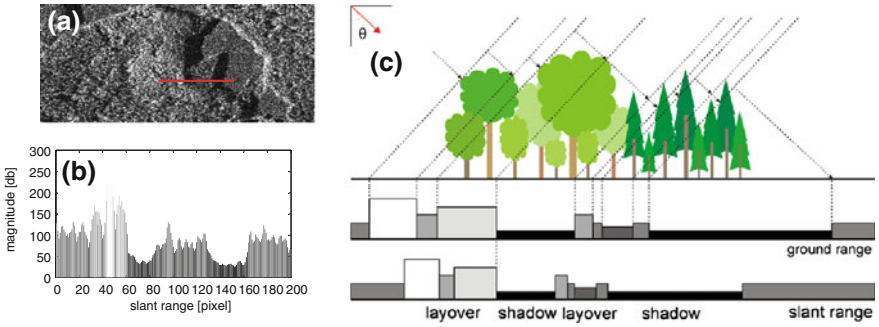

Fig. 7 Magnitude signature of deciduous trees and conifers and red marked slant range profile (**a**), slant range magnitude profile crossing deciduous trees and conifers (**b**), and scheme of backscattering situation for given profile (**c**). Bavarian Forest test area

Extraction of Forest Heights: The extraction of forest heights focused on the analysis of the already mentioned layover and shadow areas at forest borders. Similar to optical data, where the illumination by sun leads to the shadow, also the length of radar shadow s_{slant} contains information of object height. Furthermore, the length of the layover phenomenon (Bamler 2000) l_{slant} leads to a nearly similar relation between incidence angle θ and object height h (see Eq. 2), which allows in some cases a redundant estimation of the object height.

$$h = s_{\text{slant}} \cdot \cos\theta \qquad \text{and} \qquad h = \frac{l_{\text{slant}}}{\cos\theta} \tag{2}$$

Next to the "simple" height estimation, more complex height relations can be analyzed due to growing situations visualized in Fig. 7. Deciduous trees in near range appear bright in the magnitude profile due to the high volume scattering. Behind them, a short shadow part can be observed caused by the height difference between deciduous trees and following conifers. Subsequently, the lower volume scattering of conifers leads to lower magnitude values in the slant range profile. The shadow area afterwards corresponds to the conifer height. With the assumption of nearly homogenous height distribution in small areas of same tree species, for this example the extraction of conifer and deciduous tree height is possible. Of course, competitive effects such as gaps, stands, clear-cut rests, or spurious shadow areas hamper height extraction by this method.

Besides this theoretical description of height extraction, our initial work focused on the comparison of layover and shadow measurements. Therefore, manual slant range measurements are accomplished in a forest area covered from ascending and descending orbit to achieve the mentioned redundant estimations. Furthermore, temporally correlated field measurements were realized. A magnitude image marked with the calculated tree heights is shown in Fig. 8. In Table 6, the estimated and the measured heights are listed.

The measurements based on the layover areas (l) show higher differences to the ground truth measurements than the ones based on shadow areas (s). In most

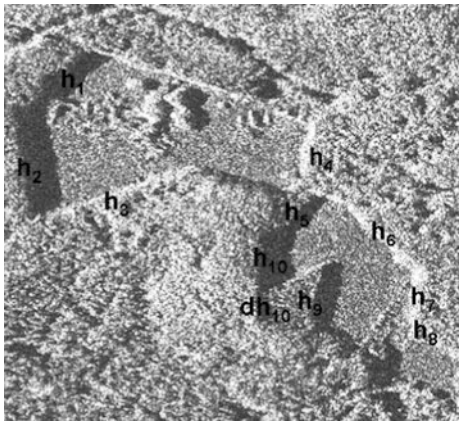

Fig. 8 SAR magnitude image with marked locations of height estimation, Bavarian Forest

Table 6 Summery of height estimation by manual image based and field measurements

Height	Descending orbit	Ascending orbit	Ground reference
h_1	25 m (*l*)	26 m (*s*)	appr. 30 m
h_2	27 m (*l*)	29 m (*s*)	aprx. 30 m
h_3	18 m (*s*)	–	aprx. 30 m
h_4	29 m (*s*)	27 m (*l*)	32.5 m
h_5	–	15 m (*s*)	20.5 m
h_6	13 m (*s*)	26 m (*l*)	21–32 m
h_7	29 m (*s*)	32 m (*l*)	30.5–32.5 m
h_8	13 m (*s*)	14 m (*l*)	15.5 m
h_9	15 m (*s*)	18 m (*s*)	20.4–24.6 m
h_{10}	25 m (*l*)	28 m (*s*)	30.5 m
dh_{10}	–	10 m (*s*)	–

cases, heights extracted from SAR images are underestimated, which can be contributed to the partial penetration of the tree crowns at the very top. A rigorous assessment between extracted and real measured height values is difficult. This is due to spurious shadow areas in the SAR images and large height variations at the real forest boundary. Nonetheless, the values of h_9, h_{10}, and dh_{10}, show that the concept of combining relative heights (Fig. 7) fits quite well for this example. The implementation of a semi-automated and fully automated approach for forest height extraction is in process.

Estimation of Forest Density: In addition to the boundaries and the heights, the forest density is also an important parameter to describe forest characteristics. Forest density is related to stand **age** and **gap** occurrence. Next to the *CoV* layer, also a shadow layer, an intermediate result of the forest boundary extraction, is useful for this estimation. Especially, shadow areas enclosed from forest regions are a measure of gappy forest areas. As older the forest as more gaps occur and as rougher the surface appearance. Based on pyramid like changing of the segmentation level, the discrimination between open space, glades, gaps and gappy

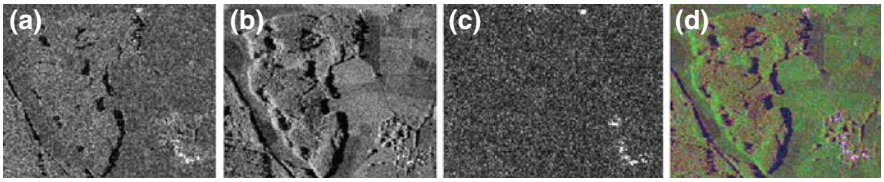

Fig. 9 Input layers of classification; coefficient of variation (**a**), SAR magnitude (**b**), interferometric coherence (**c**), result of CoVAmCoh layer stacking (**d**). Freising test area, subset

growth could be possible. Implementations toward density determinations for gap detection and age estimates are still in process.

Classification of Forest Types: The classification of different forest types is an additional task of this project. As first goal, discrimination into three classes—deciduous, conifer and mixed forest is envisioned. Therefore, three information layers are investigated, the *CoV*, the amplitude and the coherence. The local coherence *Coh* describes the correlation between two repeat-pass SAR images (S_1 and S_2), whereby high *Coh* values (~ 1) indicate coherent areas (e.g., urban area) and low Coh values (~ 0) independent signals due to high variation (e.g., vegetation).

$$Coh = \left| \frac{\langle S_1 \cdot S_2^* \rangle}{\sqrt{\langle S_1^2 \rangle \cdot \langle S_2^2 \rangle}} \right| \tag{3}$$

A reasonable way to visualize the contained information is the CoVAmCoh-Analysis presented in Schulz et al. (2009). The three input layers shown in Fig. 9 are arranged like RGB layers, with *CoV* as red, amplitude as green and *Coh* as blue layer.

The additive colour mixing emphasizes local features, for example, changes appear yellow, deciduous trees bright green, and fallow land blue. The eCognition software is a useful tool for multi-resolution segmentation. It is also useful for the fuzzy classification of the data based on suitable membership functions adapted to the three classes (deciduous, conifer and mixed forest).

4 Integration of RE and TS-X Evaluations

The integration of synergistic and complementarities options from both data types are considered of major importance for the DSS. Forest characterisation and change detection are presented as examples.

In Table 7 the ability of forest parameter determination of the two systems are weighted against the success of the most precise remote sensing method for this parameter. Solely, for the diameter at breast height (dbh), one if not the most important parameter in practice, no reference RS system is available, and a RS data based evaluation is not possible.

Table 7 Forest parameter determination accuracy at the local to regional scale from the RE and TS-X in comparison to competing Earth Observation systems. As reference the system with the best performance is given (+++)

RS system type/ parameter	RapidEye	TS-X	World View-2	Hyperspec. Scanner	Aerial photogr. (LVG)	LIDAR
Forest area	++	++	+++	++	+++	+++
Border length	++	++	+++	++	+++	+++
Stand height	–	+	+	±	++ (st)	+++
Gap	+	++	+++	++	+++	+++
Single tree	±	+	+	±	++	+++
Crown diameter	–	±	+	±	++	++
Dbh	–	–	–	–	–	±
Stand structure	+++	±	+++	+++	+++	+++
Conif./broadl.	+++	±	+++	+++	+++	+++
Broadl. species	++	–	++	+++	++	+
Conif. species	+	–	+	+++	++	++
Timber volume	±	±	+	+	++	+++
Age	±	±	+	+	++	+++
Repetition frequency	+++	+++	±	–	±	–
Data take restrictions	+	+++	+	+	+	+++
Area coverage	+++	++	±	–	+	–
Data evaluation costs	+++	+	±	+	++	+
Information costs	+++	+	±	++	++	+

+++—reference, ++—good, +—fairly good, ±—estimate, – not possible; dbh = diameter at breast height; data evaluation costs = work load for data analysis per unit area; Information costs = quality of information weighted against are coverage; st = stereoscopic analysis required; LVG = data of the regular Bavarian State survey; area coverage = annual is set as reference

The analysis of Table 7 lets us easily identify the synergy potential between TS-X and RE. While the advantages of RE are in species differentiation, area coverage and costs, TS-X is adding information on stand height, gap detection, single tree detection (in some cases) and has no data take restrictions in the emergency case.

The complementarities are given for the parameters area, border length and gap detection, all of them parameters describing static structure elements. The simultaneous data take and evaluation of that data during the development phase allow to determine the assessment accuracy and to use that information in case only one data set is available (disaster scenario).

With regard to change detection, the high repetition frequencies of the two systems are the key properties, allowing the immediate detection after occurrence. In case of TS-X repeat-pass data allows the detection of changes, e.g., by evaluating the already mentioned coherence, which is a measure initially introduced to assess the quality of the phase stability of an interferogram. Since coherence is a

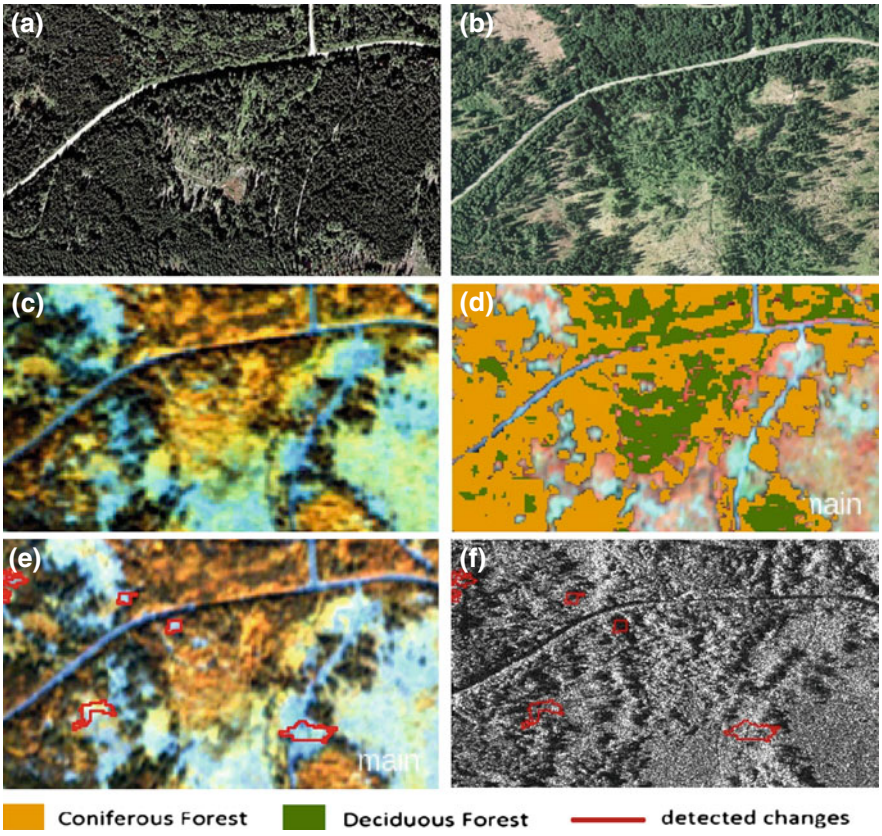

Fig. 10 Example of an information flow in the sense of the DSS for the forest–wood chain under development demonstrated for a subset of the Bavarian Forest test area. Aerial image from 2000 documenting the initial stage (**a**), aerial documenting damages after a storm event (**b**), RapidEye image May 2009 still reproducing the situation from 2001 (**c**), RapidEye image classification August 2009 (**d**), RapidEye image August 2009 with border line of changes compared to the situation in May (**e**), and TerraSAR-X proving no changes since August 2009 (**f**)

very sensitive measure (see Fig. 9c), considerable noise is expected making it necessary to rely on segment-based approaches for classification. A priori information seems essential.

For RE changes related to shifts in phenologic development are investigated with the aim of tree species differentiation (instable parameter behaviour). The static parameters area, gaps, border length, tree species group distribution, etc. are accessible from each data take.

Within the DSS for the forest wood chain, the advantages of both system types are combined. For establishing the data base, the information is extracted from both systems (synergy). In the fast response case, the complementarities of

information provision are used to get information about the event. The extracted information is cross checked with the established data base.

Figure 10 demonstrates the information flow within the DSS. Aerial photographs of the regular three year cycle of the Bavarian State survey are used to cross check and update existing forest data bases (10a). In the following winter season 2000/01 a storm event damaged large areas. According to the concepts of the DSS, satellite data should be analysed to decide whether a supplementary very high resolution data take is necessary for steering clearing measures. In our example from the Bavarian Forest test site, aerial photographs were taken in 2001 (10b) for bark beetle monitoring reasons. The damages of the storm throw from winter 2000/01 are still well displayed by the RE image from May 2009. The multi-seasonal classification is used to crosscheck and update the forest management records (c, d). Changes occurring between May and August 2009 are easily to be identified by an automatic change detection proceeding (e). Once the data base is regularly updated even in a fast response case under cloudy sky conditions the affected areas are detectable by SAR systems, in our example by TS-X (f).

5 Discussion

Despite that the presented results are stated as preliminary, it is possible to give some statements and to give an estimate of the success.

Hypothesis 1: *Forest management relevant parameters are derivable from Rapid Eye and TeraSAR-X data*. Hypothesis was tested on base of multi-seasonal RapidEye and TerraSAR-X data. It was examined in up to five test sites of different growth regions characteristics in Bavaria, and it is likely to be stated as confirmed. The parameter derivation success is not as high as in case of the reference systems for that parameter (Table 7). However, results are sufficient to support the aims of the envisaged DSS for the forest-wood chain. These findings are in line with the findings of deKok et al. (1999).

Hypothesis 2: *The combination of both data sets improves the forest determination*. The investigations confirmed the hypothesis validity. Specific advantages in parameter extraction using data from both sensors are contributing to a more precise determination of the forest characterisation. As shown in Table 7, especially in case of gap detection and height estimates, TS-X is delivering more accurate results than RE. While RE is contributing with a better stand structure description, at present confirmed solely at the tree species group level, but with a prospect of tree species differentiation. Nevertheless, because it was not possible to evaluate the data sets taken at the same period of time, this hypothesis needs to be further investigated before it is categorized as ‘proved’.

Hypothesis 3: *The complementarities of the two sensor concepts facilitate fast reactions in the disaster case*. The concepts leading to hypothesis 3 assume that even small changes are detectable, once the data base is established and regularly updated by evaluating the same RS data type sets. Change detection is required,

either to compare the changes over years or in case of a clearly defined situation of a sudden event like a storm throw or a biotic calamity. In the concept of the DSS for the forest wood chain, such a calamity should be detectable by both sensor types. The microwave sensor can detect at any daytime or under any cloud coverage condition, while the optical sensor, which definitely requires clear sky conditions, is therefore not as flexible. On the other hand, systems like RE or later, ESA's Sentinel, are promising a high temporal repetition frequency and will be used to analyse the event further.

Whether the event was of a category that made it necessary to have a very high resolution imaging campaign is decided after crosschecking the classification results with the data base records. Once such an event is categorized as disastrous and the clearing urgency is high to very high, an additional data take with very high resolution systems like aerial photographs or LIDAR may be a cost efficient logistic option for steering the operations.

A data flow test confirming the hypothesis was performed with the presented change detection study at a test site in the Bavarian Forest (Fig. 10). A test case did not occurred during the reported period such the hypothesis cannot be finally confirmed.

Worth to be discussed are other findings of the study highlighting integration needs and bottlenecks of different nature affecting the success of the integration in the frame of the envisaged DSS. We will restrict the discussion on differences in recording the retrieved parameter and on pointing on the need of harmonisation of definitions.

In case of the tree species group differentiation task, forest management data bases are the only ones offering the required level of detail. Such data bases exist solely for forest areas with an administration, what applies on state forests, community forests and big private forest areas. One third of the Bavarian forests, about 800.000 ha belong to the 'small private forest' category and are covering areas not larger than 30 ha each. For such type of forests, the proposed system will be able to offer a consistent data base, of course not with that level of detail as for then the state forests with regular ground based inventories. However, even in case of the state forests and community forests with state of the art data bases the system under development will be of advantage. Such the records of the Bavarian State forest management data base are giving solely the percentage of forest tree species per stand, but not the position. The trend in forest planning is to larger and even larger stands and longer inventory cycles. The object based classification applied for this study is deciding per object. One object is defined by homogeneity criteria and is in general associated to a tree species type of comparable age. The percentage per stand is calculated by summing up the objects belonging to the respective stand. The position of each object is exactly known. This is a big advantage compared to the forest management records. Growth simulators are more and more used as planning instruments in forest management, allowing assessing different alternatives and their consequences. Especially growth simulators acting on base of competition models like SILVA (Pretzsch et al. 2002) will take advantage from this additional information in the future.

The need of harmonisation became already obvious at a very basic stage of the discussion: Which is the appropriated and generally accepted definition of 'forest', or, on the practical side, which 'official' forest layer should be used to compare the results? Even in the same county, in our case Bavaria, different authorities and administrations e.g., for forestry, nature conservation, the Bavarian State survey, etc., established their own data bases using different definitions for 'forest'. Following the most intuitive idea to use the forest management maps, the sources on which the decisions in forestry are based on, one must fail because the forest border is defined by the stem position. Remote sensing data derived results are crown projection controlled. For old growth broadleaved forest, this simple difference may introduce a positioning error for forest borderline determination of 10 m and more once that map is used as reference for validating RS derived results. Of course, this has consequences for forest area determination as well. Some other official sources like ATKIS do not consider the forest management road network. The dense Bavarian State forests road network must be subtracted before this data set is used as reference.

The discussion may be continued on different other topics. The study clearly reveals that there are many 'interface' problems to be solved until an operational solution may become possible. These problems do not directly touch the remote sensing and data evaluation context.

6 Conclusion and Outlook

The results presented above show the current state of implementation and are thus preliminary in some sense. The extracted parameters indicate the potential of Remote Sensing to support the forest-wood chain but their values should be considered as an initial feasibility test after putting together all the relevant imagery and geodata needed for the analysis. Nevertheless, it is possible to derive some conclusions about the concept itself and about the remote sensing data investigated as well.

The optical RapidEye data belong to the high (5–30 m), the SAR TerraSAR-X data are on the transition to the very high (0.5–5 m) spatial resolution class. Different to LIDAR or digital aerial photography techniques single tree observations are not possible. Exceptions are solitary trees or standards left for seed production or shading. After the presented first results we are far away from claiming a ready to use solution for practice, However, the results deliver a couple of arguments for the combined use of multispectral and SAR data for monitoring and fast response situations like sudden calamities.

The concept seems appropriate to deliver management relevant information useful for interim inventories. Such interim inventories are not intended to deliver all detailed information of a regular inventory cycle. However, they should help to give an overview about the main parameter, such as:

- Tree species distribution (e.g., coniferous/broadleaved/mixed)
- Changes in area coverage (e.g., the conversion of stands after felling or as result of calamities)
- Management measures
- Information on stand structure parameters (e.g., number and position of standards, gaps and tree type mixture—single tree mixture, group wise)
- Information needed for the strategically/tactical planning level of a forest enterprise.

Most, if not all, of these information are retrievable more or less automatically from data sets like those offered by a combination of microwave and multispectral data. Again, not necessarily with a quality as that required for decision making, but surely with a sufficient accuracy for decision support and fast response actions!

In the context of global change phenomena, especially the observed increase of frequency and intensity of calamities, the presented combination of microwave and optical systems of the very high to high category seems well appropriated for fast reaction emergency systems all over the world. While the microwave system is delivering the first information about the extent of an event, without being hindered by clouds or daytime, the optical system will deliver the details needed for reconditioning logistics in forestry. A basic point in this context is an already existing GIS data base of the forests, allowing the fast assessment of the changes.

Still an open question is how to connect the results with existing concepts and especially the task of harmonisation of definitions hindering an integration of remote sensing derived information in practice.

Acknowledgments We wish to thanks the Federal Ministry of Economics and Technology, within a program of the Space Agency of the German Aerospace Center (DLR) for funding this research work presented under number 50EE0919 in the frame of the program on "synergistic use of RapidEye and TerraSAR-X data for applications".

References

Ackermann N, Thiel C, Borgeaud, M, Schmullius, C (2010) Potential of fusion of SAR and optical satellite imagery for biomass estimation in temperate forested areas. In: Proceedings of the ESA living planet symposium, Bergen, Norway

Anonymous (2001). Waldgesetz für Bayern. 25. August 1982 (BayRS 7902-1-L): Letzte Änderung 22. Juli 2005 (GVBI 2005, 313).Bayerisches Staatsministerium für Ernährung, Landwirtschaft und Forsten (StMELF), München

Baatz M, Schäpe A (2000). Multiresolution segmentation—an opotimization approach for high quality multi-scale image segmentation. In: Proceedings of the AGIT-symposium Salzburg 2000, Vol XII. Salzburg, pp 12–23

Bamler R (2000) Principles of synthetic aperture radar. Surv Geophys 21(2–3):147–157. doi:10.1023/A:1006790026612

Cloude S.R, Papathanassiou K.P (2008) Forest vertical structure estimation using coherence tomography. In: IEEE proceedings of geoscience and remote sensing symposium, pp 275–278

Congalton RG (1991) A review of assessing the accuracy of classifications of remotely sensed data. Remote Sens Environ 37:35–46

DeKok R, Schneider T, Baatz M, Ammer U (1999) Object based image analysis of high resolution data in the alpine forest area; In: Proceedings joint WSf ISPRS WG I/1, I/3 and IV/4: sensors and mapping from space 1999, Hannover, Sept 27–30

De Zan F, Papathanassiou K, Lee SK (2009) Tandem-L forest parameter performance analysis. In: Proceedings of international workshop on applications of polarimetry and polarimetric interferometry, Frascati, Italy, pp 1–6

Eckert. S. (2006): A contribution to sustainable forest management in patagonia—object-oriented classifiucation and parameter extraction based on ASTER and landsat ETM + data; Verlag des GeographischenInstituts der Uni. Zürich, Remote Sensing Series, Vol 45. pp S.154

Felbermeier T, Hahn A, Schneider T (2010) Study on user requirements for remote sensing applications in forestry. In: Proceedings of the ISPRS symposium TC VII, July 5–7, 2010, Vienna, Austria

Fehlert G-P (1984) Kalibrierung von MSS-Satellitenbilddaten zur Auswertung zeitlicher Reflexionsänderungen an Fichtenbeständen; DFVLR-FB 84–44

Heurich M (2006) Evaluierung und Entwicklung von Methoden zur automatisierten Erfassung von Waldstrukturen aus Daten flugzeuggetragener Fernerkundungssensoren. Forstliche Forschungsberichte München. 202/2006

Hilbert C, Schmullius C, Zink M (2010) Derivation of forest structure using satellite, multifrequent radar and lidar data in Thuringian Forest, Germany. In: Proceedings of silvilaser 2010, Freiburg, Germany

Katzur L, Franke W (2007) Qualitätssicherung bei der Bearbeitung der ATKIS®-Produkte. Vermessung Brandenburg, Heft 02:15–26

Kenneweg H, Förster B, Runkel M (1991) Diagnose und Erfassung von Waldschäden auf der Basis von Spektralsignaturen; In DLR Abschlußdokumentation—Untersuchung und Kartierung von Waldschäden mit Methoden derFernerkundung. Teil A, Oberpfaffenhofen

Kautz M, Dworschak K, Gruppe A, Schopf R (2011) Quantifying spatio-temporal dispersion of bark beetle infestations in epidemic and non-epidemic conditions. For Ecol Manag 262(2011):598–608

Kirscht M, Rinke C (1998) 3D reconstruction of buildings and vegetation from synthetic aperture radar (SAR) images. In: Proceedings of IAPR workshop on machine vision applications MVA"98, Makuhari, Chiba, Japan, pp 228–232

Knoke T, Schneider T, Hahn A, Griess VC, Rößiger J (2012) Forstbetriebsplanung als Entscheidungshilfe. Ulmer Verlag Stuttgart, p 408. ISBN 978-3-8001-7611-3

Koch B (2010) Status and future of laser scanning, synthetic aperture radar and hyperspectral remote sensing data for forest biomass assessment. ISPRS J Photogramm Remote Sens 65:581–590

Kourgli A, Belhadj-Aissa A (2009) SAR image classification using textural modelling. In: Proceedings of radar conference—surveillance for a safer world, Bordeaux, pp 1–6

Lee JS, Papathanassiou KP. Hajnsek I, Mette T, Grunes MR, Ainsworth T, Ferro-Famil L (2005) Applying polarimetric SAR interferometric data for forest classification. In: IEEE proceedings of geoscience and remote sensing symposium, Vol 7. Pp 4848–4851

Lemp D, Koch B (2009) Forest monitoring using TerraSAR-X data—evaluation of processing methods and first results. In: Proceedings of TerraSAR-X science meeting 2009

Lillesand T, Kiefer R, Chipman J (2004) Remote sensing and image interpretation. Wiley, New York, p 763. ISBN 13: 978-0471152279

Pretzsch H (2002): Application and evaluation of the growth simulator SILVA 2.2 for forest stands, forest estates and large regions. Forstwissenschaftliches Centralblatt 121(Suppl.1):28–51

Rall H, Martin K (2002) Luftbildauswertung zur Waldentwicklung im Nationalpark Bayerischer Wald 2001—Ein neues Verfahren und seine Ergebnisse zur Totholzkartierung. In: Berichte aus dem Nationalpark, Nationalparkverwaltung Bayerischer Wald 1 (2002)

Reigber A, Moreira A (2000) First demonstration of airborne SAR tomography using multibaseline L-band data(5). IEEE Trans Geosci Remote Sens 38(5):2142–2152. doi:10.1109/36.868873 (Part 1)

Reitberger J, Schnörr CL, Heurich M, Krzystek P, Stilla U (2008a) Towards 3D mapping of forests: a comparative study with first/last pulse and full waveform LIDAR data; the international archives of the photogrammetry. Remote Sens Spat Inf Sci 37:1397–1403 (Part B8)

Reitberger J, Schnörr CL, Heurich M, Krzystek P, Stilla U (2008b) Analysis of full waveform LIDAR data for the classification of deciduous and coniferous trees. Int J Remote Sens—3D Remote Sens For 29(5):1239–1242. doi:10.1080/01431160701736448

Reitberger J, Schnörr CL, Krzystek P, Stilla U (2009) 3D segmentation of single trees exploiting full waveform LIDAR data. ISPRS J Photogramm Remote Sens 64:561–574. doi:10.1016/j.isprsjprs.2009.04.002

Sato M, Koike T (2003) Classification of tree types by polarimetric Pi-SAR. In: IEEE proceedings of geoscience and remote sensing symposium, Vol 1. Pp 431–433

Schulz K, Boldt M, Thiele A (2009) COVAMCOH-ANALYSIS: a method to improve the interpretation of high resolution repeat pass SAR images of urban areas. In: Proceedings of SPIE, remote sensing for environmental monitoring, GIS applications, and geology IX Vol. 7478:747805—747809 74780 doi: 10.1117/12.830441

Schneider T, de Kok R, Buck A, Manakos I (2000) Objektorientierte Bildanalyse—Paradigmawechsel in der thematischen Auswertung von Erdbeobachtungsdaten ? In: Lehrstuhl für Landnutzungsplanung und Naturschutz (2000): Landnutzungsplanung und Naturschutz. Aktuelle Forschungsberichte. Festschrift zur Emeritierung von Professor Dr. Ulrich Ammer. Freising, pp 234–258 ISBN 3-89685-564-6

Seitz R, Rappl A, Straub C, Troyke A (2011) Forstliche Fernerkundung an der LWF, AFZ-der Wald, 13/2011, pp 11–13

Straub C, Weinacker H., Koch B (2008) A fully automated procedure for delineation and classification of forest and non-forest vegetation based on fullwaveform laser scanner data. Int Arch Photogramm, Remote Sens Spat Inf Sci 37(8/11):1013–1019

Tiede D, Lang S, Hoffmann C (2006) Supervised and forest type-specific multi-scale segmentation for a one-level-representation of single trees. Int Arch Photogramm, Remote Sens Spat Inf Sci 36(4):C42 (Salzburg, Austria. http://www.commission4.isprs.org/obia06/)

Thiele A, Schulz K, Thoennessen U, Cadario E (2006) Orthorectification as Preliminary Step for the fusion of data from active and passive sensor systems. In: Proceedings of IEEE international conference on multisensor fusion and integration for intelligent systems, doi: 10.1109/MFI.2006.265629, pp 479–484

Volden E., Solberg AS, Huseby RB (1998) Forest classification using spectrometer and SAR Data. 1998 In: IEEE proceedings of feoscience and remote sensing symposium, Vol 5, pp 2732–2736

Waser LT, Ginzler C, Kuechler M, Baltsavias E (2008) Potential and limits of extraction of forest attributes by fusion of medium point density LiDAR data with ADS40 and RC30 images. In: SilviLaser 2008 8th international conference on LiDAR applications in forest assessment and inventory, Edinburgh, UK, Sept 18–19, 2008, pp 625–634

Zhang Z, Ni W, Fu A, Guo Z, Sun G, Wang D (2008) Estimation of forest structural parameters from Lidar and SAR data. Int Arch Photogramm, Remote Sens Spat Inf Sci 37:1121–1126 (part B8)

Multispectral Remote Sensing of Invasive Aquatic Plants Using RapidEye

Sebastian Roessler, Patrick Wolf, Thomas Schneider and Arnulf Melzer

Abstract Some invasive aquatic plants are thought to benefit from recent climate warming. Their frequent observation is only feasible using satellite data. Earlier studies used airborne hyperspectral sensors like HyMap to discriminate different plant species—this is a very cost intensive method with an environmental impact through numerous flights. A fully automated processing chain to assess the distribution of invasive species, as well as their abundances and biomass is restricted to spaceborne sensors. The research presented here investigates the ability of multi-seasonal multispectral remote sensing data (RapidEye) to differentiate between vegetated and non vegetated areas, as well as species composition at a subpixel level. This is done by combining *in situ* derived information about the apparent optical properties of the water body and reflectance measurements of *Elodea nuttallii* and *Najas marina*. The information about the current state of the water body is used to produce depth-invariant combinations of spectral bands using a simple physically based semiempirical method. *In situ* reflectance measurements were processed with the same method and subsequently used in a Matched Filtering spectral unmixing approach. The results show a good separation between vegetated and bare litoral areas. A reliable differentiation of plant species still requires further method development.

S. Roessler (✉) · P. Wolf · T. Schneider (✉) · A. Melzer
Limnological Institute, Technische Universität München, München, Germany
e-mail: sebastian.roessler@mytum.de

T. Schneider
e-mail: Tomi.Schneider@lrz.tum.de

J. M. Krisp et al. (eds.), *Earth Observation of Global Changes (EOGC)*,
Lecture Notes in Geoinformation and Cartography, DOI: 10.1007/978-3-642-32714-8_7,

1 Introduction

Submerged macrophytes in freshwater lakes are used as longterm indicators for nutrient conditions (Melzer 1999). Climate change is thought to favour invasive submersed macrophytes in freshwater ecosystems (Rahel and Olden 2008) and therefore to have profound influence on lake ecosystems. Two invasive species, *N. marina* and *E. nuttallii* have been subject of multidisciplinary research for several years, as it is assumed that increasing water temperature promotes their expansion. *N. marina* is indigenous to Europe, while *E. nuttallii* is a neophytic species originating in North America. The species differ in their expansion speed with *E. nuttallii* expanding much faster. Since the trophic state of these ecosystems is strongly correlated to water temperature, adequate monitoring of these species will give important information about the development of lakes in a warming climate. In this study the application of different space—and airborne sensors for identification and monitoring of invasive aquatic plants have been tested.

Until now, a frequent observation of the expansion behavior of invasive species is restricted to hyperspectral airborne remote sensing sensors which provide the needed geometric and spectral resolution (Pinnel 2007). This is—for frequent observations—a very expensive method and has major ecological impact through flight related emissions of greenhouse gases. Therefore, a fully automated monitoring system must be based on spaceborne sensors with satisfying spectral, radiometric and geometric resolutions and a short revisit time, enabling on-demand information about the current state. The multispectral data provided by RapidEye fulfills these requirements.

The questions we addressed were: Can multispectral remote sensing combined with frequent *in situ* observations and/or model prediction help to distinguish submerse macrophytes in shallow freshwater environments? Which statements can be made in terms of species composition, abundance of invasive species, as well as their expansion behavior and vitality? RapidEye is ideally suited to address this problem. Moreover, the short revisit time at a geometric resolution of 5 meters allows a realistic description of the spatially and temporally heterogeneous vegetation communities. Multi-seasonal RapidEye data were obtained from the RapidEye Science User Archive (RESA) covering the vegetation period from May to September 2011.

2 Materials and Methods

2.1 Study Site

The study site was Lake Starnberg (47°55'N, 11°19'E) situated 25 km southwest of Munich (Fig. 1). It covers an area of 56 km^2 and is Germany's fifth largest lake. The length is 20 km, the maximum width 4.7 km and the maximum depth is

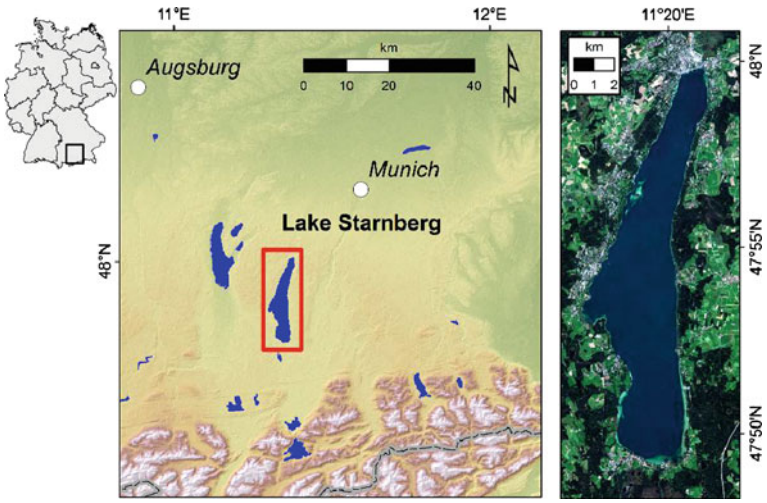

Fig. 1 Location of Lake Starnberg and RapidEye subset from 03/09/11

127.8 m (on average 53.2 m). The lake was formed by the Isar-Loisach-Glacier during last glacial period (Fesq-Martin et al. 2008). Extended litoral terraces are situated on the western shore. At this lakeside, testsites were selected according to high abundances of *Najas marina* and *Elodea nuttallii*, as well as other common macrophytes like *Potamogeton perfoliatus* and *Chara* spec., which were also spectrally measured to compare their reflectance properties.

The former oligotrophic lake turned into a mesotrophic state after 1950 due to discharge of wastewater. After installation of a sewage disposal system, water quality improved. Present Phytoplankton concentrations range between 2.4 and 4.8 µg l^{-1} in winter and 6–12 µg l^{-1} in summer, respectively. The average annual primary production is 889 g C m^{-2} y^{-1} (Pinnel 2007).

2.2 In Situ *Data and Processing*

In situ measurements were performed using three RAMSES submersible spectroradiometers (TRIOS GmbH), which were triggered simultaneously. The sensors recorded hemispherically the downwelling (E_d) and upwelling (E_u) irradiance, and the upwelling radiance (L_u) with a field of view of 7°, respectively.

Data acquisition took place during the growing season between August and Oktober 2010 at solar noon (±2 hours) to get reflectances at low sun zenith angles (30° at maximum). Above each of the patches measurements were made at two different water depths (i.e. to include the water column with its constituents). The first measurement was just beneath the water surface (R_{0-}), the second just above the vegetation surface (R_b). In both sensor positions 20 single spectra were

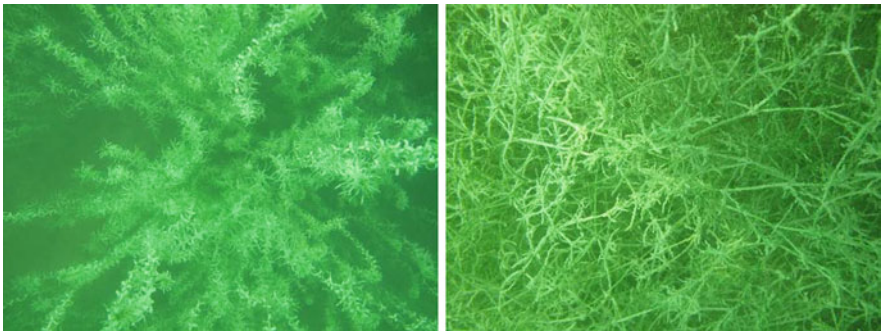

Fig. 2 Photos taken under water of *Elodea nuttallii* (*left*) and *Najas marina* (*right*)

recorded. In Fig. 2, pictures taken from an attached stereo camera system are shown. The photos were taken at the lower sensor position, located approximately 20 cm above the vegetation surface.

After an automatic calibration with MSDA_XE software (version 8.5) by TRIOS GmbH, the data were resampled to an equal wavelength raster, ranging from 320 to 950 nm with a spectral sampling interval of 3.3 nm. Further calculations (i.e. the remote sensing reflectance, attenuation) were performed with Python(x,y).

Apart from *in situ* spectral measurements, sediment samples were taken during diving trips and spectrally characterized in the laboratory using an ASD-FR field spectrometer (Analytical Spectral Devices Inc.). Samples were taken at 18 locations on the western shore at three different depths to generate a complete spectral library for all common sediment types.

Further biophysical parameters such as coverage (percentual amount of leaves, stalks, sediment and shade), growth height, biomass and pigment composition were collected at each penological state when spectral measurements were performed. The database serves as a basis for the development of a coupled reflection/growth model for the macrophytes of interest (*E. nuttallii* and *N. marina*).

2.3 RapidEye Data and Processing

Multispectral remote sensing data were obtained from the RapidEye Science Archive (RESA) within the project no. 455. A time series of Lake Starnberg was recorded between 6th May and 3rd September 2011. The scenes were delivered as level 3A products including standard radiometric and geometric corrections. Atmospheric correction was performed using ATCOR 2 (Richter 1996) for flat terrain implemented in PCI Geomatics™ (version 10.2.3). The resulting bottom-of-atmosphere (BOA) reflectance images were mosaiced and further processed to

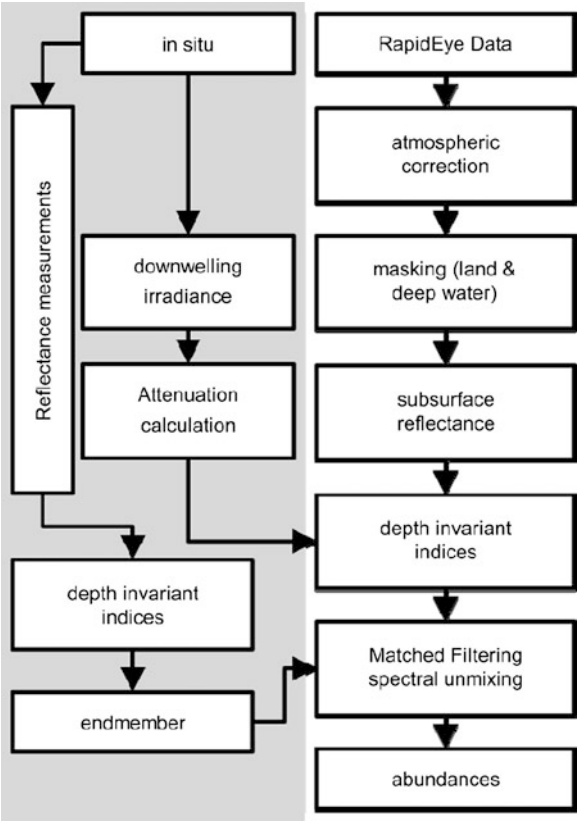

Fig. 3 Processing flow chart showing the combination of *in situ* measurements and RapidEye data

correct for water specific properties. Figure 3 gives an overview of how *in situ* measurements were included in the processing of RapidEye images.

Due to low variation of the reflectance signal in the near infrared over optically deep water (Kay et al. 2009), sun glint correction was not carried out. To identify water bodies, a normalized difference water index (NDWI) was calculated using the reflection in the green and near-infrared wavelength domain (McFeeters 1996) using Eq. 1:

$$NDWI = \frac{\rho_{green} - \rho_{NIR}}{\rho_{green} + \rho_{NIR}} \quad (1)$$

Although other authors (Lira 2006) propose a principal component analysis, we achieved good segmentation results with a NDWI threshold of 0 to delineate water bodies (pixel with values greater than 0 are assigned to water). Since only shallow water areas are of interest, a further threshold was applied using a deepwater corrected Red Index (RI) calculated with Eq. 2 (Spitzer and Dirks 1987).

$$RI = \frac{\rho_{red} - \rho_{\infty,red}}{\rho_{red}} \tag{2}$$

With ρ_{red} being the reflection value of each pixel in the red and $\rho_{\infty,red}$ the mean red reflection over optically deep water. Taking the variations of deepwater reflectance into account, an influence of the bottom signal was found if the Red Index value exceeded 0.15. This value is empirically defined for Lake Starnberg depending on the water constituents. Pixels with an NDWI value greater than 0 and a Red Index values greater 0.15 were further assigned to shallow water and processed.

The water leaving reflectance measured by the sensor above the surface (R_{rs}) is including the reduction of the signal due to the refraction of the upwelling radiance at the water surface. This decrease of water leaving signal intensity is described by dividing the sigal with the squared refractive index of water ($n_w^2 = 0.56$). Taking the reflection factors of E_d (σ), L_u^- (σ_L^-) and E_u (σ^-) into account, the water leaving Remote Sensing reflectance can be calculated with Eq. 3 (Lee et al. 1998):

$$R_{rs} = \frac{(1-\sigma)\left(1-\sigma_L^-\right)}{n_W^2} \cdot \frac{r_{rs}}{1 - \sigma^- \cdot Q \cdot r_{rs}} \tag{3}$$

Lee et al. (1998) found as typical values for nadir viewing sensors $(1-\sigma)\left(1-\sigma_L^-\right)/n_{W^2} = 0.518$ and $\sigma^- \cdot Q = 1.562$ for transforming reflectances from beyond to above the water surface. Solving Eq. 3 for r_{rs}—which is measured *in situ*—leads to the Eq. 4 which can be used as approximation (Lee et al. 1999):

$$r_{rs} \approx \frac{R_{rs}}{0.518 + 1.562 R_{rs}} \tag{4}$$

In order to get information about subsurface bottom types at different depths, the exponentially decreasing light intensity has to be considered. This loss of radiation (vertical diffuse attenuation) is a function of scattering due to suspended particles and absorption of water constituents (phytoplankton, suspended particulate matter, gelbstoff and the water itself). Models have been developed to retrieve water constituents from remotely sensed or *in situ* data (Gege 2004). The correction of the decrease of light beam due to properties of the water column requires the knowledge of wavelength-dependant attenuation coefficients, water depths or the reflectance spectra of the substrate, respectively. Heege et al. (2003) developed a physically based process chain to derive bottom reflectances using a spectral library of known substrate albedo spectra. Instead of predicting the bottom reflectance, Lyzenga (1978, 1981) used a semi-empirical method that compensates the effects of variable depths by calculating depth-invariant indices. This method has been used successfully for bathymetric studies with known substrate (Mishra et al. 2004), but can also be used to map different benthic habitats of varying depths (Hedley and Mumby 2003; Mumby et al. 1998; Tassan 1996). To account for the exponential depth dependance of the received signal, a linearization of each band was performed using the natural logarithm of each spectral band (Lyzenga

1978). Linear combinations of the log-transformed reflectance values were used to produce depth-invariant indices (Eq. 5) as described by Lyzenga (1981):

$$Y_{i,j} = \frac{K_j \ln(\rho_i - \rho_{\infty i}) - K_i \ln(\rho_j - \rho_{\infty j})}{\sqrt{\left(K_i^2 + K_j^2\right)}} \tag{5}$$

where K_i and K_j are the attenuation coefficients in band i and j, and $Y_{i,j}$ the calculated depth-invariant index between these bands. The natural logarithm is calculated from the reflectance values of shallow water areas reduced by the reflectance of deep water in the same band ($\rho_i - \rho_{\infty i}$). The index $Y_{i,j}$ is related to the bottom reflectance (r_i) as follows (Eq. 6) (Lyzenga 1981):

$$Y_{i,j} = Y_{i,j0} + \frac{K_j \ln r_i - K_i \ln r_j}{\sqrt{\left(K_i^2 + K_j^2\right)}} \tag{6}$$

The value $Y_{i,j0}$ is a constant for fixed illumination conditions and concentrations of water constituents. However, it can be omitted by adding an artificial water column to the *in situ* measured reflectance using known attenuation coefficients (K_d) and deepwater reflection (r_∞). The simulated shallow water reflection is calculated using Eq. 7 (Philpot 1989):

$$r_{shallow} = r_{bottom} \exp^{-2K_d z} + r_{deepwater}(1 - \exp^{-2K_d z}) \tag{7}$$

From the simulated reflectances of known substrates (derived from *in situ* spectral measurements), depth-invariant indices were calculated for each RapidEye scene representing the current conditions of water constituents and illumination geometry. The indices were used as endmembers in subsequent spectral unmixing of image derived depth-invariant indices.

The required diffuse attenuation coefficients (K_d) for the downwelling irradiance of the five spectral bands of RapidEye can either be derived from image data with known substrate at different depths (Armstrong 1993) or can be calculated with *in situ* measured spectra. We used measurements of the downwelling irradiance (E_d) at different depths ($z_2 > z_1$) recorded for the different times we achieved RapidEye data. The attenuation coefficients were calculated using the Eq. 8 (Maritorena 1996):

$$K_d = \frac{\ln\left[\frac{E_d^-(z_1)}{E_d^-(z_2)}\right]}{z_2 - z_1} \tag{8}$$

The RAMSES derived hyperspectral attenuation coefficients (Fig. 4, left) were spectrally averaged according to the channel specific sensitivity of RapidEye using the spectral response functions of each band. Averaging was performed using ENVI™ 4.7. The resulting attenuation coefficients for 4 selected RapidEye Scenes are shown in Fig. 4 (right).

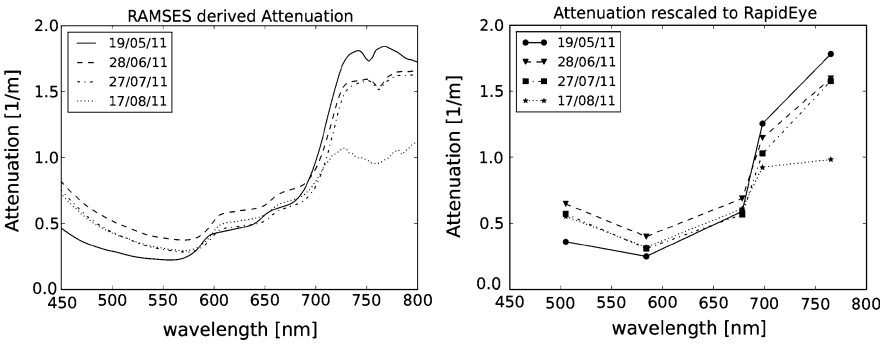

Fig. 4 Attenuation coefficients derived from *in situ* measurements (*left*) and spectrally rescaled to the five bands of RapidEye (*right*)

Depth-invariant indices according to Eq. 5 were calculated after preprocessing for all possible six band combinations between channels 1–4 (the NIR band was omitted due to strong water absorption). Subsequently, linear spectral unmixing was performed using the Matched Filtering method (Manolakis and Shaw 2002). This method was chosen since the three *in situ* derived endmembers (*E. nuttallii*, *N. marina* und uncovered sediment) presumably do not represent all possible coverages of Lake Starnberg's litoral zone. Every pixel was assigned a score value for the possible endmembers affiliation. Values near 1.0 indicate a perfect match (abundance of 100 %), values between 0.0 and 2.0 suggest a contribution of the endmember to the overall signal to a certain extent. Score values below 0 rule out an affiliation of this endmember.

3 Results and Discussion

3.1 In Situ *Data*

The *in situ* reflectance measurements above vegetation patches of *E. nuttallii* and *N. marina* show strong variations especially in the red edge and the near infrared region. The main explanation for this is the strong variation of the downwelling irradiance caused by waves. In Fig. 5, the deviation factor for different sensor depths is shown. It is calculated by dividing all recorded spectra with the lowest measured intensity.

With increasing depth the variation decreases, since the influence of waves decreases with increasing water column. At a depth of 5 m almost no deviations appear. Unlike the irradiance intensities, the radiance measurements are less influenced by waves. However, there are certain variabilities caused by plant movement. As meadow-like growing *Characea* are less influenced by waves,

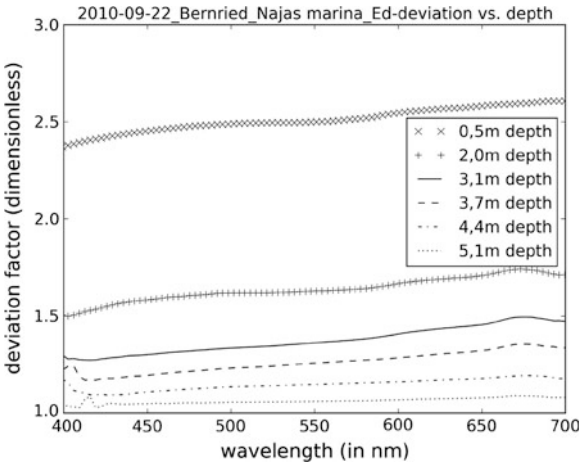

Fig. 5 Deviation factor of the downwelling irradiance for different sensor depths

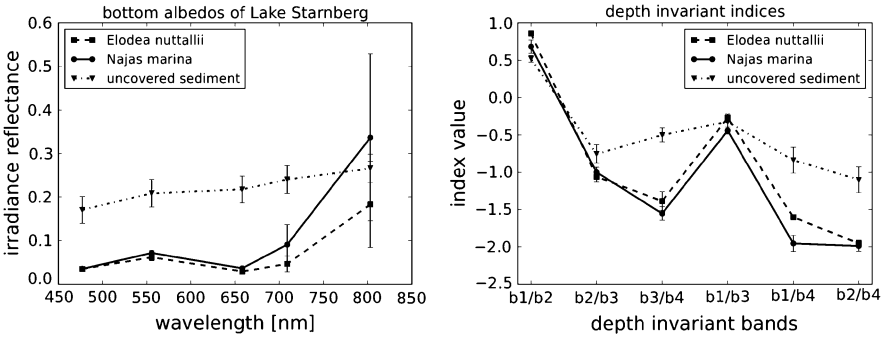

Fig. 6 Reflectance measured above the bottom over different targets (*left panel*) and calculated depth-invariant indices (*right panel*)

measurements are more stable. Variabilities of high growing macrophytes like *E. nuttallii* and *N. marina* increase with waves.

Due to the high standard deviation of measured reflectance spectra from different macrophytes or sediment coverages there is a great overlap between *N. marina* and *E. nuttallii* (Fig. 6, left). However, the calculated depth-invariant ratios between the spectral bands of RapidEye are less affected by variations and provide good separability in certain artificial bands. The right panel of Fig. 6 shows the six possible depth-invariant band combinations.

The calculated indices indicate that band combinations may exist for which a separation of different species is possible as well as a discriminatation of bare soil and vegetated surfaces. To identify band combinations best suited for the identification of macrophytes (i.e. *N. marina* and *E. nuttallii*) as well as uncovered sediment, separability measures were calculated for all possible band combinations.

Table 1 Calculated separability measure for possible band combinations for the depth-invariant indices

Used depth-invariant bands	Jeffries-Matusita index		
	Elodea nuttallii/*Najas marina*	*Elodea nuttallii*/uncovered sediment	*Najas marina*/uncovered sediment
All	1.56931166	2.00000000	1.98296533
(1) b1/b2	1.07808005	1.99998320	1.91085016
(2) b2/b3	1.17638898	1.99999987	1.93642036
(3) b3/b4	1.32375258	1.99999997	1.91254893
(4) b1/b3	1.24110761	1.99999989	1.94254478
(5) b1/b4	1.18262100	1.99999186	1.84942206
(6) b2/b4	1.05027142	1.99999438	1.84366436

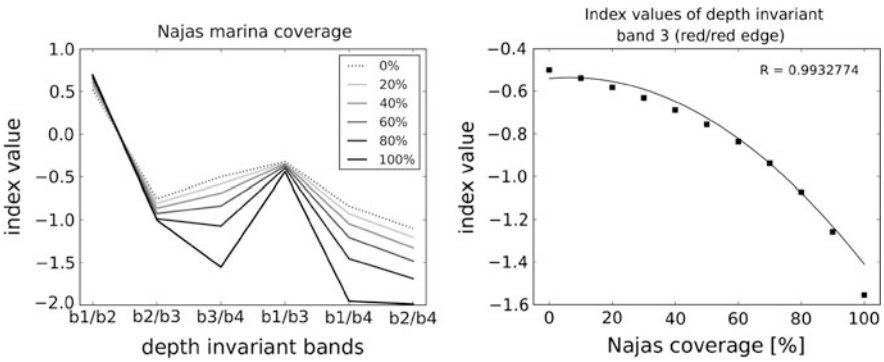

Fig. 7 Depth-invariant indices calculated for different coverages of *Najas marina* (*left*) and relationship between vegetation coverage and index value of depth-invariant band 3 (*right*)

As typical measures for Remote Sensing applications the Jeffries-Matusita Index (Richards 1999) was calculated using the software ENVI™ 4.7 (Table 1).

Between *E. nuttallii* and *N. marina*, only depth-invariant band 3 (red/red edge) and band 4 (blue/red) show comparatively good separability, however according to Richards (1999) only index values greater than 1.9 indicate good separability

Between uncovered sediment and *E. nuttallii*, almost all calculated depth-invariant indices are well suited for separation. However, as seen in Fig. 6 (bottom panel), especially the depth-invariant bands 3 (red/red edge), band 5 (blue/red edge) and band 6 (green/red edge) show completely different values compared to vegetated surfaces. Since it is less affected by absorption of colored dissolved organic matter (cDOM), the depth-invariant band 3 can be used to differentiate between vegetated surfaces and bare bottom.

To evaluate the non-linear development of the index value of depth-invariant band 3, different coverages of *N. marina* were used to calculate depth-invariant

indices (Fig. 7, left). The different index values of depth-invariant band 3 shown in Fig. 7 (right) serve as threshold values to assess vegetation coverage from image data.

3.2 Remote Sensing Data

The Lyzenga (1978, 1981) based method for calculating depth-invariant bands was applied to 4 RapidEye scenes from summer 2011 (06/05/11, 28/06/11, 16/07/11, and 20/08/11). After masking of land and optically deep water areas (using Eqs. 1 and 2), depth-invariant indices were calculated with the attenuation values derived from *in situ* measurements for the subsurface reflectance (Eq. 5) of shallow water areas with the values given in Fig. 4 (right). The artificial band 3 (green/red edge) was shown to be best suited to differentiate bare sediment from vegetated areas. In Fig. 8, this index is shown for the area surrounding the Roseninsel (situated at Lake Starnberg near the town Tutzing). This area is known for large meadows of *Characea* spec. in the northern litoral zone as well as bare soil at the northern edge of the island. *Characea* are annual plants and therefore ideally suited to test the detection of bare sediment at the beginning of the growth period. Low index values (up to −1.5) indicate vegetation, higher index values (greater −0.9) larger percentages of bare soil. The color bar is adapted to the values given in Fig. 8 (right) and scaled to coverages from 0 to 100 % (note the non-linear relationship).

Vegetation coverage increases from May onwards, although areas covered by plant detritus can also lead to low index values which would be interpreted as vegetation coverage. In June large areas in the northern litoral were already covered by plants. The vegetation coverage decreased in August.

The Matched Filtering spectral unmixing approach also showed good results for the differentiation of bare soils and vegetated areas. However, the distinction between *E. nuttallii* and *N. marina* is difficult. Unmixing was performed for all four scenes using endmember derived from Eq. 6 for the scene specific attenuation coefficients. Results for 6th of May (Fig. 9), as well as 20th of August (Fig. 10) are shown.

For a better visualisation, the area “Roseninsel” (A) and “Bernried” (B) are enlarged. As discussed above, large areas of uncovered sediment appeared north of the Roseninsel, Bernried was characterized by dense coverage of *N. marina* from July onwards. However, the score values for uncovered sediment do not show a complete coverage of soil. This is probably caused by detritus over bare ground. The shallow area of Bernried was also covered by bare silty sediment. Plants only occurred below a water depth of 3 m.

The results of the 20th of August (Fig. 10) show better identification of bare sediment compared to vegetated areas. The uncovered regions around the Roseninsel were identified as those. The differentiation of *E. nuttallii* and *N. marina* is currently not reliable. However, it can be stated, that most areas identified as *E. nuttallii* have also high values of the endmember *N. marina*. Since 2011 was a

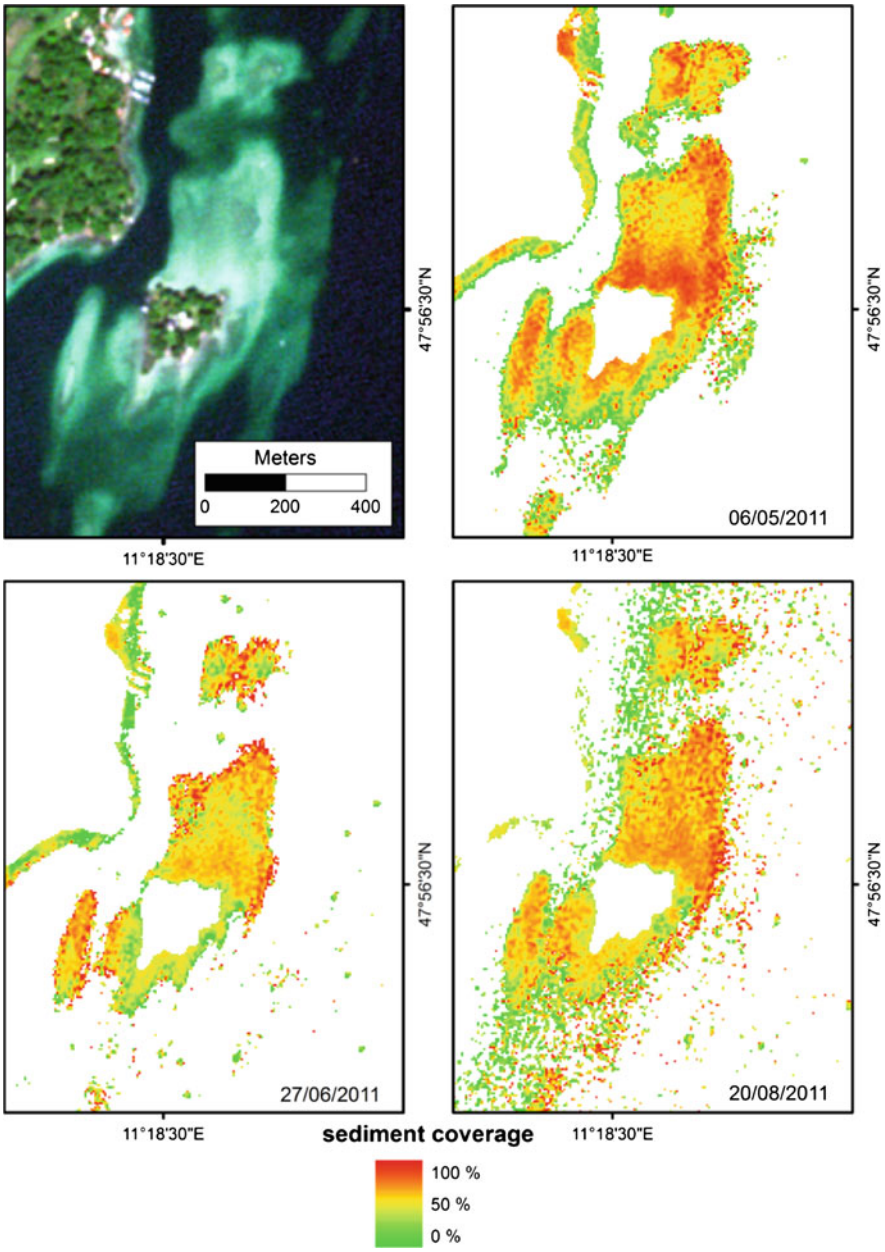

Fig. 8 Depth-invariant band 3 (*red/red edge*) for three selected dates during vegetation period 2011 (*low values*: vegetated, *high values*: bare soil)

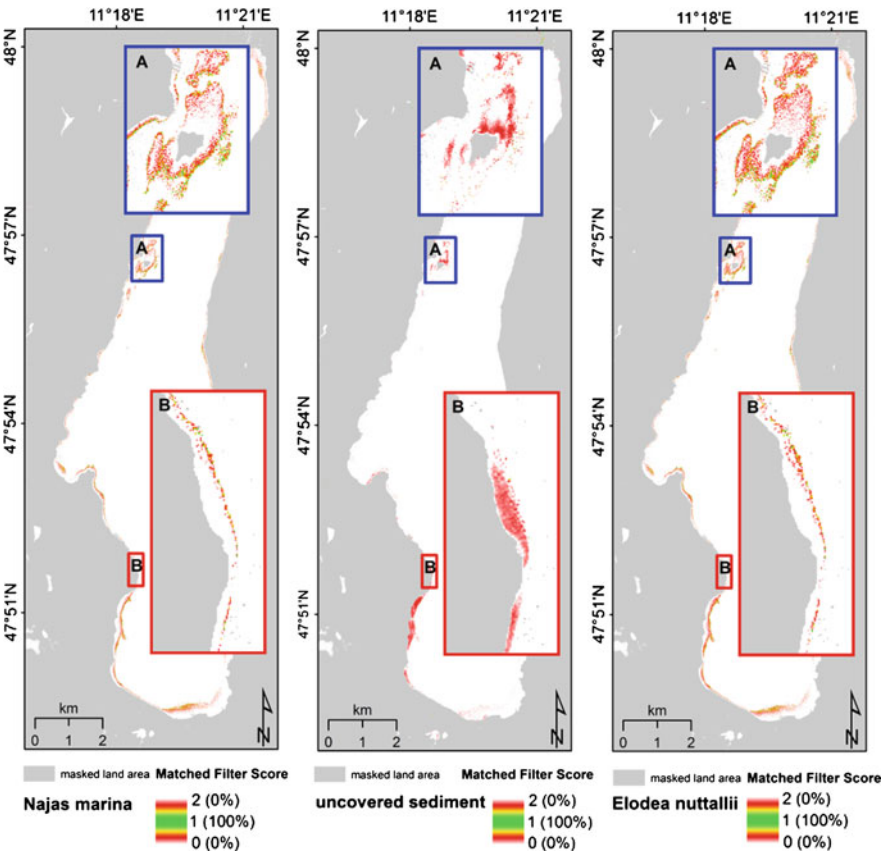

Fig. 9 Matched filter spectral unmixing result for the RapidEye scene from 06/05/11

very poor year for the growth of *E. nuttallii* (litoral mapping by scientific divers showed almost no pure stands of *E. nuttallii*) the areas classified as *Elodea* may include *Najas* patches as well.

4 Conclusion

The applied method for processing multispectral remote sensing data yields good results for the elimination of the water column provided that accurate attenuation coefficients are known or measured. An additional assumption is that the properties of the water constituents are homogenous throughout the water column. The *in situ* measured reflectance spectra are—despite the discussed problems—an ideal basis to create a multi-seasonal database throughout the growing period. During summer 2012, with ongoing RapidEye data acquisition, ground truth measurements will be

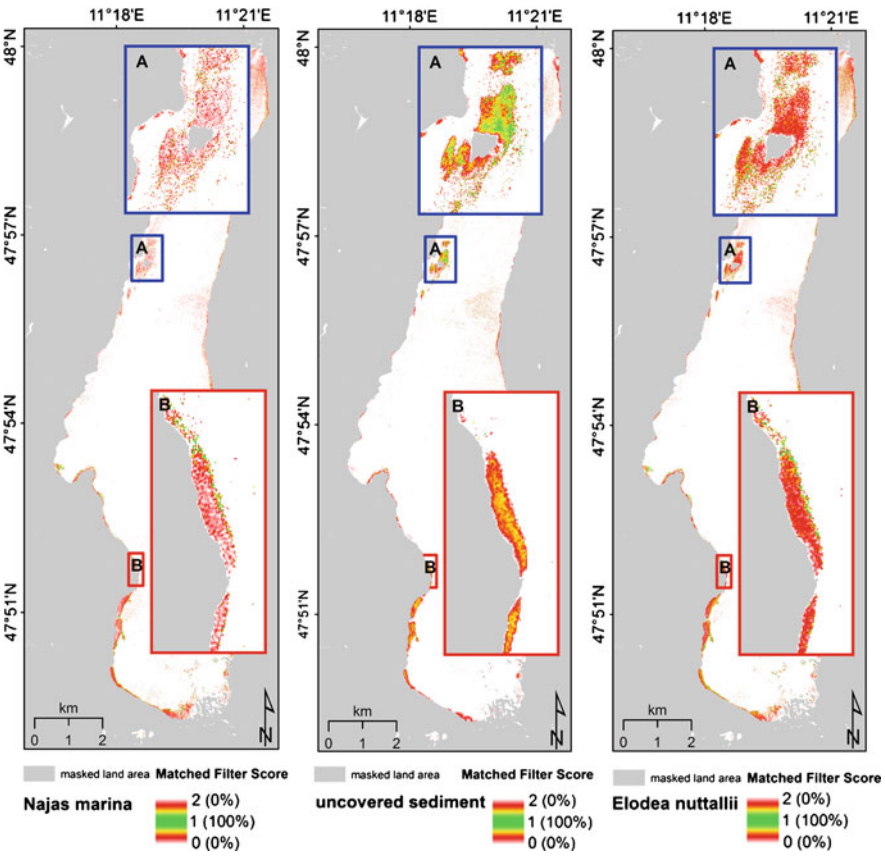

Fig. 10 Matched filter spectral unmixing result for the RapidEye scene from 20/08/11

carried out to obtain reliable endmember spectra for supervised classifications with spectral unmixing methods. Further methods will be tested to retrieve the necessary information about the apparent optical properties (i.e. attenuation coefficients) from optical deep water reflectances according to Lee et al. (2002). Litoral mapping by scientific divers will be carried out 2012 to find larger areas with pure stands of *N. marina* and *E. nuttallii* to perform an accuracy assessment of the presented method.

Acknowledgments This project is founded by the Bavarian State Ministry of Environment and Health under the number ZKL01Abt7_18457. Thanks to the colleagues from the Limnological Institute who helped us during field work and to the Rapid Eye Science archive (RESA) who thankfully provided us with the data within the project no. 455.

References

Armstrong RA (1993) Remote sensing of submerged vegetation canopies for biomass estimation. Int J Remote Sens 14(3):621–627

Fesq-Martin A, Lang A, Peters M (2008) Der Starnberger See—Natur- und Vorgeschichte einer bayerischen Landschaft. Pfeil-Verlag, München

Gege P (2004) The water color simulator WASI: an integrating software tool for analysis and simulation of optical in situ spectra. Comput Geosci 30(5):523–532

Hedley JD, Mumby PJ (2003) A remote sensing method for resolving depth and subpixel composition of aquatic benthos. Limnol Oceanogr 48(1):480–488

Heege T, Bogner A, Pinnel N (2003) Mapping of submerged aquatic vegetation with a physically based processing chain. In: SPIE-the international society for optical engineering, vol 5233. Spain, Barcelona, pp 43–50

Kay S, Hedley J, Lavender S (2009) Sun glint correction of high and low spatial resolution images of aquatic scenes: a review of methods for visible and near-infrared wavelengths. Remote Sens 1(4):697–730

Lee Z, Carder KL, Mobley CD, Steward RG, Patch JS (1998) Hyperspectral remote sensing for shallow waters. I. A semianalytical model. Appl Opt 37(27):6329–6338

Lee Z, Carder KL, Mobley CD, Steward RG, Patch JS (1999) Hyperspectral remote sensing for shallow waters. 2. Deriving bottom depths and water properties by optimization. Appl Opt 38(18):3831–3843

Lee Z, Carder KL, Arnone RA (2002) Deriving inherent optical properties from water color: a multiband quasi-analytical algorithm for optically deep waters. Appl Opt 41(27):5755–5772

Lira J (2006) Segmentation and morphology of open water bodies from multispectral images. Int J Remote Sens 27(18):4015–4038

Lyzenga DR (1978) Passive remote sensing techniques for mapping water depth and bottom features. Appl Opt 17(3):379–383

Lyzenga DR (1981) Remote sensing of bottom reflectance and water attenuation parameters in shallow water using aircraft and Landsat data. Int J Remote Sens 2(1):71–82

Manolakis D, Shaw G (2002) Detection algorithms for hyperspectral imaging applications. Sig Proc Mag IEEE 19(1):29–43

Maritorena S (1996) Remote sensing of the water attenuation in coral reefs: a case study in French Polynesia. Int J Remote Sens 17(1):155–166

McFeeters SK (1996) The use of the normalized difference water index (NDWI) in the delineation of open water features. Int J Remote Sens 17(7):1425–1432

Melzer A (1999) Aquatic macrophytes as tools for lake management. Hydrobiologia 396:181–190

Mishra D, Narumalani S, Lawson M, Rundquist D (2004) Bathymetric mapping using IKONOS multispectral data. GIScience Remote Sens 41(4):301–321

Mumby PJ, Clark CD, Green EP, Edwards AJ (1998) Benefits of water column correction and contextual editing for mapping coral reefs. Int J Remote Sens 19(1):203–210

Philpot WD (1989) Bathymetric mapping with passive multispectral imagery. Appl Opt 28(8):1569–1578

Pinnel N (2007) A method for mapping submerged macrophytes in lakes using hyperspectral remote sensingDoktorarbeit]: Technische Universität, p 164

Rahel FJ, Olden JD (2008) Assessing the effects of climate change on aquatic invasive species (Evaluación de los Efectos del Cambio Climático sobre Especies Acuáticas Invasoras). Conserv Biol 22(3):521–533

Richards JA (1999) Remote sensing digital image analysis. Springer-Verlag, Berlin 240

Richter R (1996) A spatially adaptive fast atmospheric correction algorithm. Int J Remote Sens 17(6):1201–1214

Spitzer D, Dirks RWJ (1987) Bottom influence on the reflectance of the sea. Int J Remote Sens 8(3):279–308

Tassan S (1996) Modified Lyzenga's method for macroalgae detection in water with non-uniform composition. Int J Remote Sens 17(8):1601–1607

Flash-Flood Monitoring and Damage Assessment with SAR Data: Issues and Future Challenges for Earth Observation from Space Sustained by Case Studies from the Balkans and Eastern Europe

Antonios Mouratidis and Francesco Sarti

Abstract Floods are considered as one of the most important catastrophes, as they affect more population compared to any other natural disaster worldwide. Remote Sensing techniques provide safe and cost-effective tools for monitoring, mapping and assessing the evolution and damages caused by flood events. In the Balkans and in most countries of Eastern Europe, a plethora of catastrophic floods and especially flash-floods have occurred during the last two decades, but only a small percentage of those has been studied with Earth Observation data. In this context, the objective of this study is to investigate the adequacy and efficiency, mainly in terms of temporal resolution, of Synthetic Aperture Radar (SAR) satellite data in monitoring and managing flash-flood events. To this end, the challenges and data requirements for future missions are discussed, through selected case studies from the Balkans and Eastern Europe. "Capturing" a flash-flood with SAR data is indeed proven to be a challenging task. The main issues identified in managing flash-flood phenomena with Earth Observation data, are related to the lack of frequent (6–12 h) systematic SAR acquisitions of high spatial resolution (20 m or better).

1 Introduction

Among natural disasters floods are, on global scale, considered as one of the most important catastrophes. They affect more population compared to any other natural hazard (Bell 1999), damaging natural resources and environment, but also causing

A. Mouratidis (✉) · F. Sarti
ESA/ESRIN, Via Galileo Galilei, 00044 Frascati, Italy
e-mail: antonios.mouratidis@esa.int

F. Sarti
e-mail: francesco.sarti@esa.int

J. M. Krisp et al. (eds.), *Earth Observation of Global Changes (EOGC)*,
Lecture Notes in Geoinformation and Cartography, DOI: 10.1007/978-3-642-32714-8_8,

the loss of human lives and economy worldwide. This, to a certain extent inevitable, and in part natural, phenomenon has drawn increasing attention during the last decades. This is mainly due to the escalating frequency of flood events around the world, as well as due to the evidence and warnings about a global climatic change. Consequently, efficient monitoring is a fundamental necessity during the crisis and post-crisis phases of a flooding event, in order to minimize and evaluate its impact, in terms of human safety and damage to property, but also to support zonation and risk assessment efforts.

In this context, by 2011, European Union (EU) Member States will undertake a preliminary flood risk assessment effort. Subsequently, they will develop flood hazard maps (i.e. showing flood probability) and flood risk maps (i.e. related to the potential adverse consequences of a flood). By 2015 flood risk management plans will be drawn for high risk zones. This three stage process (Directive 2007/60/EC) applies to all kinds of floods (river, lakes, flash floods, urban floods, coastal floods, including storm surges and tsunamis) on all of the EU territory and will need to be reviewed every 6 years (European Union 2007). Earth Observation (EO) data and Remote Sensing techniques provide safe and cost-effective tools for monitoring, mapping and assessing the evolution and damages caused by flood events.

According to the definitions given by the U.S. National Oceanic and Atmospheric Administration (NOAA), floods are overflows of water onto normally dry land that may last days or weeks. They are caused by rising water in an existing waterway, such as a river, stream, or drainage ditch, with the ponding of water occurring at or near the point where the rain fell. A flash flood is caused by heavy or excessive rainfall in a short period of time, generally less than 6 h. Flash floods are usually characterized by raging torrents after heavy rains that rip through river beds, urban streets, or mountain canyons sweeping everything before them. They can occur within minutes or a few hours of excessive rainfall. They can also occur even if no rain has fallen, for instance after a levee or dam has failed, or after a sudden release of water by a debris or ice jam. Depending also on the geological and geomorphological regime, the water can remain in the affected area for several days or, more commonly, run off within just a few hours, therefore increasing the demand for timely EO data acquisition.

Major flood events around the globe are being covered by initiatives realized through dedicated organizations, projects and services, such as those of the International Charter “Space and Major Disasters”, the Centre for Satellite Based Crisis Information (ZKI), the Services and Applications For Emergency Response (Safer) and SERTIT (Service Régional de Traitement d’Image et de Télédétection). Nevertheless, there are still hundreds of important flash-floods that remain to be addressed using EO information and especially Synthetic Aperture Radar (SAR) data.

In the Balkans and in most countries of Eastern Europe, a plethora of catastrophic floods -and especially flash-floods-have occurred during the last two decades. Only a small percentage of those has been studied with EO data, as the focus has been logically concentrated on major events covered by initiatives like the International Charter. Nevertheless, the cost of the “overlooked” flood

Fig. 1 Indicative catastrophes caused by a severe flash-flood of October 2006 in the prefectures of Thessaloniki and Halkidiki in North Greece

incidents in terms of human lives and infrastructure (e.g. Fig. 1) Cannot, under any circumstance, be characterized as negligible (Barredo 2009).

In this context, the objective of this study is to investigate the adequacy, mainly in terms of temporal resolution, of Synthetic Aperture Radar (SAR) satellite data in monitoring and managing these largely overlooked flash-flood events. The ultimate goal is to discuss the challenges and derive data requirements for future EO missions, through selected case studies.

Although, starting with Greece, the focus of this study is concentrated over the Balkans and Eastern Europe, similar examples of flood events, leading to similar conclusions, can be identified all over the world.

2 Data and Methodology

2.1 Identification of Flood Incidents

The first step involves the creation of a flood event registry, by thoroughly investigating news, reports and scientific papers that refer to the period of systematically available SAR data, i.e. from 1991 (launch of ERS-1) and onwards.

Incidents covered by initiatives such as the International Charter and/or those which have been already addressed with remote sensing techniques are excluded from further study, but are taken into account for statistical reasons. In Greece only, more than 300 cases have been identified, where EO data and relevant remote sensing techniques could have been implemented for monitoring, mapping and management of flood events.

The next issue is to identify and acquire suitable, with respect to their spatial, spectral and temporal resolution, EO data, in order to "capture" each flood incident and evaluate its impact. Hence, data mining is a necessary step, prior to selecting a specific case study and proceeding with any other tasks.

2.2 SAR Data Mining

Their all-weather, day and night applicability make SAR images/data appropriate for monitoring flood events (e.g. Badji and Dautrebande 1997; Yésou et al. 2000; Sarti 2004; Li et al. 2005), as the latter are normally associated with bad meteorological conditions and high percentage of cloud coverage.

SAR Polarimetry (PolSAR) and SAR Interferometry (InSAR) are two techniques that can also contribute, provided appropriate datasets are available. The benefit of PolSAR is based on the fact that the reflective properties of a surface are dependent on the polarisation of the incoming radar signal. Thus, combining like- and cross-polarizations for rapid mapping within a crisis context is recommended (Henry et al. 2007). The potential of InSAR coherence analysis for flood monitoring has also been well recognized. Due to the sensitivity of the interferometric phase to temporal changes of the surface reflectivity between passes, coherence maps can provide additional information about the flood extent, which otherwise may be difficult to derive from conventional SAR intensity and multi-temporal images (Geudtner et al. 1996).

Water in urban areas is hard to detect on radar images, as "flooded" pixels do not anymore appear profoundly darker than the surrounding area. This is attributed to the existence of multiple scatterers (buildings, infrastructure) within the built environment that scatter part of the SAR signal back to the sensor, instead of reflecting it away from the SAR instrument (typical specular reflection of the signal on smooth water surfaces). In this paper, the focus is on rural areas, where this phenomenon is insignificant.

Hence, looking for available archived SAR data, primarily from the large ERS-1, ERS-2 and Envisat archive, is the next step. The aim is to identify SAR acquisitions that coincide with the recorded (flash-) flood events.

A characteristic example of our improved capacity to "capture" flash-flood events with EO SAR data over the last 20 years is shown in Table 1. Considering the theoretical 35 day revisit time of ERS and Envisat, flash-floods are highly unlikely to be recorded by the Image Mode (IM) SAR acquisitions. This mode offers a spatial resolution of about 30 m, which is quite satisfactory. It is important

Table 1 Chances of recording a flash-flood with at least one systematic SAR acquisition in the prefecture of Thessaloniki (Northern Greece), in the area where the catastrophic flash-flood of October 2006 occurred (see Figs. 1, 2, 3, 4). Area (height × width): 10 × 10 km, Centre Lat/Lon(dd:mm:ss): 40:42:50/23:18:16

	ERS-1/2	Envisat/ASAR(IM)	Envisat/ASAR(WSM)	Sum	Probability*
1991	22	–	–	22	6.0
1992	11	–	–	11	3.0 %
1993	12	–	–	12	3.3 %
1994	17	–	–	17	4.7 %
1995	17	–	–	17	4.7 %
1996	20	–	–	20	5.5 %
1997	15	–	–	15	4.1 %
1998	8	–	–	8	2.2 %
1999	17	–	–	17	4.7 %
2000	10	–	–	10	2.7 %
2001	8	–	–	8	2.2 %
2002	11	1	3	15	4.1 %
2003	21	13	30	64	17.5 %
2004	23	17	41	81	22.2 %
2005	21	17	40	78	21.4 %
2006	20	12	72	104	28.5 %
2007	14	8	85	107	29.3 %
2008	18	7	66	91	24.9 %
2009	14	10	82	106	29.0 %
2010	14	11	69	94	25.8 %
Sum	313	96	488	897	
Acquisitions/yr	16	10.7	54.2		
Probability	4.3 %	2.9 %	14.9 %		

Probability* refers to the chance of ''capturing'' a random flood event within about 12 h of its peak (*source* EOLI catalogue, ESA)

to note that the possible overlapping of neighbouring satellite tracks is taken into account in this consideration. Additionally, data of different imaging geometries are not excluded, although a very diverse geometry will lead to poor results. Naturally, with the increase/decrease of the area of interest, more/less data become available, but an area of 10 × 10 km is a good and logical compromise for a flash-flood case study. It has to be also noted that data availability depends as well upon the acquisition strategy, the priority of acquisitions over the given location and the type of the observed area (urban, rural, special scientific interest etc.).

The specific area examined in Table 1 is of medium to high priority, on global scale. The scenario of combined ERS and Envisat (2002-to date) acquisitions does improve the chances of "capturing" the event, but not considerably. The next alternative is to also consider Wide Swath Mode (WSM) Envisat/ASAR data, giving a 400 km by 400 km image at the expense of spatial resolution, which is nominally in the order of 150 × 150 m. In this last scenario, the probability increases up to almost 30 %, especially for the period 2006–2010 (Table 1).

Of course, the chance of having a second timely acquisition, from the same swath and track, in order to follow the evolution of a particular flood phenomenon is even more limited. Thus, typically, for the mapping of the flooded areas, a change detection technique is applied, by using the "flood" SAR image and an identical SAR image under "normal" conditions and of the same season, if available (see Figs. 3, 4, 5).

Optical images and ancillary data can be later incorporated, after a specific case study has been selected, for further investigation, validation, land cover identification and damage assessment purposes (e.g. Tholey et al. 1997; Sarti et al. 2001; Yésou et al. 2003, 2007a, b). The contribution of Geographical Information Systems (GIS) in collecting, managing and presenting all primary and secondary (produced) information is in most cases of high value (e.g. Brivio et al. 2002; Irimescu et al. 2010).

2.3 Selection of Case Studies and Methodology

Case studies were selected on the basis of the temporal coincidence of the flood event and acquisition of SAR data, as well as taking into account the spatial extent and magnitude of the catastrophe. Cases with different SAR data acquisition time, with respect to the peak of the flood event, are chosen in order to demonstrate the dependence and importance of timely SAR acquisitions for obtaining high-quality results.

In this context, the examples presented thereafter in this study are based on two independent incidents from the 2006 floods in Greece and the Czech Republic. The former is a flash-flood case study, where the first available IM SAR data were acquired about 48 h after the peak of the flood. The latter is related to the extensive floods of spring 2006 in Central Europe and the IM SAR data where acquired several days after the peak of the flood event. The Czech Republic incident is used as a measure of comparison for the first case study.

For the delineation of flooded and flood-affected areas, Change Detection Analysis (CDA) was implemented. CDA encompasses a broad range of methods used to identify, describe and quantify differences between images of the same scene at different times. In this study, the False Colour Composition (FCC) was adopted and applied to SAR images. Typically, two images were used; one before and one during/after the flood. In each case study, the flood image was assigned to the red (R) channel and the "dry" image was assigned to both the green (G) and the blue (B) channel, in order to create an RGB colour composite.

With respect to this RGB image interpretation, unchanged or almost unchanged features appear as variations of the greyscale, whereas any change in the scene (expressed in a change of backscatter) from one acquisition to the other appears in colour so that:

1. Regions with significantly lower backscatter in the flood image appear in cyan, indicating possible flooded areas.
2. Regions with significantly higher backscatter in the flood image appear in red, indicating a possible increase in soil moisture.

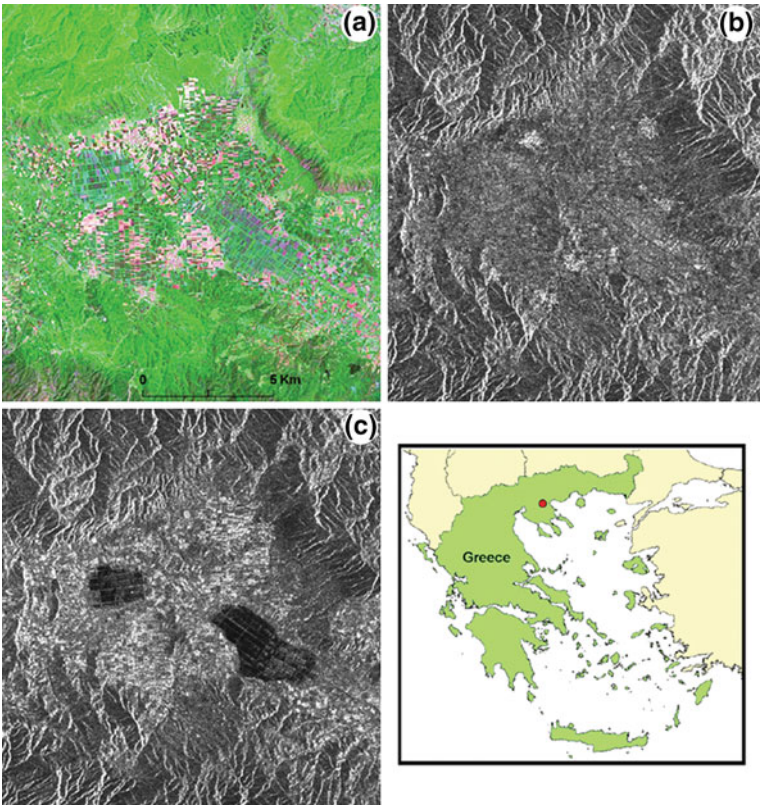

Fig. 2 Characteristic example of imaging the effects of a flash-flood by Envisat/ASAR data, about 48 h after the peak of the flood event; **a** Landsat/ETM + multispectral image (R/G/B: 3/2/1) of the study area, under normal conditions. **b** Envisat/ASAR image of the study area before the flood event. **c** Envisat/ASAR image after the flash-flood. Inundated terrain is shown in *black* (*low backscatter*), whereas surrounding areas with high moisture content are depicted in *white* (*high backscatter*)

3 The 2006 Floods in Northern Greece

Northern Greece suffered from disastrous floods in the beginning of October 2006. Fig. 2 present an example of Envisat/ASAR data, delineating the flash-flood in the prefecture of Thessaloniki (images of the catastrophe previously shown in Fig. 1). In this case, the morphology of the terrain favored the concentration of the remaining water in extended areas as shown in Fig. 2 and despite the fact that the SAR data were acquired almost 2 days after the major event, inundated areas were well delineated using change detection techniques (Fig. 3).

More specifically, in Fig. 3:

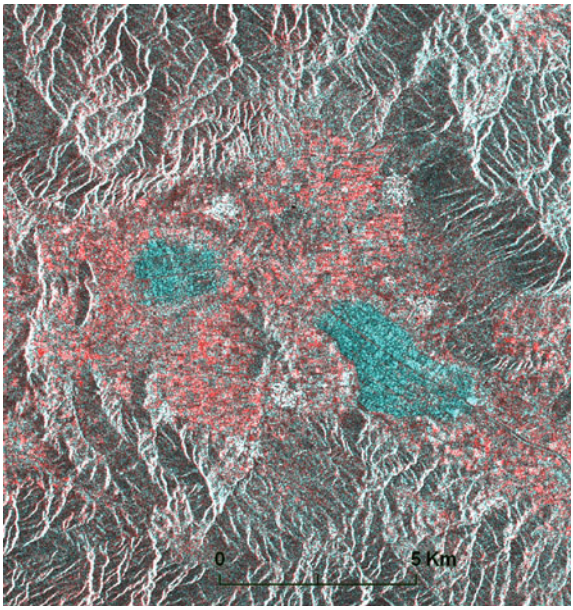

Fig. 3 Delineation of flooded areas by change detection techniques, in the post-crisis period (after 2 days) in the prefecture of Thessaloniki, using an ENVISAT/ASAR false color composite: R = 10/10/2006 (flood image), G = B=(5/10/2004 + 25/10/2005)/2 (average of two images during the same season, but under dry conditions)

a) Areas with little or no change ($R \approx G \approx B$) are depicted in shadings of the grey scale (white to black), the result thus being approximately equivalent with that of each image independently.
b) Flooded areas are presented in cyan, as their backscatter in the flood image is very low ($R \ll G$, $R \ll B$).
c) Wet areas (high moisture content, resulting in high backscatter in the flood image) are reddish ($R > G$, $R > B$).

On the contrary, for the same flood event and over the rest of the area covered by the same ASAR dataset (approx. 100 × 100 km), results fail to provide reliable information, concerning not only the magnitude, but even the occurrence of the catastrophe (Fig. 4). In this case, contrary to Fig. 3, just a few noteworthy patches of inundated area (circles) can be detected. Thus, the results are misleading, as one would conclude that the effect of the flash-flood in this area was not so strong; yet this was the one of the many areas within the same SAR image frame that were devastated by the flash-flood, with the water level reaching several meters. Validation with ground truth data for this flash-flood can be found in Vouvalidis et al. (2006) and Nikolaidou et al. (2010).

4 The 2006 floods in the Czech Republic

Large swathes of Czech Republic, Slovakia, Romania and the German Region of Saxony were flooded during spring 2006. In the Czech Republic, a state of emergency was declared for the whole area of the South Moravian department

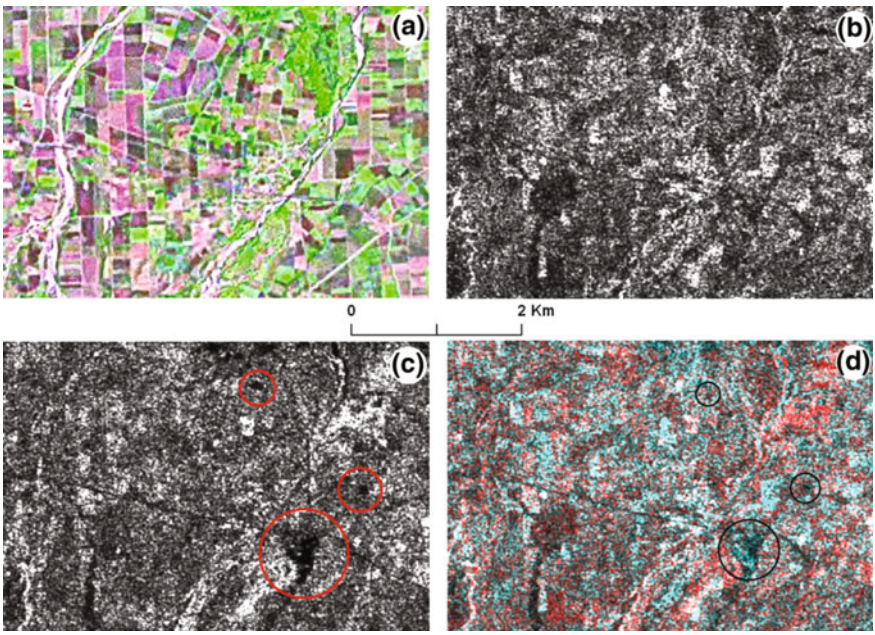

Fig. 4 Indicative extract from the broader area covered by the dataset of Fig. 3; **a** Landsat/ETM + multispectral image (R/G/B: 3/2/1), under normal conditions. **b** Envisat/ASAR image before the flood event. **c** Envisat/ASAR image after (48 h) the flash-flood. **d** False color image composition and interpretation of colors equivalent to Fig. 3 (Nikolaidou 2009; Nikolaidou et al. 2010)

and consequently came into force in parts of the following departments: South Czech, Middle Czech, Olomouc, Pardubice, Ústí and Zlín. Five towns were evacuated. Some 4,200 persons had to leave their homes. Five people were confirmed dead. Flood emergency situations were announced by half of the country's 14 regional authorities. Figure 5 presents the affected areas near Mělník, in the vicinity of the confluence of the Labe and Vltava rivers. The SAR data used were acquired several days after the peak of the flood event, when the water level had already been stabilized. The international charter for space and major disasters was activated (call ID: 117/118) for this flood event as well, but using WSM data.

5 Discussion and Conclusions

In this study, the availability of satellite SAR data with respect to (flash-)flood events was investigated on the basis of case studies from the Balkans and Eastern Europe. The purpose to demonstrate the need for timely SAR acquisitions, to evaluate the current probability of imaging a flash-flood event and to contribute to a better definition of data requirements for future SAR missions.

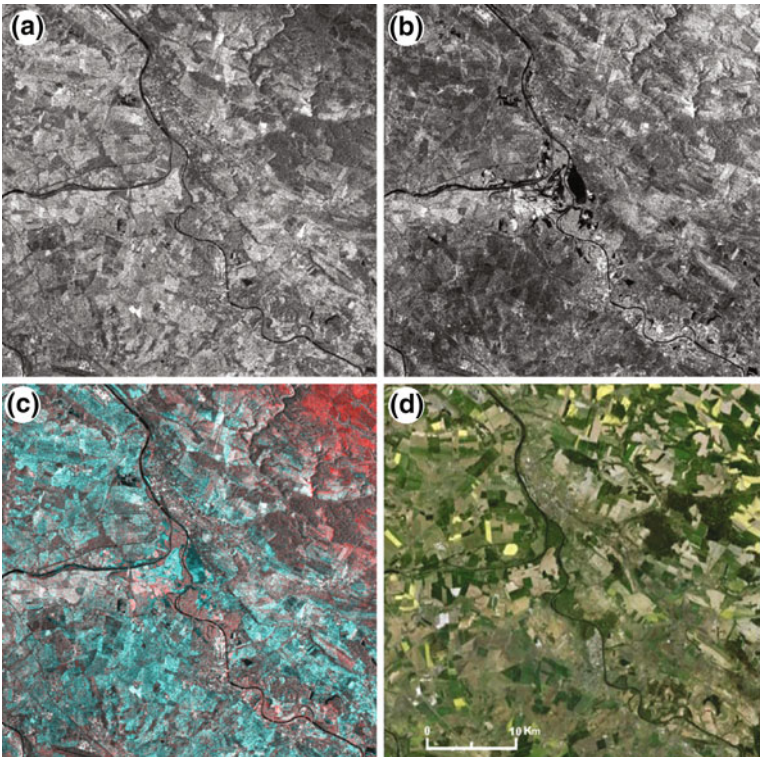

Fig. 5 Mělník area, 30 km north of Prague, Czech Republic. **a** ERS SAR image of march 3rd (before the flood). **b** ERS SAR image of April 6th (crisis). **c** false color composite: R = 06/04/2006 (flood image), G = B=03/03/2006 (dry conditions). Areas with higher probability of having been inundated are presented in cyan, whereas areas with exceptionally high moisture content appear reddish. **d** Google Earth™ image of the area

The results of Figs. 2 and 3 for the Thessaloniki flash-flood are of equivalent quality with the results obtained in the flood case study of the Czech Republic when the affected areas were well "visible" by the SAR instrument for several days (Fig. 5). Nevertheless, a typical flash-flood, 2 days after the peak of its occurrence, is far from this ideal case, as it was demonstrated in Fig. 4.

Thus, it is evident that more timely acquisitions (not existing for the Thessaloniki case whatsoever) bare the potential of producing significantly better results.

The experience gained after 20 years of systematic Earth Observation with SAR data, has well demonstrated the efficiency of these active instruments in imaging and monitoring flood events at various scales. The main issue that has not yet been resolved is related to the increase of SAR observations to a frequency that would allow, to record and ultimately to follow the evolution of random flash-flood phenomena. For that purpose, dense acquisitions (6–12 h) at high spatial resolution (20 m or better) would be necessary.

Although the EO capacity has considerably increased over the last two decades, at the moment, unless initiatives like the International Charter are activated, the chances of capturing a flash-flood event at its peak, with a high resolution SAR are quite low. In this direction, current and near-future SAR missions (e.g. TerraSAR-X, COSMO-SKyMed, Radarsat-2, Sentinel-1), are expected to substantially improve the efficiency, by which floods are monitored using both systematic and on-demand SAR data acquisitions. This will be achieved through their enhanced repeat cycle, spatial resolution, as well as polarimetric and interferometric capabilities.

However, until significant progress in the multi-temporal capabilities of high resolution satellite SAR systems is achieved, wide swath modes of medium–low resolution, like Envisat's ASAR/WSM, although not ideal for combining them with high-resolution optical data for damage assessment and management, will continue to have an important contribution to "capturing" random (flash-)flood events.

Acknowledgments This study is supported by ESA in the framework of a category-1 project (ID: 7529) and by the Aristotle University of Thessaloniki, Greece. John S. Latsis Public Benefit Foundation (http://www.latsis-foundation.org/en/1/homepage.html) is acknowledged for providing financial support, within its "Call for 2011 Research Projects", to extend this work on flood monitoring and management with EO data over more areas in Greece.

References

Badji M, Dautrebande S (1997) Characterization of flood inundated areas and delineation of poor drainage soil using ERS-1 SAR imagery. Hydrol Process 11:1441–1450

Barredo JI (2009) Normalized flood losses in Europe: 1970–2006. Nat Hazards Earth Syst Sci 9:97–104

Bell FG (1999) Geological Hazards. Their assessment, avoidance and mitigation. E and FN SPON, London

Brivio PA, Maggi M, Colombo R, Tomasoni R (2002) Integration of remote sensing data and GIS for accurate mapping of flooded area. Int J Remote Sens 23:429–441

European Union (2007) Directive 2007/60/EC of the European parliament and of the council of 23 Oct 2007 on the assessment and management of flood risks. Official J Eur Union L 288/27

Geudtner D, Winter R, Vachon PW (1996) Flood monitoring using ERS-1 SAR interferometry coherence maps. In: Proceedings of the IEEE international geoscience and remote sensing symposium, IGARSS 1996, 27–31 May 1996, Lincoln 2:966–968

Henry J-B, Chastanet P, Fellah K, Desnos Y-L (2007) Envisat multi-polarized ASAR data for flood mapping. Int J Remote Sens 27:1921–1929

Irimescu A, Craciunescu V, Stancalie G, Nertan A (2010) Remote sensing and GIS techniques for flood monitoring and damage assessment. study case in Romania. BALWOIS 2010, Ohrid, FYROM, 25–29 May 2010, http://balwois.com/balwois/administration/full_paper/ffp-1475.pdf. Accessed 24 June 2011

Li J, Yésou H, Huang S, Li J, Li X, Xin J, Wang X, Andreoli R (2005) ENVISAT ASAR medium and high resolution images for near real time flood monitoring in China during the 2005 flood season. In: Proceedings. 2005 dragon symposium, mid-term results, Santorini, Greece 27 June–1 July 2005 (ESA SP-611)

Nikolaidou M (2009) Utilization and contribution of remote sensing and geographical information systems (GIS) technology to the detection of flooded areas southern of lake Volvi: an environmental approach, Master thesis, school of geology, aristotle university of Thessaloniki (In Greek, with English abstract)

Nikolaidou M, Mouratidis A, Oikonomidis D, Astaras T (2010) Mapping the catastrophic 2006 flood events in Thessaloniki and Halkidiki with Envsat/ASAR data. In: Proceedings of the 9th Panhellenic Geographical Congress, Athens, 4–6 Nov 2010, 163–171 (In Greek, with English abstract)

Sarti F (2004) Potentiels, limitations et évolutions de la télédétection optique-radar et de l'interférométrie radar pour le suivi des changements et des déformations de surface: applications scientifiques et applications pré-opérationnelles de gestion des risques naturels. Thèse, Univ. Paul Sabatier Toulouse

Sarti F, Inglada J, Landry R, Pultz T (2001) Risk management using remote sensing data moving from scientific to operational applications. In: Proceedings of X SBSR, April 23–27, 2001, Brasil, p 11

Tholey N, Clandillon S, De Fraipont P (1997) The contribution of spaceborne SAR and optical data in monitoring flood events: examples in Northern and Southern France. Hydrol Process 11:1409–1413

Vouvalidis K, Albanakis K, Mourtzios P, Nikolaidou M, Papadopoulou S, Stavrianou K (2006) The flood event of the Melissourgos village, Thessaloniki Perfecture, October 2006. A geomorphological approach, Bull Geological Society of Greece, 39:86–95

Yésou H, Chastanet P, Fellah K, Jeanblanc Y, De Fraipont P, Bequignon J (2000) Contribution of ERS SAR images and ERS coherence data to a flood system on the Meuse basin—France. In: Proceedings of ERS-ENVISAT Symposium "looking at our Earth for the new millennium", Gothenburg, 16–20 Oct (ESA SP-461)

Yésou H, Clandillon S, Allenbach B, Bestault C, De Fraipont P, Inglada J, Favard JC (2003) A constellation of advantages with SPOT SWIR and VHR SPOT 5 data for flood extent mapping during the september 2002 Gard event (France). In: Proceedings of the IEEE international geoscience and remote sensing symposium, IGARSS '03, 21–25 July 2003, Toulouse 1:567–569

Yésou H, Allenbach B, Andreoli R, Battiston S, Bestault C, Clandillon S, Fellah, K, Meyer, C, Scius H, Tholey N, De Fraipont P (2007a) Synergy of high resolution SAR and optical data for flood monitoring: the 2005–2006 central European gained experience. Envisat symposium 2007, Montreux (ESA SP 636)

Yésou H, Fellah K, Tholey N, Clandillon S, Batiston S, Allenbach B, Meyer C, Bestault C, De Fraipont P (2007b) large plain flood mapping and monitoring based on EO data: five years of improvements from ERS SAR to ENVISAT MERIS ASAR synergy. In :Proceedings of the IEEE international geoscience and remote sensing symposium, IGARSS 2007, 23–28 July 2007, Barcelona, 1155–1158

Ozone Seasonal Variation with Ground-Based and Satellite Equipments at Évora Observatory: Portugal During 2007–2010

Ana F. Domingues, Daniele Bortoli, Ana Maria Silva, Manuel Antón, Maria João Costa and Pavan Kulkarni

Abstract The present study deals with the retrieval and analysis of O_3 total columns over the Évora Observatory (South of Portugal) for the period 2007–2010. The data-set presented in this paper is derived from spectral measurements carried out with the UV–Vis. Spectrometer for Atmospheric Tracers Measurements—SPATRAM, installed at the Observatory of the Geophysics Centre of Évora (CGE) –Portugal (38.5°N; 7.9 °W, 300 m asl). The results obtained applying Differential Optical Absorption Spectroscopy (DOAS) methodology to the SPATRAM measurements of zenith sky scattered radiation are presented in terms of seasonal variations of O_3. The O_3 retrieved with SPATRAM instrument confirms the typical seasonal cycle for middle latitudes reaching the maximum during the spring and the minimum during the autumn. The ground-based results obtained for O_3 column are also compared with data from Ozone Monitoring Instrument (OMI) instrument onboard Aura Satellite.

A. F. Domingues (✉) · D. Bortoli · A. M. Silva · M. Antón · M. J. Costa · P. Kulkarni
Geophysics Centre of Évora, University of Évora, Évora, Portugal
e-mail: ana.filipa.domingues@gmail.com

A. M. Silva · M. J. Costa
Department of Physics, University of Évora, Évora, Portugal

M. Antón
Department of Physics, University of Extremadura, Badajoz, Spain

D. Bortoli
Institute of Atmospheric Sciences and Climate, Bologna, Italy

J. M. Krisp et al. (eds.), *Earth Observation of Global Changes (EOGC)*,
Lecture Notes in Geoinformation and Cartography, DOI: 10.1007/978-3-642-32714-8_9,

1 Introduction

Ozone (O_3) is a key compound in the chemistry of the atmosphere. This trace gas represents only about 0.0012 % of the total atmospheric composition but it is involved in several atmospheric phenomena (Antón et al. 2011; Bortoli et al. 2009a; Bortoli et al. 2009b). For example, ozone plays a relevant role in controlling the chemical composition of the atmosphere. The photolysis of ozone near 300 nm followed by reaction with water leads to production of OH. OH radicals are sometimes called the "cleansing agent" of the atmosphere and therefore a variety of atmospheric species like CO, CH_4, NO_2 and halocarbons are removed from the atmosphere by reaction with it. Because ozone absorbs thermal radiation it also plays an important role in the energy budget of the troposphere (Platt and Stutz 2008).

While the tropospheric ozone is known as the "bad ozone" for it is a secondary pollutant and its capacity to alter the global climate system, the stratospheric ozone is known for being the "good ozone". The motives are well known. In the troposphere O_3 is harmful to humans and plants and it is a component of smog and an important greenhouse gas. The stratospheric ozone layer, containing 90 % of the atmospheric ozone, is responsible for the absorption of ultraviolet (UV) radiation, particularly UV-B (320–280 nm) and UV-C above 220 nm (Staehelin et al. 2001), harmful for animals and plants.

Ozone is formed by two different mechanisms in the stratosphere and troposphere. In the stratosphere O_2 molecules are split by short-wave UV radiation into O atoms which combine with O_2 to form O_3. This process is the kernel of the Chapman Cycle *(*Platt and Stutz 2008). On the other hand the tropospheric ozone is formed by reactions involving NO_x ($NO + NO_2$) and Volatile Organic Compounds (VOC).

In the troposphere, NO_2 is decomposed by solar radiation as shown in Eq. 1

$$NO_2 + h\nu \longrightarrow NO + O(^3P) \tag{1}$$

where hν is the energy of solar radiation. Then other reaction (Eq. 2) follows Eq. 1. The O atom combines with O_2 in presence of other atmospheric molecule M.

$$O(^3P) + O_2 + M \longrightarrow O_3 + M \tag{2}$$

In the end O_3 is oxidised by NO leading to NO_2 formation (Eq. 3)

$$O_3 + NO \longrightarrow NO_2 + O_2 \tag{3}$$

The chemical conversion of NO to NO_2 is the fundamental factor in the tropospheric O_3 formation. If this conversion occurs without the ozone but with other reaction cycles of hydroxyl (HO_x), NO_x and peroxy radicals there isn't a net formation of ozone. It is important to note the contribution of anthropogenic sources of NO_x in the atmosphere such as combustion of fossil fuel (power stations, industry, and automobiles), forest fires and artificial fertilization. All these sources enhance

the presence of NO_x in the atmosphere that contributes to the increase in the O_3 concentration (Platt and Stutz 2008; Logan 1985).

Increases in ozone are a concern to the community in part because of the adverse effects of the gas on vegetation and human health, but also because the changes in ozone could affect the concentration of OH which in turn could influence the concentration of the other trace gases removed from the atmosphere by reactions with OH.

Concerning the stratosphere S. Chapman proposed in the 1920 s the following mechanism to the stratospheric ozone formation which starts with the photolysis of oxygen molecules (Eq. 4) for radiation with wavelengths below 242 nm.

$$O_2 + h\nu \xrightarrow{(\lambda < 242\text{nm})} O(^3P) + O(^3P) \tag{4}$$

After that reaction the oxygen atoms (O (^{3}P)) can: (a) combine with an oxygen molecule to form ozone with the collision with a third body that can be N_2 or O_2 (Eq. 5); (b) can react with an existing ozone molecule (Eq. 6) or (c) combine with other oxygen atoms to form O_2 (Eq. 7).

$$O(^3P) + O_2 + M \longrightarrow O_3 + M \tag{5}$$

$$O(^3P) + O_3 \longrightarrow O_2 + O_2 \tag{6}$$

$$O(^3P) + O(^3P) + M \longrightarrow O_2 + M \tag{7}$$

The photolysis of O_3, as described in Eq. 8, also provides the O atoms at a much higher rate than Eq. 1.

$$O_3 + h\nu \xrightarrow{\lambda(612nm)} 612\text{nm})O(^3P) + O_2 \tag{8}$$

The above set of reactions explains the steady state of O_3 concentration in the atmosphere in which the production of O atoms is in balance with their destruction.

During the 1960s, studies revealed that some other chemical reactions were taking place in the atmosphere beyond the "Chapman Reactions". In fact there are many other trace gas cycles that affect the O_3 concentrations in atmosphere, like ClO, BrO, NO_2, HO_2 and halocarbon species as CH_3Cl, $CFCl_3$. The monitoring of ozone levels gained more importance since the discovering of the depletion in ozone layer—the so called "Ozone Hole" over Antarctica. Nowadays, the interest in studying ozone and other gases directly or indirectly involved in the ozone chemical cycles is one of the main topics of the scientific community. Atmospheric compounds, such as NO_2 and BrO, are monitored with ground based instruments as well as with satellite and airborne equipments. Among the different data analysis techniques, the Differential Optical Absorption Spectroscopy (DOAS) is recognized as a powerful tool for the retrieval of the columnar abundances of ozone and other compounds playing a key role in the ozone chemical cycles.

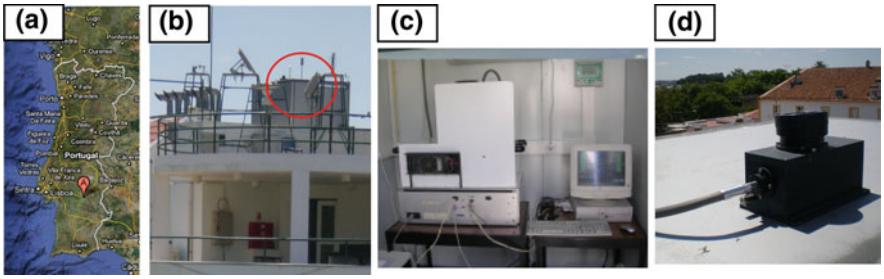

Fig. 1 The location of the Observatory (**b**) of the Geophysics Centre of Évora- CGE in Évora (38.5°N; 7.9 °W, 300 m asl), Portugal (**a**) (adapted from http://maps.google.com/). The SPATRAM (**c**) instrument installed at the Observatory of the CGE inside a container (red circle) and the VErtical LOoking Device- VELOD (**d**), installed on the top of the container, which connects to the Optic Fiber Input device of SPATRAM

DOAS uses the interaction of radiation with matter to determine the presence and abundance of molecules or atoms in a sample and it is based on the Lambert–Beer extinction law. The description of this spectroscopic technique can be found in literature (Platt and Stutz 2008).

The scope of this work is the retrieval of O_3 total columns during 2007–2010 from spectral measurements carried out with the UV–Vis. Spectrometer for Atmospheric Tracers Measurements (SPATRAM) installed at the Observatory of the Geophysics Centre of Évora (CGE)-Portugal. In the next sections the description of the SPATRAM instrument and specifics of the data processing methodology used in the retrieval and analysis of O_3 total columns over the Évora Observatory are presented. The results are also discussed and compared with the Ozone Monitoring Instrument (OMI) data.

2 Instrumental Setup and Method

2.1 SPectrometer for Atmospheric TRAcers Measurements

The multipurpose UV–Vis. SPATRAM (Bortoli et al. 2010) (Fig. 1c) is a scanning spectrometer and it measures the zenith scattered radiation in the 250–900 nm spectral range. The main products are the daily total column and the vertical profiles of NO_2 and O_3. The monochromator equipping SPATRAM allows for the decomposition of light in its wavelengths using a grating by Jobin–Yvon of 1200 grooves/mm with a typical dispersion of 2.4 nm/mm at 300 nm and spectral resolution ranging from of 0.05–0.2 nm depending on the spectral interval analyzed.

The equipment (Fig. 1c) installed at Geophysics Centre Observatory in Évora (Fig. 1b) allows for multiple input of the radiation: (1) from the Optic Tower Input (Fig. 2) which is the primary input that is composed by a pair of flat and spherical mirrors that focus the light beam on the entrance slit; (2) from the two lateral

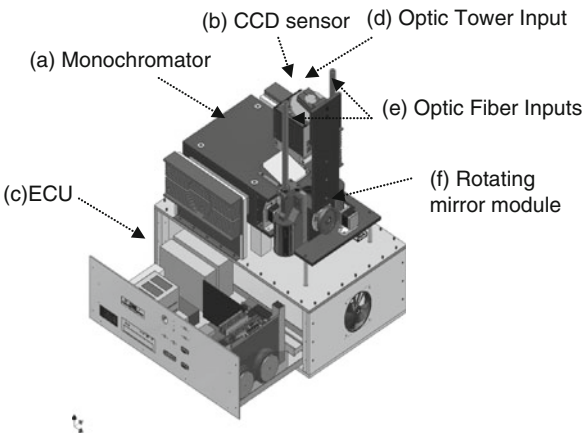

Fig. 2 Representation of the main modules of the SPATRAM **a** monochromator, **b** ventilated box containing the CCD sensor, **c** Electronic Control Unit, **d** optic tower input, **e** optic fiber inputs, **f** rotating mirrors (Adapted from Bortoli 2009)

inputs called Optic Fiber Inputs (Fig. 2), where the signal is carried to the entrance slit with an optical fiber connected to a very simple optical system, and (3) an additional input for spectral and radiometric calibration. In the optic fiber input the radiation is collected by the VELOD (VErtical LOoking Device) (Fig. 1c). The light beam reaches the monochromator thanks to the title mirror in the Rotating Mirror Module (Fig. 2). This module allows for choosing between the primary input (pointing to the vertical), the optical fiber ones and the additional input for spectral or radiometric calibration. Once the light beam reaches the monochromator is decomposed in their wavelengths thanks to the holographic grating. The latter rotates by means of a stepper motor attached to the grating that allows for the analysis of the whole spectral interval of about 60 nm windows. The radiation is finally collected by a mirror that sends it to the CCD sensor. The CCD sensor is composed of 1024 $\times$ 254 pixels over the length of 1 inch and each pixel has the dimension of 24 m, giving a full dimension of 25.4 $\times$ 6.6 mm.

The SPATRAM is handled by a software tool (DAS—Data Acquisition System) that was developed in order to manage all the spectrometer devices and for automatic schedule measurements in automatic mode.

The Electronic Control Unit (ECU) of the instrument composed by all the power sources, CCD camera drivers, stepper motors and an industrial mono-board CPU provides also the storage of the measured spectral data as well as the preprocessing of the data and of their first analysis. DOAS methodology is applied to the spectral data measured with SPATRAM.

The output of DOAS algorithms is the Slant Column Density (SCD) which is defined as the integral of the number density along the path of measurement in the atmosphere. The unit of SCD used in this work is molecules per cm^2. An important step in the interpretation of DOAS observations is the conversion of SCD in Vertical Column Densities (VCD) using calculated Air Mass Factors (AMF). The AMF is obtained using a Radiative Transfer Model (RTM) (Platt and Stutz 2008; Rozanov et Rozanov 2010). In this particular case the AMF calculation is performed with the Atmospheric Model for Enhancement Factor Computation (AMEFCO) (Petritoli

et al. 2002). This RTM is based on the Intensity Weighted Optical Path (IWOP) approach considering a single scattering diffusion process and the a priori assumption of the vertical ozone profile.

2.2 Ozone Monitoring Instrument

OMI onboard the National Aeronautics and Space Administration's Earth (NASA) Observing System (EOS) Aura satellite, on flight from 15 July 2004, is a nadir viewing imaging spectrograph that measures the solar radiation backscattered by the Earth's atmosphere and surface over the entire wavelength range from 270 to 500 nm with a spectral resolution of about 0.5 nm and with a very high spatial resolution (13 × 24 km) and daily global coverage. Trace gases derived from OMI instrument include O_3, NO_2, SO_2, HCHO, BrO and OClO (Levelt et al. 2006). The OMI total ozone column data used in this work were obtained with OMI-TOMS algorithm based on the TOMS V8 algorithm. This algorithm uses measurements at 4 discrete 1 nm wide wavelength bands centered at 313, 318, 331 and 360 nm (Kroon et al. 2008).

3 Data Analysis and Results

In this section the diurnal and seasonal evolution of O_3 VCD values, for the period comprised between 1st January of 2007 and 6th July of 2010 obtained at Évora-Portugal with the SPATRAM instrument, are presented and discussed. Comparisons of these ground-based measurements with satellite retrievals of O_3 VCD values derived from OMI instrument are also shown and examined.

3.1 Daily Variation of Ozone

To obtain the O_3 SCD the DOAS algorithms are applied in the 320–340 nm spectral range. The data obtained with SPATRAM instrument comprises all the solar zenith angles (SZAs) between the highest daily solar elevation (minimum SZA) and approximately 93° of SZA. Due to the wavelength dependency of the AMF and since the lowest error associated to the measurements is obtained for the higher values of SZA, the O_3 VCD are interpolated for the SZA of 87°. In order to investigate the typical diurnal variation of O_3, the SCD of this gas is plotted versus the SZA during one day, as shown in Fig. 3.

The O_3 SCD values are very similar during the morning and afternoon. It is evident, by the analysis of Fig. 3, that for ozone the differences between AM and PM values are almost absent. In fact, the diurnal photochemical activity of the

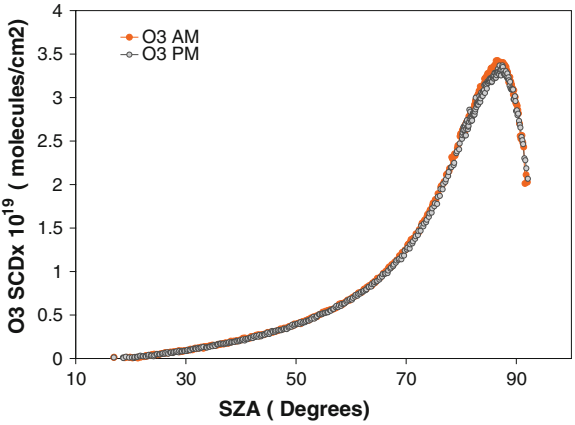

Fig. 3 Time series of the O_3 SCD obtained with the SPATRAM equipment installed at Évora Observatory for the 30th May 2010

stratospheric ozone is not as strong as, for example, the NO_2 diurnal photochemical activity, so the PM data series present approximately the same values as the AM ones. The same diurnal behavior is registered on the other days of the study period.

3.2 Seasonal Variation of Ozone

In Fig. 4 the O_3 VCD time series are plotted versus the time of the year in order to examine the seasonal behavior of this gas. In addition the OMI O_3 values are compared with the O_3 VCD values derived from SPATRAM instrument for the same period. The results obtained using the SPATRAM instrument corroborate the well-known fact that the maximum of O_3 VCD values in mid-latitudes are found in spring and the minimum values in fall. This O_3 cycle is seen in all years with the maximum of monthly mean values (± one standard deviation) registered in May 2007 (373 ± 26) DU, April 2008 (336 ± 6) DU, May 2009 (353 ± 9) DU and April 2010 (399 ± 11) DU and the minimum registered in October 2007 (293 ± 12) DU, January 2008 (242 ± 18) DU, September 2009 (304 ± 11) DU and January 2010 (302 ± 38) DU. There were no data available during the time period between 16th October and 15th December of 2007 due to maintenance of the spectrometer. In summer periods the O_3VCD values have tendency to decrease as autumn approaches, but in 2008 this reduction is not so pronounced as in 2007, as it can be seen in Fig. 4.

The seasonal behavior of O_3 registered at Évora′s Observatory is consistent with the literature for the northern mid-latitudes (Antón et al. 2011; Schmalwieser et al. 2003; Chen and Nunez 1998). Although the explanation of total ozone tendency has still not been quantified, the likely contribution processes have been identified. In the middle-latitudes and specifically over the Iberian Peninsula the total ozone column presents a strong seasonal variability mainly caused by

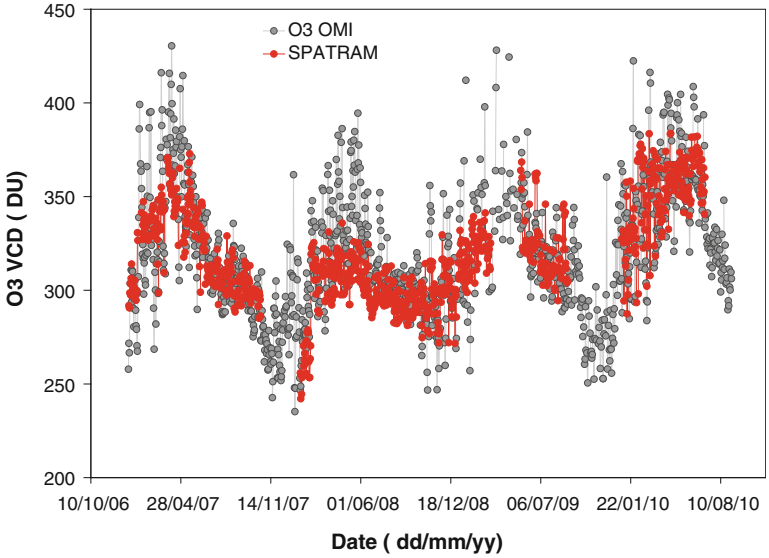

Fig. 4 Time series of the O_3 VCD obtained with the SPATRAM equipment installed at Évora Observatory for the SZA of 87°, during 2007–2010, and the O_3 data from the OMI instrument aboard the EOS—Aura satellite

dynamical factors such as Dobson-Brewer circulation (Antón et al. 2008, 2009b, Staehelin et al. 2001, Weber et al. 2011).

The comparison between the SPATRAM and the OMI data describes the same seasonal behavior. However, the values of O_3 VCD are normally lower than the ones derived from the OMI satellite instrument. The mean deviation, of the comparison, calculated using the relative error expression, is of about 7 % with higher values during the spring seasons. The main reason for the differences found between the SPATRAM and OMI instruments could be due to the fact that the OMI data presented in Fig. 1, are the O_3 total column values corresponding to the daily overpass of the AURA satellite over a pixel of about 300 Km^2 containing the Évora station while the SPATRAM Field Of View (FOV), determined by the monochromator f number (f# = 5), is of about 1×10^{-5} sr.

In Fig. 5 the scatter plot of the SPATRAM and OMI dataset is shown. In this plot only the data from the OMI time series obtained for a distance lower than 50 km from the Évora station are taken into account and are obtained from the daily overpass file analyzing the geo-references of each satellite ground pixel. The SPATRAM data and the "filtered" OMI dataset are in good agreement as evidenced from the correlation coefficient obtained (R = 0.83). Considering the full OMI dataset the R decrease to a value of 0.7.

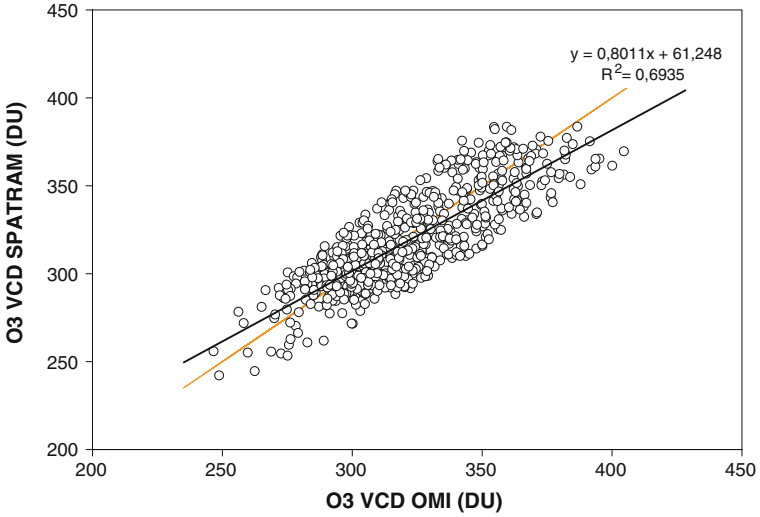

Fig. 5 Scatter plot of the O_3 data from the OMI instrument aboard the EOS—Aura satellite versus O_3 SPATRAM data retrieved at Évora Observatory for the SZA of 87°, during 2007–2010 period including the regression line (*black line*) and the unit slope (*yellow line*)

4 Conclusions

The main purpose of this study is the use of the SPATRAM and DOAS methodology for the retrieval of ozone column content at Évora Station from 1st January of 2007 to 6th July of 2010. The comparison of the ground- based SPATRAM derived O_3 VCD data with the correspondent satellite (OMI) O_3 measurements was also envisaged. The daily variation of the O_3 data derived from the SPATRAM reveals that a) the O_3 concentration during the day is approximately uniform and b) the O_3 seasonal trend shows a maximum in spring months and a minimum in autumn, in the North Hemisphere as expected. The comparison of the SPATRAM data—O_3 VCD- with the satellite data (OMI instruments) highlights that the SPATRAM data presents similar patterns as the satellite measurements. The O_3 VCD deviation is about 7 %.

Acknowledgments The first author is financially supported by the Portuguese FCT grant SFRH/BD/44920/2008. The author acknowledges NASA team for the accomplishments of all satellite missions and to all scientists that participate in the acquirement and provision of the environmental data. This research was partially funded by the FCT project PTDC/AAC-CLI/114031/2009.

References

Antón M, Bortoli D, Costa MJ, Kulkarni PS, Domingues AF, Barriopedro D, Serrano A, Silva AM (2011) Temporal and spatial variabilities of total ozone column over Portugal. Remote Sens Environ 115:855–863

Antón M, Bortoli D, Vilaplana JM, Kroon M, Silva AM, Domingues AF, Serrano A, Cancillo M, De la Morena B (2009a). Comparison of OMI-DOAS satellite total ozone column observations with ground-based data from direct and diffuse solar irradiance in the Southwest Iberian Peninsula. In: Proceedings of atmospheric science conference, Barcelona, pp 144

Antón M, López M, Vilaplana JM, Kronn M, Bañon M, Serrano A (2009b) Validation of OMI-TOMS and OMI-DOAS total ozone column using five brewer spectroradiometers at the Iberian Peninsula. J Geophys Res 114:D14302

Anton M, Serrano A, Cancillo ML, Garcia JA (2008) Total ozone and solar erythemal irradiance in the Southwestern Spain: Day-to-day variability and extreme episodes. Geophys Res Lett 35:L20804

Bortoli D, Silva AM, Costa MJ, Domingues AF, Giovanelli G (2009) Monitoring of atmospheric ozone and nitrogen dioxide over the south of Portugal by ground-based and satellite observations. Opt Express 17(15):12944–12959

Bortoli D, Silva AM, Giovanelli G (2010) A new multipurpose UV-Vis spectrometer for air quality monitoring and climatic studies. Int J Remote Sens 31(3):705–725

Chen D, Nunez M (1998) Temporal and spatial variability of total ozone in southwest Sweden revealed by two ground-based instruments. Int J Climatol 18:1237–1246

Domingues AF, Bortoli D, Antón M, Silva AM. (2009) Ozone, nitrogen dioxide and BrO columns over Évora- Portugal during 2007–2008. In: Richard HPi, Klaus S, Adolfo C, Evgueni IK, Christopher JM (eds) Proceedings of SPIE Europe remote sensing of clouds and the atmosphere *XIV,* SPIE, Vol. 7475, pp 74751L

Kroon M, Veefkind JP, Sneep M, Mcpeters RD, Bhartia PK, Levelt PF (2008) Comparing OMI-TOMS and OMI-DOAS total ozone column data. J Geophys Res 113:D16S28

Levelt PF, Van den oord G, Dobber MR, Mälkki A, Visser H, Vries J, Stammes P, Lundell JOV, Saari H (2006) The Ozone Monitoring Instrument. IEEE Trans Geosci Remote Sens 44(5):1093–1101

Logan J (1985) Tropospheric ozone: seasonal behaviour, trends and anthropogenic influence. J Geophys Res 90(D6):10463–10482

Petritoli A, Giovanelli G, Ravegnani F, Bortoli D, Kostadinov I, Oulanovsky A (2002) Off-axis measurements of atmospheric trace gases from an airborne UV-Vis spectroradiometer. Appl Opt: Lasers, Photonics Environ Opt 41(27):5593–5599

Platt U, Stutz J (2008) Differential optical absorption spectroscopy principles and applications. Springer, Berlin, pp 65–75 (135–158)

Rozanov VV, Rozanov AV (2010) Differential optical absorption spectroscopy (DOAS) and air mass factor concept for a multiply scattering vertically inhomogeneous medium: theoretical consideration. Atmospheric Measurements Techniques Discussions 3:697–784

Schmalwieser AW, Schauberger G, Janouch M (2003) Temporal and spatial variability of total ozone content over Central Europe: analysis in respect to the biological effect on plants. Agric For Meteorol 120:9–26

Staehelin J, Harris NRP, Appenzeller C, Eberhard J (2001) Ozone trends: a review. Rev Geophys 39(2):231–290

Weber M, Dikty S, Burrows JP, Garny H, Dameris M, Kubin A, Abalichin J, Langematz U (2011) The Brewer-Dobson circulation and total ozone from seasonal to decadal time scales. Atmos Chem Phys 11:11221–11235

Integration of InSAR and GNSS Observations for the Determination of Atmospheric Water Vapour

Fadwa Alshawaf, Thomas Fuhrmann, Bernhard Heck, Stefan Hinz, Andreas Knöpfler, Xiaoguang Luo, Michael Mayer, Andreas Schenk, Antje Thiele and Malte Westerhaus

Abstract High spatially and temporally variable atmospheric water vapour causes an unknown delay in microwave signals transmitted by space-borne sensors. This delay is considered as a major limitation in Interferometric Synthetic Aperture Radar (InSAR) applications as well as high-precision applications of Global Navigation Satellite Systems (GNSS). On the other hand, the delay could be quantified to derive atmospheric parameters such as water vapour. Temporal variability of water vapour is well estimated from ongoing GNSS measurements, while InSAR provides information about the spatial variations of water vapour. This project aims at assimilating InSAR phase observations and spatially-sparse GNSS measurements for the determination of atmospheric water vapour. In this contribution GNSS-based water vapour calculations and assessment of different strategies are presented. Work in progress is also reported including some preliminary results.

1 Introduction

Atmospheric water vapour is one of the most important factors in weather and climate studies. Its significance arises from the fact that it is a primary contributor

F. Alshawaf (✉) · S. Hinz · A. Thiele
Institute of Photogrammetry and Remote Sensing (IPF),
Karlsruhe Institute of Technology (KIT), Karlsruhe, Germany
e-mail: fadwa.alshawaf@kit.edu

F. Alshawaf · T. Fuhrmann · B. Heck · A. Knöpfler · X. Luo ·
M. Mayer · A. Schenk · M. Westerhaus
Geodetic Institute (GIK), Karlsruhe Institute of Technology (KIT),
Karlsruhe, Germany

J. M. Krisp et al. (eds.), *Earth Observation of Global Changes (EOGC)*,
Lecture Notes in Geoinformation and Cartography, DOI: 10.1007/978-3-642-32714-8_10,

to greenhouse effects. Greenhouse gases greatly influence the temperature average of the Earth's surface. Physorg (2006) observed that a 1 % increase of the water vapour content increases the surface temperature average by more than 4°C. Water vapour is a meteorological parameter that is characterized by high temporal and spatial fluctuations; therefore, its content should be continuously determined. Conventional meteorological devices such as radiosondes and radiometers are employed for measuring water vapour content. Radiosondes provide measurements at a fine vertical resolution but they are limited in observing the temporal and horizontal variations due to high costs (Bevis et al. 1992). Radiometers do not measure short-scale spatial variations of water vapour and are more suitable for use over oceans (Bevis et al. 1992).

We aim at analyzing atmospheric effects in the observations from two satellite systems, namely Global Navigation Satellite Systems (GNSS) and Interferometric Synthetic Aperture Radar (InSAR). The main focus is the Earth's neutral atmosphere (the neutrosphere) where water vapour is allocated. A key property of GNSS is that they provide measurements at a high temporal resolution which is required for observing temporal variations of the neutrosphere. Spatial variations of the neutrosphere are analyzed using spatially highly-resolved InSAR observations. Neutrospheric delay is split into a dry component and a wet component (Hopfield 1969). It is also common to split this delay into a hydrostatic and a non-hydrostatic part. The dry delay is caused by the dry gases while the wet is caused by the water vapour.

1.1 Previous Work

Specific focus of our earlier work was put on the evaluation of GPS measurements for high-precision positioning including precise modelling of the dry and the wet components of the neutrospheric delay (Mayer 2006). The dry component is simply calculated from an a priori empirical model based on air pressure and temperature (Saastamoinen 1973). The wet component, however, is highly variable in time and space since it is induced by water vapour. The wet delay is divided azimuthally into isotropic and anisotropic parts. Under the assumption of azimuthally isotropic neutrosphere, the isotropic part is determined from an empirical model added with the estimated site-specific neutrospheric parameter. The anisotropic part of the wet delay can be extracted from the residuals (after least-squares adjustment) of GNSS phase observations (Luo et al. 2007). Further studies were carried out for integrated perceptible water vapour (IPWV) determination using the strategy of Precise Point Positioning (PPP) based on mitigating site-specific errors such as multipath effects and antenna phase centre variations (Fuhrmann et al. 2010).

On the other hand, InSAR has been exploited in the past 20 years to derive high-resolution topographic maps (Zebker and Goldstein 1986) and for the determination of the Earth's crustal deformation (Massonnet et al. 1993). One of

the major error sources of repeat-pass InSAR is due to the time delay of the phase signal when traversing the Earth's atmosphere. Many researches have been carried out for the purpose of eliminating or at least mitigating the atmospheric distortion in InSAR observations (e.g., Onn 2006; Li et al. 2006; Knospe and Jónsson 2007; Meyer et al. 2008). GPS has been used to improve the performance of InSAR by reducing the neutrospheric delay (Van der Hoeven et al. 2002; Rommen et al. 2009). In the context of water vapour analysis, a main advantage of InSAR is the high spatial resolution (e.g., 20 m for ENVISAT data). This is very important for modelling the spatial variations of water vapour. The usage of high spatially resolved water vapour estimations based on InSAR to improve numerical weather models is under research (Pierdicca et al. 2009).

1.2 Objectives and Outline

The objective within this work is to investigate the potential of integrating InSAR and GNSS phase observations for atmospheric studies. GNSS enable highly accurate calculations of the neutrospheric delay at high temporal resolution without further costs. InSAR measurements, on the other hand, have high spatial resolution over wide areas (e.g., 100 km) which is required for observing spatial variations of the neutrospheric delay. The combination of GNSS and InSAR is expected to provide a high benefit for reconstructing highly-resolved water vapour fields which is a key requirement for climate studies as well as satellite-based applications (e.g., GNSS-based high-precision positioning and surface displacement detection using InSAR).

In this paper, a basic concept on the integration of InSAR and GNSS measurements for water vapour mapping is introduced. In the next section, the case study and the data set are described. The main concept of InSAR and GNSS combination is presented in Sect. 3. Fundamentals of atmospheric phase signal in InSAR are presented in Sect. 4. The calculation of neutrospheric zenith total delay (ZTD) using GNSS is described in Sect. 5. A conclusion and outlook of further work are presented at the end of the paper.

2 Case Study

Our focus in this study is the estimation of water vapour maps by a proper integration of both InSAR and GNSS measurements. GNSS and SAR observations are collected within the Upper Rhine Graben (URG) area in Germany and France. This region (Fig. 1) is well covered by the homogenously distributed permanent sites of the GNSS Upper Rhine Network (GURN) (Mayer et al. 2009). The tectonic surface displacement rate in there is very small (Rózsa et al. 2005), which

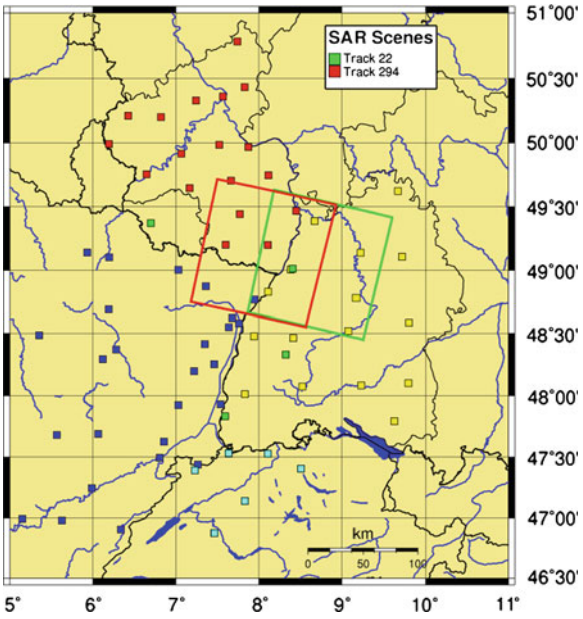

Fig. 1 URG region, the location of GURN sites is shown by the *little squares*. The *green* and *red frames* show the location of SAR footprints within URG

justifies the assumption that its contribution to the interferometric phase is minimal (see Sect. 4).

GNSS measurements are provided from the sites of GURN with a temporal resolution of 30 s. Many sites have data profiles longer than 8 years. Interferograms are formed from SAR images, kindly delivered by European Space Agency (ESA), from both ENVISAT and ERS-1/2. The SAR image covers the area shown either by the green or the red square in Fig. 1. ENVISAT scenes are acquired during descending passes (tracks 22 and 294, 100 km coverage, 20 m resolution, and 35 days repeat cycle) in the period 2003–2009. Figure 2 exhibits the available SAR images of both tracks and the corresponding acquisition time and perpendicular baseline.

Besides ENVISAT data, six ERS-1/2 Tandem pairs over the year 1996 are processed. Temporal decorrelation and ground motion are expected to be minimal for short time periods, and these interferograms can be used to study seasonal variations of water vapour. The atmospheric phase observed in an interferogram, a so-called atmospheric phase screen (APS), is the difference between two atmospheric phase delays measured every 11 days (TerraSAR-X) or 35 days (ENVISAT). Additionally, it is expected in the future to establish radar missions that provide SAR images with shorter repeat cycles (e.g., COSMO-SkyMed system).

Phase contributions due to topography are removed using a Digital Elevation Model (DEM) of 5 m resolution and a height accuracy of 20 cm. In some areas DEM from the Shuttle Radar Topography Mission (SRTM) are required. Oversampling in space is used to increase the spatial density of the data.

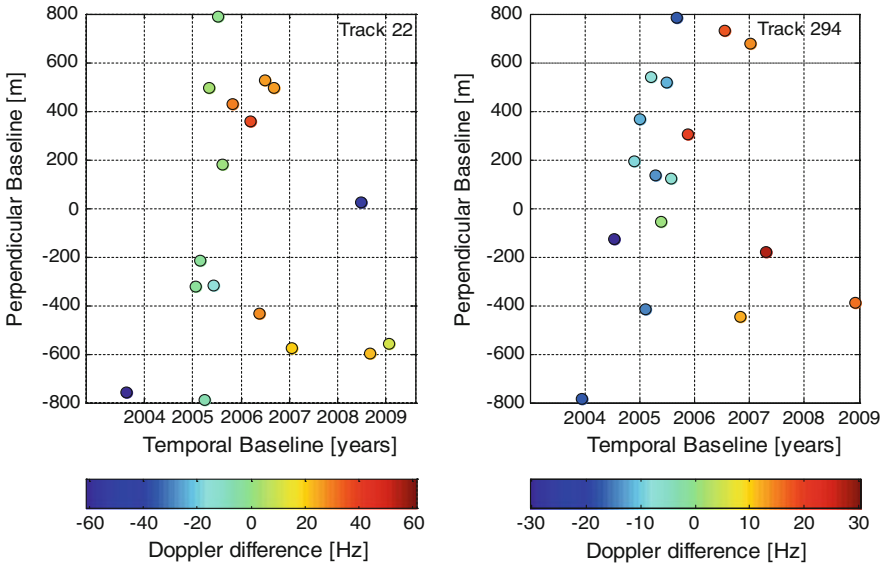

Fig. 2 Available ENVISAT data of tracks 294 and 22 with the temporal and spatial baselines

Table 1 GNSS, InSAR, WRF data used for water vapour determination

	System	Temporal resolution	Spatial resolution	Data availability
GNSS	GPS	30 s	Point wise	Since 2002
InSAR	ENVISAT	35 days	20 m	2003–2009
	ERS-1/2	1 day		1996
WRF	WRF 3.1	10 min	3 km	2005

Meteorological data (i.e., pressure, temperature, and relative humidity) required for IPWV determination in both GNSS and InSAR are received from numerical weather model simulations, one model known as Weather Research and Forecasting (WRF, http://www.wrf-model.org/index.php). WRF generates simulations of meteorological parameters such as air temperature, air pressure, relative humidity as well as IPWV. Table 1 summarizes the properties of the data used in this study.

3 Concepts

We focus on the time delay component induced in GNSS and InSAR observations by water vapour. Unlike other studies that treat this component as noise which should be eliminated, we investigate this component for water vapour mapping. The concept is based on quantifying water vapour from observations acquired by

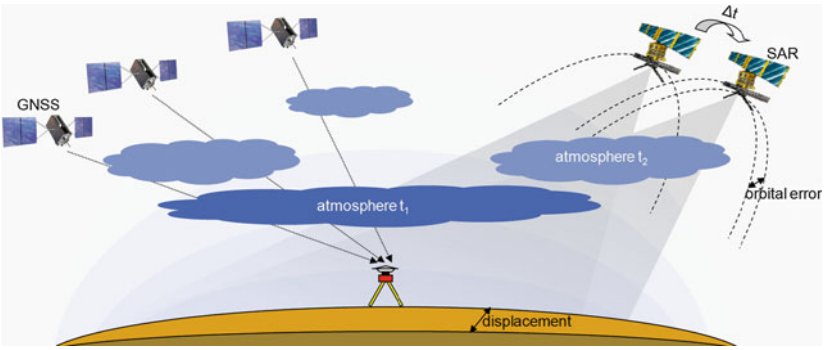

Fig. 3 IPWV determination based on the combination of GNSS and InSAR observations

GNSS sites and InSAR images of the same area. Figure 3 shows a simple sketch of the approach where a repeat-pass SAR satellite provides acquisitions of a certain spatial coverage and several GNSS sites are distributed in the same area.

The density of the GNSS sites is limited compared to the spatial resolution of InSAR. Therefore, GNSS enables continuous and accurate determination of IPWV at each receiver but not at the pixel resolution of InSAR. Moreover, estimates of the zenith IPWV are obtained by combining GNSS measurements over a reversed cone above the antenna. InSAR, however, provides APS of high spatial resolution which are converted into temporally-differenced IPWV maps. The objective is to reconstruct absolute values of IPWV from InSAR APS with the aid of GNSS. It is important to mention that InSAR provides one observation every couple of weeks.

For building 2D water vapour fields from InSAR, it is required to discriminate atmospheric signals from contributions due to ground displacement. The displacement signal is considered here as 'noise' which has to be removed. Other phase components such as topography and orbital trends are also removed and the remaining image, called APS, is most likely due to the neutrosphere. The APS is translated into slant-directed neutrospheric total delay to be compared with GNSS results. Time series of GNSS-based ZTD are calculated at the SAR acquisition date using PPP. ZTD is then mapped to the line-of-sight of the radar. Temporal differences of SWD are built to emulate InSAR.

The quality of the SWD calculated using GNSS differs for different SAR acquisition times due to different GNSS satellite geometries which regulate the number of available sites. One should also consider errors introduced by interpolations and mapping of the GNSS data to the radar and vice versa. The next step is to reconstruct absolute values of the delay by combining both GNSS and InSAR, which is a non trivial task. Results of IPWV achieved by INSAR and GNSS will be compared with the WRF IPWV maps.

It is worth mentioning here that achieving precise calculations of IPWV from GNSS measurements requires meteorological observations, for example, pressure, temperature and relative humidity. These data are indispensable for modelling and eliminating the neutrospheric dry part. This applies also to InSAR where the dry

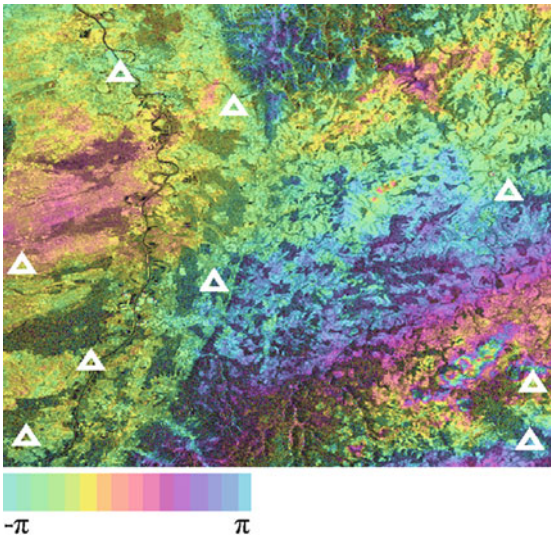

Fig. 4 Interferogram over URG from images acquired: 26 and 27 March 1996, topographic phase removed, $2\pi = 28$ mm delay; *white triangles* indicate the location of the GNSS sites

delay should be modelled and removed if it is not totally reduced through the interferometric process. Meteorological data are received currently from the WRF simulations.

4 Neutrospheric Delay in InSAR

InSAR phase observations contain contributions from different components, among them is the phase delay due to signal propagation through the neutral atmosphere. The interferometric phase for each pixel in an interferogram is given by the superposition of different contributions such as topography, Earth surface displacement, and atmosphere. The main focus of this work is the phase component due to the neutral atmosphere. Other phase components (e.g., due to Earth's topography) will be eliminated. InSAR phase for each pixel in the interferogram is given by:

$$\phi_{\text{int}} = \phi_{topo} + \phi_{displ} + \phi_{atm} + \phi_{orbit} + \phi_{flat} + \phi_{noise} \tag{1}$$

where ϕ_{topo} is the topographic phase component. ϕ_{displ} is the phase component due to the Earth surface displacement between the two SAR acquisitions. ϕ_{atm} is defined as differential phase shift caused by the propagation of the signal through the atmosphere. The phase component due to the inaccuracy of satellite orbit is given by ϕ_{orbit} and ϕ_{flat} is the phase component due to the Earth curvature. ϕ_{noise} is the component due to the system thermal noise and the loss of coherence between the two observations. Figure 4 shows an interferogram (slant-range geometry) and the GNSS sites located within.

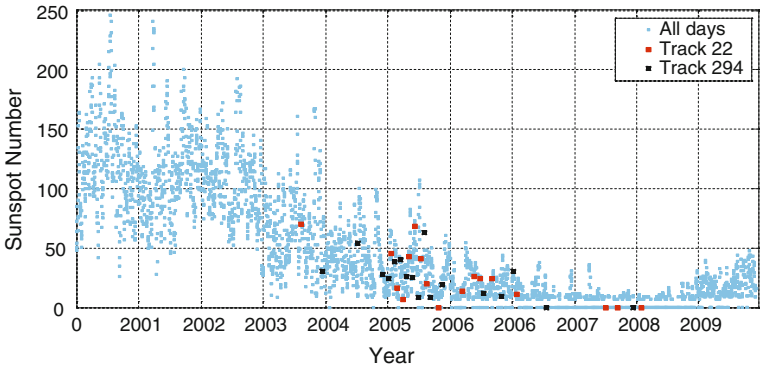

Fig. 5 Daily sunspot number for the past 10 years. *Red* and *black dots* show the sunspot number at the SAR acquisition time

The influence of the Earth's ionosphere on C-band InSAR observations is usually minimal (Onn 2006); therefore, we assume that InSAR phase is mainly influenced by the neutrosphere. This assumption will be validated in the future based on GNSS data. The ionospheric activity was determined by observing the sunspot number at the SAR overpass dates (Fig. 5). Low sunspot numbers indicate smaller solar activity and hence, small ionospheric effect on the satellite signals (http://sidc.oma.be/index.php, Klobuchar 1996).

Once all other components are eliminated, an APS is extracted. APS contains information of vertically stratified water vapour and horizontal turbulent mixing of water vapour.

As with GNSS, InSAR neutrospheric signal can be divided into two components, dry and wet. Unlike GNSS, however, InSAR neutrospheric phase is the difference of the atmospheric effects influencing the SAR scenes at two acquisition times. Hence, the interferometric phase due to the neutral atmosphere ($\phi_{\mathrm{int},na}$) is written as:

$$\phi_{\mathrm{int,na}} = \phi_{\mathrm{int,dry}} + \phi_{\mathrm{int,wet}} \tag{2}$$

where $\phi_{\mathrm{int,dry}}$ is the phase shift due to dry gases while $\phi_{\mathrm{int,wet}}$ is due to water vapour. Zebker et al. (1997) observed that the dominant variations in InSAR neutrospheric phase are mainly due to water vapour while the hydrostatic effects are minimal. $\phi_{\mathrm{int},na}$ observed for each pixel in an interferogram is given by:

$$\phi_{\mathrm{int},na} = \frac{4\pi}{\lambda \cos\theta}[ZTD(x,y,t_2) - ZTD(x,y,t_1)] \tag{3}$$

where *ZTD* is the zenith total delay due to the neutrosphere, and t indicates the acquisition time of SAR images. The factor $1/\cos\theta$ is used for projecting the zenith directed neutrospheric delay into the satellite line-of-sight. θ is the satellite look angle and it is $\sim 23°$ for ENVISAT. This simple mapping function has been commonly used in other studies (e.g., Hanssen 2001; Onn 2006; Meyer et. al.

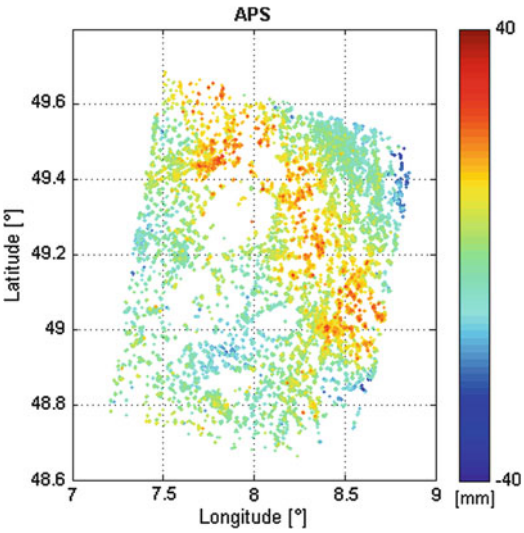

Fig. 6 Differential neutrospheric delay extracted from InSAR (track 294), *master* 27 June 2005 and *slave* 23 April 2007. Forest areas are almost empty of PS points

2008). The dry delay in our work will be simply determined and compensated using meteorological data. Once eliminated, the wet delay can be translated into differential IPWV (DIPWV) using the empirical factor Π (a typical value of 0.15, Bevis et al. 1994) as follows:

$$\mathrm{DIPWV} = \Pi \cdot \frac{\lambda \cos\theta}{4\pi} \phi_{\mathrm{int,wet}} \tag{4}$$

Persistent Scatterer Interferometry (PSI), particularly Stanford Method for Persistent Scatterers (StaMPS) is applied for extracting APS from interferograms (Hooper et al. 2007). PSI allows to estimate phase components such as the surface displacement at the persistent scatterers positions with a high accuracy. In the same way, PSI can be used to split the neutrospheric phase component. Estimating the neutrospheric delay at scattered points is adequate to derive 2D path delay fields due to the spatial correlation property of the neutrospheric signal. Figure 6 shows an APS calculated by applying PSI to an ENVISAT image stack of track 294.

Since InSAR provides temporally relative 2D water vapour measurements. It is targeted to reconstruct absolute 2D IPWV fields corresponding to each observation time. For that purpose, IPWV determined from GNSS measurements will be integrated with InSAR. Another approach investigated by Cavalié et al. (2007) who accomplished studies on the reconstruction of absolute IPWV from InSAR observations using least squares inversion. This approach requires a large number of SAR images which is not the case for the selected data set of URG.

5 Neutrospheric Delay in GNSS

A high potential source for the determination of water vapour is the analysis of GNSS phase measurements, particularly in regions with highly dense networks. GNSS signals are delayed by the Earth's atmosphere which is considered a main limitation for high-precision geodetic applications; however, it makes GNSS a reasonable tool for atmospheric sounding.

The ionosphere is a dispersive medium for L-band microwaves, which makes it possible to suppress its influence on GNSS signals by using linear combination of dual frequencies. The neutrosphere (dry gases + water vapour) is non-dispersive; therefore, it is common to estimate a so-called site-specific neutrospheric parameter within GNSS data processing. The quality of the calculated neutrospheric delay depends not only on the processing strategy but also on the observations quality (e.g., presence of multipath, antenna errors). Currently, we are doing neutrospheric studies using GPS signals, and different GNSS measurements (e.g., GLONASS, GALILEO) will be investigated in the future.

5.1 Wet Delay Calculations

The wet part of the neutrospheric delay is divided azimuthally into isotropic and anisotropic parts. Assuming the neutrosphere is stratified vertically above a GPS antenna, a zenith-directed total delay (ZTD) is calculated in the Bernese GPS Software 5.0 (BS5, Dach et al. 2007) using 24 h of GNSS observations. One sample of ZTD is calculated every 30 min and reduced to zenith wet delay (ZWD) by subtracting the zenith-directed dry delay (ZDD). ZDD is calculated from the Saastamoinen model based on meteorological observations. ZWD is mapped to the satellite line-of-sight using the Niell mapping function, Niell (1996). This is given by the first term of Eq. 5. The deviation of the neutrosphere from the azimuthal symmetry is considered by introducing horizontal tropospheric gradients given by the second and the third terms of Eq. 5. To obtain the total slant wet delay (SWD), an anisotropic component is extracted from the residuals of the phase observations and it is given by the last term of Eq. 5. Bender et al. 2008 calculated the SWD by combining the first and the last terms of Eq. 5. Interpolations in time are done to improve the temporal resolution of the IPWV series. The SWD is then translated into IPWV using the empirical constant Π.

$$SWD = ZWD \cdot MF_{niell} + \Delta^n \cdot \frac{\partial MF_{niell}}{\partial z} \cdot \cos A + \Delta^e \cdot \frac{\partial MF_{niell}}{\partial z} \cdot \sin A + \upsilon \qquad (5)$$

Δ^n, Δ^e are the tropospheric gradients, respectively, in the northing and easting directions (Meindl et al. 2004). A is the satellite azimuth angle and the anisotropic wet component calculated from the residuals is given by υ. ZWD is calculated using the following relation:

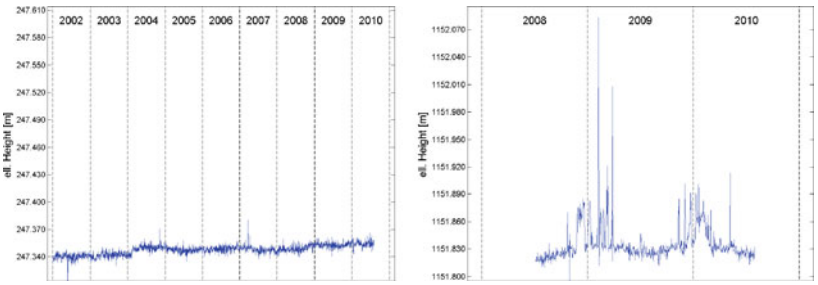

Fig. 7 Time series of ellipsoidal height of GURN sites; *left* site 0392 (Tauberbischofsheim, Germany), *right* site AUBU (Aubure, France)

$$ZWD = ZTD - ZDD_{met} \tag{6}$$

where ZDD_{met} is calculated from Saastamoinen apriori model (Saastamoinen 1973) using meteorological data. Interpolations of meteorological data at GNSS sites are required if the sites are not equipped with meteorological sensors.

The quality of the neutrospheric delay calculated from GNSS measurements depends highly on the following factors:

1. Accuracy of the antenna position, in particular the height component: Studies are carried out to analyze the quality of GURN sites. Time series of site coordinates are calculated from phase observations and analyzed to detect different effects such as discontinuity due to, for example, instruments exchange or weather conditions such as presence of snow. Figure 7 shows time series of the vertical coordinate of two GURN sites. In the left graph, a discontinuity is observed (at the end of year 2003) which is basically caused by instrumentation change, while the right figure shows high fluctuations in the time series since the measurements are taken under snow cover (Knöpfler et al. 2010).
2. Site-specific multipath and antenna errors: The quality of the GNSS measurements may become inconsistent under the existence of site-specific multipath and antenna errors. One way of compensating multipath errors by spatial stacking of phase residuals was proposed by Fuhrmann et al. (2010). Residuals contain information about the azimuthally anisotropic part of the wet delay as well as multipath and antenna errors. The developed stacking method reduces such errors based on the repeated satellite geometry. The remaining part is due to neutrospheric delay. Figure 8 exhibits values of IPWV calculated form GNSS phase observations with/without applying the stacking method. The upper graph shows more variability due to the existence of the site-specific errors in the residuals. Applying the stacking approach to the residuals reduces these effects and leads to less deviation as to see in the lower graph.
3. Observation weighting: The quality of GNSS measurements is strongly correlated with the satellite elevation angle. Therefore, it is common to use elevation-dependent weighting methods in GNSS software packages. Luo et al.

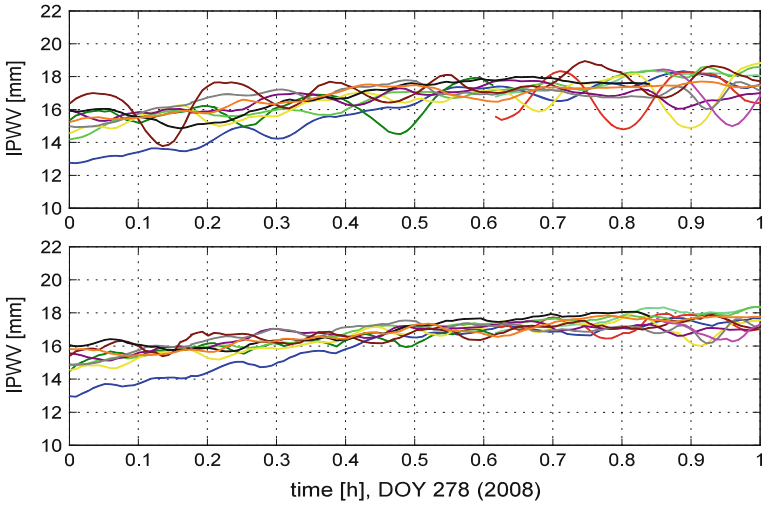

Fig. 8 Influence of residual stacking method on IPWV. Site Sélesat (TANZ), all available satellites, the *upper* IPWV without using stacking, the *lower* IPWV using stacking

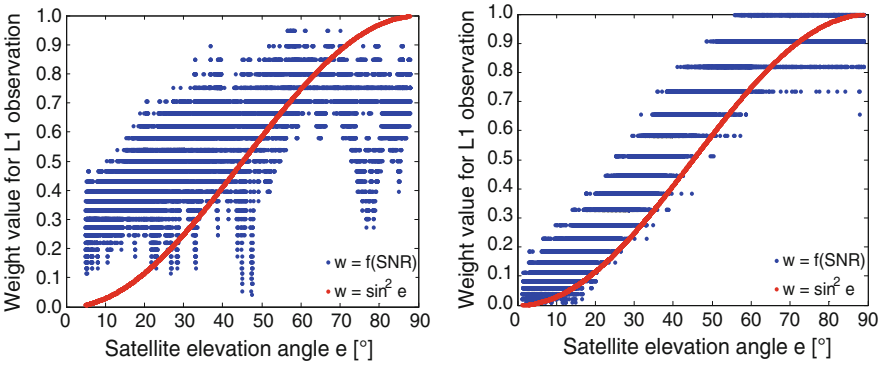

Fig. 9 Comparison of weight values of L1 observations; *left site* TZGD, *right site* LEIC

(2008) found out that this method becomes obsolete if the observations are strongly affected by multipath, signal diffraction or antenna errors. Instead, an improved weighting model based on signal-to-noise power ratio (SNR) was developed. Tests indicate that using this model the accuracy of the estimated IPWV improved by 25 % compared with the conventional elevation-dependant model. Figure 9 compares weighting values of GPS L1 observations received at two sites. The red curve (elevation-based) shows that signals received at high elevation angles get high weights. When a signal is received at a high elevation but a low quality, it is more reasonable to grant it a low weight as shown in blue in the left graph (SNR-based).

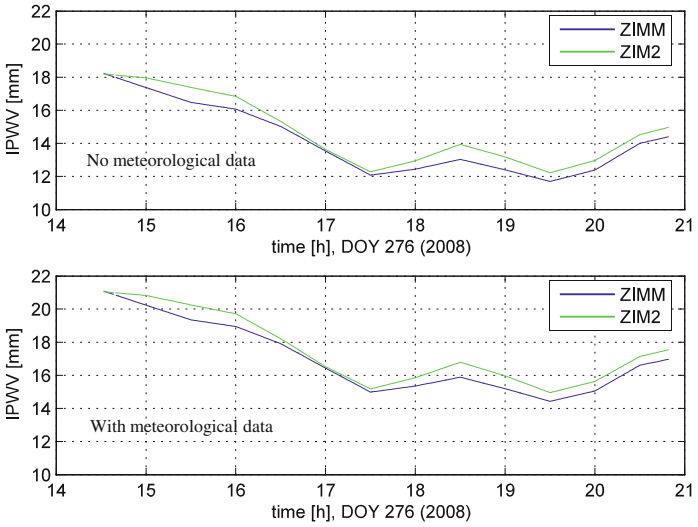

Fig. 10 Effects of using meteorological data, Zimmerwald sites: ZIMM, ZIM2, satellite PRN6

4. Meteorological data: Calculations of the wet delay require meteorological observation such as pressure, temperature, and relative humidity. In Fuhrmann et al. 2010, it was shown that calculating the wet delay as shown in Eq. 6 gives more precise results than using site-specific neutrospheric parameter estimated without using meteorological observations. Figure 10 shows the effect of calculating the wet delay based on meteorological observations (lower graph show an increase in IPWV value). The ZDD component calculated in the BS5 can still contain a fraction of the wet delay; therefore, using meteorological data improves the results.

5.2 DGNSS Versus PPP

Different techniques have been employed for neutrospheric delay calculations, namely Differential GNSS (DGNSS) (Davis et al. 1985) and GNSS Precise Point Positioning (PPP) (Witchayangkoon 2000). In DGNSS, double differences of GPS phase observations between two or more sites are employed, basically, to eliminate satellite and receiver clock errors and reduce atmospheric effects. The results depend on the site quality and the baseline length. In this method, the common part of the neutrospheric delay between both sites cancels out and cannot be totally reconstructed, but it could be used to study the correlation between different GNSS sites (Alber et al. 2000).

PPP investigates linear combinations of phase measurements which eliminates the ionospheric effects. This method enables precise reconstruction of absolute neutrospheric delay at each GNSS site. The processing is done for each site

independent from others; therefore, the presence of a failure at one site affects only the results of this site. PPP, however, requires highly accurate information of satellites orbits and clocks which is delivered by the International GNSS Service (IGS). Ionosphere-free linear combinations make GNSS carrier phase ambiguities non-integer values which have to be estimated during data processing, this leads to less accuracy compared to DGNSS. As presented above, we have a good experience in the field of neutrospheric delay and IPWV calculations from GNSS observations. Different strategies and different factors affecting IPWV calculations have been considered and analyzed to achieve accurate results.

6 Conclusions and Outlook

In this paper, we have presented a concept of combining InSAR and GNSS for building water vapour fields. Interferograms are formed from SAR images in the Upper Rhine area in Germany. PSI was applied to extract APS maps which are translated into path delay to be compared with GNSS. If existent, the surface displacement component has to be first estimated and subtracted. Time delay induced by water vapour in the GNSS phase observations have been determined at the SAR acquisition time. Several factors have been considered to improve the quality of water vapour products provided by GNSS, i.e., using well-performing sites, investigation of phase residuals, observation weighting based on the signal-to-noise ratio, and inclusion of meteorological data in the calculations.

It is necessary to compare the path delay values calculated from GNSS and InSAR. The different systems geometries and the distinct ways of calculating the path delay impose a careful selection of comparison strategies. APS maps should be compared with data sets that have a better spatial resolution such as the products of WRF or MERIS (MEdium Resolution Imaging Spectrometer). APS maps are relative measurements of atmospheric delay; therefore, we aim at deriving absolute delay maps with the aid of the GNSS information of path delay.

Acknowledgments The authors would like to thank the ESA for providing us with ERS and ENVISAT data. We would like also to thank the Landesamt für Geoinformation und Landentwicklung Baden-Württemberg for providing us with laser DEM data. Thanks also go to the data suppliers of permanently operating GNSS networks: RENAG (France), RGP (France), Teria (France), Orpheon (France), SA*POS*®-Baden-Württemberg (Germany), SA*POS*®-Rheinland-Pfalz (Germany), swisstopo (Switzerland), European Permanent Network, and IGS.

References

Alber C, Ware R, Rocken C, Braun J (2000) Obtaining single path phase delays from GPS double differences. Geophys Res Lett 27(17):2661–2664

Bender B, Dick G, Wickert J, Schmidt T, Song S, Gendt G, Ge M, Rothacher M (2008) Validation of GPS slant delays using water vapour radiometers and weather models. Meteorol Z 17(6):807–812

Bevis M, Businger S, Herring TA, Rocken C, Anthes RA, Ware RH (1992) GPS meteorology: remote sensing of atmospheric water vapour using the global positioning system. J Geophys Res 97(D14): 15787–15801

Bevis M, Businger S, Chiswell S, Herring TA, Anthes RA, Rocken C, Ware RH (1994) GPS meteorology: mapping zenith wet delays onto precipitable water. J Appl Meteorol 33: 379–386

Cavalié O, Doin MP, Lasserre C, Briole P (2007) Ground motion measurement in the Lake Mead area, Nevada, by differential synthetic aperture radar interferometry time series analysis: probing the lithosphere rheological structure. J Geophys Res 112. doi:10.1029/2006JB004344

Dach R, Hugentobler U, Fridez P, Meindl M (2007) Bernese GPS software version 5.0. Astronomical Institute, University of Bern, Switzerland

Davis JL, Herring TA, Shapiro I, Rogers AE, Elgened G (1985) Geodesy by interferometry: effects of atmospheric modeling errors on estimates of base line length. Radio Sci 20(6):1593–1607

Fuhrmann T, Knöpfler A, Luo X, Mayer M, Heck B (2010) Zur GNSS-basierten Bestimmung des atmosphärischen Wasserdampfgehalts mittels Precise Point Positioning. KIT Scientific Reports 7561/Schriftenreihe des Studiengangs Geodäsie und Geoinformatik 2010, 2; ISBN 978-3-86644-539-0, KIT Scientific Publishing, 2010

Hanssen R (2001) Radar interferometry: data interpretation and error analysis, vol 2, 1st edn. Kluwer Academic Publishers, Dordrecht

Hopfield H (1969) Two-quartic tropospheric refractivity profile for correcting satellite data. J Geophys Res 74(18):4487–4499

Hooper A, Segall P, Zebker H (2007) Persistent scatterer InSAR for crustal deformation analysis, with application to Volcán Alcedo, Galápagos. J Geophys Res 112(B07407)

Klobuchar JA (1996) Ionospheric effects on GPS. In: Parkinson B, Spilker J, Axelrad P, Enge P (eds) Global positioning system: theory and applications, vol 1. American Institute of Aeronautics and Astronautics, Washington, pp 485–515

Knöpfler A, Masson F, Mayer M, Ulrich P, Heck B (2010) GURN (GNSS Upper Rhine Graben Network)—status and first results. In: FIG Congress 2010—facing the challenges—building the capacity, Sydney, Australien, 11–16 Apr 2010

Knospe S, Jónsson S (2007) Covariance estimation, geostatistical prediction and simulation for InSAR observations in presence of strong atmospheric anisotropy. In: Proceedings of fringe 2007 workshop, ESA SP-649

Li Z, Fielding EJ, Cross P, Muller J (2006) Interferometric synthetic aperture radar atmospheric correction: GPS topography-dependent turbulence model. J Geophys Res 111:B02404. doi:10.1029/2005JB003711

Luo X, Mayer M, Heck B (2007) Bestimmung von hochauflösenden Wasserdampffeldern unter Berücksichtigung von GNSS-Doppeldifferenzresiduen. Universität Karlsruhe (TH), Schriftenreihe des Studiengangs Geodäsie und Geoinformatik, Heft Nr. 2007/2

Luo X, Mayer M, Heck B (2008) Extended neutrospheric modelling for the GNSS-based determination of high resolution atmospheric water vapour fields. Boletim de Ciencias Geodesicas 14(2), Curitiba/Brasilien, 149–170

Massonnet D, Rossi M, Carmona C, Adragna F, Peltzer G, Feigl K, Rabaute T (1993) The displacement field of the landers earthquake mapped by radar interferometry. Nature 364:138–142

Mayer M (2006) Modellbildung für die Auswertung von GPS-Messungen im Bereich der Antarktischen Halbinsel. Deutsche Geodätische Kommission, Reihe C, Heft Nr. 597, München

Mayer M, Knöpfler A, Masson F, Ulrich P, Ferhat G, Heck B (2009) GURN (GNSS Upper Rhine Graben Network)—research goals and first results of a transnational geo-scientific network. Accepted to be published by Springer in the proceedings of IAG 2009 Scientific Assembly "Geodesy for Planet Earth"

Meindl M, Schaer S, Hugentobler U, Beutler G (2004) Tropospheric gradient estimation at CODE: results from global solutions. J Meteorol Soc Jpn 82(1B):331–338. doi:10.2151/jmsj.2004.331

Meyer F, Bamler R, Leinweber R, Fischer J (2008) A comparative analysis of tropospheric water vapour measurements from MERIS and SAR. In: Proceedings IEEE international geoscience and remote sensing symposium, IGARSS, 2008, IV-228–IV-231

Niell AE (1996) Global mapping functions for the atmosphere delay at radio wavelengths. J Geophys Res 101(B2):3227–3246

Onn F (2006) Modeling water vapour using GPS with application to mitigating InSAR atmospheric distortions. Phd. Dissertation, Stanford University, Stanford, California

Physorg (2006) Greenhouse theory smashed by biggest stone. Published 14 Mar 2006, cited 28 Aug 2007, www.physorg.com/news11710.html

Pierdicca N, Rocca F, Rommen B, Basili P, Bonafoni S, Cimini D, Ciotti P, Consalvi F, Ferretti R, Foster W, Marzano FS, Mattioli V, Mazzoni A, Montopoli M, Notarpietro R, Padmanabhan S, Perissin D, Pichelli E, Reising S, Sahoo S, Venuti G (2009) Atmospheric water vapour effects on spaceborne interferometric SAR imaging: comparison with ground-based measurements and meteorological model simulations at different scales, In: Proceedings IEEE international geoscience and remote sensing symposium, IGARSS, 2009, V-32–V-323

Rommen B, Mika A, Gale L, Zelle H, Hanssen R, Liu S, Matzler C, Morland J, Wegmuller U, Werner C, Santoro M (2009) The ESA METAWAVE project: correcting for atmospheric water vapour effects in InSAR products, antennas and propagation. In: EuCAP 2009. 3rd European conference on, Berlin, ISBN: 978-1-4244-4753-4

Rózsa S, Heck B, Mayer M, Seitz K, Westerhaus M, Zippelt K (2005) Determination of displacement in Upper Rhine Graben area from GPS and leveling data. Int J Earth Sci (Geol Rundsch) 94:538–549

Saastamoinen J (1973) Contributions to the theory of atmospheric refraction. Bulletin Géodésique (48), 279–298, (48), 383–397, (49), 13–34

Van der Hoeven A, Hanssen RF, Ambrosius B (2002) Tropospheric delay estimation and analysis using GPS and SAR interferometry. Phys Chem Earth 27(2002):385–390

Witchayangkoon B (2000) Elements of GPS precise point positioning. Doctoral dissertation, Department of Spatial Information Science and Engineering, Graduate School, University of Maine, 265

Zebker HA, Goldstein RM (1986) The displacement field of the landers earthquake mapped by radar interferometry. J Geophys Res 91:4993–4999

Zebker HA, Rosen PA, Hensley S (1997) Atmospheric effects in interferometric synthetic aperture radar surface deformation and topographic maps. J Geophys Res 102:7547–7563

Part III
Global Change and Change Detection

A Hybrid Approach to Disseminate Large Volume Sensor Data for Monitoring Global Change

Theodor Foerster, Albert Remke and Georg Kaspar

Abstract Monitoring global change is one of the major challenges in the twenty first century. It requires accessing large volumes of various data, collected by a multitude of remote and in situ sensors. Various approaches (file-based, service-based and satellite-based) have demonstrated significant disadvances, which can be concluded as inappropriate. In this article, we describe a hybrid approach using a satellite-based system for accessing sensor data on distributed nodes and then disseminating the data on the web through web services. The approach is demonstrated based on the satellite-dissemination system of GEONETCast using two use cases for raster-based (MSG-2) and feature-based (MODIS) data.

1 Introduction

Monitoring global change requires various data, collected by a multitude of remote and in situ sensors worldwide. This large volume of data cannot be disseminated over the web exclusively due to limited bandwidth. Also disseminating it only through satellite systems is not reasonable, due to proprietary standards of the

T. Foerster (✉)
Institute for Geoinformatics, University of Muenster, Muenster, Germany
e-mail: theodor.foerster@uni-muenster.de

A. Remke
52°North GmbH, Muenster, Germany
e-mail: remke@52north.org

G. Kaspar
Center for Digital Media, University of Muenster, Muenster, Germany
e-mail: georg.kaspar@unimuenster.de

J. M. Krisp et al. (eds.), *Earth Observation of Global Changes (EOGC)*,
Lecture Notes in Geoinformation and Cartography, DOI: 10.1007/978-3-642-32714-8_11,

received data (i.e. different file formats), missing concepts for attaching metadata and the costs to receive the data at each node. In this paper a hybrid approach is described, in which central nodes receive the sensor data through a satellite dissemination system and make the data available in a structured, standardized and customizable way through web service interfaces for specific use cases and for a limited number of client applications.

The hybrid approach is presented based on the GEONETCast satellite dissemination system (Wolf and Williams 2008) as a representative of a satellite-based dissemination system and is using principles of Spatial Data Infrastructures (as a representative approach for organizing geodata in a network-based environment). The hybrid approach results in distributed archives of real-time and historical environmental data, which are accessible on the web.

At our department such a node for disseminating GEONETCast data is under development. The hybrid approach is exemplified by two different use cases focusing (a) on publishing meteorological remote sensing data (Schmetz et al. 2002) and (b) on publishing data about fire events extracted from Moderate Resolution Imaging Spectroradiometer (MODIS) (Justice et al. 1998). The presented use cases are implemented based on Free and Open Source Software.

This article contributes to the efforts of publishing large volume of data on the web. As the documented research shows (Sect. 2.3), this has not been fully achieved yet. Therefore, we advocate the use of standards and propose a hybrid approach of satellite-based and web-based data dissemination. Additionally, it contributes to the Persistent Test bed initiative of the Association Geographic Information Laboratories Europe (AGILE), Open Geospatial Consortium (OGC) and the European Spatial Data Research (EuroSDR) for research and teaching (Hobona et al. 2009).

Section 2 provides an overview of state-of-the-art dissemination of large volume sensor data through GEONETCast and the web. Based on the analysis, the hybrid approach is presented (Sect. 3), which is then demonstrated by two use cases in Sect. 4. Finally, the article ends with a conclusion.

2 Related Work

This section summarizes basic concepts of GEONETCast and Web Services. The presented concepts are later on applied to realize the hybrid approach of disseminating large volume of sensor data.

2.1 GEONETCast

GEONETCast is a satellite-based dissemination system for environmental data created by remote and in situ sensors. GEONETCast is a part of the Global Earth

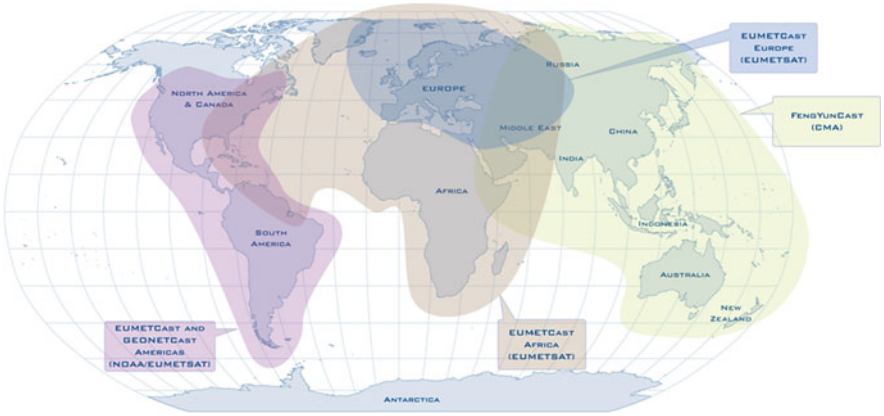

Fig. 1 GEONETCast overview (GEO 2012)

Observation System of Systems (GEOSS). In particular, GEONETCast is a task in the Group on Earth Observations (GEO) Work Plan and is led by EUMETSAT, the United States, China, and the World Meteorological Organization (WMO). Many GEO members and participating Organizations contribute to this task. The dissemination of GEONETCast products is managed by regional centers using regional satellite-based dissemination systems:

- FENYUNCast(Asia)
- EUMETCast (Africa & Europe)
- GEONETCast Americas (North and South America).

An overview of the different regional satellite-based dissemination systems and their coverage is depicted in Fig. 1.

With its over 180 products GEONETCast offers a broad thematic range from spectral transmission and climate measures (i.e. surface temperature, precipitation) to disaster management (e.g. fire monitoring). The data is free for use in research and education. Additional data is available under specific license agreements.

One of the freely available products is MODIS data, which is part of Nasa's Earth Observation System. MODIS provides a set of land surface products, which are described in Justice et al. (1998). In particular, MODIS fire data (MOD14) has been selected for this study and also serves as a basis for other derived products of MODIS.

Another example of available GEONETCast data is Meteosat Second Generation (MSG-2), which consists of 12 channels of which 11 channels have a resolution of 3 km (Schmetz et al. 2002). The 12 channels are collected from visible to infrared spectrum. The raw MSG-2 data received from GEONETCast is transformed into GeoTiff format and can thereby be directly served in state-of-the-art applications and Web Services.

Both data sets are used to examine vector and raster-based data dissemination of GEONETCast data (Sect. 4).

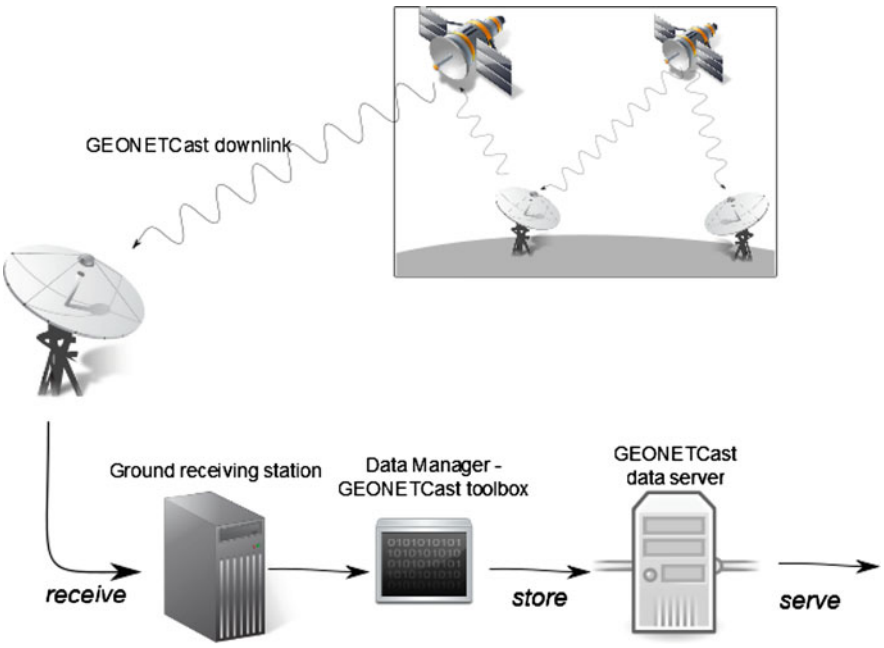

Fig. 2 Technical setup to retrieve GEONETCast products

To receive such GEONETCast products, a common technical setup is available. The setup is depicted in Fig. 2 and consists of three steps: receive, store and serve. The GEONETCast ground station receives the data from the GEONETCast satellites through a standard TV dish (connected through TV-card) and decodes the received data stream. The GEONETCast Toolbox (Maathuis et al. 2008) acts as a data manager to filter the desired products, which are then stored in a structured way on the data server. The data server is able to manage user access and serves the data through the file system. It is important to note, that in some setups the data server and the ground receiving station are hosted on the same computer. For the technical setup as used for this implementation these two components are separated on different machines for scalability and maintenance reasons (e.g. the data server has a periodic backup).

Based on this technical setup each node can be configured and the required data can be published (Sect. 3).

2.2 Web Services and Spatial Data Infrastructures

Web Services are defined as self-describing components, providing functionality and data on the web through a common interface (Alonso et al. 2004). A major aspect is thereby the encoding of metadata for the functionality as well as for data.

To share geodata between organizations of different countries, as for instance described by the INSPIRE directive (INSPIRE 2007), Spatial Data Infrastructures (SDIs) are created. They aim at integrating different data and heavily depend on Web Services and sufficient metadata. Geospatial Web Services are specified by the Open Geospatial Consortium (OGC) (Kralidis 2007). The three OGC web service interfaces for disseminating raster-based data (Web Coverage Service) and vector-based data (Web Feature Service) as well as the portrayal of the data (Web Map Service) are described.

2.2.1 Web Coverage Service

To serve coverage data on the web as for instance mostly provided by GEONETCast, the Web Coverage Service (WCS) has been specified (OGC 2006). It allows users to query coverage data and especially grid data regarding multiple aspects (space, time and channel). To interact with a WCS instance, three operations are required. *GetCapabilities* provides the service metadata and describes the different data available at the specific instance. To retrieve further information about a specific dataset, *DescribeCoverage* can be called by the client. The returned metadata describes the coverage including the following parameters (with OGC parameter names):

- extent (spatial domain)
- temporal resolution (temporal domain)
- the geographic layout of the grid (GridCRS)
- available channels (Axis).

Based on this metadata *GetCoverage* can be called to retrieve the designated data. Such coverage data can for instance be encoded in GeoTiff format (Ritter and Ruth 1997).

2.2.2 Web Feature Service

Web Feature Service (WFS) interface allows users to query and access feature data consisting of (multiple) points, lines or polygons (OGC 2005). The communication with WFS is based on the Internet Protocol HTTP using an XML-based encoding the so-called WFS Filter encoding. To retrieve specific features from a WFS, the get Feature operation is used, which receives messages as WFS Filters. WFS returns feature data (as result of the WFS Filter query) in the Geography Markup Language (GML) or also for instance in KML. KML is the data encoding established and used by Google-based applications. To also create and store new features on a WFS over the Web, a transactional interface has been developed. The additional operations of the so-called WFS-T (T stands for transactional) are insert, update, delete.

2.2.3 Web Map Service

To portray the data through a Web Service the OGC specified the Web Map Service (WMS) (OGC 2004). It delivers plain images depicting the selected aspect of the geodata. For the given study, WMS is used, as it allows users to portray the data without downloading it.

2.3 Web-Based GEONETCast Products

Related work about enabling GEONETCast data for the web has been reported by Davies et al. (2009). They also used MODIS data for monitoring fires and served this data on the Web. However, their setup involved a lot of manual steps and the access to the data was limited to portrayal (no querying possible). Additionally, the Center for Weather Forecast and Climatic Studies (CPTEC) of the National Institute for Space Research in Brazil (INPE) provides a web portal to access data about fire events. This portal only provides limited querying capabilities and does not allow users to integrate the data available in the portal into other applications.

Some attempts about enabling MSG-2 for web-based access have been reported. For instance Carvalheiro et al. (2010) describe a web-based dissemination system using a web page, displaying the data in a browser-based map viewer (Google Maps).

The presented review shows, that a hybrid approach for disseminating this kind of data is missing. Moreover, interoperability only plays a little role in the documented attempts. The presented architecture in this article is more comprehensive regarding both aspects, as it is based on live streaming of data through GEONETCast using Web Service interfaces. These Web Service interfaces allow users to query the data and also to integrate it into other applications such as Google Earth. Finally, the described implementation is based on Free and Open Source Software and can be re-built with low cost, if required.

3 Approach

The hybrid approach for dissimilating large volume of sensor data consists of two tasks. One task is to receive the data at a designated node using the technical setup described in Sect. 2.2. This node is configured with a satellite dish and stores designated data received from for instance GEONETCast on the data server. The other task is to dissimilate this data on the web. The hybrid approach is depicted in Fig. 3. Since GEONETCast data is provided in different file formats (e.g. plain text, GeoTiff) a format conversion may be necessary to enable standardized access. The dissemination of GEONETCast data on the web requires sufficient metadata and can be seen as the main advantage of the hybrid approach, as at the receiving

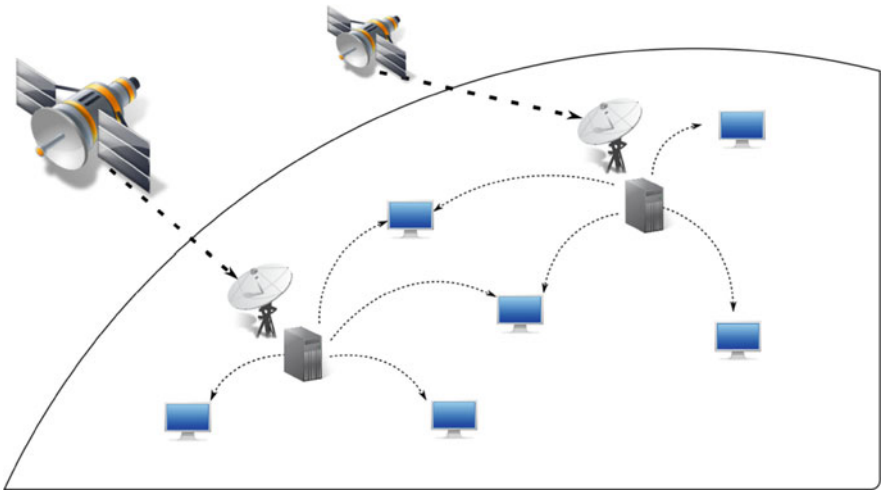

Fig. 3 Overview of the hybrid approach

nodes, metadata for the products is not directly available. Additionally, the web service allows users to access the data in a customized way. In particular, users are able to query the data using spatial and temporal filters. This is an additional advantage over the file-based access provided by the receiving station. A customized access can be based on standards as described by the OGC (Sect. 2.2). Based on these standards the data is directly accessible from existing applications. Using such existing applications and standards allows users to integrate this data with other sources for monitoring global change.

Operating these nodes over the long term, allows users to access an archive of data, which has suitable metadata attached and which allows users to monitor global change on a spatio-temporal scale. The creation of metadata is initiated once and is updated constantly by the Web Service automatically.

The Web Service endpoints for the designated GEONETCast data, can also be used as input for existing Web Services, that for instance provide web-based geo process models. The Web Service endpoints for GEONETCast data as well as the available geo process models can be made available through cloud computing (Foster et al. 2008) to provide designated quality of service.

Different nodes can be configured to serve different data thereby it is possible to set up a distributed network of web services for GEONETCast data. Serving only the required data through specific nodes also allows the providing organizations to scale their data services. Finally, client applications can retrieve different GEONETCast data from different nodes based on suitable metadata over the web and integrate such data with other sources to monitor global change.

In comparison to the existing approaches which are documented in Sect. 2.3, the presented approach has several advantages:

- Complete—The approach has been demonstrate for the two types of data, vector and raster-based. Thereby, it is complete in comparison to the other approaches, which either focus on one of the two, nor give full access to the data itself.
- Scalable and distributed—Due to the distributed nature of the nodes, the approach is scalable. Different applications will use different nodes, moreover the distribution supports novel techniques of distributed processing such as MapReduce (Cary et al. 2009).
- Standardized—As the distributed nodes are accessible through standardized web service interfaces serving data in standardized formats, the data and services can be integrated seamlessly in a wide range of applications.
- Extensible—Based on the distributed and standardized nature of the approach, the nodes can be extended with additional logic and capabilities (e.g. caching, cloud computing) to reduce performance bottlenecks, if applicable. Additionally, the nodes can be individually enhanced to support additional data formats.

4 Use Cases

The described approach is examined based on two use cases, which are implemented as part of the GEONETCast node at our faculty. In the first use case, meteorological remote sensing data is available through a browser-based application (Foerster et al. 2010a). In the second use case, MODIS data received from GEONETCast is processed to extract data about potential fire events (Foerster et al. 2010b).

4.1 Web-Based Meteorological Data

Meteorological data supports many types of analysis. Often this data needs to be up-to-date to take appropriate decisions. Thus accessing up-to-date meteorological data on a global scale is a requirement of many users. In this use case, up-to-date MSG-2 data received from GEONETCast data stream is made web-accessible through WCS interface. The WCS instance serves only 11 of the 12 available channels, as GeoTiff format can only handle different channels with equal resolutions, thus the 12th band (high resolution visible light) cannot be included (resolution 1 km).

The data server was connected directly to the WCS instance. We chose the Map Server software[1] as the Geospatial Web Service product. Map Server allows us to serve the data through WCS interface (data access) as well as WMS interface (data

[1] Map Server website: www.mapserver.org.

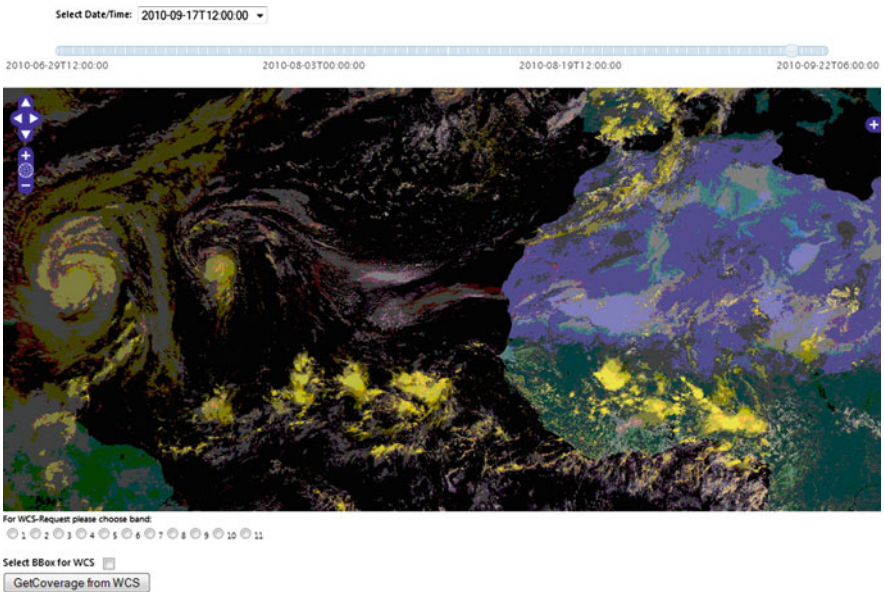

Fig. 4 Screen shot of the browser-based client accessing meteorological data from GEONET-Cast depicting hurricane Karl in the Gulf of Mexico in september 2010

portrayal). Users are thereby able to inspect the data (using WMS interface) without downloading it. An example of a browser-based application accessing the data through WMS interface is given in Fig. 4. The browser-based application allows the user to specify the data regarding time, geographic extent and specific channel. In the given example, data of hurricane Karl in the Gulf of Mexico in September 2010[2] is portrayed (based on channel 1 of MSG data collected at visible spectrum). The user can now select a geographic extent on the map, of which he wants to receive data. Based on this selection, the browser-based application generates a WCS-compliant URL, which can be used to download the designated coverage from the WCS instance. This URL can be used as input for web-based geo process models for performing geo change research.

This service can also be integrated into other applications based on the standardized WCS interface. For designated applications metadata is available through WCS Describe Coverage operation. Based on this metadata the application can integrate the data accordingly through WCS Get Coverage operation.

[2] Timestamp: 17th September 2010, 12:00.

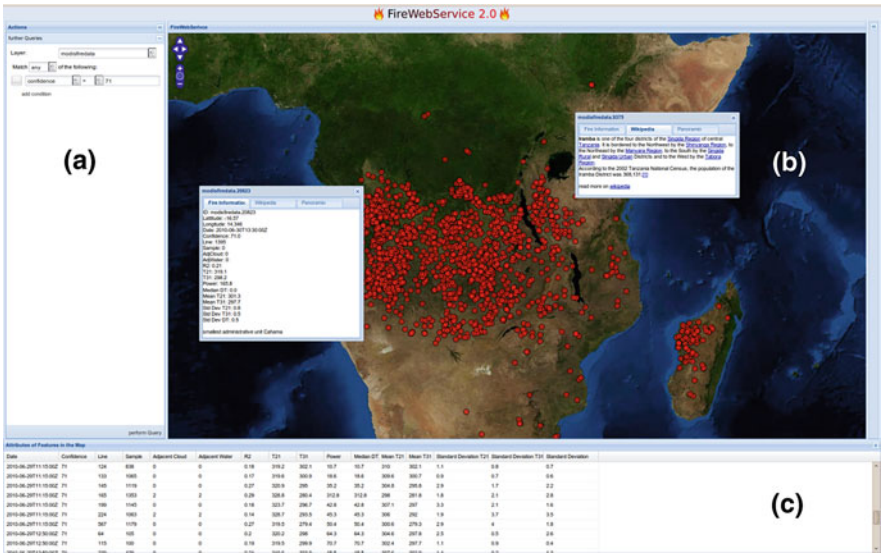

Fig. 5 Screenshot of the browser-based application for the fire web service with map of sub-Sahara region—different views: **a** query view. **b** map view. **c** tabular view

4.2 Web-Based Fire Web Service

Fire is a natural phenomenon and poses a threat especially when reaching built-up areas. Although it is a natural hazard a rigorous suppression leads to even more severe fires. Using fire for cultivating agricultural land has become an established element. However, an excessive application also leads to severe problems. Finally, monitoring such fires is required and different data is already available such as the MODIS fire products (Justice et al. 1998).

The fire events extracted from MODIS data are available as point-based data. For easy and customized access of this data, Web Service technology is used. To demonstrate the use case, an interoperable architecture (based on OGC standards) is applied to monitor fire events. In particular, a WFS-T is constantly updated with extracted point-based data from MODIS imagery served by GEONETCast. Users can access and query the data through a browser-based client and can use e.g. Google Earth to combine the data with other sources.

The browser-based application allows users to integrate the fire data with other third party sources such as Wikipedia or images from for instance Panoramio. Integrating the data with other third party sources is necessary to provide comprehensive information to the user and is possible due to established standards for data and Web Services. An example of the browser-based application is depicted in Fig. 5. The different parts of the interface are attached to the several tasks, which are described in the following:

a. Query data—The user is able to query the fire data available on the Fire Web Service based on its attributes (including time). By querying the temporal dimension, it is possible to not only receive up-to-date data about fire events, but also historic data. Another important attribute is the confidence value of a fire event, which indicates the possibility of a fire. The confidence value is a result of the applied fire detection algorithm performed on the MODIS data.
b. Map data—The result of the query can be inspected in the map view, in which the fire events are located on freely-available imagery such as from Blue Marble (Stockli et al. 2005). Each fire event on the map can be clicked for further details.
c. Inspect attribute table—Based on the query, the data can also be inspected using a tabular view.

The fire data can also be integrated into Google Earth by KML format as supported by the WFS interface. The attributes of the fire can be inspected directly by the user. However, a query mechanism for the data such as provided by the browser-based application is not available.

5 Conclusion

In this article we describe a hybrid approach for disseminating large volume of sensor data based on a satellite-based dissemination system such as GEONETCast and the web. The data is received from the satellite system at distributed nodes and disseminated on the web through web service interfaces. This allows to overcome the bottleneck of central services, which need to serve all data on the web, but also to operate cost-efficient, as the receiving node can share the data with other nodes at no costs. Additionally, the use of interoperable web service interfaces allows us to provide the data with appropriate metadata and allows users to directly integrate the data into existing applications for research on global change.

The hybrid approach has been demonstrated based on two use cases (Sect. 4) for disseminating raster- and vector-based data (Foerster et al. 2010a, b). The use cases have been implemented using Free and Open Source Software.

Future research needs to evaluate the performance and scalability of the hybrid approach by implementing additional use cases with a broader user community as for instance the Persistent Test bed initiative. For extracting specific information products out of the web-enabled GEONETCast data, web-based processing needs to be integrated. In particular, processing the available data using web-based functionality available OGC Web Processing Service interface needs to be investigated (Foerster et al. 2011). To ensure performance of web-based processing of GEONETCast data, mechanisms such as caching and streaming of geodata need to be considered. Additionally, new methods for discovery and automated metadata creation are required for sharing of GEONETCast data across

the web. Discovery has become more crucial considering the presented hybrid approach as specific content is only available at selected nodes.

Acknowledgments The presented work is based on a MSc. study project (title: GEONETCast) in spring 2010 at the Institute for Geoinformatics, University of Muenster, Germany. The contributions of the study project are highly acknowledged.

References

Alonso G, Casati F, Kuno H, Machiraju V (2004) Web Services, 1st edn. Springer, Berlin

Carvalheiro LC, Bernardo SO, Orgaz MDM, Yamazaki Y (2010) Forest fires mapping and monitoring of current and past forest fire activity from meteosat second generation data. Environ Model Softw 25(12):1909–1914. doi:10.1016/j.envsoft.2010.06.003

Cary A, Sun Z, Hristidis V, Rishe N (2009) Experiences on processing spatial data with mapreduce. In: Winslett M (ed), Scientific and Statistical Database Management, vol 5566. Springer, Berlin, , pp 302–319. Retrieved from http://www.springerlink.com/index/10.1007/978-3-642-02279-1_24

Davies DK, Ilavajhala S, Wong MM, Justice CO (2009) Fire information for resource management system: archiving and distributing MODIS active fire data. IEEE Trans Geosci Remote Sens 47:72–79. doi:10.1109/TGRS.2008.2002076

Foerster T, Fechner T, Fritze H, Loock F, Remke A (2010) Low-cost satellite-based products for the web—the example of Fire web service. In: Bogorny V Vinhas L (eds), Proceedings of 11th Brazilian symposium on geoinformatics. Presented at the GeoInfo 2010, pp 57–66, Sao Jose dos Campos: MCT/INPE

Foerster T, Schaeffer B, Baranski B, Brauner J (2011) Geospatial web services for distributed processing—applications and scenarios. In: Zhao P, Di L (eds) Geospatial web services: advances in information interoperability. IGI Global, Hershey, pp 245–286

Foerster T, Trame J, Remke A (2010) Web-based GEONETCast data for geochange research. In: Henneboehl K, Vinhas L, Pebesma E, Camara G (eds), GIScience for environmental change symposium proceedings, vol 40. Presented at the GIScience for environmental change, Campos do Jordao (Sao Paulo), Brazil: AKA Verlag, pp 1–6

Foster I, Zhao Y, Raicu I, Lu S (2008) Cloud computing and grid computing 360-degree compared. 2008 grid computing environments workshop . Presented at the 2008 grid computing environments workshop, Austin, pp 1–10. doi:10.1109/GCE.2008.4738445

GEO (2012) Geonetcast website. Retrieved from http://www.earthobservations.org/geonetcast.shtml

Hobona G, Jackson M, Gould M, Higgins C, Brauner J, Matheus A, Foerster T et al. (2009) Establishing a persistent interoperability testbed for european geospatial research. In: Haunert J, Kieler B, Milde J (eds), 12th AGILE international conference on geographic information science. Presented at the AGILE 2009, IKG, Leibniz University of Hanover, Hanover

INSPIRE (2007) Directive 2007/2/EC of the European parliament and of the council of 14 March 2007 establishing an infrastructure for spatial information in the European community. Official J Eur Union, 18

Justice CO, Vermote E, Townshend JRG, Defries R, Roy DP, Hall DK, Salomonson VV et al (1998) The moderate resolution imaging spectroradiometer (MODIS): land remote sensing for global change research. IEEE Trans Geosci Remote Sens 36:1228–1249. doi:10.1109/36.701075

Kralidis AT (2007) Geospatial web services: the evolution of geospatial data infrastructure. In: Scharl A, Tochtermann K (eds) The geospatial web, advanced information and knowledge processing series. Springer, London, pp 223–228

Maathuis B, Mannaerts C, Retsios B (2008) The ITC geonetcast-toolbox approach for less developed countries. In: Proceedings of commission VII, The international archives of the photogrammetry, remote sensing and spatial information sciences. Presented at the ISPRS congress Beijing 2008, vol 37, Beijing. Int Soc Photogram Remote Sens, pp 1301–1306

OGC (2004) OGC web map service interface (Implementation specification). Retrieved from http://www.opengeospatial.org/standards/wms

OGC (2005) *web feature service implementation specification* (implementation specification no. OGC 04-094). Retrieved from http://www.opengeospatial.org/standards/wfs

OGC (2006) Web coverage service (OGC Implementation specification no. OGC 06-083r8). In: Whiteside A, Evans JD (eds), Open geospatial consortium

Ritter N, Ruth M (1997) The GeoTiff data interchange standard for raster geographic images. Int J Remote Sens 18(7):1637–1647. doi:10.1080/014311697218340

Schmetz J, Pili P, Tjemkes S, Just D, Kerkmann J, Rota S, Ratier A (2002) An introduction to meteosat second generation (MSG). Bull Am Meteorol Soc 83(7):977–992. doi:10.1175/1520-0477(2002)083<0977:AITMSG>2.3.CO;2

Stockli R, Vermote E, Saleous N, Simmon R, Herring D (2005) The blue marble next generation—A true color earth dataset including seasonal dynamics from MODIS. Retrieved from http://earthobservatory.nasa.gov/Features/BlueMarble/bmng.pdf

Wolf L, Williams M (2008) GEONETCast—delivering environmental data to users worldwide. IEEE Syst J 2(3):401–405. doi:10.1109/JSYST.2008.925978

Data Harmonisation in the Context of the European Spatial Data Infrastructure: The HUMBOLDT Project Framework and Scenarios

Paolo Villa, Roderic Molina and Mario A. Gomarasca

Abstract Harmonised geo-information is a basic need for fulfilling the task of creating a Spatial Data Infrastructure which is reliable and efficient, handling different data sources and different services for discovery, portrayal and retrieval of geo-data as a crucial asset. At the European level, the road to an ESDI follows the guidelines contained in the ISPIRE Directive of the EC. With the aim of implementing a framework for harmonisation of data and services in geo-information domain, the European Community has supported the development of HUMBOLDT project, under the INSPIRE Directive and in the context of GMES Initiative. The two-pronged approach to geo-data harmonisation of HUMBOLDT comprises a technical side of framework development and an application side of scenario testing and validation. This paper presents an overview of the harmonisation framework implemented by HUMBOLDT project complemented by two short application cases based on thematic Scenarios of the project, one on the topic of protected areas and the other on maritime use cases. Protected Areas Scenario aims to transform geo-information, managed by park authorities, into a seamless flow that combines multiple information sources from different governance levels (European, national, regional), and exploits this newly combined information for the purposes of planning, management and tourism promotion. Ocean Scenario, on the other side, is essentially constituted by a centrally running geoportal that allows users to view oil spill information in 3 regions over European Seas, making

P. Villa (✉) · M. A. Gomarasca
CNR-IREA, Institute for Electromagnetic Sensing of the Environment,
Via Bassini 15, Milan, Italy
e-mail: villa.p@irea.cnr.it

R. Molina
GISIG, Geographical Information Systems International Group,
Via Piacenza 54, Genoa, Italy

J. M. Krisp et al. (eds.), *Earth Observation of Global Changes (EOGC)*,
Lecture Notes in Geoinformation and Cartography, DOI: 10.1007/978-3-642-32714-8_12,

use of the HUMBOLDT Framework components and providing an overall portrayal interface. Both Scenarios demonstrate the usefulness and capabilities enabled by geodata harmonisation following the HUMBOLDT approach.

1 Introduction

The implementation of the INSPIRE Directive, in the context of the roadmap to the establishment of an European Spatial Data Infrastructure (ESDI), has created a necessity for easy and convenient conversion between different models of geospatial data (Vanderhaegen and Muro 2005; Donaubauer et al. 2006).

Moreover, Digital Earth vision (Gore 1999) envisages new perspectives and points of view for all the scientific disciplines and technical sectors linked to geo-information sharing and utilisation, to a better knowledge and management of our planet. A crucial point in Digital Earth vision is the integration of services, tools and data (Grossner et al. 2008).

At the European level, the road to geo-information sharing and integration is deeply inscribed into the process of implementation of an European Spatial Data Infrastructure (ESDI) which follows the guidelines contained in the INSPIRE (Infrastructure for Spatial Information in Europe) Directive of the European Union (Commission of the EC 2007). Data model transformation across heterogeneous systems can be hampered by differences in terminology and conceptualization, particularly when multiple communities are involved (Annoni and Smits 2003). Due to traditional heterogeneity of spatial data throughout Europe, the challenge of creating a trans-national SDI has to face the topics of data harmonisation and service integration, tackled by a number of international cooperation projects in Europe during the last years (Eriksson and Hartnor 2006; Hall 2006).

The topic of geodata harmonisation finds its relevance also in the field of Earth Observation applied to Global Change studies, in particular from the point of view of:

- Cross-border and trans-national environmental issues (e.g. hydrographic boundaries do not conform to political boundaries and when tackling a natural hazard case the need is to make heterogeneous geo-information harmonised and interoperable)
- Continental to global scale (e.g. environmental/humanitarian crises linked to global change scenarios need an international approach and effective data sharing)
- Environmental domain harmonisation applications are demonstrated within HUMBOLDT (e.g. Protected Areas and Ocean Scenarios).

In order to achieve consistency between cross-border datasets and applications, the EC has promoted the implementation of geodata harmonisation procedures and tools, and supported the development of HUMBOLDT project, starting from october 2006. During its development, HUMBOLDT has implemented a

framework for harmonisation of spatial data which overcomes a number of deficiencies in interoperability and semantic gaps, as well as supports a vast range of application domains, data models and processes (Bernard et al. 2005; Smits and Friis-Christensen 2007).

Main result and milestone of HUMBODT is the implementation of efficient, cost-effective, reliable, generic, interoperable and sustainable solutions for the issue of spatial data harmonisation and integration of geographic services a geo-service architecture framework. This objective has been reached in strong connection with INSPIRE rules and teams guidance, using international standards (OGC, ISO) and using as core reference the users' requirements and needs, finally establishing a community of users and developers (http://community.esdi-humboldt.eu/), composed by research partners, public institutions and private companies, which has ensured the endurance sustainability of HUMBOLDT Framework well after the formal end of the project (Villa et al. 2007).

2 Geodata Harmonistation with HUMBOLDT

HUMBOLDT (http://www.esdi-humboldt.eu/) is a 54 month (2006–2011) EC supported project which aims at contributing to the implementation of a European Spatial Data Infrastructure (ESDI) that integrates the diversity of spatial data available for a multitude of European organisations. The main goal of HUMBOLDT is to enable organisations to document, publish and harmonise their spatial information. The software tools and processes created demonstrate the feasibility and advantages of the initiative INSPIRE (Infrastructure for Spatial Information in Europe) as planned, meeting the goals of Global Monitoring for Environment and Security (GMES).

Under the coordination of Fraunhofer Institute for Computer Graphics 28 project partners from 14 European Countries work together on 12 work packages. The HUMBOLDT project partners represent a multitude of data users and providers, from private companies to public authorities, including universities and other research institutions, which ensured as broad and comprehensive as possible perception of spatial data management and processes.

The work packages are organized along a two-pronged approach (see Fig. 1) has been designed and followed. This approach focuses on integrating both concrete application requirements but also technical innovations, best practices and research results (Villa et al. 2008).

An essential element of the application driver side of the project is the development of so-called HUMBOLDT Scenarios in which the different components are applied and tested under realistic conditions and which represent different GMES application fields, ranging from border security to urban planning, risk management and the protection of nature.

An essential element of the application driver side of the project is the development of so-called HUMBOLDT Scenarios in which the different components

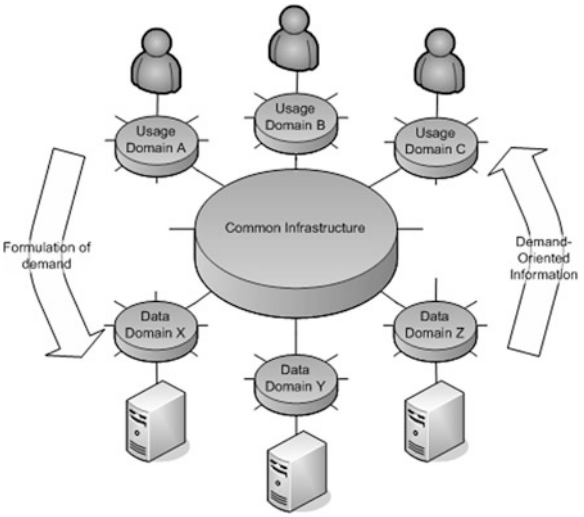

Fig. 1 The user-driven approach of HUMBOLDT project to geodata harmonisation

are applied and tested under realistic conditions and which represent different GMES application fields, ranging from border security to urban planning, risk management and the protection of nature.

For these Scenarios, a process analysis is done which shows the steps necessary to harmonise data and metadata. The different stakeholder groups have to act as drivers, to ensure that the technological development fulfils their requirements as good as possible.

During the years, a number of application Scenarios were addressed by the HUMBOLDT partnership. They are organized along the core themes defined for GMES:

- **Border Security**: Effective Border Control and Security in Rural Areas
- **Urban Planning**: European Urban Management Information Systems
- **Urban Atlas**: Enforcing GMES in Urban areas mapping core services
- **Forest**: Saxony and Czech Cross-Border Forest Scenario
- **Protected Areas**: Management of Protected Areas
- **ERiskA**: Environmental Risk
- **Transboundary Catchments**: Cross border water basin Management
- **Ocean**: Oil/Contaminants spill crisis impact and management
- **Atmosphere**: Integration for Atmospheric Data Distribution.

3 Harmonisation Framework

In the scientific context of geo-data harmonisation under a European perspective, the main technical outcome of HUMBOLDT project consist in the delivery and implementation of the HUMBOLDT Framework for data harmonisation and service integration. This software framework is the hull for the various data

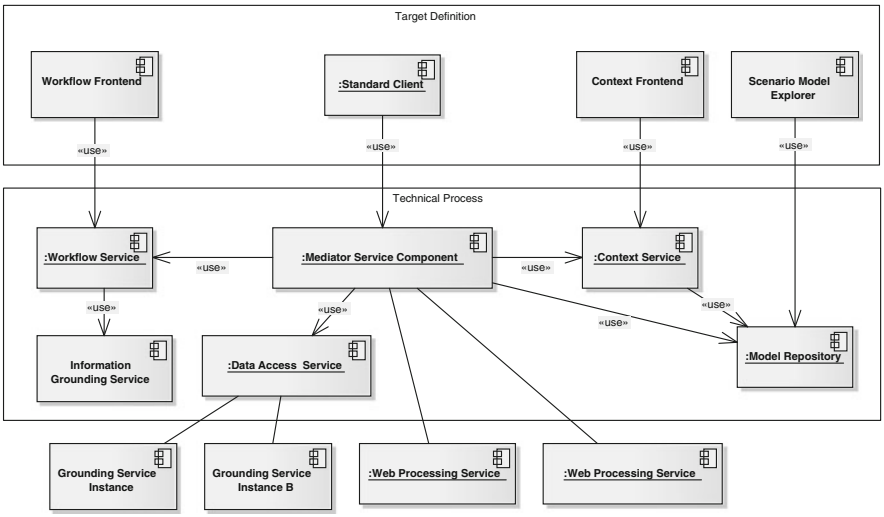

Fig. 2 Overview of HUMBOLDT framework components

harmonisation scenarios and provides the common functionality required by the Scenarios. Its potential users are the developer community and the application developers using it to create end-user applications and scenarios (Schulze Althoff and Giger 2009).

The Framework (see Fig. 2) offers a base for Scenarios and project-external data harmonisation instances and it will also profit from this usage and the feedback that will inevitably be generated (Fitzner and Reitz 2009). The Framework has been evaluated against those Scenarios and instances for its developer-friendliness, capabilities in addressing user's needs and robustness.

The architecture of the HUMBOLDT Framework, SOAP based, has been centered on an approach which comprises as the fundamental part a Mediator Service, a proxy which acts as controller of the service components that are part of the Framework for Service Integration. It offers a number of standard OGC interfaces like WMS, WFS or WCS to clients. The **HUMBOLDT Mediator Service** combines a number of different functionalities and hides them behind standard OGC interfaces. It is a Workflow Engine, capable of executing chains of geoprocessing services as well as a Feature Portrayal Service, dynamically portraying Features and serving them via the OGC WMS interface. The Mediator Service orchestrates a set of more specialized interfaces which are also integrated in the Framework architecture, as:

- **The HUMBOLDT GeoModel Editor**

An easy-to-use editor for application experts, aiming at collecting all required information on the geodata. The HUMBOLDT GeoModel Editor is producing and providing a graphical and a textual representation of the data model containing basic spatial data types.

- **The HUMBOLDT Alignment Editor**

A tool with a rich graphical user interface for defining mappings between concepts in conceptual schemas (application schemas created with the HUMBOLDT GeoModel Editor), as well as for defining transformations between attributes of these schemas.

- **The Context Client**

It allows users to create and manage contexts and user/organisation profiles. Within this approach, the term Context refers to a set of constraints on geospatial data sets, such as constraints on language, spatial reference system or bounding box.

- **The Workflow Designer**

The graphical user interface of the Workflow Design and Construction Service (WDCS). It allows users to register, manage and graphically compose geoprocessing components into workflows.

- **The Context Service**

It enables users to formulate and formalise their demand on geospatial data. It allows users to specify the behaviour of a standard OGC conformant data providing web service, i.e. the Mediator Service, by providing their requirements on spatial data in the form of a set of constraints, i.e. the context.

- **The Workflow Service**

The Workflow Service delivers executable workflows comprised of download and processing services to the Mediator Service.

- **The Information Grounding Service**

In this approach, there is also an overlay component dealing with catalogue-like functionality. This component is called the Information Grounding Service (IGS). The IGS is a cascading catalogue in the sense that it holds information on other catalogues and metadata stores in addition to metadata of data sources.

- **The Model Repository**

The Model Repository is a service component that allows maintenance of application schemas (e.g. those created with the HUMBOLDT GeoModel Editor) and mappings between those (e.g. those created with the HUMBOLDT Alignment Editor).

- **A Set of Transformation Services**

Coordinate Reference System Transformation Service; Schema Transformation Service; Multiple-Representation Merging Service; Edge Matching Service; Language Transformation Service.

The transformation and harmonisation process and its feasibility and efficiency, strongly depends on the availability of the description of transformation rules from the viewpoint of the conceptual schema level.

All those aspects and issues are being tackled within the HUMBOLDT project environment, on the path leading to the actualization of INSPIRE efforts into an ESDI.

4 Application Scenarios for Data Harmonisation within GMES

4.1 Protected Areas Scenario

The Protected Areas Scenario in the context of the HUMBOLDT project focuses on transforming geo-information, managed by park authorities, into a seamless flow that combines multiple information sources from different governance levels (European, national, regional), and exploits this newly combined information for the purposes of planning, management and tourism promotion. This is demonstrated using HUMBOLDT tools a Desktop and Web GIS environment together with a server environment.

One of the main objectives of the HUMBOLDT project is to provide tools to map and transform complex database and application schemas. In this sense, the current work of the Protected Areas Scenario is focused in harmonizing Protected Areas data from various countries using the HUMBOLDT Alignment Editor. The aim of this tests is the creation of step-by-step examples on how to use the HALE tool covering different aspects of schema mapping and different functions in terms attribute transformation, giving special relevance to testing and exploit the Annex I Protected Sites data theme for INSPIRE-compliant data provision (Villa et al. 2011).

All the operations have been done using Open source tools, from the pre-processing of the data sets to the visualisation of final results.

The Scenario defines a number of use cases for which detailed user stories have been developed to address and examine planning and management issues, as well as tourism added value. The Scenario develops the harmonisation process via active engagement with various stakeholders at the national and trans-national levels including national authorities and European agencies.

More specifically the use cases investigated by the Scenario are related to a strategy of which the pursued aims are:

- **Creation** of a geo-spatial **repository** where stakeholders contribute and share available geo-information from any source; final users can browse this information.
- **Management** (use of geo-information by planners and officers)
- **Promotion** of its assets for a **sustainable use** (access to geo-information by citizens in order to receive their useful feedback).

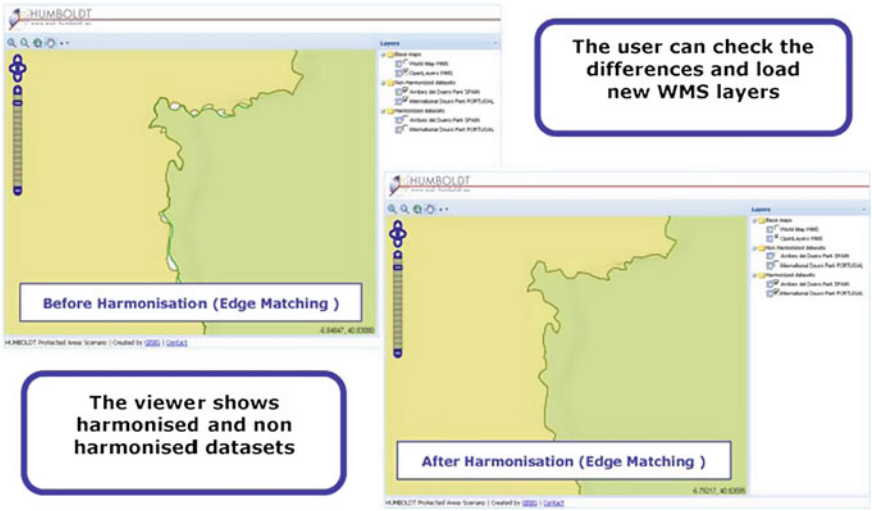

Fig. 3 Example of edge matching service WPS results over cross-border (Spain and Portugal) protected areas data layers

Namely, the HS Protected Areas is investigated in order to provide harmonisation support especially for the interaction between various levels of work and administration: management bodies, local stakeholders, national authorities, European agencies, cross-border administrative bodies.

The Scenario is tested in two areas, one between Portugal and Spain, covering the Douro river natural Park in Portugal and the Arribes del Duero Park in Spain, and in Italy, covering the Beigua Regional Park. An example of harmonisation using HUMBOLDT Edge Matching Service in the context of Protected Areas Scenario is given in Fig. 3.

The below scheme of actors is drawn upon the following classification of purposes in using geo-data and geo-information:

- **Preservation**
- **Re-naturalisation** (for example in changing situations such as landscape change and protected landscape)
- **Exploitation** (for sustainable development)
- **Commercial use** (e.g. for tourism)
- **Science and education.**

Beside the scope of use, you can consider the kind of target users, an example of which are the end users, involved in browsing geo-information (aggregated information: the lowest level of access) or geo-data (information elements). They are decision makers, tourism operators or citizens (the last ones intended as persons).

As already mentioned, Protected Area Scenario is structured into Use Cases that consist in applications of different harmonisation instances related to different

requirements and users. A brief summary of the considered use cases is given here (of which the the first two will be developed in detail):

- **Management of a Protected Area**—The main task is to create plans and managing the protected area.
- **Tourism valorisation in a Protected Area**—The main task is to exploit at the best the area and enjoy its offer of nature.
- **Impacts of infrastructure on a Protected Area**—The main task is to communicate the impact of infrastructure on protected areas.
- **Data processing in a Protected Area**—The main task is enabling local authorities to perform environmental analysis on protected areas geodata.

4.2 Ocean Scenario

The Ocean Scenario aims to answer common queries and provide information to policy makers and scientists such as where oil and chemical spills have occurred and what is the potential threat of an oil spill impacting on a protected area of the marine environment. Therefore the Ocean Scenario considers many aspects of oil spills including model trajectory predictions, pollution reports and sensitive area information. This Scenario develops through 4 national use cases (France, Greece, UK, Netherlands) demonstrating data harmonisation across all of the ocean area test cases, shown in a common and unique geoportal.

In the context of the France use case, for example, a pollution report is recorded by the CEDRE (French Institution in charge of oil drifts and pollution events) each time a pollution event occurs in France. It gathers information on the pollution such as its classification, date, position and geographical extent as well as other features.

CEDRE pollution reports (POLREP) gather information on the pollution event such as its classification, date, position and geographical extent as well as other features. It also mentions the observer identity, the wind strength and direction, the sea state, the pollution source when it is known, and if a statement was made or not.

A synthesized information is produced to the users, as decision makers, on a daily basis on the evolution of the oil spill using the most appropriate data stored either inside or outside. The Scenario needs to search, browse, visualize, and download ocean data produced by various data providers (see example in Fig. 4).

A pollution incident could cross borders, and it is important that those data could be available from different countries and be displayed together (Schaap and Lowry 2010). The Ocean Scenario aims at solving these requirements by use of the HUMBOLDT tools and where applicable demonstrate the INSPIRE approach. In order to combine, query and view data from different sources, INSPIRE sets out target schemas for specific data types. The Ocean Scenario partners (France, UK,

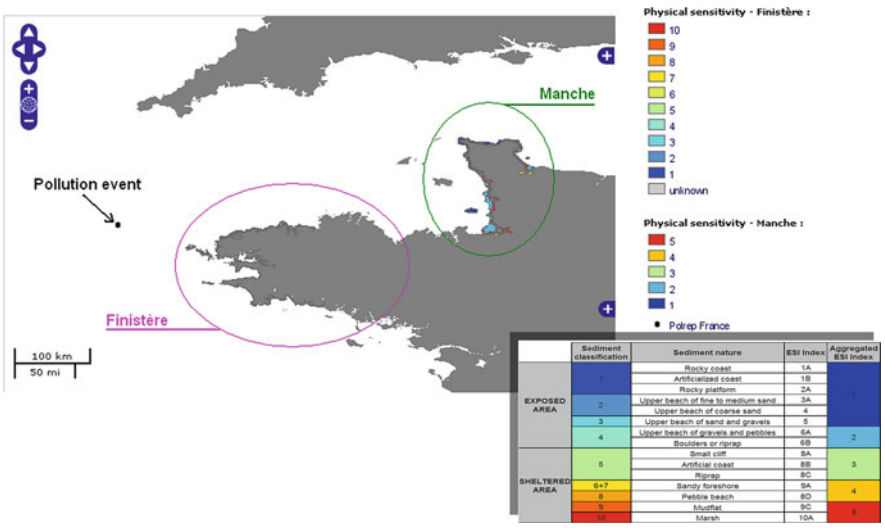

Fig. 4 Example of classification schema mapping with HALE over north France ocean scenario datasets in the context of oil spill crisis management

Greece) had to define their own target model for Polrep in order to be able to share the Polrep data. Then, the INSPIRE Protected Sites Data Specification was chosen as the target model for protected sites. Finally, as French administrative units provide different environment sensitive index (ESI) for their coasts, we also need to harmonise, at a national level, these indices into a common sensitive index. So the main task is to define a mapping between the source and the target models and then execute such transformation to the data sources in order to make data available for the Ocean Scenario.

An example of Ocean Scenario application is a simulation of a pollution event monitoring. The pollution event threatens the French waters: an oil tanker has crashed at the channel entrance and oil is leaking from tanks.

We arbitrarily decide that two administrative units will be affected by the pollution: Finistère and Manche. Those two administrative units produce a physical sensitive index on their coasts but they are not expressed in the same scale of values and with the same reference.

In this case, we have to define a common sensitive index for both Finistère and Manche administrative units. In the Manche administrative unit, an aggregated Environment Sensitive Index (ESI) based on 5 classes is used while a sediment classification based on 10 classes is used in the Finistère. As it is more difficult to display effectively 10 indexes than 5, and impossible to recreate information from 5 classes to 10, we will set the Manche sensitive index as a common sensitive index.

In order to transform the classification from Finistère to the one from Manche, we will use the mapping defined above thanks to the ESI Index. To perform such harmonisation the following HUMBOLDT tools have to be used:

- **The HUMBOLDT Alignment Editor** (HALE); a HUMBOLDT tool with a rich graphical user interface for defining mappings as well as transformations.
- **The Conceptual Schema Transformer** (CST); that is a HUMBOLDT Web Processing Service for applying a schema transformation from a schema mapping.

5 Conclusions

This paper has described the structure and approach of the HUMBOLDT project, giving a rationale for the implemented harmonisation framework capabilities and discussing the outcomes of two use cases for geodata harmonisation based on application Scenarios over protected areas and ocean themes.

The major aim of HUMBODT is the implementation of efficient, cost-effective, reliable, generic, interoperable and sustainable solutions for the issue of spatial data harmonisation and integration of geographic services in the framework of an ESDI. This objective is to be reached by putting INSPIRE principles into practice, applying international standards and using as core reference the users' requirements and needs, finally establishing a community of users and developers.

HUMBOLDT framework is an architecture of software components and services aimed at managing the harmonisation process of geo-information within the European context. The methodology of the HUMBOLDT development is based on a dual approach, comprising both a technological and an application side, and on an iterative process of implementation, during which the solutions found are tested and validated with the cooperation of an application momentum, composed of Scenarios which cover topics of utmost importance in GMES.

Among those Scenarios, Protected Areas Scenario focus the harmonisation works on schema mapping and transformation of the structure and geometry of datasets of Protected Areas for the purposes of planning, management and tourism promotion, and demonstrates HUMBOLDT capabilities for geodata harmonisation in protected areas domain. Another example presented deals with Ocean Scenario, which aims to answer common queries and provide information to policy makers and scientists such as where oil and chemical spills have occurred and what is the potential threat of an oil spill impacting on a protected area of the marine environment.

Future outlook on activities related to geodata harmonisation, which are in the focus of the future activities of the ongoing efforts made by the HUMBOLDT Developers Community can be summarized in a short list as:

- Deeper investigation of the process of geo-information harmonization itself on a larger basis, to see what patterns emerge between data providers and consumers;
- Handling very different types of data in one contiguous infrastructure;

- Efficient execution of the process, taking into account optimizations possible by combining multiple steps;
- Development of user guidance concepts for geospatial data alignment processes, including development of languages for geospatial domain experts to describe alignments;
- Handling of semantic mismatches.

HUMBOLDT project shows challenges both to geosciences research, covering topics in data harmonisation at a continental scale, and to economic and political management of such a large and heterogeneously composed consortium of partners.

The outcomes and benefits of geodata harmonisation through HUMBOLDT approach are centered on the reduction of implementing efforts for the future ESDI, both from a technological point of view and a cost-effective approach to geodata sharing, especially in the field of: supporting geo-information management in cross-border and cross-domain applications, enhancing data and data access availability, making easier the handling of geospatial information through integrated and standardized added value services.

Those benefits regard both specialised and non specialised users of spatial data, from policy makers, planners and managers, to European citizens and their organisations, at a level which varies from local to regional to European.

Acknowledgments This paper describes work carried out by the partners of the HUMBOLDT project which is funded under the Sixth Framework Programme of the European Union (Aerospace/GMES), with contract number SFP5-CT-2006-030962.

References

Annoni A, Smits PC (2003) Main problems in building European environmental spatial data. Int J Remote Sens 24(20):3887–3902

Bernard L, Kanellopoulos I, Annoni A, Smits PC (2005) The European geoportal—one step towards the establishment of a European spatial data infrastructure. Comput Environ Urban Syst 29:15–31

Commission of the European Communities (2007) Directive 2007/2/EC of the European Parliament and of the council of 14 March 2007 establishing an infrastructure for spatial information in the European community (INSPIRE). Official J, L 108, 25/04/2007, pp1–14

Donaubauer A, Fichtinger A, Schilcher M, Straub F (2006) Model driven approach for accessing distributed spatial data using web services—demonstrated for cross-border GIS applications, Proceedings of the XXIII FIG congress, Munich (Germany), 8–13th of Oct 2006

Eriksson H, Hartnor J (2006) Data harmonisation requirements (RISE project), retrieved from: http://www.eurogeographics.org/eng/documents/RISE13_Data_Harmonisation_Requirements_v1.0.pdf. Accessed 20 April 2011

Fitzner D, Reitz T (2009) A lightweight introduction to the HUMBOLDT framework V3.0. HUMBOLDT public project report, retrieved from: http://www.esdi-humboldt.eu/files/0982-a5_2-d3__3_0__a_lightweight_introduction-fhg-igd-004-final.pdf. Accessed 27 March 2012

Gore Albert (1999) The digital earth: understanding our planet in the 21st century. Photogram Eng Remote Sens 65(5):528

Grossner K, Goodchild MF, Clarke K (2008) Defining a digital Earth system. Trans GIS 12(1): 145–160

Hall M (2006) A Semantic Similarity Measure for Formal Ontologies, Master Thesis in Informatics, Institut fur Informatik-Systeme, Alpen-Afria Universitat Klagenfurt, March 2006, retrieved from: http://harmonisa.uni-klu.ac.at/downloads/thesis_mark_hall.pdf. Accessed 13 August 2012

Schaap DMA, Lowry RK (2010) SeaDataNet—pan-European infrastructure for marine and ocean data management: unified access to distributed data sets. Int J Digital Earth 3(1):50–69

Schulze Althoff J, Giger C (2009) Concept of data harmonisation process. HUMBOLDT public project report, retrieved from: http://www.esdi-humboldt.eu/files/0954-a7_0_d2__concept_of_data_harmonisation_processes-ethz-001-final.pdf. Accessed 27 March 2012

Smits PC, Friis-Christensen A (2007) Resource discovery in a European spatial data infrastructure. IEEE Trans Knowl Data Eng 19(1):85–95

Vanderhaegen M, Muro E (2005) Contribution of a European spatial data infrastructure to the effectiveness of EIA and SEA studies. Environ Impact Assess Rev 25(2):123–142

Villa P, Reitz T, Gomarasca MA (2007) HUMBOLDT project: implementing a framework for geo-spatial data harmonization and moving towards an ESDI. Geoinformation in Europe, Proceedings of the 27th EARSeL symposium, Millpress, pp 29–36

Villa P, Gomarasca MA, Reitz T (2008) HUMBOLDT project for data harmonization in the framework of GMES and ESDI: introduction and early achievements. In: The international archives of the photogrammetry, remote sensing and spatial information sciences, vol 37, Part B4, pp 1741–1746

Villa P, Molina R, Gomarasca MA, Roccatagliata E (2011) Harmonisation requirements and capabilities towards an ESDI: the HUMBOLDT protected areas scenario. Int J Digital Earth. doi:10.1080/17538947.2011.585183

Detailed Damage Assessment After the Haiti Earthquake

Danielle Hoja, Thomas Krauss and Peter Reinartz

Abstract In the post crisis phase a much more detailed analysis can be done with higher accuracy and less pressure of time compared to the general situation assessment of the rapid mapping process directly after the crisis. In this investigation the analysis is concentrated on the urban area of the capital town of Port-au-Prince. In order to develop a service for detailed damage assessment, methods of (semi-)automatic change detection are used and compared, since up to now, damage information was mainly derived by visual interpretation. Any improvement in terms of accuracy and speed of analysis is of relevance to users in this context. The results of the different change detection algorithms achieved using the Haiti datasets are compared to each other and also to the database of the Haiti Action Plan for Reconstruction and Development (PDNA). The results are very promising although further improvements have to be made.

1 Introduction

Directly after a crisis or catastrophe an important part of information generation for the response and relief effort is the production of crisis maps (rapid mapping) for humanitarian relief organisations. For immediate aid and the general situation assessment fast information is needed about damages to infrastructure and affected areas. This analysis is expected as fast as possible and even important if not exact in all details.

D. Hoja (✉) · T. Krauss · P. Reinartz
Remote Sensing Technology Institute, German Aerospace Center (DLR),
Wessling, Germany
e-mail: danielle.hoja@dlr.de

J. M. Krisp et al. (eds.), *Earth Observation of Global Changes (EOGC)*,
Lecture Notes in Geoinformation and Cartography, DOI: 10.1007/978-3-642-32714-8_13,

A more detailed analysis of the damage situation can be done in the post crisis phase with much higher accuracy, but with less pressure of time. Users are interested in a detailed damage assessment to support the estimation of losses and funds needed for reconstruction. The information may be used during post-conflict needs assessments, in donor conferences or in bilateral/multilateral negotiations. Some time after a crisis in the rehabilitation and reconstruction phase, the development of the infrastructure rebuilding can be monitored by the same methodology. Especially a supervision of an appropriate utilisation of the allocated funds is of interest to the donators.

All these services, i.e. rapid mapping directly following a crisis or catastrophic event, long-term damage assessment and reconstruction monitoring, are developed in the EU project GMES Services for Management of Operations, Situation Awareness and Intelligence for Regional Crisis (G-MOSAIC) and applied to datasets acquired after crisis situations as the Haiti earthquake. They are all implemented in so-called "Service Chains" describing the data flow and processing done by several partners in the project.

On January 12, 2010 a severe earthquake took place at the coast of Haiti with a magnitude of 7.0 causing major damage. The epicentre was registred about 10 km deep and 16 km southwest of the capital city Port-au-Prince. In the city a large number of buildings such as the palace, government and UN buildings, embassies and hospitals were affected or destroyed. Telecommunication as well as electricity and water supply failed.

In this chapter we show first results of the long-term damage assessment service chain in the context of the Haiti earthquake. Section 2 provides an overview of the available datasets and the preprocessing applied. Section 3 presents three change detection methods and their application to the data. This is followed by conclusions and an outlook in Sect. 4.

2 Datasets and Preprocessing

The analysis is concentrated on the urban area of the capital town of Port-au-Prince. Different datasets are available for the analysis, mainly scenes of the very high resolution (VHR) GeoEye-1 satellite providing data with 50 cm ground sampling distance (GSD) and stereo capabilities. Three scenes were acquired: October 2009 (before crisis, no stereo), January 2010 (four days after the earthquake, stereo) and August 2010 (after crisis, stereo). The rapid mapping results collected in the database Post Disaster Needs Assessment and Recovery Framework (PDNA) are used for comparison. Also the airborne data used to receive these PDNA database are available for the study. Additionally, manual change detection was applied directly with the datasets for a first evaluation of the algorithms taking into account the state of change directly at the time of acquisition of the satellite images. The challenges of validating image-based results to each other and to ground truth data for damage assessment products is described in

(Kerle 2010), e.g. rapid mapping results typically not evaluated due to lack of time and the contrast between the vertical perspective of the image data (rubble piles, disintegrated roofs) versus the field perspective (collapsed walls).

An important requirement for automatic change detection is a very good co-registration of pre- and post-disaster scenes. One of the scenes to be analysed is defined as reference scene and all other images are co-registered onto this scene. The automatic processing chain developed at DLR combines the orthorectification with the co-registration, so only one resampling step is necessary (Müller et al. 2010). After an automatic image matching with respect to the reference scene, the information for the direct georeferencing (attitude data or RPC) is adjusted using these matched points. With this information and a digital surface model (DSM) the scene is orthorectified providing co-registered results with better than ½ a pixel accuracy. Additionally a pansharpening is applied to the datasets taking into account the high spatial resolution of the panchromatic image as well as the radiometric information of the multispectral data. Figure 1 shows a subset of the co-registered and pansharpend images of the Haiti dataset.

As two of the scenes were available as stereo scenes, a new approach was tested to orthorectify the images using the digital surface model generated by the stero pairs. This leads to more accurate results compared to the orthorectification using other DSM (e.g. SRTM) not only due to the better resolution but also due to the better co-registration of images and DSM (d'Angelo et al. 2010). Therefore, at first digital surface models are derived by dense stereo matching and forward intersection and sub-sequent interpolation into a regular grid. Orthorectified images are produced in the second step using the affine RPC correction and the generated DSM.

The resulting DSM contains a small amount of blunders, e.g. due to matching errors in regions with sparse texture. These blunders cause some distortions in the resulting orthoimage that are responsible for some errors in the change detection. In future, these blunders have to be removed and data gaps in areas where the matching failed or outliers were removed have to be filled, e.g. with SRTM data using the delta surface fill method (Grohman et al. 2006).

3 Change Detection Methods: Application and Results

Both service chains of long-term damage assessment and reconstruction monitoring use the methods of change detection (CD). Up to now, damage information was mainly derived by visual interpretation of pre- and post-disaster satellite data. Any improvement in terms of accuracy and speed of analysis using the methods developed within the G-MOSAIC project is of relevance to users in this context.

Singh (1989) provided a first overview of change detection methods. The fundamental conclusion was that various procedures of change detection produce different maps of change even in the same environment. Methods are classified into different categories, e.g. pixel- vs. object-based, analysis of image data vs. classification results, etc. Lu et al. (2004) grouped the change detection methods into seven categories

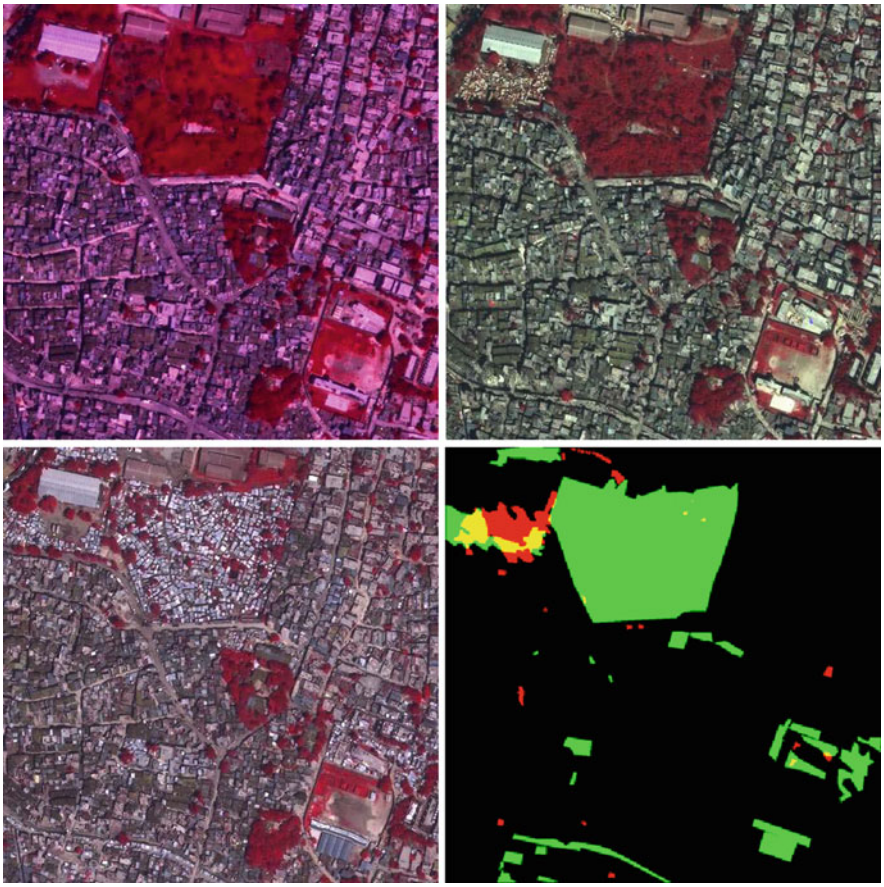

Fig. 1 Subset (500 × 500 m) of Port-au-Prince, Haiti showing the development of a refugee camp after the earthquake on 2010/01/12. (*Top left*) GeoEye, 2009/10/01—PRE; (*Top right*) GeoEye, 2010/01/16—PO1; (*Bottom left*) GeoEye 2010/08/18—PO2; (*Bottom right*) manual measured changes between PRE → PO1 (in *red*) and between PO1 → PO2 (in *green*) (areas changed in both time frames are *yellow*)

including algebra, transformation, classification, advanced models, Geographic Information System (GIS) approaches, visual analysis and other not so frequently used approaches. Different comparisons of methods revealed that simple methods may perform better than complex methods (e.g. Coppin and Bauer 1996; Liu et al. 2004). Since segmentation and object definition introduce new challenges into the image processing, work in this project was concentrated on pixel-based algorithms.

After the co-registration, the simple algebraic change detection method of differencing is applied to the datasets. It is relatively easy to implement and provides fast results. In a second step a more complex method from the transformation category, namely multivariate alteration detection (MAD) is applied. Finally 3D change detection as advanced method of the algebra category is tested.

The results gained automatically are investigated manually for the high accuracy requested by the user. However, such a semiautomatic service chain is still faster than a complete manual analysis.

3.1 Basic Change Detection: Image Differencing

For image differencing, an additional pre-processing step is necessary. Due to some acquisition parameters such as different acquisition dates and view angles of the sensor, there are changes that are not of interest to the user (virtual changes). The radiometric correction step aims at reducing these differences of the two temporal images caused by the variation in light and atmospheric conditions at the two acquisition dates (Bovolo and Bruzzone 2007). Here histogram normalization is used for image differencing. The histogram of the pre-event image (October 2009) is taken as reference and the histograms of the two post-event images are adjusted to it.

Next, the two co-registered images are simply subtracted pixel by pixel. Image differencing is mathematically the easiest and the most widely used automatic change detection approach that has been applied in various geographical environments (Singh 1989). Ideally, the value zero represents areas of no change while positive or negative values stand for changed areas in the difference image. Since many factors such as inaccurate co-registration can lead to virtual changes, pixels in no change areas do not necessarily have zero values. The critical step of image differencing is deciding where to place the threshold boundaries between change and no-change (Singh 1989).

The selection of the correct threshold is often done using some in situ information or the result of a manual analysis. Since the algorithm is planned as completely automatic, the threshold selection is based on statistical values. Pixels in the range of "mean ± standard deviation" are considered "no change", pixels outside this range are considered "change". These values were received in a similar study (Liang 2010; Liang et al. 2011). For multispectral images, different ways exist to deal with the single bands. In our approach, all steps are carried out for each band separately. Only after the thresholding of the image differencing result, the results obtained by single bands are combined. Best results were received taking into account only pixels indicating a change in at least three bands.

Figure 2 shows the examplary result for the changes between the two post-disaster images (four days and seven months after the earthquake). The upper left image shows the difference for band 3. The histogram (top right) shows the result for all 4 bands. The values are changed into 8bit (by adding 256 and dividing by 2). Mean value for band 3 is 127.8 (similar for all bands), the standard deviation is 17.3 (smallest value, up to 27.9 for band 2). The lower left image shows the resulting change detection map (binary image). After the removal of pixels indicating change only in one or two bands, some morphological operators were also applied (opening, closing) to remove spurious pixels. In the lower right corner the image is overlayed with the manual measurement.

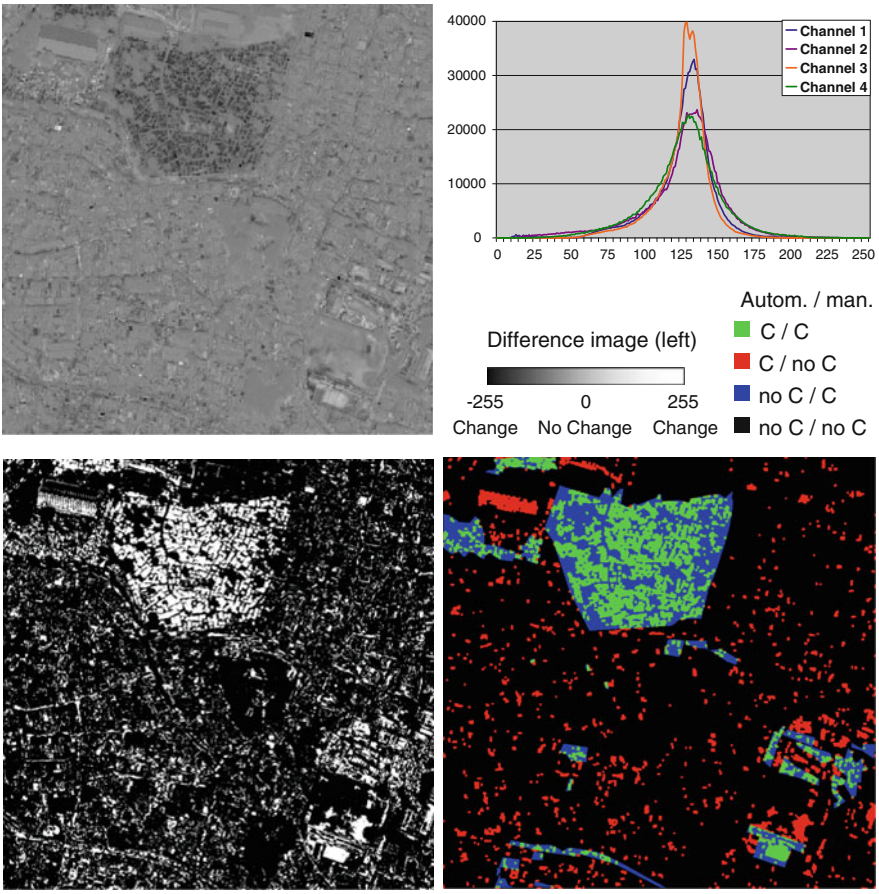

Fig. 2 Same detail as Fig. 1. (*Top left*) difference image; (*Top right*) histogram of difference; (*Bottom left*) resulting binary change detection map, *White* = change; (*Bottom right*) overlay of difference binary map ("Autom.") and manual measurement ("man."; C = Change)

The colours in this overlay image indicate the correctness of the automatic algorithm in comparison to the manual measurement. Green areas indicate changes in both the automatic derived binary map as well as in the manual measurement, whereas black indicates "no change" in both change maps. Blue colour indicates areas, which have changed according to the manual measurement but were not detected by the automatic algorithm. As can easily be seen, there are no solely blue areas, they occur only in combination with green areas. So there are at least some changes nearby, and a manual verification of the automatic measurements will finish with the correct result. Additionally, it can be seen, that the manual measurement marked large areas of change (green and blue together), e.g. the complete refugee camp as one changed area. As can be seen in Fig. 1, there are still some trees inside this area, which of course do not appear as change in the automatic

algorithm. Finally, red colour indicates areas defined by image differencing as change, but not in the manual measurement. These areas are mostly changes not of interest (i.e. vegetation changes) and have to be removed in a following verification step. However, the areas to be analysed (red and green) are significantly smaller than the complete image, which has been analysed manually so far.

3.2 Multivariate Alteration Detection

To avoid radiometric correction as well as band selection, another promising difference-based change detection method is iteratively reweighted multivariate alteration detection (IR-MAD). MAD analyses multispectral data by utilizing all the bands simultaneously. The method is based on an established multivariate statistical technique: canonical correlation analysis (CCA). As CCA finds a linear combination of the original multispectral data ordered by decreasing correlation between pairs, MAD transformation determines the difference between linear combinations of the original multispectral bands ordered by variance. A detailed analysis can be found in Nielsen (2007).

IR-MAD calculates original MAD variates firstly, and then in the following iterations, puts large weights on the observations which show little change. This is achieved through calculating a measure of no change based on the sum of squared, standardized MAD variates in each iteration, little change means that the sum of squared, standardized MAD variates is small (Nielsen 2007). The iterations are continued until the largest absolute change in the canonical correlations reaches a predefined value, e.g. 10^{-3}.

Additionally to the four multispectral bands, the input image to the MAD algorithm is combined with some texture information. It is based on the idea that damaged areas should be rich in textural features compared with the same areas before damage or after reconstruction, which mainly consist of regular buildings showing fewer textural features (Liang 2010; Liang et al. 2011). The widely used texture modeling is the grey level co-occurrence matrix (Haralick 1973) due to its simplicity and low computational complexity, which has been proved very efficient in texture modeling. The textural feature inverse difference moment (indicating the local homogeneity of an image) is calculated within a 5×5 pixel window, which makes a good distinction between the original two images.

In this study, the resulting Chi-square image incorporating all the information of MAD variates is used for the final thresholding. This step is carried out using the ImageJ toolbox (Landini 2010; ImageJ Toolbox 2011) providing different automatic thresholding methods. Here, the common global thresholding method by Otsu (1979) is applied. The algorithm searches for the optimal threshold that maximizes the separability of the resultant classes in grey levels assuming that the image is composed of only two classes: object and background.

Figure 3 shows some intermediate results of applying the IR-MAD algorithm to the dataset shown in Fig. 1. The top two images are the first two variates of the

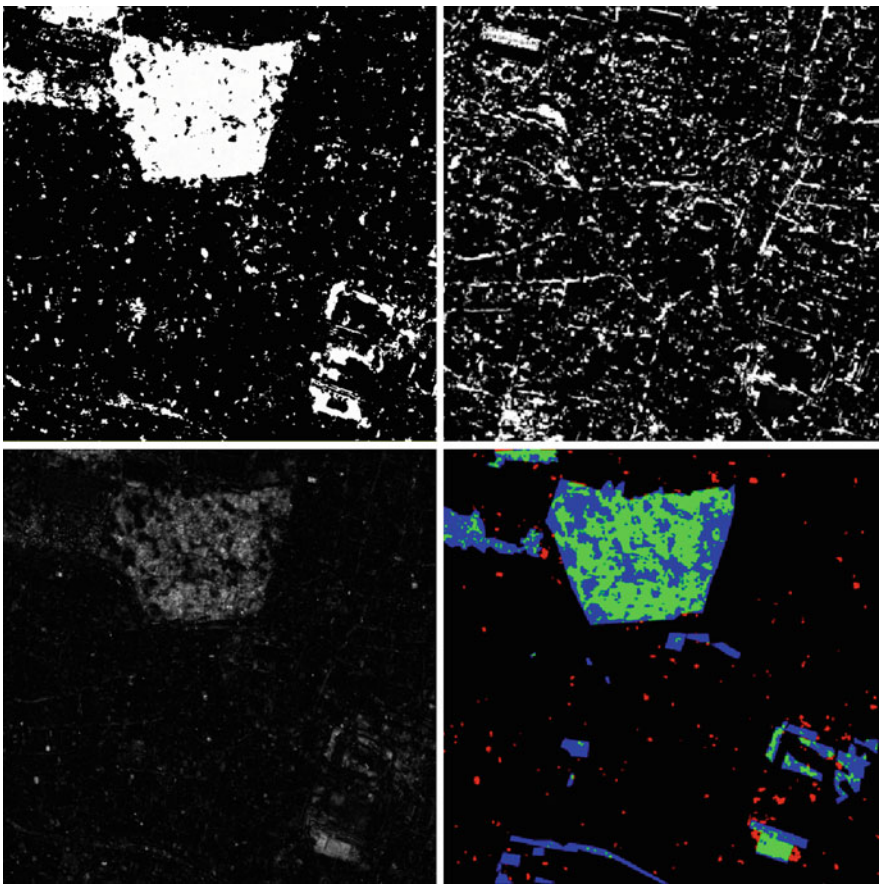

Fig. 3 Same detail as Fig. 1. (*Top*) IR-MAD variate 1 and 2, *White* = change; (*Bottom left*) result of MAD algorithm: Chi-square image, lighter = higher probability of change; (*Bottom right*) overlay of resulting IR-MAD binary map and manual measurement (legend: see Fig. 2)

algorithm. The IR-MAD algorithm results in n variates when applied to two images with n channels each. The different variates show different changes and are in descending order (therefore only the first two are shown here). The Chi-square image as combination of all variates is shown in the lower right corner. After the post-processing (thresholding and morphological operators) the image is overlayed again to the manual measurement. The distribution of green and blue areas is similar to the result of image differencing, whereas the red areas are strongly reduced. The manual verification will be much faster with this result.

3.3 3D Change Detection

A more sophisticated damage assessment analysis is applied using 3D change detection approaches. Unfortunately for most catastrophic events no height information like DSM or very high resolution satellite stereo image pairs is available for the pre-disaster time. So these approaches are normally only applicable in reconstruction applications. For monitoring issues VHR satellite stereo images are acquired following the crisis. 3D change detection methods show changes, which can hardly or even not be seen in comparing 2D imagery like changes in heights and volume of buildings, waste dumps, and other objects.

As for both of the post-crisis Haiti datasets stereo scenes were ordered, the DEM were already generated during the pre-processing (see above). Here, the DEM are used for change detection. The height differences are calculated by simple subtraction of both DEM. The resulting image can be seen in Fig. 4 (bottom). Here, another area of Port-au-Prince is choosen due to the blunders in the DEM as described above (no blunders in this area). The difference image shows clearly positive (white) and negative (dark) changes. Negative changes indicate a lower height in the second image; there some object has been removed. Positive changes indicate some increase in height. As can be clearly seen in the upper left corner, the formerly empty space has been filled with refugee tents and even some building as indicated in the DEM change map. Also in the lower part of the image, the building has been extended, which cannot be seen in the 2D images.

Next step in the 3D change detection would be the automatic post-processing of the 3D difference image as e.g. shown in (Tian et al. 2011; Chaabouni-Chouayakh et al. 2011). To receive better results, region detection is applied to the orthoimages. Further an object-based feature analysis is carried out, differentiating the regions into infrastructure (of main interest) and vegetation (not of interest). Some threshold has to be defined to finally differentiate between measurement inaccuracy and real height changes. Additionally, some improvements of the DEM generation algorithm are needed in densly populated areas.

4 Conclusions and Outlook

This chapter shows first results of the application of the service chains for damage assessment and reconstruction monitoring developed in the context of G-MOSAIC. The results of the different change detection algorithms received with the Haiti datasets are compared to manual measurements retrieved also from these datasets. Further analysis is necessary, e.g. a comparison to the PDNA database for independent results. However, as it was already experienced during the rapid mapping, only a fraction of the damages can be seen in the VHR satellite data in comparison to

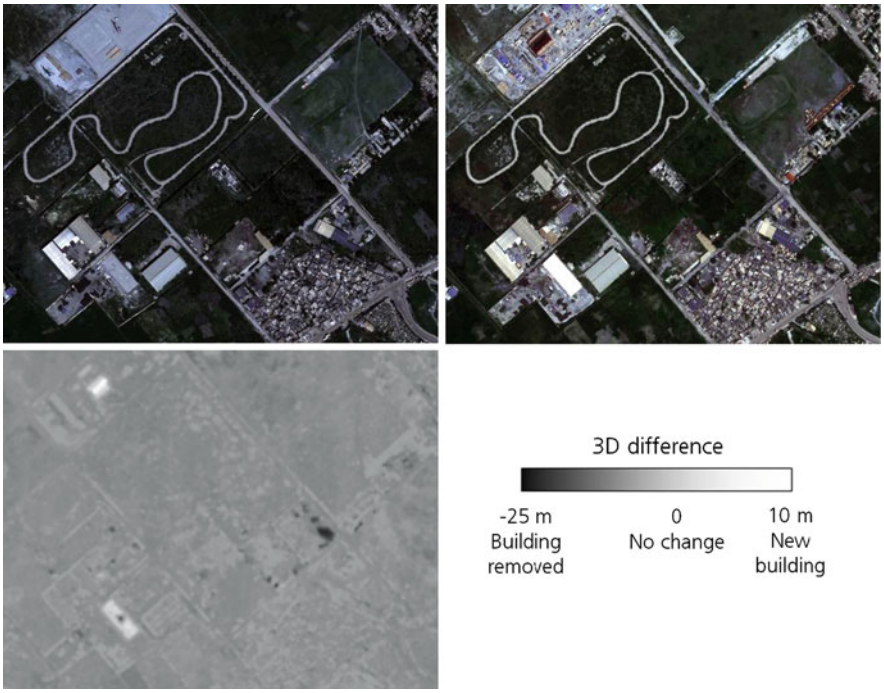

Fig. 4 (*Top*) subset (650 × 500 m) of Port-au-Prince, Haiti showing the development of another refugee camp after the earthquake on 2010/01/12 (*upper left corner*). (*Left*) GeoEye, 2010/01/16; (*Right*) GeoEye 2010/08/18; (*Bottom*) difference of DEM generated from the two stereo images

Table 1 Statistical measures for two change detection algorithms (image differencing and IR-MAD incorporating texture information) and two time frames each (PRE = 2009/10/01 → PO1 = 2010/01/16 and PO1 = 2010/01/16 → PO2 = 2010/08/18)

Quality measure	Formula	Image differencing		IR-MAD with texture	
		PRE → PO1	PO1 → PO2	PRE → PO1	PO1 → PO2
No of pixels C/C	*TP* (■)	11,091	75,072	14,352	77,517
No of pixels C/no C	*FP* (■)	111,921	68,487	59,021	10,104
No of pixels no C/C	*FN* (■)	10,975	81,032	7,714	78,587
No of pixels no C/no C	*TN* (■)	866,013	775,409	918,913	833,792
Completeness (%)	$\frac{100 \cdot TP}{TP+FN}$	50.3	48.1	65.0	49.7
Correctness (%)	$\frac{100 \cdot TP}{TP+FP}$	9.0	52.3	19.6	88.5
Quality percentage (%)	$\frac{100 \cdot TP}{TP+FP+FN}$	8.3	33.4	17.7	46.6
Overall accuracy (%)	$\frac{100 \cdot (TP+TN)}{TP+FP+FN+TN}$	87.7	85.0	93.3	91.1

the airborne data. But it can also bestated that the main areas of change are detected and give substantial hints for further manual evaluations. Therefore semi-automatic evaluation will be the method of choice for satellite data analysis in this context.

The various methods are in different development stages with the object to get a (semi-) automatic algorithm. Image differencing and IR-MAD incorporating texture information can already be applied completely automatically and only a manual verification of the results is necessary afterwards. Besides the qualitative analysis given above, Table 1 shows some quantitative statistical measures of the results. Completeness varies around 50 %, so only half of the changes are detected. But as can be seen in the figures above, no changed area remains completely undetected. The correctness is very low for the changes before/after the earthquake (9 or 19 %), whereas the changes occuring in the half year after the earthquake can be detected better. The IR-MAD algorithm incorporating texture information has a very promising value of 89 % correctness. All these figures also show that the IR-MAD algorithm usually performs better (or at least similar, but never worse) than the image differencing.

3D change detection is not yet compared to some reference data (and there are only 2D reference data available at all), but it is shown that changes can be detected. It results in the identification of changes, which can hardly or even not be seen in comparing 2D imagery like changes in heights and volume of buildings or other objects. Unfortunately for most catastrophic events no height information like DSM or just very high resolution satellite stereo image pairs are available for the pre-disaster time, but this might change in future. The intention of this research of change detection methods is that the developed methods (the best one or a combination of various) can be used in a semi-automatic way for future disaster monitoring applications where no airborne data are available.

Acknowledgments The authors acknowledge the help during processing with different parameters and the manual measurement of the test datasets carried out by Hans-Joachim Schneider and Anne de la Borderie.

The research leading to these results has received funding from the European Community's Seventh Framework Programme (FP7/2007-2013) under grant agreement No. 218822.

References

Bovolo F, Bruzzone L (2007) Image information mining in time series (IIM-TS): applicable algorithms and methods. Project report

Chaabouni-Chouayakh H, d'Angelo P, Krauß T, Reinartz P (2011) Automatic urban area monitoring using digital surface models and shape features. Joint urban remote sensing event, Munich, Germany, 11–13 April 2011

Coppin PR, Bauer ME (1996) Digital change detection in forest ecosystems with remote sensing imagery. Remote Sens Rev 13(3&4):207–234

d'Angelo P, Schwind P, Krauss T, Barner F, Reinartz P (2010) Automated DSM based georeferencing of CARTOSAT-1 stereo scenes. The international archives of the photogrammetry, remote sensing and spatial information sciences, vol 38-1-4-7/W5

Grohman G, Kroenung G, Strebeck J (2006) Filling SRTM voids: the delta surface fill model. Photogram Eng Remote Sens 72(3):213–216

Haralick RM (1973) Textural features for image classification. IEEE Trans Syst, Man Cybern 3(6):610–621

ImageJ Toolbox (2011). Image processing and analysis in Java. http://rsb.info.nih.gov/ij/, Accessed Jan 2011

Kerle N (2010) Satellite-based damage mapping following the 2006 Indonesia earthquake—how accurate was it? Int J Appl Earth Obs Geoinf 12(2010):466–476

Landini G (2010) Auto threshold and auto local threshold. http://www.dentistry.bham.ac.uk/landinig/software/autothreshold/autothreshold.html. Accessed Jan 2011

Liang W (2010) Change detection for reconstruction monitoring using very high resolution optical data. Master's thesis, TU München, 71 pages

Liang W, Hoja D, Schmitt M, Stilla U (2011) Comparative study of change detection for reconstruction monitoring based on very high resolution optical data. Joint urban remote sensing event, Munich, Germany, 11–13 Apr 2011

Liu YB, Nishiyama S, Yano T (2004) Analysis of four change detection algorithms in bi-temporal space with a case study. Int J Remote Sens 25(11):2121–2139

Lu D, Mausel P, Brondizio E, Moran E (2004) Change detection techniques. Int J Remote Sens 25(12):2365–2407

Müller R, Krauss T, Schneider M, Reinartz P (2010) A method for geometric processing of optical satellite images using automatically determined ground control information. The international archives of the photogrammetry, remote sensing and spatial information sciences, vol XXXVIII, Part 1

Nielsen AA (2007) The regularized iteratively reweighted MAD method for change detection in multi- and hyperspectral data. IEEE Trans Image Process 16(2):463–478

Otsu N (1979) A threshold selection method from gray-level histograms. IEEE Trans Syst, Man Cybern 9(1):62–66

Singh A (1989) Digital change detection techniques using remotely-sensed data. Int J Remote Sens 10(6):989–1003

Tian J, Chaabouni-Chouayakh H, Reinartz P (2011) 3D building change detection from high resolution spaceborne stereo imagery. International workshop on multi-platform/multi-sensor remote sensing and mapping, IEEE Xplore, Xiamen, China

Satellite Monitoring of Urban Land Cover Change in Stockholm Between 1986 and 2006 and Indicator-Based Environmental Assessment

Dorothy Furberg and Yifang Ban

Abstract Over the past few decades, there has been substantial urban growth in Stockholm, Sweden, now the largest city in Scandinavia. This research investigates and evaluates the evolution of land cover/use change in Stockholm between 1986 and 2006 with a particular focus on what impact urban growth has had on the environment using indicators derived from remote sensing and environmental data. Four scenes of SPOT imagery over the Stockholm County area were acquired for this study including two on 13 June 1986, one on 5 August 2006 and one on 4 June 2008. These images are classified into seven land cover categories using an object-based and rule-based approach with spectral data and texture measures as inputs. The classification is then used to generate spatial metrics and environmental indicators for evaluation of fragmentation and land cover/land use change. Based on the environmental indicators, an environmental impact index is constructed for both 1986 and 2006 and then compared. The environmental impact index is based on the proportion and condition of green areas important for ecosystem services, proximity of these areas to intense urban land use, proportion of urban areas in their immediate vicinity, and how impacted they are by noise. The analysis units are then ranked according to their indicator values and an average of the indicator rankings gives an overall index score. Results include a ranking of the landscape in terms of environmental impact in 1986 and 2006, as well as an analysis of which units have improved the least or the most and why. The highest ranked units are located most often to the north and east of the central Stockholm area, while the lowest tend to be located closer to the center itself. Yet units near the center also tended to improve the most in ranking over the two decades, which would suggest a convergence towards modest urban expansion and limited environmental impact.

D. Furberg (✉) · Y. Ban
Division of Geoinformatics, Department of Urban Planning and Environment, Royal Institute of Technology, Drottning Kristinas väg 30, 10044 Stockholm, Sweden
e-mail: slepyan@kth.se

J. M. Krisp et al. (eds.), *Earth Observation of Global Changes (EOGC)*, Lecture Notes in Geoinformation and Cartography, DOI: 10.1007/978-3-642-32714-8_14,

Keywords SPOT imagery · Object-based rule-based classification · Urban growth · Ecosystem services · Environmental indicators

1 Introduction

Over the past few decades, there has been substantial urban growth in Stockholm, Sweden, now the largest city in Scandinavia. Growth in the area is due mainly to the increasing population, which rose by 18 % between 1986 and 2006. The environment in and around Stockholm may be in the process of becoming more fragmented, especially in terms of its green areas, also known as "green wedges". Therefore, it is important to map urban land-cover changes and assess the environmental impact of these changes on the environment in a timely and accurate manner.

The objective of this research is to investigate the extent and nature of land-cover change in Stockholm from 1986 to 2006 through object-oriented, rule-based classification of satellite data, derivation of fragmentation statistics and environmental indicators based the classifications and the compilation of an environmental impact index for comparative purposes. Results are expected to reveal where and how different areas of Stockholm County have changed in terms of the impact of urban development on the natural environment in recent decades.

2 Study Area and Data Description

Stockholm municipality covers an area of around 216 km^2, while Stockholm County, a much larger region, covers 6 519 km^2 (STOCKHOLMS STADS UTREDNINGS- och STATISTIIKKONTER AB 2011). The planning authorities in Stockholm have called this area of Sweden a "green big city region." (REGIONPLANE- och TRAFIKKONTORET 2002) Greater Stockholm's "green wedges" that lead from the countryside in towards the more central parts of the city and the green links between these wedges comprise the framework of the region's green structure. Stockholm recently won the 2010 Green Capital Award from the European Union and has a vested interest in preserving the balance between its green and built-up spaces. Yet the region's population continues to grow, putting added pressure on the natural environment and increasing demand for built-up areas. This study seeks to find out what has occurred in relation to green areas and in terms of urban growth within the county of Stockholm over a recent 20 year period.

Four scenes of SPOT imagery over the Stockholm area were acquired for this study: two on 13 June 1986, one on 5 August 2006 and one on 4 June 2008. The images were selected from the height of the vegetation growing season to

maximize the differences between built-up areas and vegetation in order to reduce detection of unreal changes caused by seasonal differences between years. Two scenes from 2006 were sought but an appropriate 2006 growing season image over the northern parts of Stockholm County was simply not available. The scene from 2008 is therefore used as a substitute. The SPOT imagery from 1986 was from SPOT 1 with a resolution of 20 m, while that of 2006 and 2008 was from SPOT 5 with a resolution of 10 m.

The specific study area is based on the extent of the satellite images and, excluding an edge buffer, includes all or part of the territory of 18 municipalities in Stockholm County (see Fig. 1). The total land area covered by the satellite images is approximately 2,220 km^2. The major land cover classes in the area are low-density residential areas (LDB), high-density residential built-up areas (HDB), industrial/commercial areas, forest, open land, forest and open land mixed, and water. The HDB class is somewhat unique in this study since much of the "high density built-up" areas in the city center of Stockholm are composed of buildings that have businesses on the ground floor but residences on the above floors. Therefore the HDB areas classified in the center of Stockholm do include some commercial areas, which could at the same time be classified as residential. In contrast, the industrial/commercial class includes for example industrial park areas as well as shopping centers.

A number of GIS datasets were collected including data on land cover, transportation networks and noise disturbed areas. This data was used in the construction and calculation of the environmental indicators.

3 Methodology

3.1 Geometric Correction and Mosaicking

The SPOT scenes from each date were geocorrected to vectors from the Swedish National Land Survey's (SNLS) GSD topographic map collection [Lantmäteriet (SNLS) 2010] using a polynomial approach with at least eight GCPs each. The pairs of images from the two different decades were then mosaicked together using PCI Geomatica.

3.2 Classification of Satellite Data

3.2.1 Segmentation and Rules-based Classification

Various image processing and classification algorithms were tested and compared. The best results were obtained from an object- and rule-based classification approach using texture measures as well as spectral data as inputs. A pixel-based

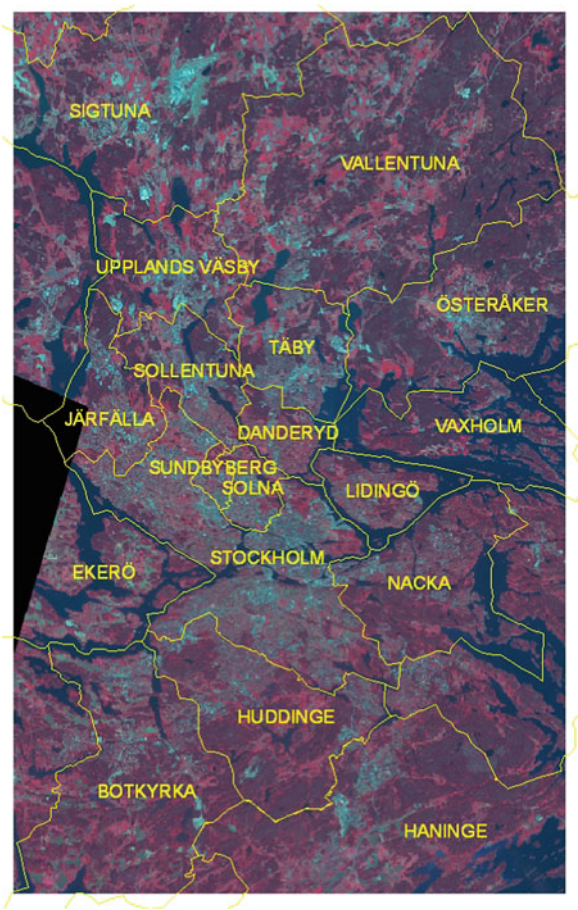

Fig. 1 This image shows the extent of the study area: Stockholm county municipalities included in the study are outlined and labeled in yellow with 2006 and 2008 SPOT imagery as backdrop

maximum likelihood classification was at first tested on the 2006 image (higher resolution) without satisfactory results. Yet this initial classification was later used as an additional input to the rules-based classification that followed. Based on trials, the green, red and near-infrared spectral bands as well as mean, standard deviation and correlation textures of the red band were selected as input data. Texture measures were included since previous studies have shown that texture measures such as grey-level co-occurrence matrix can improve the classification accuracy of optical satellite imagery (Shaban and Dikshit 2001; de Martino et al. 2003; Herold et al. 2003).

Segmentation was performed on the two images using Definiens eCognition software (Definiens AG 2007). Image segmentation can be defined as the division of an image into spatially continuous, disjoint and homogeneous regions, also known as objects. The procedure for the multi-scale image segmentation can be described as a bottom-up region merging technique. It starts with each pixel which is assumed to be an image object. Pairs of objects are merged to form larger

objects based on a homogeneity criterion which is comprised of color and shape components. A 'merging cost' is assigned to each possible merge. A merge takes place if the merging cost is less than a user-specified threshold, which is scale parameter in Definiens. The procedure stops when there are no more possible merges (Ban et al. 2010). In this study, the scale parameter was 20 and the homogeneity criteria were set at 0.1 for shape and 0.5 for compactness. These parameters were selected based on trials and provided the most appropriate objects for classification in that they most closely represented discrete areas of the different land cover types found in the region.

Rules were then sequentially constructed using an object's mean value of different input data to separate the different classes in order of easiest to separate to most difficult to separate. For example, water could be separated from everything else first based on values from the green spectral layer, then built-up areas were separated from non-built up based on values in the initial pixel-based classification, and so on. Areas that were satisfactorily classified early on were then excluded when performing the more fine-tuned rule-based classifications that were subsequently necessary for land cover categories that are often difficult for a single classification algorithm to distinguish. The process could therefore be considered as a type of sequential-masking classification. Once the segmentation-based classifications of the two dates were completed, accuracy assessments were performed using at least 600 random sample vector points for each land cover class.

3.2.2 Incorporation of Existing GIS Data

The GSD Topographic map was used to fill in data gaps so that analysis units located on the outskirts of the study area might have completeste classification information. Other existing GIS data sources for the Stockholm region were considered for incorporation into or improvement of the classification but for various reasons did not prove suitable. The SNLS has a land cover classification (from GSD Topographic map, Lantmäteriet [SNLS] 2010, 5 × 5 m), but this data does not provide as much detail when compared with the classification from 2006 (even though the resolution is better) and the map collection has no historical land cover data. Swedish Corine Landcover data (Lantmäteriet 2002) was not used for similar reasons. Its precision is measured at 85 % while the segmentation-based classifications in this research reach over 90 %.

3.3 Methods for Landscape Change Analysis

Two methods for landscape change analysis were employed in this study. First, spatial metrics were used to evaluate land cover change and specifically fragmentation for the whole study area. The metrics used are described in Sect. 3.3.1 and the results provided under Sect. 4.3.1. The second method is intended to

estimate environmental impact of the land cover change and consists of the calculation of five environmental indicators and their compilation into an environmental impact index. Explanation of the environmental indicators and the index is given in Sect. 3.3.2 and the results in Sect. 4.3.3. These two methods are not connected but are intended to provide complementary information.

To give an idea of how green and urban areas changed according to existing administrative boundaries in the study area, the percent change in large forested areas and in urban areas per municipality or parish is provided in Sect. 4.3.2. This information provides a bit more insight into the change over the whole of the study area and may be useful for city planning, since the focus of the information from the environmental indicators is in general on the less developed, more natural areas of the region.

3.3.1 Fragmentation Statistics

Evaluation of landscape fragmentation due to spatio-temporal changes was evaluated using selected spatial metrics generated from the Fragstats software (McGarigal et al. 1995) based on the classifications. The seven original land cover classes were aggregated to three classes: urban, natural and water classes for generation of the metrics. Forest, Open land, and Forest and open land mixed were aggregated to the natural class; HDB, LDB and Industry/Commercial to the urban class; while water remained its own class. This was done in order to minimize issues related to the difference in resolution between classifications being compared. The metrics calculated and used in this study are class area percentage (CAP), patch density (PD), area-weighted mean shape index (AWMSI), area-weighted mean perimeter to area ratio (AWMPAR) and connectance index (CONNECT). The area-weighted shape metrics are used since they give more weight to larger patches and thus the influence of the original difference in resolution of the classifications is thereby further minimized. AWMSI equals the sum of all patch perimeters divided by the minimum perimeter given a maximally compact patch with the same area multiplied by proportional patch abundance. AWMPAR is composed of the sum of the ratios of patch perimeter to area multiplied by proportional patch abundance. CONNECT measures connectivity of the land cover type and is defined based on the number of functional joinings between patches of the corresponding patch type, where each pair of patches is either connected or not based on a user-specified distance criterion. This statistic is reported as a percentage of the maximum possible connectance given the number of patches in the land cover class. A one kilometer distance was set for calculation of connectance based on trials and using the water class as a control group (the assumption being that the water class changes minimally over the 20 year period). The metrics values are then used for comparative evaluation rather than as stand-alone measurements.

3.3.2 Construction of a Comparative Index using Environmental Indicators

The purpose of the environmental impact index is to assess and compare the condition of the large green areas that provide several of the Stockholm region's essential ecosystem services. Bolund and Hunhammar (1999) have described a number of these specific to the Stockholm area, including air filtration, rainwater drainage, micro-climate regulation and noise reduction. The unit of analysis for the environmental impact indicators and index is the large forested area or LFA. LFAs are defined according to information from several of the Stockholm Regional and Traffic Planning Authority's regional planning documents (for example STOCKHOLMS LÄNS LANDSTING REGIONPLANEKONTORET 1985 and REGIONE- och TRAFIK-KONTORET 1996) and one in particular on green structure in and around Stockholm:

> Green high value areas are large, coherent spaces that have specific importance within the categories of social, natural science and cultural environment values. They are the most important parts of a [green] wedge. They should be large, at least 3 square kilometres, so that they are big enough to preserve regional qualities, even qualities that are sensitive to disturbances and edge effects, and biological diversity (REGIONPLANE- och TRAFIKKONTORET 2008).

In this study, large forested areas were determined from the classifications by combining two land cover classes: "forest" and "forest and open land mixed". All areas that were greater than 3 km^2 were checked against the satellite imagery and road network to ensure that they did indeed fulfil the criteria outlined above. There were 30 of them in the study area extent in 1986 and 33 of them in 2006 (three of those from 1986 became divided due to the construction of new roads).

The Stockholm Regional and Traffic Planning Authority's report on Stockholm's green structure, having established the requirement for size of large green areas (>3 km^2), goes on to specify a further requirement important for ecosystem services:

> [Green] wedges should have a minimum width of 500 meters. This width is needed to accommodate several different types of natural areas that can act as connectivity routes for flora and fauna. This width also provides for variable natural areas for people to enjoy, including undisturbed environments. This width is also important for creating the "city breeze" that leads to the air exchange between the city's hard surface areas and the cooler natural spaces (REGIONPLANE- och TRAFIKKONTORET 2008).

These criteria were the basis for selecting the five indicators of the environmental impact index, namely: Area, Perforation, Proximity to intense urban land use, Urban perimeter and Noise. These indicators and the rationale for using them are explained below.

Since all of the LFAs established for 1986 and 2006 based on the size requirement meet the width criteria (500 m), the first indicator (Area) is simply based on the size of the large forested area. The assumption here is that larger green areas are more resistant to disturbance, more resilient if disturbed and provide ample shelter for flora and fauna. The second indicator (Perforation) is a measure of the physical condition of the LFAs, specifically their degree of intactness or perforation. Have they been disturbed by clear cut areas or roads? The degree of perimeter is used as a measure of

perforation of the area (using both internal and external perimeter). The length of perimeter of the LFA is divided by the minimum possible length given the same area (i.e. as a perfect whole circle). The third indicator measures the proximity of LFAs to intense urban land use. Dense urban and industrial areas produce pollution in the form of heat, emissions and contaminants which larger forest areas are to some extent able to compensate for (Bolund and Hunhammar 1999). But their proximity places pressure on these green areas. This proximity index (I_{prox}) is intended as a rough measure of that pressure. It is calculated as the area weighted distance between each LFA and all HDB and industrial/commerical areas, with both the size of the urban areas and that of the LFA taken into account ($I_{\text{prox}} = A_{\text{LFA}} * \sum (D^2/A_{\text{U}})$) where A_{LFA} = area of large forested area, D = distance between LFA and urban patch, A_{U} = area of urban patch (centroids of LFAs and HDB/Industrial/Commercial areas are used to calculate distances). The fourth indicator (Urban perimeter) takes into account the immediate vicinity of the LFAs or the composition of their perimeter. Depending on the type of land cover there, they will be more insulated from or more exposed to various stressors. The percent of the LFA's perimeter that borders urban land use is calculated since this type of land cover will place the most pressure on the green area. Finally, the fifth indicator or degree of disturbance from noise in the LFA is measured based on a dataset created by the Stockholm Regional and Traffic Planning Authority, which indicates outdoor noise levels across the county. The amount of area per LFA exposed to noise levels above 55 dB (The World Health Organisation's limit for outdoor noise, WHO 1999) is calculated.

The method for compiling the index is simple in order to ensure as much transparency as possible. No weighting system of the indicators was used since a just system of weights is difficult to establish and defend and would require at the very least consultation and decisions from a panel of local experts. Instead a balance among the indicators selected was sought. Once all indicators were calculated, the analysis units were ranked according to each indicator. An average of the indicator rankings was taken to provide an overall index score.

The major advantage of the index and indicators is that they are comparative (the same methods and standards are used to derive them from each classification for each analysis unit). They can therefore be used as a measure of the differences between 1986 and 2006. Calculation of valid stand-alone indicator values is more difficult and not attempted here.

4 Results and Discussion

4.1 Geometric Correction and Mosaicking

The results from the geometric correction of the satellite images were satisfactory. The average X RMS error for the 2006 image was 3 m and the average Y RMS error was 3.3 m; for the 2008 image these were 2.6 and 3.1 m respectively. For the

1986 images, the average X RMS was measured at 4.4 m, while the average Y RMS error was 6.8 m.

4.2 Classification of Satellite Data

The results of the segmentation-based classifications over the Stockholm region are reported in Table 1. The overall accuracies were 92 % for both 1986 and 2006.

The texture features were instrumental in creating rules that ultimately successfully assigned objects to the correct land cover types. This was especially true when it came to isolating built-up areas such as LDB from other types of mixed but natural landscape and HDB from industrial areas. In regard to the lower resolution of the 1986 imagery, the objects generated by the segmentation for 1986 were for the most part of a similar size as those for 2006, but the 2006 segmentation did have a greater amount of smaller objects which led to a slightly more detailed classification, especially when it came to correctly isolating forest and open land mixed.

4.3 Landscape Change Analysis

4.3.1 Fragmentation Statistics

Looking at the change in class area percentage between 1986 and 2006, natural land cover dropped and urban areas increased by approximately 1.5 % of the whole landscape or just over 33 km^2. Urban areas increased by just under 10 % while natural areas decreased by 2 %. Both the natural and urban land cover areas became worse in terms of connectivity and their patch density and shape complexity increased over the 20 year period (see Table 2). The change in shape complexity and connectivity is shown graphically in Fig. 2.

If we look at the changes in the fragmentation statistics in conjunction with the changes in CAP, we get a better idea of the nature of the change in the natural and urban land cover classes. Natural areas decreased both in terms of land area as well as connectivity while patch density increased. These are indications that natural areas were becoming more fragmented through shrinkage or attrition of patches. The fact that patch shapes became more irregular would also suggest that previously larger natural patches were reduced by perforation or division in ways that increased their perimeter relative to area, such as by roads and/or clear-cuts. Urban areas on the other hand increased in terms of land area and patch density but decreased in connectivity. This suggests that new patches appeared out in the natural landscape and relatively near existing built-up areas, but not in direct conjunction with existing urban patches. The increase in shape complexity also supports the idea that several new, smaller and less compact patches came into existence.

Table 1 Accuracy scores and confusion matrices for the segmentation-based 1986 and 2006 classifications

1986 overall accuracy: 92.4 %
1986 overall kappa statistic: 0.91
1986 confusion matrix:

Land cover class	Water	LDB	HDB	Industry/commercial	Forest	Forest and open land mixed	Open land	Totals	User's accuracy (%)
Water	721	0	0	0	1	0	0	722	99.86
LDB	0	662	18	18	0	21	3	722	91.69
HDB	0	9	570	41	0	1	2	623	91.49
Industry/commercial	0	2	15	498	0	0	1	516	96.51
Forest	0	25	1	4	703	36	9	778	90.36
Forest and open land mixed	1	18	2	5	2	513	35	576	89.06
Open land	1	9	3	35	1	35	670	754	88.86
Totals	723	725	609	601	707	606	720	4691	
Producer's accuracy (%)	99.72	91.31	93.6	82.86	99.43	84.65	93.06		

2006 overall accuracy: 92.1 %
2006 overall kappa statistic: 0.91
2006 confusion matrix:

Land cover class	Water	LDB	HDB	Industry/commercial	Forest	Forest and open land mixed	Open land	Totals	User's accuracy (%)
Water	744	0	0	0	0	0	0	744	100.00
LDB	0	684	61	12	1	3	3	764	89.53
HDB	4	21	509	23	0	0	0	557	91.38
Industry/commercial	0	9	27	524	2	0	5	567	92.42
Forest	8	8	1	2	714	44	11	788	90.61
Forest and open land mixed	0	18	1	0	0	551	7	577	95.49
Open land	0	24	5	40	33	8	727	837	86.86
Totals	756	764	604	601	750	606	753	4834	
Producer's accuracy (%)	98.41	89.53	84.27	87.19	95.20	90.92	96.55		

4.3.2 Land Cover Change

Municipalities or parishes where percentage of LFAs changed significantly (a drop or increase of more than approximately 2 %) between 1986 and 2006 are listed in Table 3. Negative changes in percent are due mainly to either clearing of forest and/or division of existing LFAs while positive changes are mainly due to areas of regrowth. Those administrative units that lost the most in terms of square kilometers of LFA were Österåker-Östra Ryd, Täby and Boo. Those that gained the most were Vaxholm, Huddinge and Norrsunda. These findings on areas of improvement/deterioration from the perspective of administrative boundaries coincide more or less with the findings from the environmental impact index (the environmental perspective) as discussed below.

Municipalities or parishes where percentage of urban areas changed significantly (either a drop or increase of more than approximately 1 km^2) between 1986 and 2006 are listed in Table 4. Positive changes in percentage are mainly due to areas of urban expansion. Negative changes, on the other hand, are mainly due to improved detection of small green areas (such as lawns, trees and small parks lining streets and subdivisions) in and amongst urban areas in the 2006 classification. This indicates that urban areas were slightly overestimated in the 1986 classification and therefore that the percentage increases calculated are conservative and thus reliable. The administrative units that experienced the most increase in terms of square kilometers of urban areas were Österåker-Östra Ryd, Boo and Vaxholm. Looking at loss of LFA area and increase in urban area together, it appears that Österåker-Östra Ryd and Boo gained urban areas at the expense of sections of LFAs. Vaxholm on the other hand experienced increases in both, which suggests that urban development did not occur in direct contact with the LFA there, rather parts of it were allowed to regrow.

4.3.3 Environmental Impact Index Results

The environmental impact indicator results consist of a series of tables that can be provided by the authors upon request. In general, positive changes in area and perforation signified regrowth of forest in that particular LFA. Changes in rank for the proximity to intense urban land use indicator depended mainly on the location of new industrial/commercial or HDB areas. Negative changes in the percent of urban perimeter indicator were caused by construction of new LDB areas or roads in direct proximity to LFAs. Positive changes in the area affected by noise were most often due to loss of part of the area in the LFA affected by noise.

Each LFA is ranked according to each indicator and a subsequent average ranking across the indicators provides its overall environmental impact index score. These overall index scores are shown in Table 5 for both years.

North Vallentuna has the highest ranking in both years primarily due to the fact that it has very little or no urban perimeter and that it is relatively far from most intense urban land use areas. Boo, Skarpnäck, and Danderyd_Täby had consistently

Table 2 Class area percentage and selected fragmentation metrics

Class level	CAP	PD	AWMSI	AWMPAR	Connectance
Units	%	#/km^2	None (index)	None (ratio)	None (index)
Natural					
1986	71	0.25	11	43	1.18
2006	69.5	0.46	19	73	0.92
Urban					
1986	15.9	0.16	24	106	0.83
2006	17.5	0.45	39	191	0.52
Water					
1986	13	0.07	10	69	1.00
2006	13	0.08	10	72	1.00

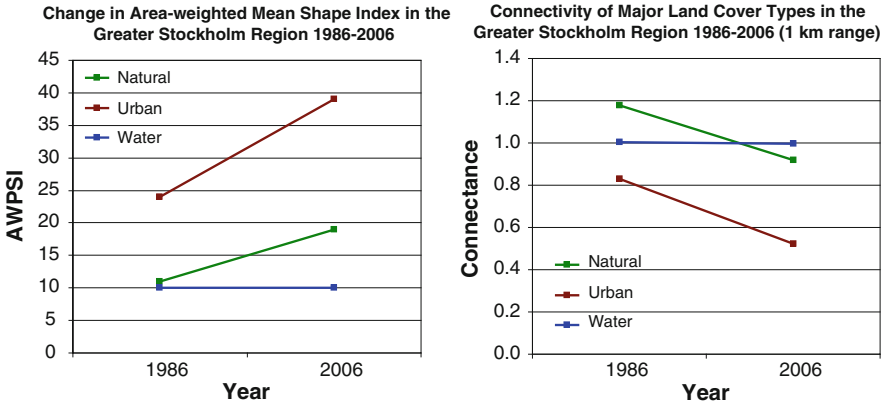

Fig. 2 Change in AWMSI (*Left*) and connectivity (*Right*) of major land cover types between 1986 and 2006

Table 3 Significant changes in percent of large forested areas per municipality/parish

Municipality/parish	Percent 1986	Percent 2006	Difference %	Difference km^2
Boo	25.5	21.9	−3.6	−1.6
Ed	29.1	32.5	3.4	1.3
Huddinge	44.4	48.1	3.7	2.7
Lovö	9.6	12.4	2.8	1.3
Norrsunda	20.6	23.7	3.0	2.3
Trångsund	26.3	30.6	4.3	1.5
Täby	10.4	6.4	−4.0	−2.8
Vaxholm	16.5	19.3	2.8	3.1
Viksjö	19.6	16.2	−3.4	−0.5
Österåker-Östra Ryd	39.6	37.8	−1.7	−3.7

Table 4 Significant changes in percent of urban areas per municipality/parish

Municipality/parish	Percent 1986	Percent 2006	Difference (%)	Difference (km^2)
Boo	15.1	25.4	10.4	4.7
Botkyrka	17.8	19.4	1.6	1.5
Bromma	54.6	48.8	−5.8	−1.6
Farsta	54.1	42.0	−12.1	−2.1
Huddinge	16.8	19.6	2.8	2.0
Norrsunda	2.8	5.1	2.3	1.8
Saltsjöbaden	12.1	17.5	5.4	1.5
Solna	47.5	41.0	−6.5	−1.4
Trångsund	15.9	19.6	3.7	1.3
Täby	26.2	28.2	2.0	1.4
Vallentuna	3.6	5.4	1.8	2.9
Vaxholm	3.3	6.4	3.1	3.4
Österhaninge	12.6	14.5	1.9	2.1
Österåker-Östra_Ryd	6.2	10.5	4.3	9.2

Table 5 Environmental impact index: average ranking in order of best (1) to worst (30) for 1986 compared to 2006

ID	Parish/municipality	1986 ranking	2006 ranking	ID	Parish/municipality	1986 ranking	2006 ranking
26	North Vallentuna	1	1	5	West Norrsunda	16	13
30	East Vallentuna	2	10	22	Huddinge	17	7
11	Vaxholm	3	2	7	Trångsund	18	6
14	Central Österåker	3	17	27	Viksjö	18	20
18	Central Vallentuna	3	5	2	Haninge	20	17
4	West Österåker	6	12	17	Norrsunda Vallentuna	21	26
16	Ed	7	9	9	East Nacka	22	16
20	East Österåker	8	29	21	Flemingsberg	23	24
10	Lovö	9	3	19	Sankt Mikael	24	22
25	North Norrsunda	10	15	24	Sollentuna_Fresta	24	10
6	North Österåker	11	13	23	West Nacka	26	28
12	Sollentuna_Järfälla	12	7	28	Jakobsberg_Kallhäll	27	24
1	Huddinge_Botkyrka	13	21	3	Boo	28	30
29	Täby_Vallentuna	13	4	8	Skarpnäck	28	22
15	Ed_Kallhäll	15	26	13	Danderyd_Täby	28	18

low rankings for nearly all indicators in 1986 and this was again the case for Boo in 2006, while Danderyd_Täby moved up dramatically as a result of forest regrowth on its northern side.

The environmental impact index scores are shown graphically in Fig. 3 for 1986 and 2006. This figure displays clearly some of the geographic differences in the ranking scores. In 1986, the lowest ranked analysis units tend to be nearer the central Stockholm area, while the highest ranked units tend to be on the northern and eastern outskirts of the study region. The configuration in 2006 is more difficult to characterize, with the

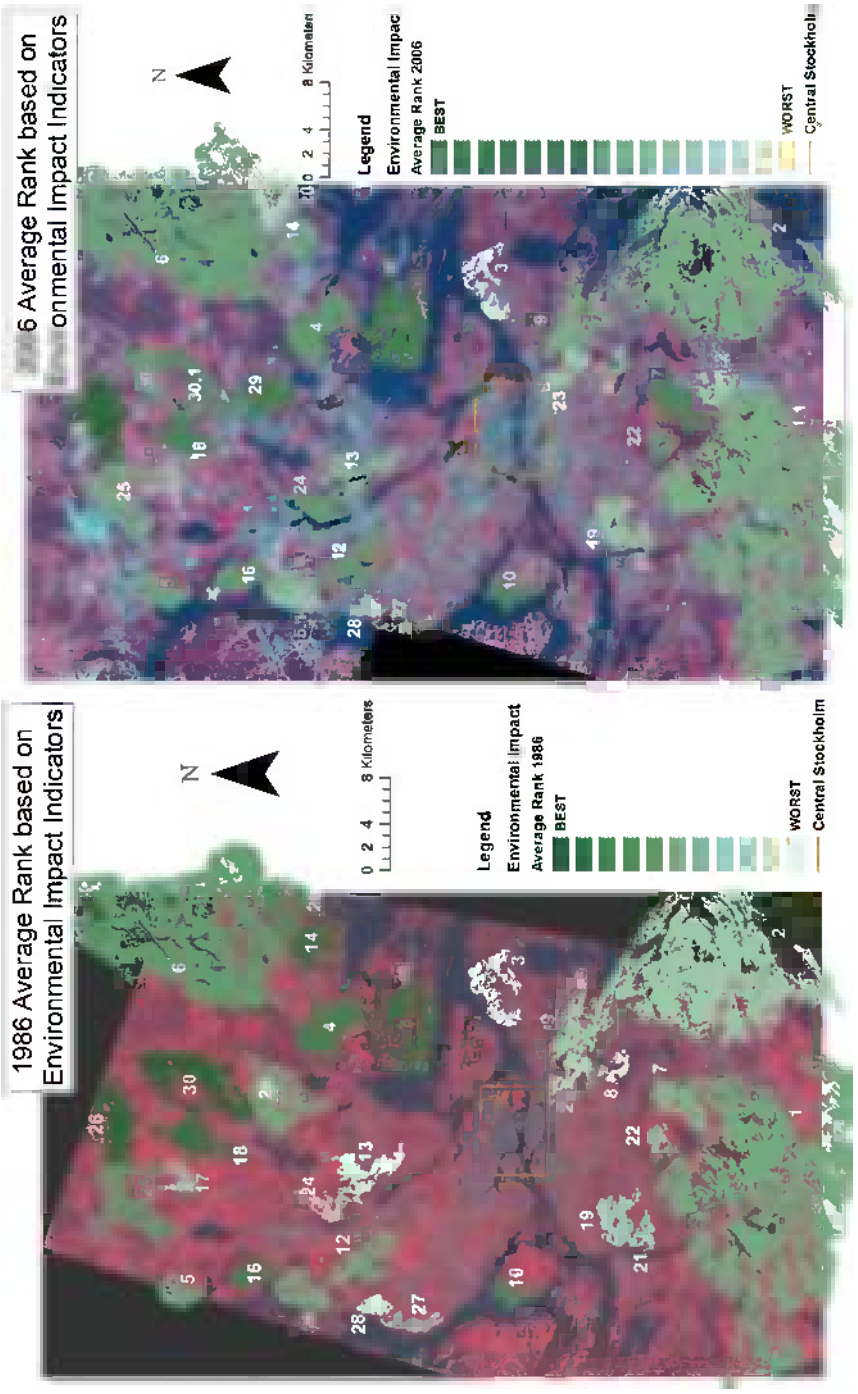

Fig. 3 Environmental impact index average rank per LFA for 1986 (*Left*) and 2006 (*Right*)

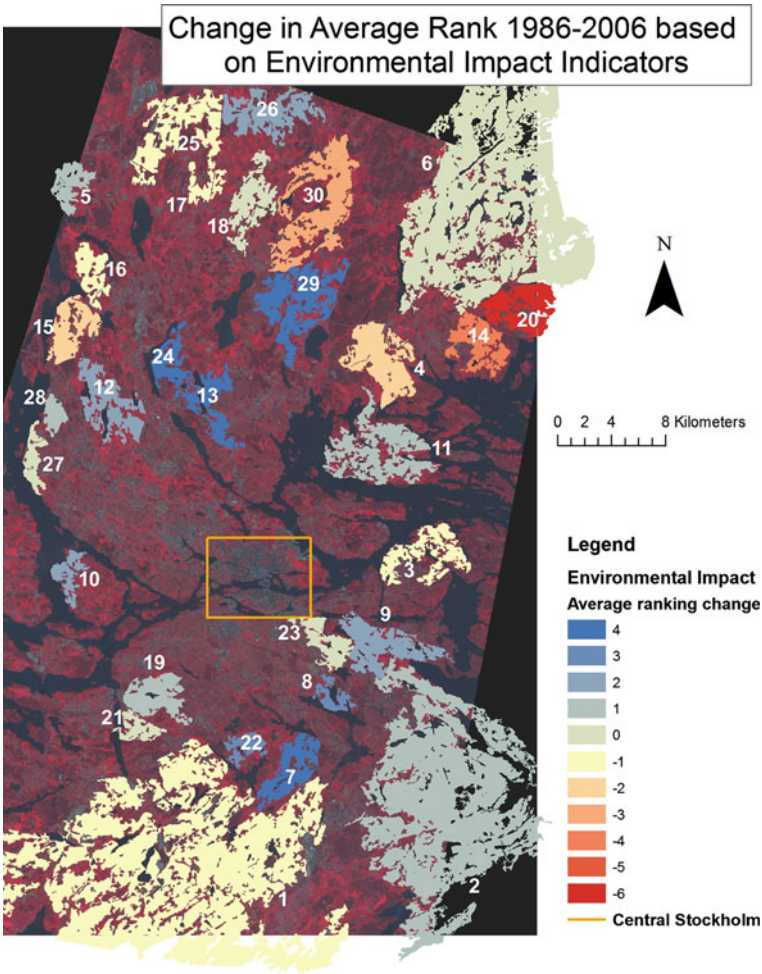

Fig. 4 Change in average ranking between 1986 and 2006 based on the Environmental Impact Indicators

highest and lowest ranked units more evenly scattered throughout the study area. There does not seem to be any trend according to size either, apart from the fact that the smaller LFAs tend to be either the highest or lowest ranked units while the larger LFAs tend to rank in the middle. This is true of both years.

The change in environmental impact average ranking per LFA is shown in Fig. 4. This figure indicates which regions have improved the most in general in terms of environmental impact and which have improved the least. Several of the more centrally located LFAs moved up in rank mainly due to improved standing for the proximity to intense urban land use indicator, since most of the new industrial/commercial and HDB areas were constructed more towards the outskirts

Table 6 Most improved and most deteriorated LFAs according to change in ranking per environmental impact indicator

Indicator	Most improved	Most deteriorated
Area	13. Danderyd_Täby	29. Täby_Vallentuna
Perforation	29. Täby_Vallentuna	20. East Österåker
Proximity to intense urban land use	10. Lovö	30. East Vallentuna
Urban perimeter	29. Täby_Vallentuna	14. Central Österåker
Noise	29. Täby_Vallentuna	11. Vaxholm 13. Danderyd_Täby

of the study region. Those that dropped in rank the most did so due to increases in LDB areas in their immediate vicinity, such as in the case of East Österåker (20), or due to increased proximity to intense urban land use as well as division or fragmentation, as in the case of East Vallentuna (30). However, this figure is misleading in the case of Täby_Vallentuna (29). This LFA lost a significant portion of its area due to construction of new roads and urban areas. Yet this circumstance led to its improvement in terms of perforation, urban perimeter and noise. Had the area indicator carried more weight in taking the average of indicators, the change would not have been positive for this LFA.

The most improved and deteriorated LFAs per indicator are listed in Table 6. As discussed earlier, LFA Danderyd_Täby improved most in terms of area thanks to a section of forest regrowth on its north side. Täby_Vallentuna (29) deteriorated most due to the loss of about 50 % of its area due to construction of new roads and the resulting fragmentation. This loss, however, in effect led to its improvement in ranking in terms of perforation (the remaining area was more compact than the previous whole), for urban perimeter (the previous perimeter was more intricate and skirted LDB areas) and in terms of noise (less area now affected). East Österåker (20) worsened most in terms of perforation due to construction of new LDB areas that increased the length of its perimeter. For the proximity indicator, Lovö (10) improved most by default since no new industrial/commercial or HDB areas were constructed anywhere near it and it changed very little in area. East Vallentuna (30) on the other hand worsened most in this category because of the combination of the fact that it became divided in two which meant a drop in area coupled with the construction of new industrial/commercial areas relatively close by. Central Österåker (14) deteriorated most in terms of urban perimeter since it became increasingly surrounded by new LDB areas. However, Vaxholm (11) and Danderyd_Täby (13) did not really become much worse in terms of exposure to noise; the change is due mainly to a better delineation of these LFAs in the 2006 classfication, which very slightly increased the area affected by noise.

5 Conclusion

This research investigates land-cover change in Stockholm between 1986 and 2006 and analyzes the impact of those land cover changes with the help of spatial metrics and environmental indicators. They results of the statistics and index

rankings reveal how green and urban areas evolved between 1986 and 2006 and in what manner the city has expanded, especially with regard to the surrounding natural resources.

Urban areas increased and natural land cover types decreased by about 1.5 % or 33 km^2 of the study area. The landscape change metrics indicated that both became more fragmented: natural areas became more isolated or shrank whereas new small urban patches came into being. The most noticeable changes in terms of environmental impact and urban expansion were in the east and north of the study area. Although a good deal of the urban expansion between 1986 and 2006 occurred in the northwest, the LFAs in that area were relatively small. There are larger and more far reaching LFAs in the northeast and these registered more of the effects of the urban development.

The results from the environmental impact index showed that the best average ranking scores occur in the northern and eastern portions of the study area. The worst tended to be closer to the center of the Stockholm region with a few exceptions. When it came to negative changes in rankings, areas in the northeast dropped the most. This shift in the northeast was mainly due to construction of new LDB areas. Generally, in terms of changes in rankings between 1986 and 2006, the most improved analysis units are those that are closest to the central Stockholm area, while the least improved or worsened units tend to be on the outskirts of the study area due to the fact that the urban expansion has occured mostly in the suburban areas.

It is important to keep in mind that the changes in many of these analysis units according to the indicators were for the most part subtle. The Stockholm area would not be considered densely urban when compared to other major cities or capitals and it has exceptional endowments in terms of green areas and water. What may be worth noting is that the changes (especially those that were negative) were not worse or more extreme in terms of environmental impact or urban expansion. This in itself serves as an indication that the regional planning authorities have made progress towards their goal of preserving the balance between Stockholm's green and urban areas over the past few decades.

Acknowledgments This study was supported by the Swedish Research Council for Environment, Agricultural Sciences and Spatial Planning (FORMAS). The authors are grateful to the EU OASIS Program for the SPOT data.

References

Ban Y, Hu H, Rangel I (2010) Fusion of QuickBird MS and RADARSAT-1 SAR data for land-cover mapping: object-based and knowledge-based approach. Int J Remote Sens 31(6):1391–1410

Bolund P, Hunhammar S (1999) Ecosystem services in urban areas. Ecol Econ 29:293–301

de Martino M, Causa F, Serpico SB (2003) Classification of optical high resolution images in urban environment using spectral and textural information. Geoscience and Remote Sensing Symposium, 2003. IGARSS '03 Proceedings. 2003 IEEE International 1:467–469

Definiens AG (2007) Definiens Developer 7: Reference Book. Accessed on 3 Aug 2012 from http://www.pcigeomatics.com/products/pdfs/definiens/ReferenceBook.pdf

Herold M, Liu XH, Clarke KC (2003) Spatial metrics and image texture for mapping urban land use. Photogrammetric Eng Remote Sens 2003:991–1001

Lantmäteriet (2002) Swedish corine land cover data product specification: Produktspecifikation av Svenska CORINE Marktäckedata. Document number SCMD-0001. Accessed on 20 Dec 2010 from http://www.lantmateriet.se/upload/filer/kartor/kartor/SCMDspec.pdf

Lantmäteriet [Swedish National Land Survey] (2010) GSD topographic map product description: vector and raster formats. Accessed on 19 Dec 2010 from http://www.lantmateriet.se/templates/LMV_Page.aspx?id=5436&lang=EN

McGarigal K, Marks BJ (1995) FRAGSTATS: spatial pattern analysis program for quantifying landscape structure. USDA forest service general technical Report PNW-351

REGIONPLANE- och TRAFIKKONTORET (1996) Grönstrukturen i Stockholmsregionen. Rapport 1996:2 Stockholm

REGIONPLANE- och TRAFIKKONTORET (2002) Regional Utvecklingsplan 2001 för Stockholmsregionen. Program & förslag 2. ISSN 1402-1331. ISBN 91-86-57462-0. Accessed on 19 Dec 2010 from http://www.rtk.sll.se/Global/Dokument/Publikationer/Ruf2001_pof2002_2_hela.pdf

REGIONPLANE- och TRAFIKKONTORET (2008) Grönstruktur och landskap i regional utvecklingsplanering. Rapport 9:2008. Accessed on 19 Dec 2010 from http://www.rtk.sll.se/publikationer/2008/2008-9-Gronstruktur-och-landskap-i-regional-utvecklingsplanering/

Shaban MA, Dikshit O (2001) Improvement of classification in urban areas by the use of textural features: the case study of Lucknow city, Uttar Pradesh. Int J Remote Sens 22(4): 565–593

STOCKHOLMS LÄNS LANDSTING REGIONPLANEKONTORET (1985) En skogsbacke i handen är bättre än tio i skogen. Rapport 1985:1. ISSN 0280-4468

STOCKHOLMS STADS UTREDNINGS- och STATISTIIKKONTER AB (2011) Statistisk årsbok för Stockholm 2011. Accessed on 29 March 2011 from http://www.uskab.se/index.php/statistisk-arsbok-foer-stockholm.html

World Health Organization (WHO) (1999) Berglund B, Lindvall T, Schwela DH (eds). Guidelines for community noise. Accessed on 23 Dec 2010 from http://www.who.int/docstore/peh/noise/Comnoise-1.pdf

Pre and Post Earthquake Land Use and Land Cover Identification in Concepción

Carolina Rojas, Vivanco Mauricio, Opazo Sergio, Stefan Peters and Villaroel Constanza

Abstract This paper presents the pre and post earthquake identification of representative land cover and land use scenarios in the metropolitan area of Concepción in Chile. Significant land use and land cover changes will be exposed and evaluated conducting a temporal analysis of satellite image classifications.

Keywords Land use · Land cover · Satellite images · Earthquake · Concepción

1 Introduction

As part of the Chilean FONDECYT research project "Evaluation of the Metropolitan Territory using sustainable approaches and strategic environmental assessment", this work presents the identification and evaluation of representative scenarios for land covers and land uses in the metropolitan area of Concepción.

Considering the catastrophic earthquake that affected the study area in February 2010, the land use maps for the years 2009 and 2010, corresponding to pre and post earthquake scenarios (S1 and S2) were updated to visualize the future effects

C. Rojas (✉) · V. Mauricio · V. Constanza
Department of Geography, University of Concepción, Barrio Universitario, Concepción, Chile
e-mail: crojasq@udec.cl

O. Sergio
Facultad de Ciencias, Universidad de Magallanes, Punta Arenas, Chile

S. Peters
Department of Cartography, Technische Universität München, Munich, Germany
e-mail: stefan.peters@bv.tum.de

J. M. Krisp et al. (eds.), *Earth Observation of Global Changes (EOGC)*, Lecture Notes in Geoinformation and Cartography, DOI: 10.1007/978-3-642-32714-8_15,

on the development processes of the metropolitan area. The need to create these maps, also due to the lack of knowledge on land cover, is of essential importance for describing the spatial process and spatial pattern in a very dynamic metropolitan territory with accelerated urban growth.

The land covers were generated using methods for digital classification of satellite images obtained from Landsat TM (30 m). After the digital processing, the land use data were intensively analyzed and corrected. The cartographic products processed in geographic information systems are highly useful for identifying the changes in land use over the time. In our work we also analyzed the land use changes before and after the earthquake. Thereby comprehensive geospatial analysis of annual changes of land use. Subsequently, the future scenarios for urban growth were generated for the Urban and Territorial Planning of the Metropolitan Area of Concepción (MAC).

2 Study Area

The MAC is located in the southern central zone of Chile between 36°35′ and 37°00′ south latitude and 72°45′ and 73 ° 15′ west longitude. The MAC occupies a coastal territory in the Region of the Biobío. Its limits are established in the Metropolitan Urban Planning of Concepción and consist of 11 interrelated counties that concentrate a population of more than 9,00,000 inhabitants in a surface area of 2,830 Km^2.

The boundaries of MAC include 60 km of coastline, which stretch from north to south, from the county of Tomé to the county of Lota, and in between lay the counties of Concepción, Coronel, Chiguayante, Hualqui, Hualpén, Penco, San Pedro de la Paz, Santa Juana and Talcahuano. MAC settlements have developed primarily in the coastal area, where lower "Bío-Bío River" emerges as its central core. Urbanization and growth in the area follow the grid model (Espinoza and Pérez 2008), i.e., a compact expansion around the central blocks is found, but also an oil stain is spread. The urban structure of settlement is organized in a functionally bi-centric structure that is spatially polycentric; it is restricted due to the limited influence of sub-centers or less important cities in comparison with the principal city centers of Concepción and Talcahuano (Rojas et al. 2009).

3 Methods

3.1 Data Processing

The detection of the land uses was obtained by the processing of two ortho-rectificated Landsat TM 2009 images (path 001/row 085—January 18th of 2009; path 001/row 086—January 18th of 2009) and two ortho-rectificated TM Landsat

Table 1 Themes classes of land uses

Class	Description
1. Built-up areas	Built areas occupied by cities or industrial installations
2. Native forest	Ecosystem which its arboreal stratum is established by natural species; mainly different kind of forests such as: Coihue, Olivillo, Patagua, Boldo.
3. Bush	Areas where the presence of trees is less than 25 %, bushes between 10 and 100 %, and herbaceous between 0 and 100 %
4. Water spaces	Rivers, lakes and lagoons
5. Open land	Non cultivated areas without buildings: cut zones, burned areas, eroded areas and areas with almost no vegetation
6. Plantation	Forest which arboreal stratum is mainly formed by exotic species
7. Beaches, dunes and grounds	Beaches, dunes and grounds
8. Grassland	Vegetal formations where the herbaceous cover is above 25 % and the kind of trees and bushes have a spread area of <25 %; it includes the territories with rotative cultivation and hardback
9. Agricultural lands	Utilized agricultural area including cereals, horticulture and fruit cultives
10. Wetlands	Surfaces covered by pure or artificial waters, temporary or permanent waters, stable or running waters, sweet or salty waters; it includes permanent herbaceous vegetation flooded in the riversides, herbaceous wetlands and bushes, peatlands, among others moist or wetlands
11. No data	Misclassified areas without image coverage, active fires (smoke feathers) or areas fully covered by clouds

2010 images (path 001/row 085—March 26th of 2010; path 001/row 086—March 26th of 2009 post-earthquake). Both of the images were taken with a resolution of 30 m. The scenes were processed and the radiometric and the geometrics corrections were made. The georeferencing (Polynomial, Orden 3) was made according to the vectorial covers and specific control locations taken on the field.

3.2 Legend and Classification

The definition of the different theme classes were established according to the covers proposed in the map of land uses and the forest covers in 1998 by the Conaf et al. (1999). Furthermore different investigations on generalizations are proposed in the study area (Rojas, et al. 2010).

The most important aspect was the precise knowledge in the area of the "Bío-Bío" region. Furthermore some classifications methods were applied highlighted in the study of Aguayo (Aguayo et al. 2009). According to the information presented the following themes were chosen to work with (Table 1).

According to the revised bibliography and in agreement with the used images, the unsupervised classification is dismissed. Thus it is decided to follow a supervise classification. Maximum Likelihood (ML) therefore is a suitable method for the objectives in our work, especially when the source of information corresponds to Landsat satellite images (Aguayo et al. 2009; Bakr et al. 2010; Shalaby and Tateishi 2007; Wentz et al. 2006; Yuan et al. 2005). The ML classifier is a widely accepted classification method because of its robustness and simplicity. The classifier determines the probability that a pixel belongs to each class and then assigns the pixel to the class with the highest probability (Richards 1999). It assumes that the spectrum of each class is normally distributed and requires that the class be defined by a minimum n + 1 training pixels for n spectral bands (Platt and Goetz 2004). In 2009 Al-Ahmadi and Hames evaluated four classification methods to extract land use and land cover, they found that the maximum likelihood method gave the best results.supervised classification algorithms need a prior knowledge of the study area, in this sense visual recognitions were made (interpretations, aerial photography and land maps (Al-Ahmadi and Hames 2009; Conaf et al. 1999)). These recognitions allow obtaining training places (polygons) for each of the theme classes in every year of study. Later, the training areas were submitted to a statistical analysis of separability that allowed distinguishing the distance between classes and the feasibility of its discrimination.

3.3 Validation

The validation of the exact classifications was made through the confirmation of specific land spots, locations that were important to verify. First 100 of random places were generated within an area logistically accessible. Because of that a buffer with a distance less than 100 meters off the highways, roads and rural paths was considered. These spots are generally located in the waterfront, an area especially affected by the earthquake and tsunami that occurred in February 27th 2010.

Later, 250 random places were checked every year, specifically 25 spots in each of the 10 covers (excluding the "non data class"). With the processed information it was possible to obtain the level of error of the classifications per year. With the purpose to obtain the previous information the statistical accuracy Kappa was used.

4 Results

4.1 Analysis of the Separability

Considering separability values over 1.5 as an optimal distance of separability, the results of the analysis possibly showed more confusion (values < 1.5) between grassland covers (8) and the agricultural lands (9), being put together in the same

class according to its spectral characteristics. If a precise separation between classes is required, especially for later ecological focused studies, it is necessary to make use of images during different seasons, so that the comparison of the phenological differences can be made.

At the same time the boundaries between beach zones (7), sediments with open lands (5) and urbanized areas are highly dependent on the interpretation because of its low spectral separability. In these areas the earthquake and the tsunami of February 27th 2010 had a major influence, because they caused confusing zones wherein tree covers were mixed. In this case the accurate knowledge of the area is extremely useful to establish context criteria that contribute to the improvement of the classification and its results.

The covers of the native forest (2) and forest plantations (6) also generated confusion (values less than 1.4) especially in places where the native forests are fragmented and organized in patches completely surrounded of the exotic plantations of pine tree or eucalyptus.

Important part of the covers showed appropriate values of separability, above 1.0 value.

4.2 Maps Land Use and Land Cover

In Fig. 1. Two maps of the scale 1:50,000 are shown. These maps were obtained by the classification using MAC before and after the earthquake and tsunami, which occurred on February 27th of 2010.

Comparing the land cover of both years (before and after the earthquakes) it was detected that the major coverage was the forest plantation (>95,000 ha; >30 %). These forest plantations are mainly distributed in slopes of mountains of the coastal range. There the predominant species are pine tree and eucalyptus trees, with a very high density in the south of the "Bío-Bío River".

The brushwood characterized by shrubs increased its amount (>58,000 ha) from a 20 % (2009) to 22 % (2010). They are located in places with high slopes.

Within the areas of open lands (>16 %) only a slight reduction was determined. These places are characterized by small spaces next to the urbanized areas and agricultural land, also by extensive grounds in the north area, known as the dry coastal zone.

The agricultural land (>19,000 ha) has decreased from 27,000 to 19,000 ha, reducing its presence to 7 %.

The grassland highly associated to the uses mentioned before, mainly because of the rotations in the cultivation of the grassland. Grassland areas (8,000 ha) increased up to 3 %. Therefore a main characteric is the neutrality and the presence of the exotic herbaceous species.

The native forests represented a bit more than 5 % with more than 14,000 ha in 2009. In 2010 almost 18,000 ha were detected. These forests are located in humid areas with natural streams. The forests are surrounded by forest plantations;

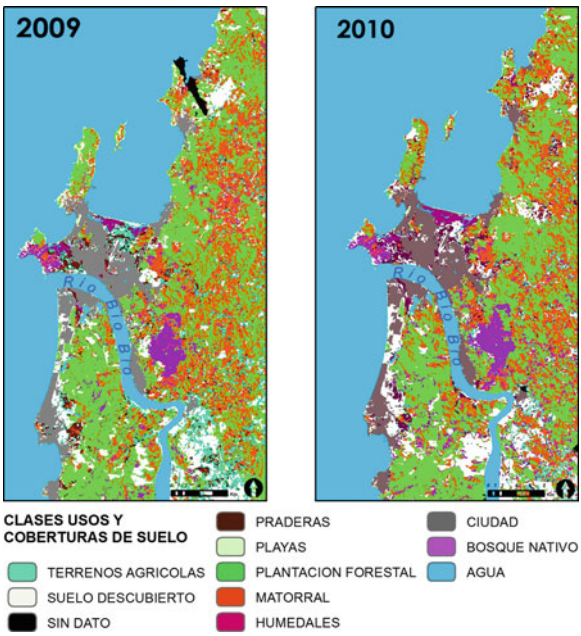

Fig. 1 Scenarios of land use cover, S1 before (*left*) and S2 after (*right*) the earthquake (Terrenos Agrícolas = Agricultural land; Suelo Descubierto = Uncovered land; Sin dato = No data; Praderas = Grassland; Playas = Beaches and dunes; Plantation Forestal = Planted forest; Matorral = Brushwood areas; Humedal = Wetland; Ciudad = built-up area; Bosque Nativo = Native Forest; Agua = Water)

probably this reason can be explain the increments of native forests, mainly for the confussion between both categories.

The coastal beaches (0.5 %) have being reduced in the surface from 2,900 to 1,600 ha (reduction of 55 %).

The wetland areas contain more than 1,000 ha, and nowadays represent the 0.45 % of MAC area. Wetlands are located in places associated to the presence of water (estuaries, lagoons, rivers).

The built-up areas have been reduced to 290 ha, but they keep their representativeness of 6 % with more than 17,000 urbanized hectares. They are located mainly in marine terraces. Finally, the water coverage represents 4 % of the total surface with more than 11,000 ha, being the most important source of the "Bío-Bío river" (Table 2).

4.3 Validation: True Land Versus Classifications

The validation of the verification spots showed a coefficient (Kappa) for the year 2009 of 0.78 and for the year 2010 of 0.77. That is to say that 78–77 % of the pixels of the land covers are properly classified.

The territories where the classes or covers represented major identification problems were the transitions between beaches, open lands and urban places in the coastal zones. Thereby wetlands and grasslands in areas of humid grounds had

Table 2 Surfaces changes of land use and land cover

Land use/ cover	Area 2009 (ha)	Percentage of area 2009	Area 2010 (ha)	Percentage of area 2010	Change (ha)	Change (%)
Built-up areas	17,381	6.07	17,087	5.97	−294	−1.69
Native Forest	14,557	5.09	17,917	6.26	3,360	23.08
Brushwood areas	58,884	20.57	63,547	22.20	4,663	7.92
Water	11,956	4.18	11,622	4.06	−334	−2.79
Uncovered land	50,063	17.49	46,282	16.17	−3,781	−7.55
Planted Forest	95,258	33.28	98,327	34.35	3,069	3.22
Beaches and dunes	2,957	1.03	1,679	0.59	−1,278	−43.22
Grassland	6,497	2.27	8,929	3.12	2,432	37.43
Agricultural Land	27,634	9.65	19,504	6.81	−8,130	−29.42
Wetlands areas	1,040	0.36	1,331	0.47	291	27.98

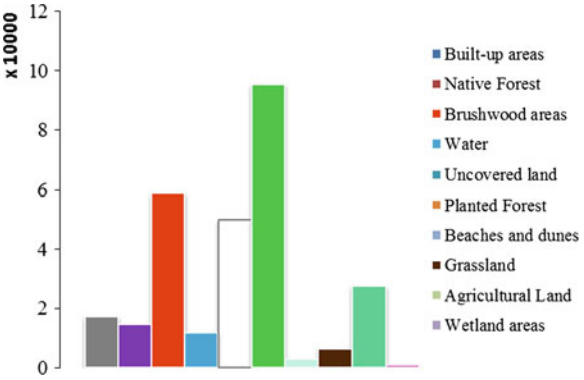

Fig. 2 Graphics surfaces of land use and land cover

important influence. In the inland there is a mixture between forest plantations, native sclerophyll forests and bushes (Figs. 2 and 3).

5 Discussion and Conclusion

In the land uses and land covers presented in this paper, the most difficult cover to identify was the beach class. This was characterized by presenting low spectral separability. It was mixed with the open lands in the coast of Tomé and Penco and with the cliff located in Talcahuano.

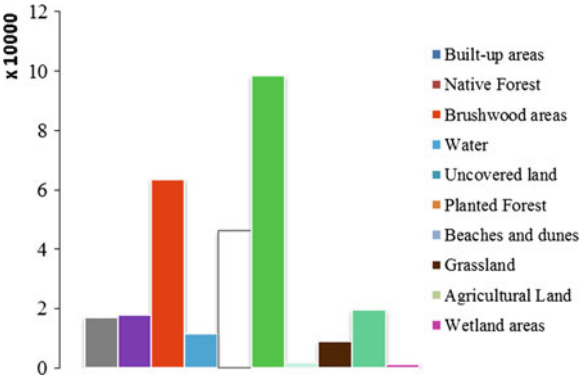

Fig. 3 Graphics surfaces of land use and land cover

Also the investigation on the mixture between urban zones, debris (because of the catastrophe) and open lands showed an identification of extensively mixed zones, decreasing the occupied surface for the beaches. The coastal zone (Talcahuano, Penco and Tomé) especially the bays oriented to the north were devastated by the earthquake and by the tsunami. These places were crushed by waves of >3 m in Talcahuano (European Commission 2010). Some authors have documented wave lifts of 0.5 ± 0.1 m in Talcahuano creeks (Quezada et al. 2010). Certainly, the natural landscape has shown up important variations. The built-up area has been reduced by the material lost and the housing damages located in the coast.

The covers that presented some complexity in its identification are wetlands and native forests areas. In this classification, the wetlands correspond to a humid land belted by water. Vegetation is also a part of the wetland ecosystem which was recognized in these maps as grasslands.

The native forests or non-forests are made of sclerophyllous species such as Olivillo, Peumo, Boldo, Hualle (tree species). The detection is accurate when the presence of these trees is important. However, in the remaining spaces which are surrounded by forest plantation, the detection of certain tree species can not be done clearly.

The interrelationships between forest plantations and bushes also present some inaccuracies, especially when the forest plantations are in the growing phase. In many cases these spaces were classified as bushes, justifying its increment.

The valid classifications are the ones that are in an exact level with accuracy above 70 %. The content of these maps are equal to the regional studies, using an inferior scale of 1:50,000. The maps constitute a considerable contribution to the development of study areas, especially in ecology and territorial planning. For example it would be efficient and important to evaluate the natural ecosystem conditions and the natural risks threat.

Acknowledgments This research was sponsored by the project "FONDECYT N° 11090163" *Valoración del Territorio Metropolitano. Aproximaciones desde su Sostenibilidad y Evaluación Ambiental Estratégica* (Evaluation of the Metropolitan Territory using sustainable approaches and strategic environmental assessment).

References

Aguayo M, Pauchard A, Azócar G, Parra O (2009) Cambio del uso del suelo en el centro sur de Chile a fines del siglo XX. Entendiendo la dinámica espacial y temporal del paisaje. Revista Chilena de Historia Natural, pp 361–374

Al-Ahmadi FS, Hames AS (2009) Comparison of four classification methods to extract land use and land cover from raw satellite images for some remote arid areas, kingdom of Saudi Arabia. Earth 20(1):167–191. doi:10.4197/Ear.20-1.9

Bakr N, Weindorf D, Bahnassy M, Marei S, El-Badawi M (2010) Monitoring land cover changes in a newly reclaimed area of egypt using multi-temporal landsat data. Applied Geography 3:592–605

Conaf., Conama., Birf., Universidad Austral de Chile., Pontificia Universidad Católica de Chile. (1999). Catastro Y Evaluación de los recursos vegetacionales nativos de Chile. Informe Regional Octava Región. Santiago, Chile

Espinoza L, Pérez L (2008) Planificación Urbana y Espacio Público en Concepción 1940–2004. Universidad de Concepción, Concepción

European Commission Join Research Centre (2010) Tsunami Chile 27 Feb 2010, part 3: estimation of coastal inundation. http://www.reliefweb.int/rw/rwb.nsf/db900SID/JBRN-838DBH?OpenDocument

Quezada J, Jaque E, Belmonte A, Fernández A, Vásquez D, Martínez C (2010) Movimientos cosísmicos verticales y cambios geomofológicos generados durante el terremoto Mw = 8,8 del 27 de febrero de 2010 en el centro-sur de Chile. Revista Geográfica del Sur 2:11–45

Platt RV, Goetz AFH (2004) A comparison of AVIRIS and landsat for land use classification at the urban fringe. Photogramm Eng Remote Sens 70(7):813–819

Richards JA (1999) Remote sensing digital image analysis. Springer, New York

Rojas C, Muñiz I, García-López MÁ (2009) Estructura urbana y Policentrismo en el Área Metropolitana de Concepción. Estudios Latinoamericanos Urbanos Regionales Eure 35(105):47–70

Rojas C, Salado MJ, Pino J, Martori J (2010). Área Metropolitana de Concepción: algunas dinámicas espaciales relacionadas a la sostenibilidad urbana. Geolibro Concepción Metropolitano (AMC). Evolución y Desafíos. In: Leonel P, Rodrigo H (eds) Santiago: Geolibros—Instituto de Geografía Pontificia Universidad Católica de Santiago, pp235–251

Shalaby A, Tateishi R (2007) Remote sensing and gis for mapping and monitoring land cover and land-use changes in the northwestern coastal zone of Egypt. Appl Geogr 27(1):28–41

Wentz E, Stefanov W, Gries C, Hope D (2006) Land use and land cover mapping from diverse data sources for an arid urban environments. Comp Environ Urban Syst 30(3):320–346

Yuan F, Sawaya KE, Loeffelholz BC, Bauer ME (2005) Land cover classification and change analysis of the twin cities (Minnesota) metropolitan area by multitemporal landsat remote sensing. Remote Sens Environ 98:317–328

Part IV
Spatial Modelling, GIS and Geovisualization

A GIS Based Approach to Embedded Fire Modelling: A South African Case Study

Bolelang Sibolla and Julian Lloyd Smit

Abstract The purpose of this study is to illustrate the role of GIS in predictive fire modelling and fire management. This is achieved through the development of a fully GIS-integrated fire model. A fire behaviour model is developed and the results are used in the fire spread model as input. The study is conducted in the Kruger National Park, South Africa.

1 Introduction

Fire is very important for maintaining harmonious relationships in ecosystems and is used by fire management across the world to regulate growth of vegetation in natural conservation areas. However, improper management of fire may lead to hazardous behaviour resulting in the loss of property and life. In order to avoid fire management turning into a hazardous exercise and in order to apply the proper regulation of the available fire-susceptible biomass, the most effective fire management policies are continuously sought. Scientific decision support systems in the form of fire modelling tools are implemented in order to provide fire managers with a platform to test and plan these fire management activities.

Fire management tools have evolved from hand written charts that were used in the 1970s to computer based applications in recent years. This has occurred as a result of the rapid development of computer systems. The use of Geographic Information Systems (GIS) has been explored in the development of fire modelling tools due to its nature and ability to accurately and spatially represent features. The

B. Sibolla · J. L. Smit (✉)
Geomatics Division, School of Architecture, Planning and Geomatics,
University of Cape Town, Cape Town, South Africa
e-mail: julian@afrimapgis.co.za; Julian.Smit@uct.ac.za

J. M. Krisp et al. (eds.), *Earth Observation of Global Changes (EOGC)*,
Lecture Notes in Geoinformation and Cartography, DOI: 10.1007/978-3-642-32714-8_16,

ability of GIS techniques and the extent to which they can be used in fire modelling has been a subject of debate in recent times, with specific focus on the level of integration that can be achieved between GIS and environmental modelling techniques, of which fire modelling is a part of.

The integration of environmental models with GIS is viewed in line with the following categorisation (Brimicombe 2003): loose coupling, tight coupling, and embedded coupling. Loose coupling refers to the case where the GIS and Environmental model share data files, and GIS are used for storage of these files. In tight coupling GIS and Environmental modelling functionality are accessed through a common interface. In fully integrated or embedded systems, environmental modelling functionality is available entirely within a GIS platform or vice versa.

Environmental models comprise mainly of mathematical and statistical functions. The most widely used and oldest form of integration in this respect is loose coupling, where the files are transferred between GIS and stats packages. The disadvantage of this integration is that problems may arise due to incompatibility of file formats and metadata. Important information about the data can get lost in the multiple analyses and transfer processes (Brenning, 2001).

Attempts have been made to integrate GIS packages with statistical and mathematical packages in order to provide more advanced mathematical and statistical modelling functionality. However, most attempts have been under tight coupling, where statistical packages are accessed though GIS. Such an example is that of integration of GRASS GIS software and 'R' statistical language.

GRASS (Geographic Resource Analysis Support System) is an the most popular and probably oldest running open source GIS package to date, comprehensive with raster, vector, topological, and basic mapping functionality. Researchers have also added their own tools onto the GRASS platform thereby increasing the functionality (Neteler, 20).

'R' is a programming language and environment for performing statistical operations. It offers a computing and graphical environment in which statistical techniques can be performed and implemented. The 'R' programming language includes conditional statements, loops and user defined functions as well as a variety of statistical models such as clustering, time-series analysis and linear modelling (Brenning 2001). R's gstat, geoR and geoRglm packages provides a wide range of tools for geostatistics (Andrade Neto et al. 2005).

'R' works with data stored in memory hence when working with large data sets it is often preferred that an external database such as PostgreSQL, MySQL or other be used. This leads to a further requirement that the user have knowledge of SQL (Andrade Neto et al. 2005).

Embedded coupling, the most desirable method of integration is enhanced by embedding modelling tools within a GIS by using a programming language and in most cases, interoperability technologies such as COM (Component Object Model).

COM is suggested to enable interoperability, which eliminates problems caused by lack of communication between the two different models which are possibly written in two completely different languages with different libraries. COM

specifies an object model and programming requirements that enable interaction between such objects and they can be reused at binary levels, hence developers do not need to have access to the source code or libraries to extend the system (Eldrandaly et al. 2005).

The GIS platform of choice in this study is Esri's ArcGIS 9, ModelBuilder. Although a proprietary software, ArcGIS is used widely in universities, research institutes, environmental agencies, government and others in South Africa. ModelBuilder uses most of ArcGIS geoprocessing tools in a workflow environment, a factor that made this software most attractive. The significance of a workflow environment in research and experimental tools is that it allows the user to parameters and variables of the model, without requiring one to rewrite the whole model. ArcGIS geoprocessing tools were developed, to extend functionality, in Arcobjects and VB.Net. A range of alternate GIS platforms including open source options could have been used for this study, and the scripting required could have been done in another other language such as python. The authors were however, more 'comfortable' with the ArcGIS development environment.

Fire modelling in the context of environmental modelling, and within GIS platforms has been explored by a number of scientist. The studies range from factors that drive fires, to ways of representing the shape of a spreading fire and analysis of the behaviour of a fire as it propagates. These studies are then categorised as fire behaviour models, fire risk models and fire spread models. Fire risk models have been established around the world such as the Canadian National Fire Danger Rating System, that is based on the FWI (fire weather index), FOP(fire occurrence potential) and the FBP (fire behaviour potential) as outlined by Willis (2001). Other systems include the United States NFDRS, which has the components, SC (spread Component), ERC (Energy release component) and BI (burning index). In Australia the McArthur fire indices and in South Africa, the South African Fire Danger index (Willis 2001). All of these risk rating systems are based on sub models that describe the behaviour of wild fires.

Fire behaviour models are generally mathematical models. The fire phenomenon is represented in terms of mathematical calculations or probabilities, based on the relationship between factors that influence the behaviour of fires. Such models are further classified as empirical, deterministic or probabilistic models. Empirical models are based on the study of a number of fire experiments performed either in the laboratory or outdoors under known conditions. Statistical equations usually in the form of regression analysis are then derived following observations of these fires; and these equations are subsequently used to model the fire behaviour (Glasa and Halada 2008). Deterministic models can further be classified as physical models and semi-empirical models. Physical fire spread models are based on the transfer of heat energy from burning to un-burnt area, following the laws of physics that govern energy transfer and combustion (Albright and Meisner 1999; Favier 2004; Johnston et al. 2005; Glasa and Halada 2008). Semi-Empirical (Physical-Statistical) models exhibit both the properties of physical models and statistical analysis. They use the laws of physics to model the transfer of heat energy between burning fuel and un-burnt areas. These derived physical properties

are then applied to a number of experimental fires to derive statistical correlation (Albright and Meisner 1999; Glasa and Halada 2008). Probabilistic models are based on the probability that a fire will spread from one location to another. Unlike the other types discussed above, these models do not actually calculate fire behaviour characteristics and variables. In these models the probability of the factors to cause a fire are assessed separately and then they are combined to measure the overall probability (Albright and Meisner 1999).

Fire spread models fall within two general categories, namely vector models and grid based models. Grid based models represent the modelled surface as a set of regular grid cells, usually square but irregular grids have also been found, whereas the vector models represent the landscape as a continuous surface (Albright and Meisner 1999; Pastor et al. 2003; Yassemi et al. 2008). The vector based models assume the propagation of a fire front as a polygon (usually an ellipse) that grows with respect to time. These models use Huygen's theory of wave propagation, where one fire front generates wavelets that create new fire fronts (Yassemi et al. 2008; Finney, 1998). The most widely used grid based fire spread models employ the use of Cellular Automata and Bond Percolation (Pastor et al. 2003; Yassemi et al. 2008). Cellular automata (CA) employ the use of logical rules that govern the spread from one cell to another whereas Bond percolation is a probability based technique. Grid based models are easier to implement in a GIS environment as opposed to vector models, because of the native gridded raster format inherent in GIS.

2 Objectives and Motivation for the Study

This paper explores the level of integration that can be achieved between fire modelling, as a division of environmental modelling, and GIS. The paper serves to provide and illustrate a robust solution to achieving full integration between the two techniques. This level of integration is illustrated by demonstrating the role that GIS plays in fire management through the development of a GIS embedded, predictive, wind driven, surface fire model. The paper also serves to provide more insight into fire modelling through the use of advanced GIS platforms.

The following criteria are used to assess the level of integration achievable through GIS platforms:

- Implementation of fire modelling formulae into a GIS platform
- The suitability of the GIS environment for implementation of fully embedded fire models
- The ability of GIS to handle temporal, dynamic processes.

Subsequently, required improvements in fire modelling technology for GIS are assessed based on the results demonstrated in this study.

3 Study Area

The area of study is the Kruger National Park in South Africa. Kruger National Park is one of the areas that experience high levels of fire activity, hence the reason why it was chosen. The fires experienced in the park are manmade fires that occur as a result of fire management experiments and also fires as a result of arson. Arson fires contribute high percentage of fire activity in the park.

The Kruger National Park is located in the northern part of South Africa between latitudes 23 and 26°S and longitudes 30 and 32̊E, in the provinces of Mpumalanga and Limpopo, see Fig. 1. The park was established in 1926 and it covers approximately two million hectares (1,948,528 ha), with elevation ranging between 260 and 839 m above sea level (Van Wilgen et al. 2000). The type of vegetation found in this region is Savanna grasses and trees, which are also found in almost half of the African continent. Most rainfall is experienced in the summer months. On average the rainfall pattern in the Kruger national park can be explained by extended wet and dry periods. The rainfall pattern has an effect on the fire regime of the park and most fires occur during the dry winter season (Van Wilgen et al. 2000; Govender 2003).

4 Methodology

The embedded fire model developed in this study accounts for the important aspects of fires: fire behaviour and fire spread. The fire behaviour model demonstrates the risk that a fire will occur in an area, whereas the fire spread model simulates the predicted propagation of a fire pending an ignition event. Full integration is achieved by combining these models in such a way that the fire spread model uses the results of the fire behaviour model as input and the interaction between the two models is seamless. The fire behaviour model is in turn based on prevailing meteorological conditions, characteristics of the resident vegetation and the topographic aspects of the affected region. All tasks are performed in the same GIS environment. Figure 2 provides an overview of the fire behaviour model and the fire risk model and these are discussed below.

4.1 Fire Behaviour Model

The fire behaviour model performs calculations for the variables that describe the characteristics of wild fires: fire intensity, flame height, and rate of spread. The fire intensity is a measure of how hot a fire is burning, it is described as a measure of the rate at which heat energy is released by a fire (Trollope et al. 2002). According to Trollope 2002, fire intensity is correlated with many other fire behaviour

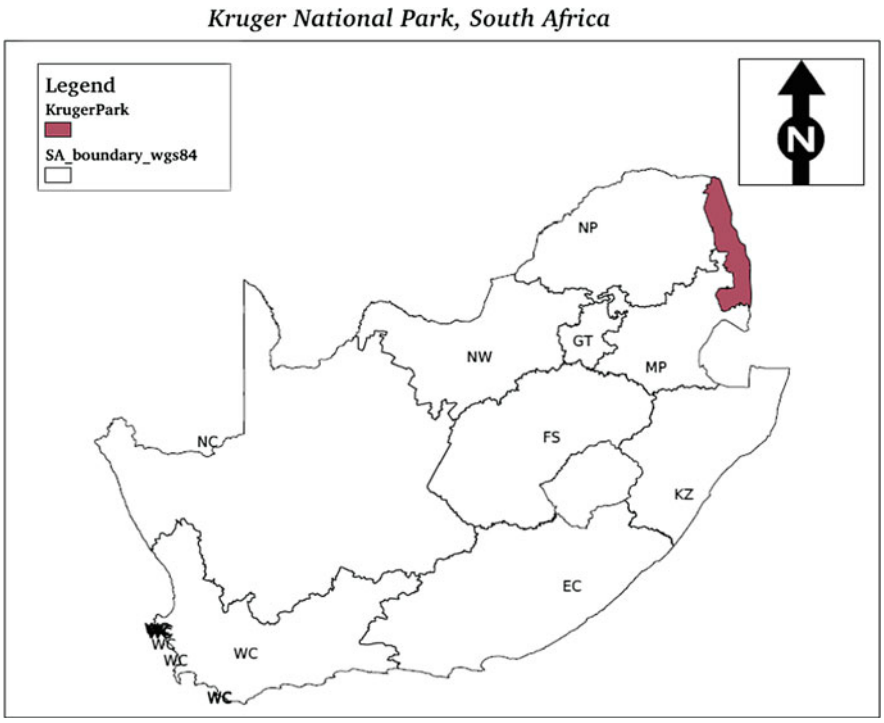

Fig. 1 Location of Kruger National Park, South Africa

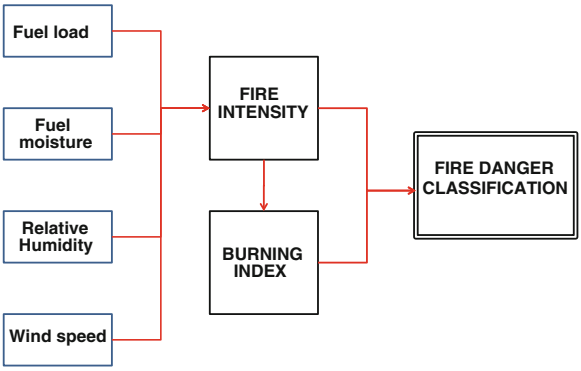

Fig. 2 Overview of the fire behaviour model

characteristics such as flame length, flame angle, and rate of spread of fire and therefore can alone be used in predictive fire studies to give an indication of the potential danger that a fire that would ignite in that specific area would pose.

The fire intensity model used in this study is a semi-empirical based model developed by Trollope et al. (2002). Following research conducted in the Savanna

grasslands of South Africa, in the Eastern Cape Province and Kruger National Park. The fire intensity equation is shown below:

$$\mathrm{FI} = 2729 + 0.8684(x_1) - 530(x_2)^{\frac{1}{2}} - 0.907(x_3)^2 - 596(x_4)^{-1} \quad (1)$$

where:

x_1 is the fuel load (kg/ha)
x_2 is the percentage fuel load moisture
x_3 is the percentage relative humidity
x_4 is the wind speed (m/s)

An additional advantage to Trollope's equation, other than the fact that it was developed for the Savanna grassland context, is that it is based entirely on weather and fuel variables that can be directly measured from the ground (and ground stations for weather data), displayed spatially and analysed in a GIS. The data sources for this model can also be acquired through remote sensing techniques, although in order to better evaluate the accuracy of this model, measured parameters were used as input. The following sections discuss the data acquisition and pre-processing.

Fuel loads were acquired from ground measurements taken at discrete locations within the park. The wind speed and humidity measurements were acquired from discrete weather stations within the park. These discrete (vector) data are interpolated from point locations to form a continuous surface that encompasses the entire park in raster format. Two interpolation methods were considered: Kriging and Inverse Distance Weighted (IDW). IDW is a deterministic interpolation method based on the surrounding measurements. IDW assumes that the weight of the variable being measured decreases with increasing distance from the measurement. It should be used when there measurements are dense enough to capture the local surface variation of a study area (Childs 2004). Kriging is a statistical method that argues that measurements close to each other have some spatial correlation and measurements further apart from each other are spatially independent. Kriging generally provides more reliable results as it does not limit the interpolation to the known value range, and does not assume a stable rate of change in the degree of spatial variation (Esri 2008).

The expectation is that Kriging generally provides better interpolation results. However, in this study area the methods yielded results with little difference, thus the easier to implement IDW was adopted. The effect of roads and rivers was accounted for as barriers in the interpolation process as seen in Fig. 3.

Figure 4 shows discrete fuel load measurements and Fig. 5 shows the interpolation using Kriging and IDW. In this case IDW interpolation was performed with a distance power of 2 and maximum point distance of 10 m. Kriging was performed using a third order polynomial trend surface.

The fuel moisture content was acquired through the calculation of vegetation indices using remotely sensed data, from MODIS Terra and Aqua satellite sensors. This was achieved by measuring water content in the vegetation using the NDWI

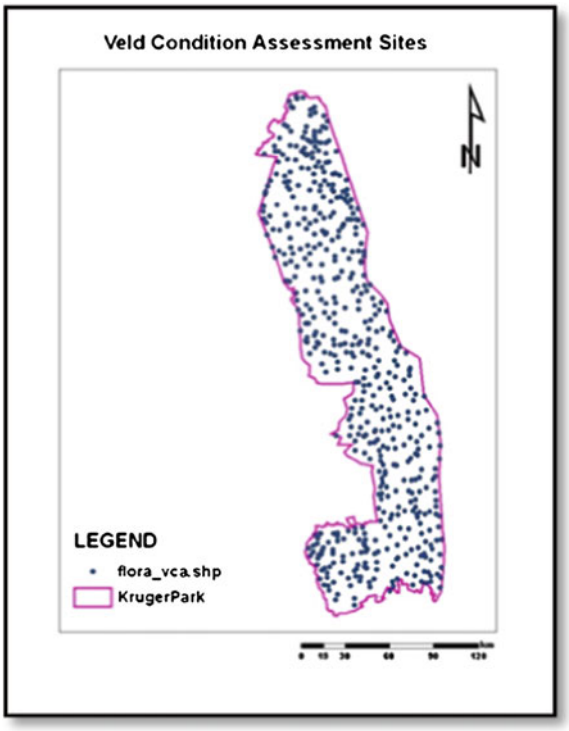

Fig. 3 Main roads overlayed on interpolated fuel load map, fuel loads are lower along the main roads

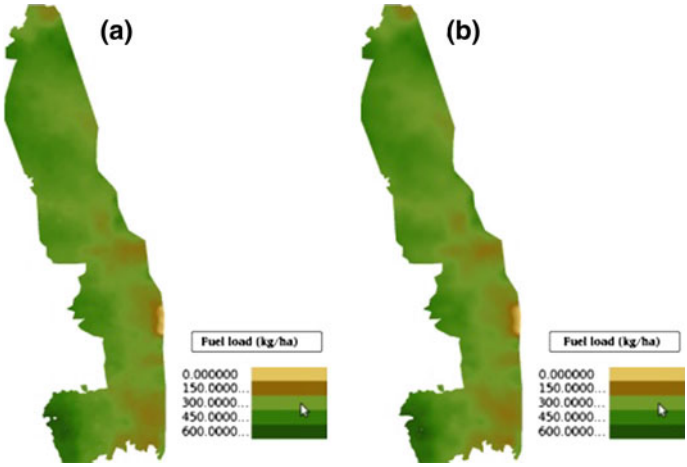

Fig. 4 Measurements of fuel load acquired at discrete locations within the park

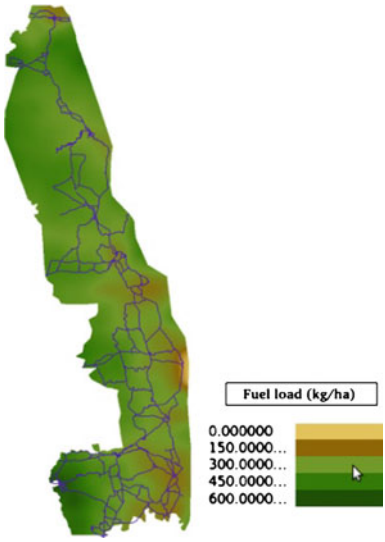

Fig. 5 Interpolated point fuel load measurements using **a** IDW and **b** Kriging

(Normalised Difference Water Index). The NDWI directly evaluates the amount of water that is available in vegetation. The calculation of this index is as follows:

$$NDWI = (\rho_{NIR} - \rho_{SWIR})/(\rho_{NIR} + \rho_{SWIR}) \quad (2)$$

where:

ρ_{NIR} is the reflectance of the Near Infra—Red band

ρ_{SWIR} *is the reflectance of the short Infra—Red ban*d

The Red band is strongly absorbed by chlorophyll and is strongly reflected by water whereas, the SWIR band is strongly absorbed by water and chlorophyll, and is strongly reflected by bare soil. The NDWI is used due to its direct relationship with fuel moisture and its better performance over the NDVI (Normalised Difference Vegetation Index) in the study area, according to a study conducted by Verbesselt et al. (2006).

The NDWI values range from 1 to 1, indicating low water content to very high water content respectively. A study conducted by Gao (1996), shows that healthy vegetation has positive NDWI values and dry vegetation has negative values. Fire studies are interested in vegetation that has low NDWI values; this is the dry vegetation which is more likely to burn hence producing high fire intensity levels.

While calculated NDWI values range from 1 to 1, the fire intensity calculation requires fuel moisture content as a percentage from 0 to 100 %. As a result the range of NDWI values has to be changed to suit the required scale and yet still representing low water content and high water content correctly. The fire intensity also requires fuel moisture as a percentage; the adjustments discussed here are achieved through Eq. 3, which is the equation for fuel moisture content shown below:

Table 1 The (unit-less) fire danger ratings of Mpumalanga and Limpopo provinces of South Africa (by SAFDRS)

	INSIGNIFICANT (BLUE)	LOW (GREEN)	MODERATE (YELLOW)	HIGH (ORANGE)	HIGH- EXTREME (RED)
MPUMALANGA LOWVELD	0 - 4	5 -19	20 - 24	25 - 27	≥28
LIMPOPO LOWVELD	0 - 4	5 - 19	20 - 24	25 - 27	≥ 28

$$FMC = \left(\frac{(NDWI + 1)}{2}\right) \times 100 \tag{3}$$

The calculations for the fire danger index follow the calculations for the fire behaviour. The burning index is selected to provide an indication of an areas susceptibility to fire danger. Hence it is used as the fire danger index in this case. The reason for this is that a study was conducted to compare the results of the burning index to the values derived from the SAFDRS and these compared very well.

The burning index calculated in this model is based on the equation derived in the USA Fire Danger Rating System. The burning index is used to quantify the fire danger arising from the calculation of fire intensity. Although this equation was developed in the USA it is used because similarities have been found between the behaviour of surface fires in the South African Savannas and the tall grass American prairies, where this equation was initially developed (Trollope et al. 2002). The burning index (BI) is calculated as follows:

$$\text{Burning Index}\,(BI) = k[j(FI/60)]^{0.46} \tag{4}$$

where:

FI Fire Intensity
k 10/ft
j 100 (a scalar parameter for SA savannas)

Table 1 shows the ranges of fire danger based on the values of the burning index per region.

4.2 Fire Spread Model

The spread of a fire in this model is determined by the transfer of heat energy and rate of spread of fire, and is developed based on the Cellular Automata (CA)

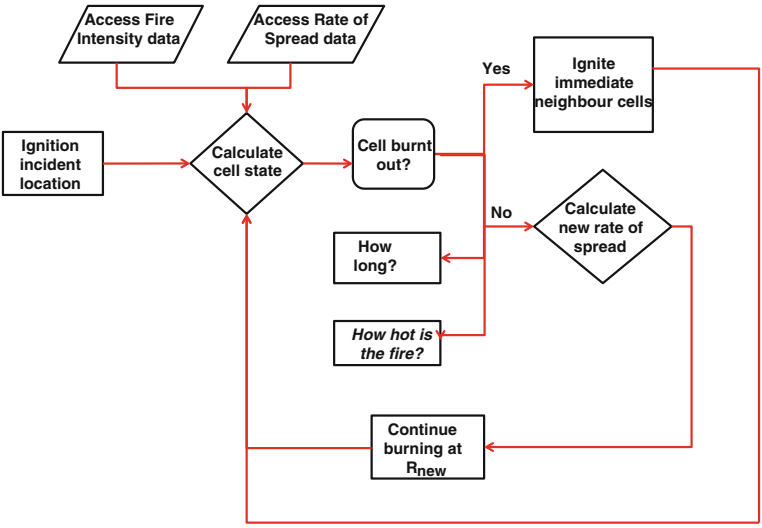

Fig. 6 Overview of the CA based fire spread model

modelling approach. This model considers the spread of fire in all directions and not just the forward wind direction. The rate of spread calculated within the fire behaviour model is used as the basic fire characteristic from which the spread is simulated. A summary of the CA based fire spread model is represented by Fig. 6.

The calculation for rate of spread is based on the fire intensity that was derived for the fire behaviour model. The fire intensity model only uses parameters that have been proven by Trollope (2002) to have the most effect in the study area, hence the effects of some variables such as aspect have not been included, although this could be useful in another area. The calculation of rate of spread is illustrated in Fig. 7.

The CA model developed in this study is based on a square lattice of cells hence all data is represented in grid raster format. Cellular automata was selected to model the fire spread in GIS because of its gridded nature which is easy to emulate in raster GIS. The assumption made is that each CA cell, which is also a raster image pixel, exhibits homogenous conditions of the phenomenon it is representing. This CA based fire spread model relies on the calculation of the rate of spread of fire, the prevailing wind conditions, and a cell neighbourhood of 8 contiguous pixels, which are often referred to as the Moore Neighbourhood. This means that the CA model performs operations considering 9 cells as a unit in time. Figure 8 shows the centre cell and its contiguous neighbours; the Moore Neighbourhood.

The fire propagation process is controlled by letting a cell occupy one state at a time. A cell in the proposed model can be in either one of the following three finite states: not burning, burning or burnt out. All cells start out in the not burning state.

Transitions rules are used to govern the spreading of fire from one cell to the next. These rules are outlined as follows:

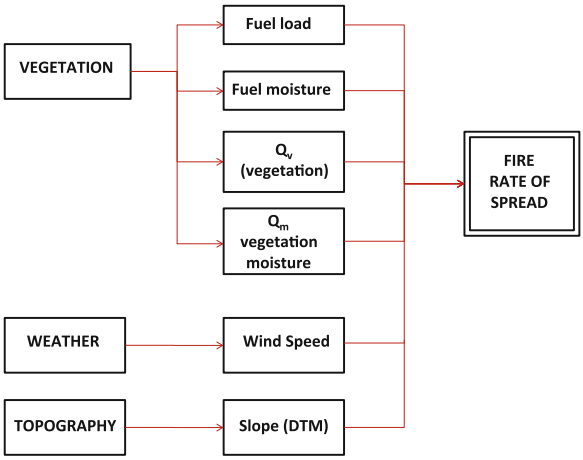

Fig. 7 The derivation of the fire rate of spread from vegetation, weather, topography and heat components

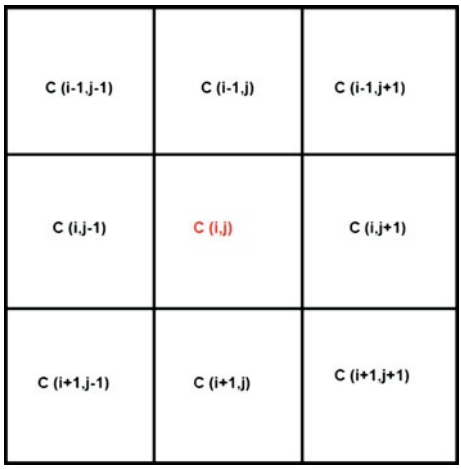

Fig. 8 A representation of the Moore neighbourhood used in the CA model

- Fire spreads to a cell if at least one of its neighbours has burned as far as the boundary between the two cells.
- The fuel in a cell burns only if it receives heat energy that is enough to bring about combustion
- A burnt out cell cannot be reignited and cannot continue burning after all the fuel has burnt out.
- A cell will not burn if it does not contain any fuel

Following Fig. 8, the CA model performs operations on 9 cells at a time as a unit. The cell operations and model processes are discussed in this section in line with Fig. 4. At the beginning of a fire event, one cell which is the centre cell is ignited, and the state of this cell changes from 'not burnt' to become an actively 'burning' cell. The cell continues to burn until the fire reaches the boundary of the

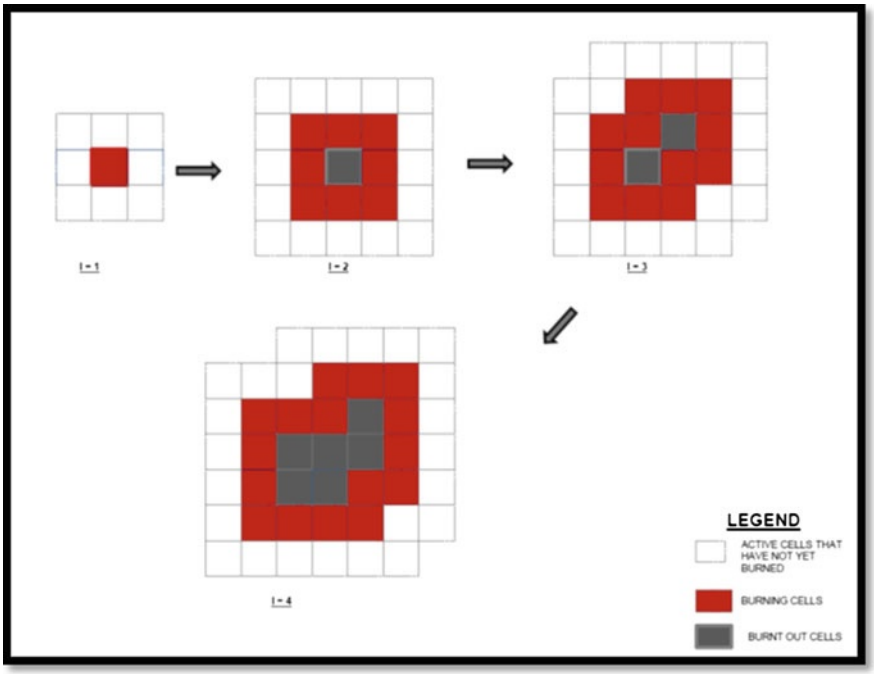

Fig. 9 Illustration of the first few stages of a growing CA fire

cell. Once the fire reaches the boundaries, this is a trigger event that alerts the neighbouring cells and the model acquires information about these cells and performs calculations to determine if the heat received is enough to ignite these neighbouring cells. If there is not enough heat the cell state remains as 'not burnt', if the heat is sufficient to cause ignition in the neighbour cell, the cell changes state to 'burning'.

At this stage one of two things could happen if the heat is not enough to ignite any neighbours, the burning cell burns until it burns out and fire ceases. If any neighbour is ignited, process continues and fire grows. At this stage the model determines if the previous cell is still burning or has burned out. If it has burnt out it becomes dormant and cannot be reignited otherwise it carries on burning. The newly ignited cells also become focus cells and the process repeats until the fire burns out as a result of any of the above mentioned fire stopping events. Figure 9 shows the first few stages as a fire grows.

Using CA modelling in a GIS environment has a number of advantages. The regular grid structure of CA, used in this study, is similar to that of raster data format hence no major adjustments need to be done to the input data. Manipulation of this data is also facilitated with no difficulty. Complex situations are modelled with ease, based on simple transition rules through the use of cellular automata.

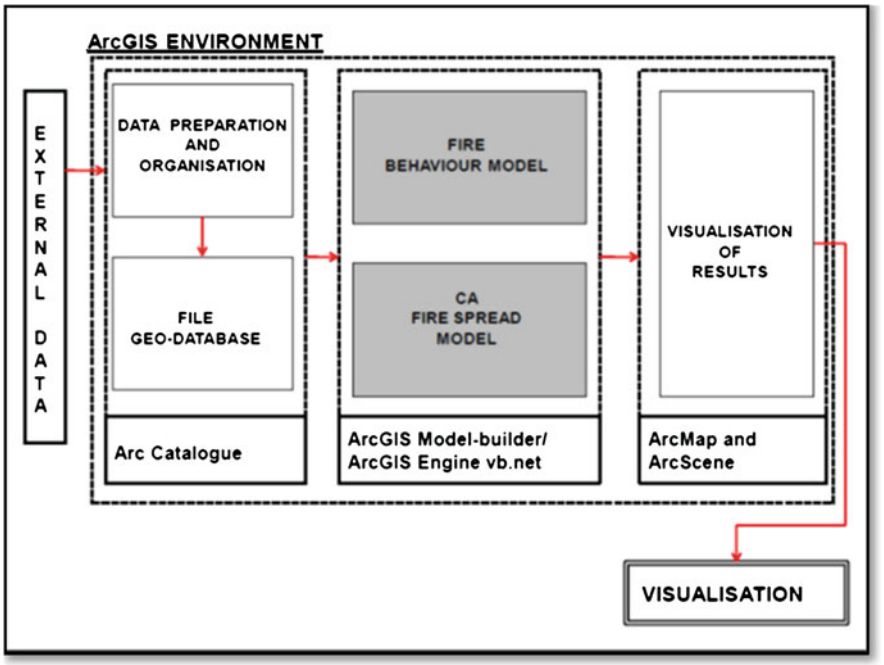

Fig. 10 Overall system Architecture of fire model on the ArcGIS platform

CA makes it possible to perform dynamic modelling in a raster based GIS environment.

This cellular automata based fire spread model is implemented in the ArcGIS ModelBuilder geoprocessing environment, and requires the development of a custom geoprocessing function tool using ArcObjects and VB.net to account for more complex calculations and operations. This facilitates the fast and effective performance of the model and compensates for the functional limitations of ModelBuilder.

Figure 10 shows the overall structural parts of the model as implemented in ArcGIS. This demonstrates the fully integrated nature of the model, where all operations are performed internally within one platform with the only entry and exit points being the raw data inputs and the processed maps and animated output files of the predicted fires.

5 Results

This model was validated by comparing the attained results with previous, actual fire events in the study area that have been documented. Quantitative analysis, in the form of Sorenson's Coefficient for Similarity Analysis was used to evaluate the

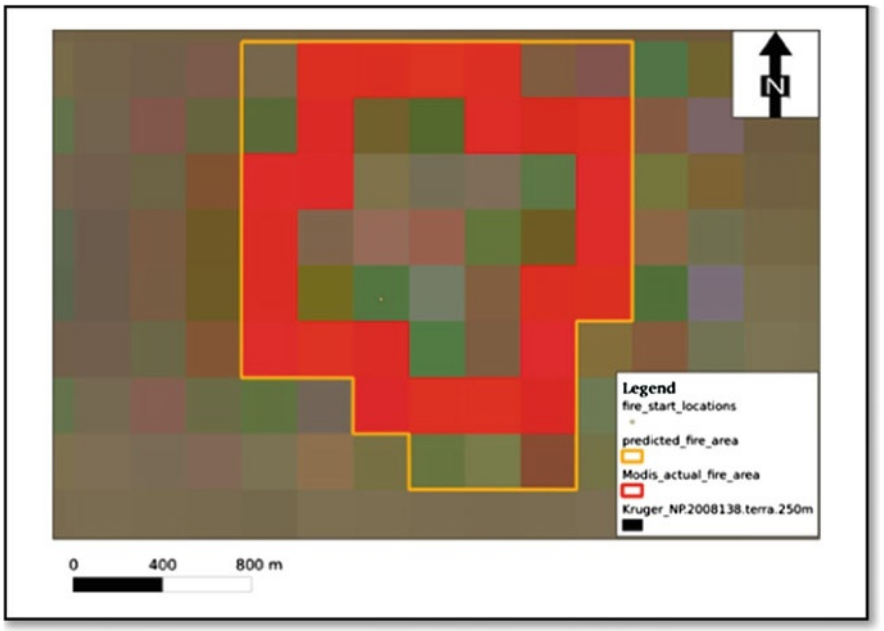

Fig. 11 Comparison of predicted fire area with active fire outline from MODIS

results. The model was tested using fire events that occurred under varying conditions which include amongst others, wind speed, biomass content, and combustion period. Upon this evaluation, the model proved most successful where fires burned under moderate wind speed and a combustion period of less than 24 h, giving a best accuracy of 88 % and worst performance at 66 %, with 2 of the 5 test cases reporting a 66 % result. The model over-predicts the area burnt during a fire incident, under high wind speed conditions.

Figure 11 shows a comparison of the predicted fire area compared to the actual fire area as detected by MODIS sensors on board Terra and Aqua satellites.

Table 2 shows some results of the qualitative analysis of the fire model. These results are derived from five test fires that represent differing fire conditions. Figure 12 is an illustration of these test fires. Fire case 1, depicted in Fig. 11, burned under moderate wind speeds and burned for a few hours. Fire case 2, (b) shows a fire that burned under low wind speed conditions and relatively low fuel load. Fire case 3 (a) burns under high wind speeds across a river. Fire case 4 (d) burns in high wind speed conditions, over a large area for over one day. Fire case 5 burns under moderate wind speeds for a long period.

Figure 13 shows the component areas according to Sorenson's coefficient for a simulated fire area. The blue area shows the area that is predicted to burn but does not actually burn (over-prediction, labelled B in Table 2), the green area represents the area that actually burned but was not predicted to burn (under-prediction,

Table 2 Quantitative analysis of prediction results using Sorenson's coefficient for similarity analysis

Case	Description	Observed area burnt (ha)	Predicted area burnt (ha)	A (ha)	B (ha)	C (ha)	SC
1	Moderate wind speed, short burning period	258.1	296.6	243.8	51.9	13.72	**0.88**
2	Low wind speed, low fuel load	191.12	185	142.87	40.77	46.48	**0.77**
3	Moderate to high wind speed, short burning period	375.86	452.2	383.44	67.23	39.04	**0.88**
4	High wind speed, long burning period, large fire	1165.21	885.23	676.46	214.9	487.8	**0.66**
5	Moderate wind speed, long burning period	438.48	886.31	439.32	438.32	15.27	**0.66**

labelled C in Table 2), and the orange area, labelled intersection area, represents the area that was predicted to burn and did actually burn (accurate predictions, labelled A in Table 2).

6 Discussions and Limitations

This embedded model is developed as a building block towards a GIS based decision support tool that can be used by none GIS expects who have a stake and interest in the minimisation of risk that results from wild fires. The main aim is to have a model that requires minimum input and interaction from the user, yet providing maximum information possible. This model is developed in such a way that it can be incorporated as part of a greater fire management application.

Future work would include developing a web enabled, distributable version of the model to make relevant information promptly available and accessible to all stakeholders. One of the most important aspects of a disaster decision support tool is to provide information timely so that it can be used to minimise the effect of the fire hazard.

A major limitation to this study was the availability of input data. Meteorological data is available in point, vector format from weather stations within the study area. Since the model is grid based, the data needs to be interpolated in order to provide a grid representation of the weather conditions. This results in inaccurate weather prediction. A weather prediction model can be implemented alternatively to improve the results.

In order to improve the results of the model, high resolution satellite imagery, both spatial and temporally, is required.

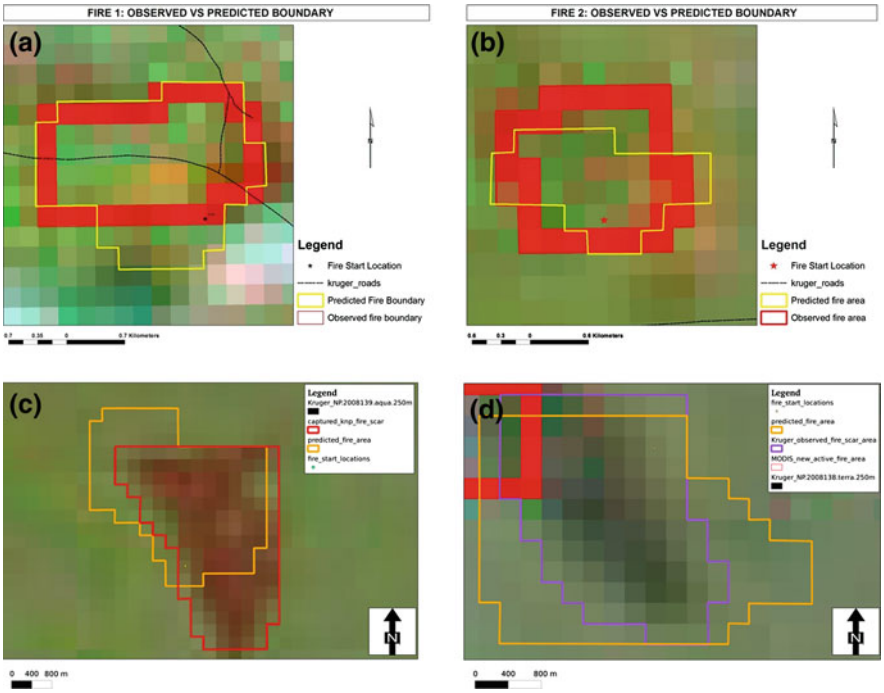

Fig. 12 The fire tested cases

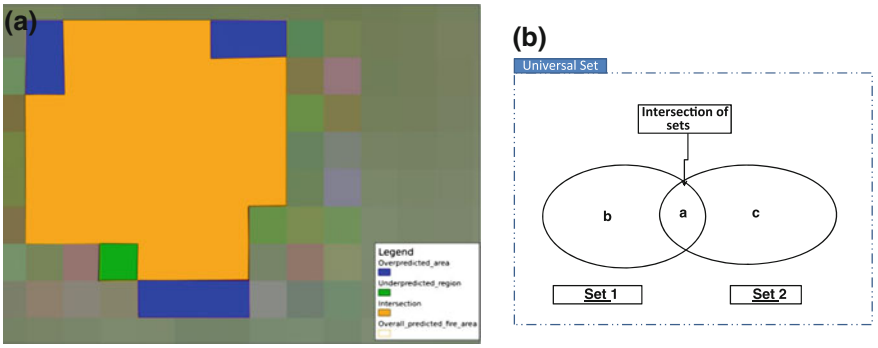

Fig. 13 Illustrations of the components of Sorenson coefficient for validation of fire spread model

7 Conclusions

Following an evaluation of the model and reasonably accurate results that were acquired, it is concluded that a fire model can be successfully embedded into a GIS. All the fire modelling equations and formulae were successfully implemented

in the GIS environment and accurate results were acquired. The dynamic growth of a fire with respect to time was successfully implemented, demonstrated and visualised through the use of GIS.

The objectives of the study were achieved and the conclusions to the research questions are as follows:

- **Complex fire modelling formulae can be executed in a GIS**. This is illustrated by the successful results acquired from the calculations of fire behaviour parameters, namely fire intensity, fire spread and their component calculations.
- **The GIS environment is suitable for full integration of fire modelling** (embedded): the ArcGIS environment was able to provide all the required functionality for the modelling. This is illustrated in Fig. 7.
- **GIS is able to cope with dynamic modelling processes**. The CA model was successfully implemented in GIS to show the spread of fire through changing states of fuel and area conditions with respect to time.

References

Albright D, Meisner BN (1999) Classification of fire simulation systems. Fire Manage notes 59(2):5–7

Andrade Neto PR, Jr Ribeiro PJ, and Fook KD (2005) Integration of statistics and geographic information systems: the R/TerraLib case. In: GeoInfo 7 2005, Campos do Jordao, Brazil

Brenning A (2001) Geostatistics without stationarity assumptions within geographical information systems. Freiberg Online Geoscience, vol 6. Available at: http://www.geo.tu-freiberg.de/fog/FOG_Vol_6.pdf. [Accessed 3 Aug 2012]

Brimicombe A (2003) GIS, Environmental Modelling and Engineering, 1st edn. Taylor & Francis, London

Childs C (2004) Intepolating surfaces in ArcGIS spatial analyst. ArcUser, July-September 2004, pp 32–35

Eldrandaly K, Eldin N, Sui D, Shouman M, and Nawara G (2005) Integrating GIS and MCDM using COM technology. Int Arab J Info Technol 2(2):163–167

ESRI (2008) What is ArcGIS, Technical report 2008

Finney MA (1998) FARSITE: fire area simulator-model development and evaluation, Technical report, pp 1–52

Gao B-c (1996) NDWI-a normalised difference water index for remote sensing of vegetation liquid water from space. Remote Sens Environ 58(3):257–266

Glasa J, Halada L (2008) On elliptical model for forest fire spread modeling and simulation. Math Comput Simul 78(1):76–88

Govender N (2003) Fire management in the Kruger National Park, Arid lands newsletter 1(54) Nov/Dec

Johnston P, Milne G, Klemitz D (2005) Overview of bushfire spread simulation systems, Bushfire CRC, 1–25 March

Pastor E, Zarate L, Planas E, Arnaldos J (2003) Mathematical models and calculation systems for the study of wildland fire behaviour. Prog Energy Combust Sci 29:139–153

Trollope WS, Trollope LA, Hartnett DC (2002) Fire behaviour a key factor in the fire ecology of African, forest fire research and wildland fire safety, Rotterdam

Van Wilgen BW, Biggs HC, O'Regan SP, Marè N (2000) A fire history of the savanna ecosystem in the Kruger National Park, South Africa, between 1941 and 1996. S Afr J Sci 96:167–180

Verbesselt J, Jonsson P, Lhermitte S, van Aard J, Coppin P (2006) Evaluating satellite and climate data-derived indices as fire risk indicators in savanna ecosystems. IEEE Transcations Geosci Remote Sens 44(6):1622–1632

Willis C, Van Wilgen B, Tolhurst K, Everson C, D' Abreton P, Pero L, Fleming G (2001) The development of a national fire danger rating system for South Africa. CSIR, Pretoria

Yassemi S, Dragicevic S, Schmidt M (2008) Design and implementation of an integrated GIS-based cellular automata model to characterize forest fire behaviour. Ecol Model 210:71–84

Visualizing Crowd Movement Patterns Using a Directed Kernel Density Estimation

Jukka M. Krisp, Stefan Peters and Florian Burkert

Abstract "Classic" kernel density estimations (KDE) can display static densities representing one point in time. It is not possible to visually identify which parts of the densities are moving. Therefore, within this paper we investigate how to display dynamic densities (and the density changes) to identify movement patterns. To deal with a temporal dimension (in our case study a dynamic crowd of individuals) we investigated the application of directed kernel density estimation (DKDE). In a case study we apply the DKDE to a point dataset presenting individuals approaching the Allianz Arena in Munich, Germany, with different speeds from different directions. Calculating the density using a directed kernel with this data, results in a density map indicating the movement direction with a visible "ripple" effect. Ripples move at different rates to the substances in which they occur. That tells us something about crowd dynamics and enables us to visually recognize the parts of the crowds that are moving plus the underlying movement directions.

J. M. Krisp (✉) · S. Peters
Technische Universität München (TUM), Bauingenieur- und Vermessungswesen, Kartographie (LFK), Arcisstraße 21, 80333 Munich, Germany
e-mail: jukka.krisp@bv.tum.de

S. Peters
e-mail: stefan.peters@bv.tum.de

F. Burkert
Technische Universität München (TUM), Remote Sensing Technology, Arcisstraße 21, 80333 Munich, Germany
e-mail: florian.burkert@bv.tum.de

J. M. Krisp et al. (eds.), *Earth Observation of Global Changes (EOGC)*, Lecture Notes in Geoinformation and Cartography, DOI: 10.1007/978-3-642-32714-8_17,

1 Introduction

Monitoring the motion patterns of people and crowd dynamics is a wide field of research. Data on individual locations is becoming available at an increasing speed and level of detail. The data can be obtained from mobile devices like individual mobile phones, aerial or other imagery. This offers a possibility to record the individual position of people forming a crowd over time and store them as a dynamic point dataset. These datasets can cover different spatial and temporal scales. Crowd monitoring may be of interest in a number of events like football games (or other sport events), concerts or festivals. Effective crowd management requires crowd monitoring in near real time and on different scales. Additionally, the information required by a monitoring method needs to be communicated effectively to the user monitoring the crowd. This is not a trivial task as crowds consist of individuals who might have different motion speeds and directions. Furthermore, crowds are quite scattered, meaning partly individuals that are close together and partly more open space between the individuals. These form a pattern with different densities within the crowd. How can we display and recognize the dynamic densities (and the density changes) within the movement patterns?

Today, data is produced at an incredible rate and the ability to collect and store the data is increasing at a faster rate than the ability to analyze it. Over the last decades, a large number of automatic data analysis methods have been developed (Thomas and Cook 2005). These data collection techniques include monitoring of moving objects from airborne image sequences: the detection and tracking of vehicles to observe moving traffic (Butenuth et al. 2009) and the detection and tracking of people including the interpretation of their behavior (Butenuth et al. 2010). Hinz (2009) shows that reliable information for the density of groups of people; their activity as well as their movement can be derived from imagery acquired from aerial camera systems. Other approaches facilitate video cameras mounted on buildings or posts. The individuals are tracked in these image sequences or video streams and displayed as moving points (Hinz 2009).

The general objective of this paper is to investigate the density calculation and representation of spatially and temporally dynamic point datasets. Our aim is to efficiently display and identify the general moving direction within a scattered crowd of individuals. Therefore, advanced clustering methods and investigations on the presentation of dynamic clusters are necessary to provide an appropriate analysis and a communication of the information. We choose to experiment with the application of a directed kernel density (DKDE) by Krisp and Peters (2011), applied to a point dataset presenting individuals approaching the Allianz arena in Munich with different speeds from different directions (Burkert et al. 2010).

2 State of the Art

Crowd monitoring and analysis is an emerging field of research. Big events in various situations like festivals, concerts, sport events or religious activities receive an increasing number of attending people, which makes crowd monitoring indispensable especially for security reasons. An overview of several crowd monitoring and analysis techniques is given in Zhan et al. (2008), including tracking and observation methodologies as well as approaches for crowd modeling and event inference. Depending on the number of monitored people and the data acquisition device, either the crowd itself or single people within the crowd can be identified. Andrade et al. (2006) use Hidden Markov Models (HMM) based on optical flow to detect emergencies in dense crowds, disregarding any tracking mechanisms and, therefore, without using single trajectories. Pellegrini et al. (2010) try to model semi-crowded scenes by estimating interactions and grouping aspects between pedestrians as well as the trajectories of the pedestrians using a third-order conditional random field (CRF). Crowd analysis and the creation of crowd data is an ongoing research topic which is in any case related to the specific application. Therefore, the data derived from crowd analysis systems can be of different characteristics like point data, vector data, image data and so on.

The combination of visualization, human–computer interaction and geostatistical data analysis helps the identification of crowd movement patterns. On a general level this may assist insight generation based on large and diverse spatial geocoded data of varying quality in areas such as civil protection and public security. This research is related to support and facilitate the concept of geovisualization (Dykes et al. 2005a) and visual analytics. From a broader perspective, geovisualization provides theory, methods and tools for the visual exploration, analysis, synthesis and presentation of data that contain geographic information (Dykes et al. 2005b; MacEachren and Kraak 2001). According to Thomas and Cook (2005), Visual Analytics is the science of analytical reasoning supported by interactive visual interfaces. The complex nature of many problems makes it indispensable to include human intelligence at an early stage in the data analysis process. Andrienko et.al. (2010; Andrienko, et al. 2007) define "Geovisual Analytics for Spatial Decision Support" as the research area that looks for ways to provide computer support to solving space-related decision problems through enhancing human capabilities to analyze, envision, reason, and deliberate. Core parts of data analysis require human judgment and domain knowledge. Concerning data presentations and transformations, the question is how to display data that is appropriate to the analytical task and effectively communicates the important content?

Visual Analytics methods allow decision makers to combine their human flexibility, creativity, and (domain experts) background knowledge with the enormous storage and processing capacities of today's computers to gain insight into complex problems. Using advanced visual interfaces, humans may directly interact with the data analysis capabilities of today's computer, allowing them to make well-informed decisions in complex situations (Thomas and Cook 2005) as moving crowds.

Continuous surface representations as kernel density estimations have advantages in the visualization and analysis of population distributions (Langford and Unwin 1994; Martin and Bracken 1991). Kernel density estimation (KDE), devised for estimating a smooth empirical probability, is now a commonly applied spatial analysis technique to transform a geographically distributed set of points into a density surface in a GIS environment (Nakaya and Yano 2010). Batty (2009) states that density is a point measure defined as the mass of some entity, such as a population of individuals or a collection of buildings described by their size, but normalized by some measure of the area they occupy. Densities in this form are dimensionless only in a 'weak' sense, because their values always pertain to some measure of area.

2.1 Kernel Density Estimation and Directed Kernel Density Estimation

A classic method to display densities for individual points is the usage of a kernel density estimation method (Cressie 1993; Silverman 1986; Tukey 1977). The standard kernel density estimation method applies a linear (or Gaussian) kernel. These kernels have a defined bandwidth (sometimes referred to as search radius) around each point. When calculating the density value for each underlying raster cell the method provides a smooth surface. Each raster cell value represents the estimated density at this particular point.

A normal distribution function is used and the points are visited by the following "three-dimensional-moving-function" (Scott 1992).

$$\widehat{f}_h(x) = \frac{1}{N \cdot h} \sum_{i=1}^{N} K(u) \text{ with } u = \frac{X - X_i}{h} \text{ and } K_G(u) = \frac{1}{\sqrt{2\pi}} \cdot \exp\left(-\frac{1}{2}u^2\right) \quad (1)$$

with:

$\widehat{f}_h(x)$	General Kernel density function
N	number of sample points
K	Kernel function (for example a linear Kernel K_l or a Gaussian Kernel K_G)
K_G	standard Gaussian Kernel function
h	smoothing parameter (bandwidth/kernel radius)
X	Point (x,y) for which the density will be estimated
$X_1, X_2, \ldots, X_N$	sample points, placed within the kernel radius h

The size of the bandwidth strongly affects the resulting density surface (O'Sullivan and Unwin 2003). An optimal bandwidth determination was investigated by Silverman (1986). As suggested by Silverman the "optimal" bandwidth can be calculated by the following equation (Eq. 2).

$$h\_opt = 1.06 * \min\left(\sqrt{\text{var}(P)}, \frac{\text{IQR}(P)}{1.34}\right) * n^{-\frac{1}{5}} \quad (2)$$

with:

P	dataset: point coordinates
h_opt	optimal bandwidth
IQR (P)	interquartile range (distance between the 1st and 3rd quartile)
var(P)	variance of P
n	number of points (length of P)

Kernel density estimates have been used for cluster detection in various fields, such as crime analysis (Ratcliffe and McCullagh 1999). Kwan (2003) uses geovisualization of activity patterns in space–time and displays the results as a continuous density surface. She applies the density estimation as a method of geovisualization to find patterns in human activities related to other social attributes. Several studies (Assent et al. 2007; Krisp 2010; Krisp and Špatenková 2010; Maciejewski, et al. 2010; Peters and Krisp 2010) investigate the classic kernel density estimation and define it as a visual clustering method. This technique supports the visual grouping of data patterns based on mutual (dis-) similarity. Nakoya and Yano (2010) describe a new approach for crime mapping using a space–time cube wherein a spatio-temporal density distribution can be visually explored in an interactive 3D GIS environment. A question is how to consider the direction and speed of movement for each individual point when displaying a density surface?

Based on the movement vector assigned to each point, we apply a directed (or tilted) kernel. Every movement vector is formed by the point position at two different times, t_1 and t_2. The directed kernel is a function that is non-symmetrical and recognizes a shifted tendency towards the point's movement direction.

Figure 1 illustrates the assignment of a directed kernel based on the movement vector. Depending on the defined kernel bandwidth, on the point speed and on the time difference between t_1 and t_2 the point position at time t_2 can be inside or outside of the kernel bandwidth. In case of a position outside of the kernel bandwidth the kernel is tilted maximal until the perpendicular projection of the kernel apex above the kernel ground circle. The more the kernel is tilted the higher is the point speed. To the points that do not change their position no vector will be assigned; therefore these points will use a non-directed (not tilted) kernel.

For each grid point (pixel) inside a kernel search radius the grid point density value is defined as the vertical intersection with the envelope of the tilted cone above the grid point position. If several kernels overlap each other the grid point density values in the overlapping area are accumulated, like in "classic" kernel density estimation. The calculation of the pixel kernel density values relies on the theorem on intersecting lines.

An alternative option is to calculate surface parameters and show how these change between the two situations. Additionally it is possible to add a vector,

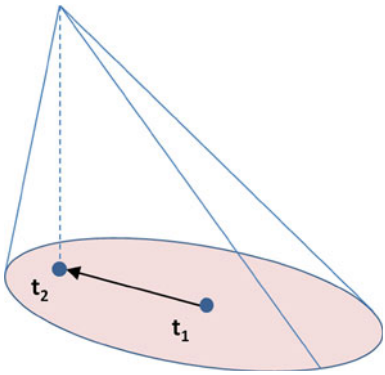

Fig. 1 Directed kernel to consider the movement direction and the speed of each point (Krisp and Peters 2010)

which allows us to identify "the underlying dynamics of the individuals that are forming the crowd".

As a case study we document the application of the directed kernel density method to a dataset representing individuals moving within the area close to the Munich football stadium (Allianz Arena). In this case the points and trajectories represent visitors approaching the stadium.

3 Case Study: Individuals Tracked as Moving Points

The input data points representing the individuals are acquired by a system for the analysis of aerial image sequences (Burkert et al. 2010). The image sequence is obtained by a wide-angle digital camera system for near real-time scenarios, called 3 K camera system (Kurz et al. 2007

The used image sequence has been taken before a soccer match in front of the stadium with thousands of people approaching to the gates. The images have been captured from an altitude of about 1000 m by the 3 K camera system using the nadir view camera. One single image covers an area of about 600 × 900 m. Each image is transformed into an orthophoto in advance by using a digital elevation model (DEM). For this purpose, navigation data is collected by an IMU (inertial measurement unit) and a GPS sensor to provide the orientation and the coordinates of the airplane. Figure 2 shows the designated area of interest for the investigations. Individuals are represented by a dot of about 5-10 pixels, the ground resolution of the images is 0.2 m. Tracking is performed within a sequence of 16 images, captured with a frame rate of 2 Hz. Therefore, the image sequence covers a time range of 7.5 s providing a sufficient moving space for motion analysis.

The monitoring of individual people is accomplished with two steps: the first part aims at deriving the trajectories of individuals from the image sequences by using a tracking-by-detection approach. Given macroscopic motion parameters, coarse regions of differing characteristics like density, activity and motion can be defined (Hinz 2009). Additionally, information about the scene is determined, for

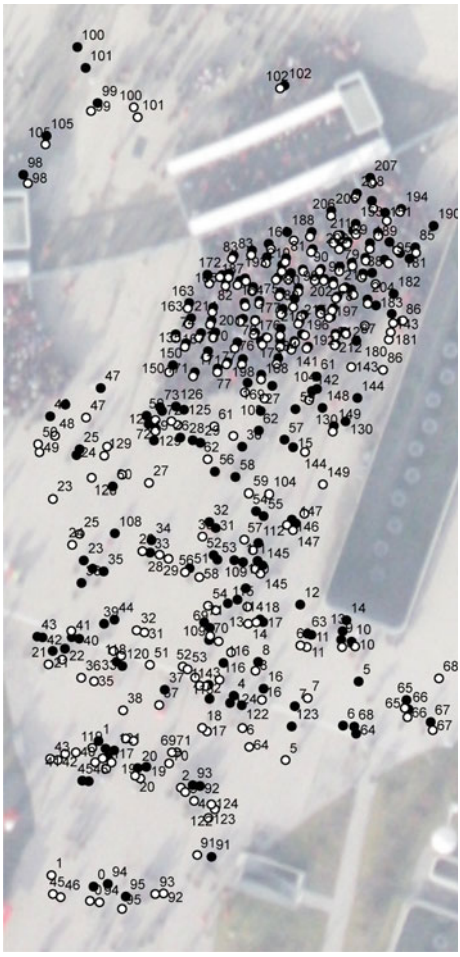

Fig. 2 Points representing individual people; each point has an individual id at a starting (*white*) and destination position (*black*)

example from GIS data, to gather knowledge about the conditions of the local environmental limits to possible room for movement. Afterwards, single people in each image are detected with a blob-based approach. The results of the detection step are image coordinates (r,c) as well as real-world coordinates for each person in each image. In the next step, these detections are tracked by linking them iteratively over the images of the sequence. From the linked coordinates of each trajectory, attributes like speed and motion direction can be calculated. The second part of the monitoring system contains the interpretation of the behavior of the people to detect exceptional events such as panic situations or brawls using the delineated motion trajectories. This is done by detecting the type of motion interaction between neighboring pedestrians by using Hidden Markov Models (HMM) (Burkert and Butenuth 2011). The start and end points used in this paper have been derived manually, as they serve as reference data for the system which

tries to analyze crowds of people automatically (Burkert et al. 2010). We used point data of the first (time 1) and the last (time 2) sequence within a time difference of 120 s. We investigated our approach also by using shorter time differences between time 1 and time 2. When the time difference was below 90 s, the ripples were less visible due to the fact that the tilting of the kernels is lower. For time differences even below 60 s trends were hardly visible. In this test data the mean distance of the points moving between time 1 and time 2 was 28 m. The maximum of this moving distance was 90 m.

3.1 Application of the DKDE-Method to the Test-Data

We apply an incremental development of the traditional kernel density estimation (KDE) processes. To deal with a temporal dimension (in this case a dynamic crowd of individuals) Krisp and Peters (2011) investigated the application of a *directed kernel density estimation (DKDE)*. A technical documentation of how the shape of the kernel within the DKDE approach influences the visual output is published in more details in Peters and Krisp (2010). Using Matlab-software we executed the following steps listed in Fig. 3a and related to the schematic Fig. 3b

The bandwidth for our test dataset was defined by using the equation shown in Eq. 2 (Silverman 1986). The "optimal" bandwidth was calculated for all points at time t1 (white points) and for all points at time t2 (black points) shown in Fig. 2. The bandwidth for the two points sets was nearly identical; with h_opt(t1) = 44 m; h_opt(t2) = 48 m. Therefore the bandwidth is set to h = 46 m and we used this bandwidth for all the density calculation. For about 20 % of our points the moving distance is larger than the value for the optimal bandwidth (46 m). The directed kernel is shifted according to the moving distance of a point between time 1 and time 2. For those points whose moving distance is higher than the used bandwidth h, the directed kernel was shifted only until the kernel edge. We performed the approach with varying bandwidths. When using smaller bandwidths, the ripples appear not as visible as with larger bandwidth.

Figure 4 shows the dataset applying a directed kernel with a 34 m bandwidth (a) and the same dataset with a 46 m bandwidth (b). When using bigger bandwidths the ripples appear to be more visible.

3.2 Results: Visualizing Dynamic Densities

Based on a movement vector assigned to each of the moving individuals, we apply a directed (or tilted) kernel to calculate and visualize the dynamic density pattern illustrated in Fig. 5a and b.

The results are displayed in Fig. 5a for the full dataset. The directed kernel density map is overlaid with thin black contour lines of the classification. These

- Reading in the given point coordinates of time t_1 and time t_2
- Defining the output area by the bottom left point and the top right point extended by one-fifth.
- Defining the resolution of the gridded ou tput points: in our case 500*500
- Calculation of all coo rdinates (x,y) for the gridded points
- Defining the bandwidth (h)
- Defining the kernel height (h_k)
- Determination of all gridded points (x_i) for each given point at time t_1 inside its search radius h
  - o Calculation of the intersection point S for each of the determined gridded point (x_i) using the trig onometric functions of triangle P(t1),P(t2),S
  - o Computation of the density height (h_i) for each gridded point (x_i) by using the theorem on intersecting lines
- Adding up the density heights (h_k) for all gridded points laying inside of overlapping search radiuses of several given points
- Exportation of the resulting "joint density" raster to a point-shapefile (x,y,z)

- Implementation of this joint density est imate output to a GIS (in our case ESRIs ArcMap)
- Visualization of the density using a blue color scheme classified with an equal interval (in our case with 32 classes)

(a)

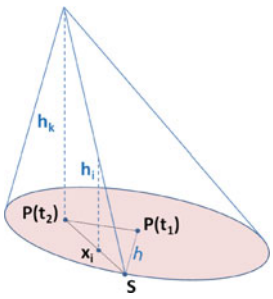

(b)

Fig. 3 **a** work steps of applying a directed Kernel density to our input data points and **b** a schematic illustration of applying the directed Kernel to calculate the density

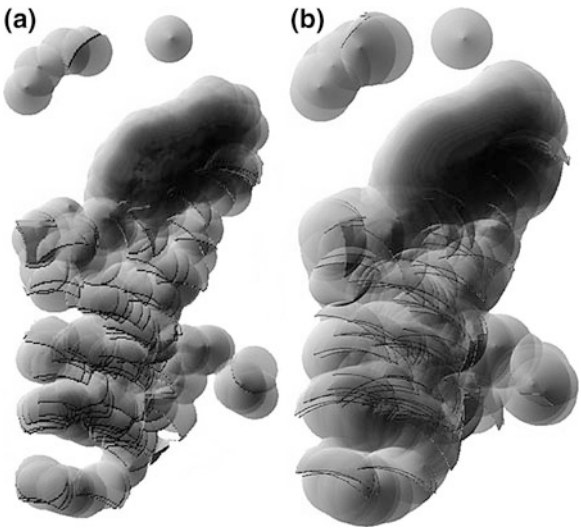

Fig. 4 Comparison of **a** 34 m bandwidth and **b** 46 m bandwidth of the test dataset

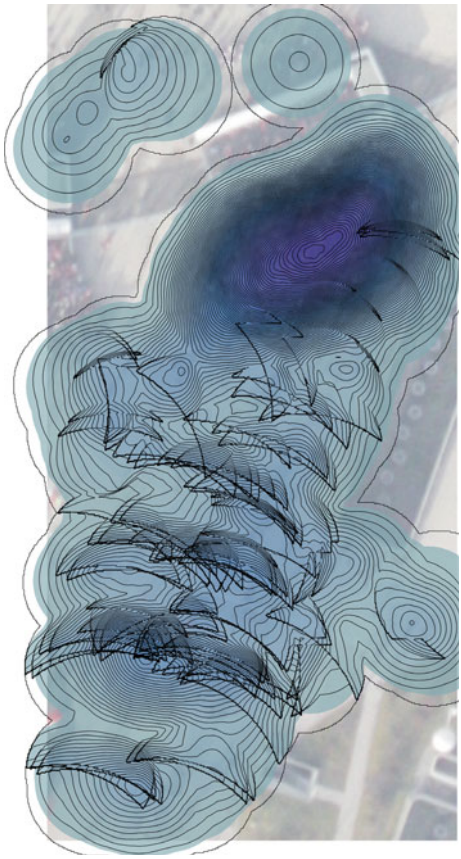

Fig. 5 **a** Result of the DKDE method applied to the Allianz Arena dataset with a color scale from dark to light blue

lines indicate a rippling effect of the underlying densities based on the movement data. As the ripples are directed from the south west towards the north east in Fig. 5b, we can "see" the general movement direction of the densely crowded parts. In the northern part of the test dataset the densities form one big dense spot with no rippling effect. That indicates no movement in this area (the crowd is standing and waiting with little or no movement).

How does the "ripple effect" in the directed kernel approach occur? When using a directed kernel the function is tilted towards the direction of movement for each point. In our case, when many points are moving towards the same direction, the directed kernels are added up resulting in higher values in the underlying raster cells that are within the movement direction. This causes sharp edges as shown in Fig. 5b.

To visualize this "ripple" effect more clearly, we can compute the contour lines based on the density surface resulting from the KDE and the DKDE. Figure 6a shows a classic KDE density map based on the points at time t1. The time t2 is not considered in this classic density surface. Figure 6b illustrates the movement

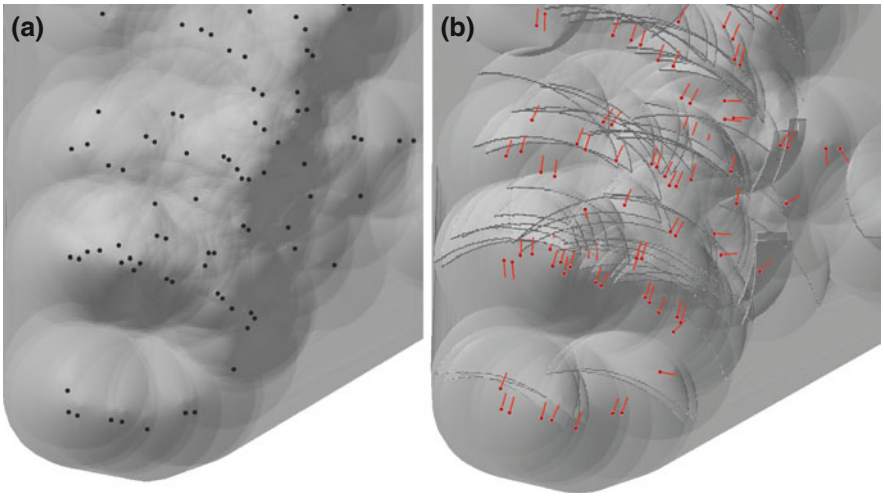

Fig. 6 Illustration of a.) result of the KDE method and b.) the "ripple" effect due to the densities based on a directed kernel

direction of each point with a vector. The density surface shows how "ripples" occur when the density is calculated with a directed kernel, which is based on the movement direction.

Figure 7 shows the contour lines for our Allianz Arena dataset with a KDE approach for one time instance and the directed kernels considering both time instances.

We investigated the approach also with using different kernel heights (see the h_k parameter in Fig. 3). When using an h_k equal to the bandwidth h the 3D-visualization of the density surface shows extremely high kernels which are not useful for a visual interpretation due to overlapping of the directed kernels. Therefore we use a kernel height h_k of 0.1 m. Figure 8 shows a three-dimensional illustration of the kernel density surface for the KDE method (8a) and it can be compared to the DKDE method (8b) showing the directed kernels.

When adding up the directed kernels, the steep rise in parts of the kernel tips tilted in such a way that clearly distinguishes them from the less steep sides. This occurs when two or more closely spaced points move in the same direction. A larger distance between two points (due to faster movement) is modeled with a larger tilt angle of the kernel. Points in the near proximity with a common direction strengthen the "ripple" effect. Ripples are not consistent. The ripple effect depends on the data. If we have individuals moving in different directions, hence there is not direction in the movement of the density, the ripple effect does not occur.

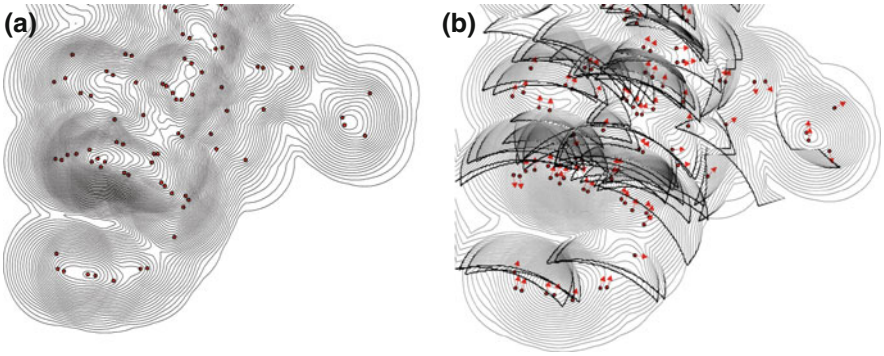

Fig. 7 *Contour lines* based on the resulting density estimation from the KDE (**a**) and DKDE (**b**) methods

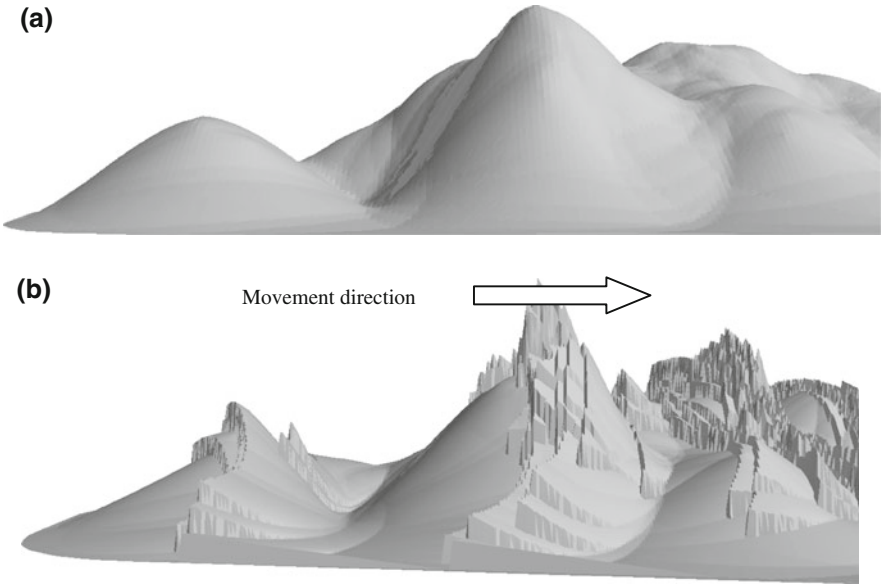

Fig. 8 Three-dimensional illustration of the KDE and the DKDE surface with sharp edges due to the directed kernels

4 Conclusions and Further Research

"Classic" kernel density estimations (KDE) can display static densities at one point in time. It is not possible to visually identify which parts of the densities are moving. With our method of applying a directed kernel density (DKDE) (based on two or more points in time) we can visually recognize the parts of the crowds that are moving plus the movement directions. Applying a directed kernel to consider

the movement direction and the speed of each individual provide a resulting density map indicating the movement direction with a "ripple" effect, shown exemplary in Fig. 5a and b.

The resulting density map is characterized by directed "ripples" or "waves". First informal discussions indicate that this method may support the visual analysis and prediction of "movement trends" based on the dynamic points (Fig. 5b). The current method is limited to the linear movement vectors between two points in time of the moving individuals. Further research may consider how the directed density calculation can be adopted to reflect full trajectories. How does the approach work (or otherwise) with more complex flows? It might be suggested that the method is likely to work best where flows are simple (with clear direction and little variation in the speeds of the individual items), but not where they are complex and contradictory. A careful visual analysis may indicate the general motion direction and the velocity in a reasonable way. Qualitative conclusions can be drawn regarding population density and activity. Further research will focus also on an empirical analysis of the resulting "wave"- visualizations with diverse users and anticipated domain experts (e.g. police, fire and rescue services). Furthermore we plan to incrementally develop this method by investigating different types of kernels to be applied. With the visual output we need to consider the size of the increasing and decreasing density changes will be displayed in more details. Additionally we intend to investigate the application of directed kernel density estimation to four-dimensional point datasets.

Acknowledgments We would like to thank Dr. Matthias Butenuth for his valuable comments in the preparation of this paper, especially sharing his expertise in the acquisition process of the population data. This research has been partly supported by the TUM IGSSE project 7.07.

References

Andrade EL, Blunsden S, Fisher RB (2006) Hidden markov models for optical flow analysis in crowds. In: International conference on pattern recognition (ICPR) (pp 460–463)

Andrienko G, Andrienko N, Demsar U, Dransch D, Dykes J, Fabrikant SI, Jern M, Kraak M-J, Schumann H, Tominski C (2010) Space, time and visual analytics. Int J Geogr Inf Sci 24(10):1577–1600

Andrienko G, Andrienko N, Jankowski P, Keim D, Kraak M-J, MacEachren A, Wrobel S (2007) Geovisual analytics for spatial decision support: setting the research agenda. Int J Geogr Inf Sci 21(8):839–857

Assent I, Krieger R, Mueller E, Seidl T (2007) VISA: visual subspace clustering analysis. SIGKDD Explorations 9(2):

Batty M (2009) Defining density. Environ Planning B: Planning Design 36:571–572

Burkert F, Butenuth M (2011) Event detection based on a pedestrian interaction graph using hidden markov models. In: Stilla U, Rottensteiner F, Mayer H, Jutzi B, Butenuth M (eds) Photogrammetric image analysis, lecture notes in computer science 6952. Springer, New York, pp 271–283

Burkert F, Schmidt F, Butenuth M, Hinz S (2010) People tracking and trajectory interpretation in aerial image sequences. Int Arch Photogram, Remote Sens Spat Inf Sci 39(3):209–214

Butenuth M, Reinartz P, Lenhart D, Rosenbaum D, Hinz S (2009) Analysis of image sequences for the detection and monitoring of moving traffic. PFG—Photogram Fernerkundung Geoinf 5:421–430

Cressie N (1993) Statistics for spatial data (revised edition ed), Wiley, New York

Dykes J, MacEachren AM, Kraak MJ (2005a) Advancing geovisualization. In: Dykes J, MacEachren AM, Kraak MJ (eds) Exploring geovisualization. Elseviers, Amsterdam, pp 693–967

Dykes J, MacEachren AM, Kraak MJ (2005b) Exploring geovisualization. Elsevier, Amsterdam

Hinz S (2009) Density and motion estimation of people in crowded environments based on aerial image sequences. Int Arch Photogram, Remote Sens Spat Inf Sci 38 (Part 1-4-7/W5, on CD)

Krisp J, Peters S (2011) Directed Kernel density estimation (DKDE). Annals of GIS 17(3):155–162

Krisp JM (2010) Planning fire and rescue services by visualizing mobile phone density. J Urban Technol 17(1):61–69

Krisp JM, Špatenková O (2010) Kernel density estimations for visual analysis of emergency response data. In: Konecny M, Zlatanova S, Bandrova TL (eds) Geographic information and cartography for risk and crisis management. Springer, Berlin, pp 395–408

Kurz F, Müller R, Stephani M, Reinartz P, Schroeder M (2007) Calibration of a wide-angle digital camera system for near real-time scenarios. In: Proceedings high resolution earth imaging for geospatial information

Kwan M-P (2003) Geovisualisation of activity-travel patterns using 3D geographical information systems. In: 10th international conference on travel behaviour research (pp. pages pending), Lucerne

Langford M, Unwin DJ (1994) Generating and mapping population density surfaces within a geographical information system. Cartographic J 31:21–26

MacEachren A, Kraak M-J (2001) Research challenges in geovisualization. Cartography Geoinf Sci 28(1):3–12

Maciejewski R, Rudolph S, Hafen R, Abusalah A, Yakout M, Ouzzani M, Cleveland WS, Grannis SJ, Ebert DS (2010) A visual analytics approach to understanding spatiotemporal hotspots. IEEE Trans Visual Comput Graphics 16(2):205–220

Martin D, Bracken I (1991) Techniques for modelling population-related roster databases. Environ Plan A 23(7):1069–1075

Nakaya T, Yano K (2010) Visualising crime clusters in a space-time cube: an exploratory data-analysis approach using space-time kernel density estimation and scan statistics. Trans GIS 14(3):223–239

O'Sullivan D, Unwin DJ (2003) Geographic information analysis. Wiley, New Jersey

Pellegrini S, Ess A, Van Gool L (2010) Improving data association by joint modeling of pedestrian trajectories and grouping. In lecture notes in computer science LNCS, 6311, 452–465

Peters S, Krisp JM (2010) Density calculation for moving points. In 13th Agile international conference on geographic information science, 10–14 May 2010, Guimarães, Portugal

Ratcliffe J, McCullagh MJ (1999) Hotbeds of crime and the search for spatial accuracy. J Geogr Syst 1:385–398

Scott DW (1992) Mulivariate density estimation. Wiley, London

Silverman BW (1986) Density estimation for statistics and data analysis. Chapman and Hall, London

Thomas JJ, Cook K (2005) Illuminating the path: the research and development agenda for visual analytics. National visualization and analytics center, http://nvac.pnl.gov/agenda.stm

Tukey JW (1977) Exploratory data analysis. Addison-Wesley Publishing Co, Reading

Zhan B, Monekesso D, Remagnino P, Velastin SA, Xu L (2008) Crowd analysis: a survey. Mach Vis Appl 19(5–6):345–357

Association Between Fire Causative Agents Within Land Cover Types and Global Fire Occurrence

M. Lucrecia Pettinari and Emilio Chuvieco

Abstract The association between the global average fire density (AFD) and some possible causative agents—lightning discharges and population density—was analyzed using the Spearman correlation rank coefficient. The analysis was performed for different global fuel types, which were defined according to land cover types and climate. The results show mostly positive correlations between the AFD and lightning, with the highest coefficient values corresponding to shrubs and grasses in the Tropical Dry and Temperate Wet climates. The highest associations between the AFD and the population density were negative, and occurred in the Tropical Wet climate with crops and grasses land cover. The correlation coefficients varied widely depending on the fuel type, and not significant association was found for the Boreal climate.

1 Introduction

Biomass burning has a wide variety of effects on earth. In some regions, wildland fires are a decisive agent of land cover change (Cochrane et al. 1999), and cause severe damages to human lives and properties, particularly in the wildland urban interface (Collins 2005). In addition, fire has global atmospheric consequences, affecting the energy balance and the biogeochemical cycles (Cardille et al. 2001; van der Werf et al. 2006).

M. L. Pettinari (✉) · E. Chuvieco
Department of geography, University of Alcala, Calle Colegios 2 (28801), Alcalá de Henares, Spain
e-mail: mlucrecia.pettinari@uah.es

J. M. Krisp et al. (eds.), *Earth Observation of Global Changes (EOGC)*, Lecture Notes in Geoinformation and Cartography, DOI: 10.1007/978-3-642-32714-8_18,

Fire occurrence is a combination of fuel availability, oxygen and ignition factors. The most important ignition sources for wildland fires are human activities and lightning discharges (Krawchuk et al. 2009; Pechony and Shindell 2009). Lightning flashes as ignition sources have been analyzed by several authors, especially at a local and regional level (Minnich et al. 1993; Frost 1999; Barroso Ramos-Neto and Pivello 2000). In some places, lightning discharges have been addressed as the main source of fire ignition (Rorig and Ferguson 1999; Zhao et al. 2007). In the last years, lightning has also been included in global pyrogeography studies. Such is the case of Krawchuk et al.(2009) and Kloster et al. (2010), who included lightning discharges as a variable in their fire parameterization algorithms for global climate models.

The importance of human factors on fire occurrence has been widely recognized (FAO 2007; Chuvieco and Justice 2010). Many studies have analyzed the role of anthropogenic activities in relation to fire occurrence, considering humans both as sources of fire (Uhl and Kauffman 1990; Moreno et al. 1998; Cardille et al. 2001; Arima et al. 2007) and as fire suppressors (Pechony and Shindell 2009; Kloster et al. 2010). Different human variables have been associated to fire occurrence, such as population density, population change, distance to populated places and gross domestic product per capita (Cardille et al. 2001; Syphard et al. 2007; Chuvieco et al. 2008), amongst others. Some of these variables have also been included in the global fire algorithms mentioned in the previous paragraph.

Within fuel availability, the amount and condition of fuels are considered the primary factor (Arroyo et al. 2008; Chuvieco et al. 2009). Fuel type maps are difficult to generate, since they require information on variables that are both complex and dynamic. Satellite images have been used to map fuel types at a local or regional scale during the last decades (Burgan et al. 1998; Riaño et al. 2002; Tian et al. 2005; Lasaponara and Lanorte 2007). However, fuel maps are not yet available at a global scale, and land cover maps have been used as rough proxies for fuel characteristics. Several global land cover maps are available with different ranges of accuracy and resolution: the Global Land Cover (GLC2000) was developed by the Joint Research Centre and based on daily SPOT Vegetation images (Bartholomé and Belward 2005); the International Geosphere Biosphere Program (IGBP) Land cover map was generated from NOAA-AVHRR images (Loveland et al. 2000); the NASA land cover MOD12Q1 product was derived from the MODIS sensor (Friedl et al. 2002); and the Globcover from ESA is based on Envisat-MERIS images (Arino et al. 2007). Even though the spatial comparison of these products shows a reasonable agreement at a global level in terms of total area and general spatial pattern, further validation is needed to identify the most consistent one (McCallum et al. 2006; Herold et al. 2008).

Climatic conditions are also a critical variable that affects fuel availability, since temperature, precipitation and relative humidity impact the flammability and combustion properties of the available fuels (Cohen and Deeming 1985; Burgan et al. 1998; Bond et al. 2005; Arroyo et al. 2008). Some of the climate classifications most widely used are the Köppen Climate Classification, that combines average annual temperature and precipitation (Lohmann et al. 1993), and the Holdridge life zones Classification (Holdridge 1987), that also includes potential evapotranspiration and the concept of biotemperature.

This paper presents an analysis on how ignition agents within fuel types correlate with fire occurrence at a global scale. The ignition agents analyzed are lightning discharges and population density as a proxy for human causative variables.

2 Data and Methods

2.1 Fire Occurrence

The target variable to explain was fire occurrence. For this study, we selected the active fire database compiled by the MODIS team after 9 years of hot-spot detections. The product is based on the Collection 5 fire product (MOD14, (Giglio et al. 2003)), which was compiled at $0.5 \times 0.5^{\circ}$ cells following the Climate Modelling Grid (CMG). The data were aggregated in raster files covering monthly periods from January 2001 through December 2009.

As a basic fire metric, the average fire density (AFD) for each cell was calculated as:

$$AFD_c = \frac{\sum_{m=1}^{M} F_{m,c}}{M \times A_c} \quad (1)$$

where AFD is in counts km^{-2} $month^{-1}$, F is the number of hotspots (active fires) detected for month m and grid cell c, M the total number of months considered (108) and A the corrected area of the cell. The corrected cell area was calculated multiplying the cell area by its percentage of land (using a land-mask obtained from the Global Land Cover 2000 product). All the cells with less than 10 % of land proportion were discarded. To avoid working with very small fraction numbers, the AFD was multiplied by 100,000 to render integer numbers in the range between 1 and 3028 (meaning a fire density between 0.00001 and 0.03028 counts km^{-2} $month^{-1}$). Values below that 0.00001 threshold were discarded from further analysis. A total of 62449 cells were finally processed (not considering Antarctica), and of them 35698 cells showed fire occurrence (see Fig. 1).

2.2 Fuel Types

The impact of each causative agent was analyzed by stratifying the fire cells by fuel types. Since there is not a global fuel type map available, we generated rough approximations to fuel types by combining global land cover data and climatic regions.

We selected the GLC2000 product for land cover since it was based on the LCCS (Land Cover Classification System, (Di Gregorio and Jansen 1998)) legend proposed by FAO (Food and Agriculture Organization), and it has shown good results in the validation exercises performed.

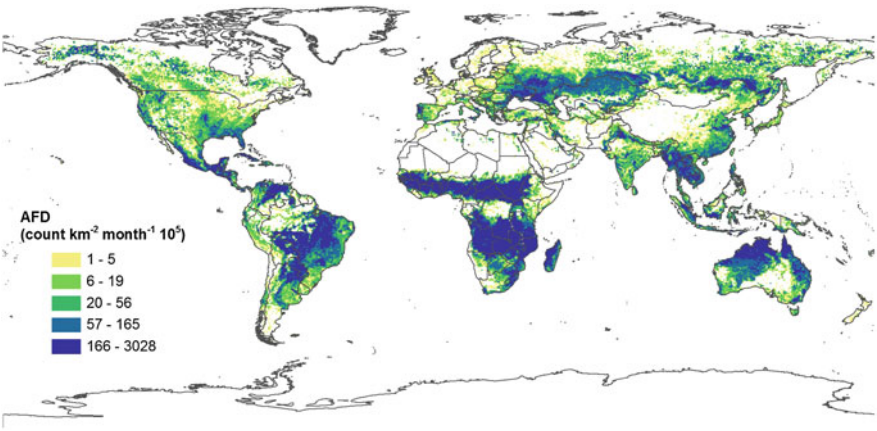

Fig. 1 Average fire density. AFD is multiplied by 10^5

Table 1 Reclassification of GLC2000 land cover types

Grouped cover types	GLC2000 land cover types
A. Trees	1. Tree cover, broadleaved, evergreen; 2. Tree cover, broadleaved, deciduous, closed; 3. Tree cover, broadleaved, deciduous, open; 4. Tree cover, needle-leaved, evergreen; 5. Tree cover, needle-leaved, deciduous; 6. Tree cover, mixed leaf type; 7. Tree cover, regularly flooded, fresh and brackish water; 8. Tree cover, regularly flooded, saline water
B. Mosaic trees	9. Mosaic: tree cover/other natural vegetation (a)
C. Shrub	11. Shrub cover, closed–open, evergreen; 12. Shrub cover, closed–open, deciduous
D. Grass	13. Herbaceous cover, closed–open
E. Mosaic Shrub-grass	14. Sparse herbaceous or sparse shrub cover; 15. Regularly flooded shrub and/or herbaceous cover
F. Crops	16. Cultivated and managed areas
G. Mosaic crops	17. Mosaic: cropland/tree cover/other natural vegetation b; 18. Mosaic: cropland/shrub or grass cover (b)
H. Bare areas	19. Bare areas; 21. Snow and ice; 22. Artificial surfaces and associated areas; 10. Tree cover, burnt

Notes extracted from Bartholomé and Belward (2005): (a) Tree cover dominant (e.g., fragmented forest cover) with or without cropping component; (b). Cropland dominant in both classes of the mosaic. Other natural vegetation may include regrowth (e.g., on abandoned cropland), shrub cover or grass cover.

The GLC2000 has a spatial resolution of 1 km^2. Land cover types had to be generalized to 0.5x0.5° cells. For doing so, the cover types were first grouped in more general categories, as shown in Table 1. Next, each group was converted to a binary scale and the mean proportion computed for each of the 0.5° cells. That value was then divided by the total land proportion of the cell to eliminate the proportion of water present (that would affect the cell land cover assignment, especially in coastal zones).

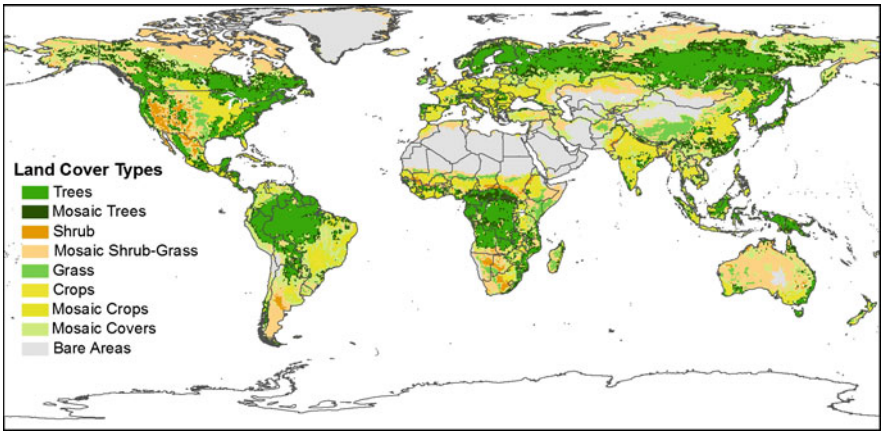

Fig. 2 0.5° generalized land cover

Then, the land cover types were assigned to the 0.5° cells as follows (see Fig. 2):

1. Trees: ≥75 % of Trees (A)
2. Mosaic Trees: 50–75 % of Trees (A) or ≥50 % of Mosaic Trees (B)
3. Shrub: ≥75 % of Shrub (C)
4. Mosaic Shrub-Grass: 50–75 % of Shrub (C), or 50–75 % of Grass (D), or ≥50 % of Mosaic Shrub-Grass (E)
5. Grass: ≥75 % of Grass (D)
6. Crops: ≥75 % of Crop (F)
7. Mosaic Crops: 50–75 % of Crops (F) or ≥50 % of Mosaic Crops (G)
8. Mosaic Cover: cells with no predominant cover, but where the different vegetation cover types represent ≥50 % of the total land area (Bare Areas (H) <50 %).
9. Bare Areas: >50 % of Bare Areas (H).

The Holdridge life zones (HLZ) system was used to account for climatic conditions. Life zones indicate groups of vegetation associations within a climatic division. The zones are classified according to the mean annual biotemperature (based on the growing season length and temperature), mean annual precipitation and potential evapotranspiration ratio. The 0.5 × 0.5° dataset used in this study was generated by the International Institute for Applied Systems Analyses (IIASA) and downloaded from the FAO database (http://www.fao.org/geonetwork/srv/en/metadata.show?currTab = simple&id = 1006, last accessed September 2011). The original 38 life-zone classes were reclassified into five climatic regions, as shown in Table 2 and Fig. 3.

Finally, a cross tabulation was performed between the land cover types and the climatic regions to define the fuel types, as shown in Table 3 and Fig. 4.

Table 2 Reclassification of Holdridge life zones

Climatic regions	Original Holdridge life zones
Boreal	Polar Desert, Polar Dry Tundra, Polar Moist Tundra, Polar Wet Tundra, Polar Rain Tundra, Boreal Desert, Boreal Dry Bush, Boreal Moist Forest, Boreal Wet Forest, Boreal Rain Forest
Temperate dry	Cool temperate Desert, Cool Temperate Desert Bush, Cool Temperate Steppe, Warm Temperate Desert, Warm Temperate Desert Bush, Warm Temperate Thorn Steppe, Warm Temperate Dry Forest
Temperate Wet	Cool Temperate Moist Forest, Cool Temperate Wet Forest, Cool Temperate Rain Forest, Warm Temperate Moist Forest, Warm Temperate Wet Forest, Warm Temperate Rain Forest
Tropical Dry	Subtropical Desert, Subtropical Desert Bush, Subtropical Thorn Steppe, Subtropical Dry Forest, Tropical Desert, Tropical Desert Bush, Tropical Thorn Steppe, Tropical Very Dry Forest, Tropical Dry Forest
Tropical Wet	Subtropical Moist Forest, Subtropical Wet Forest, Subtropical Rain Forest, Tropical Moist Forest, Tropical Wet Forest, Tropical Rain Forest

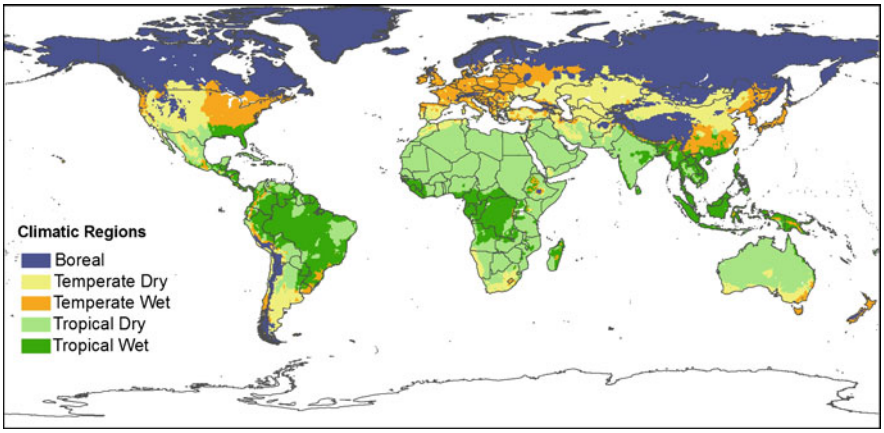

Fig. 3 Climatic regions

2.3 Lightning

The first causative agent analyzed was lightning density. Up-to-date, the only available record of global lightning flash rate is the data collected by the Optical Transient Detector (OTD) (Christian et al. 1996) and the Lightning Imaging Sensor (LIS) (Kummerow et al. 1998) satellite-based sensors. The product used it the LISOTD_HRFC_V2.2 (http://thunder.nsstc.nasa.gov/data, last accessed September 2011), which is a 0.5x0.5° gridded composite of total lightning bulk production from both sensors, expressed as a flash rate density ((flashes km^{-2}/yr^{-1}).

This product supplies the total flash rate, both intracloud (IC) and cloud-to-ground (CG) flashes, but only the CG flashes can be sources of ignition. In order to

Table 3 Cross tabulation to obtain Fuel Types

Land cover	Climatic Regions				
	Boreal	Temperate Dry	Temperate Wet	Tropical Dry	Tropical Wet
Trees	Bo-Tr	TeD-Tr	TeW-Tr	TrD-Tr	TrW-Tr
Mosaic Trees	Bo-MT	TeD-MT	TeW-MT	TrD-MT	TrW-MT
Shrub	Bo-Sh	TeD-Sh	TeW-Sh	TrD-Sh	TrW-Sh
Mosaic Shrub-Grass	Bo-SG	TeD-SG	TeW-SG	TrD-SG	TrW-SG
Grass	Bo-Gr	TeD-Gr	TeW-Gr	TrD-Gr	TrW-Gr
Crops	Bo-Cr	TeD-Cr	TeW-Cr	TrD-Cr	TrW-Cr
Mosaic Crops	Bo-MC	TeD-MC	TeW-MC	TrD-MC	TrW-MC
Mosaic Covers	Bo-MM	TeD -MM	TeW-MM	TrD-MM	TrW-MM
Bare Areas	Bo-BA	TeD-BA	TeW-BA	TrD-BA	TrW-BA

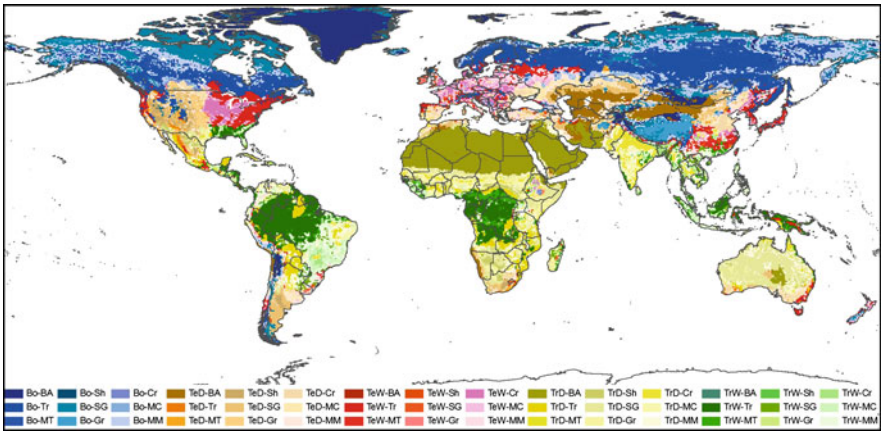

Fig. 4 Global fuel types

account only for these, we computed the relation between IC to CG flashes according to Prentice and Mackerras (1977):

$$z = 4.16 + 2.16\cos(3\lambda) \tag{2}$$

where z is the ratio of IC to CG flashes and λ is the latitude. This formula is designed for latitudes from 0° to 60°, and according to its design, it assumes that $dz/d\lambda = 0$ at $\lambda = 60°$. For this reason, all latitudes higher than 60° were assigned the z value of $\lambda = 60°$.

The resulting lightning density map is shown in Fig. 5.

2.4 Population Density

The second causative agent analyzed was the population density. The database used was the Gridded Population of the World, Version 3 (GPWv3) from the CIESIN

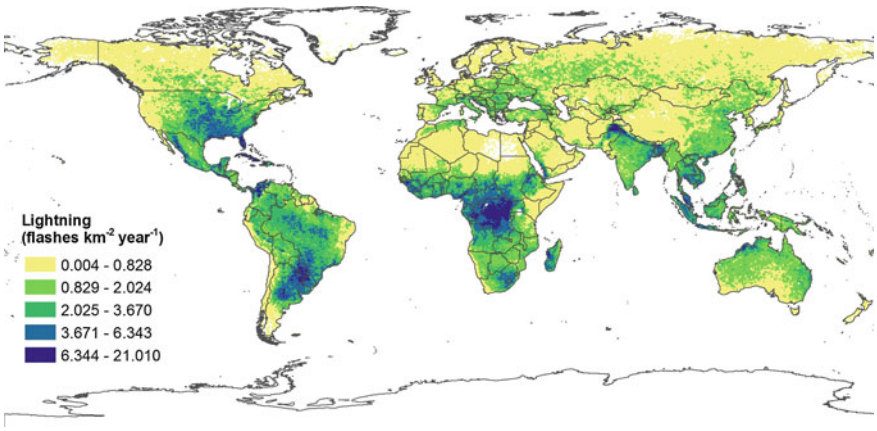

Fig. 5 Lightning density

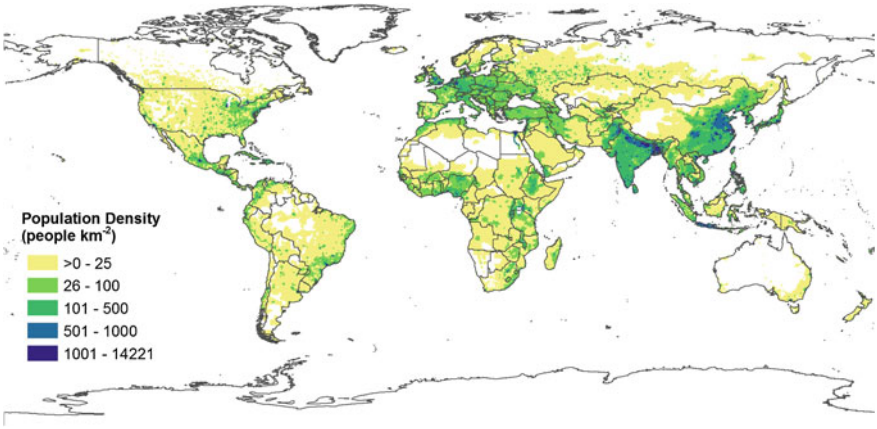

Fig. 6 Population density

(Center for International Earth Science Information, http://geodata.grid.unep.ch/, last accessed September 2011). We selected the estimations of the human population for the year 2000 in 2.5 arc-minute grid cells, with the population counts adjusted to match United Nation's totals.

The population density information was converted from the 2.5′ grid to 0.5° grid computing the mean value, and that value was corrected with the total land proportion, as it had been done in 2.2. The final map is shown in Fig. 6.

2.5 Statistical Analysis

The association between the two causative agents and the AFD was measured using the non-parametric Spearman's rank correlation coefficient (Rs):

$$R_s = \frac{T_x + T_y - \sum_1^N d_i^2}{2\sqrt{T_x T_y}} \tag{3}$$

where d is the rank difference between the two variables for case i, N the sample size, Tx and Ty are

$$T_x = \frac{N^3 - N - ST_x}{12} \tag{4}$$

$$T_y = \frac{N^3 - N - ST_y}{12} \tag{5}$$

and STx and STy are the sum of ranks for both variables. When Tx or Ty is 0 the statistic is not computed. The significance level was computed from the Student t distribution with N-2 degrees of freedom, following:

$$t = R_s \sqrt{\frac{N-2}{1-R_s^2}} \tag{6}$$

The Spearman's coefficient was computed separately for each of the Global Fuel Types in order to analyze the association between the causative agents, the fuels, and fire occurrence.

3 Results and Discussion

The results of the Spearman's rank correlation coefficient are shown in Table 4. Only the results that are significant to a 0.01 level are shown.

The lightning flashes show in general positive correlations with fire occurrence for the different fuel types. The strongest correlations belong to the TeW-BA fuel type (Rs = 0.749). This fuel type corresponds to bare areas or areas with less than 50 % vegetation cover, but no conclusions can be obtained due to the small amount of pixels of this fuel type and their spatial dispersion in North America and Asia.

The shrubs in tropical dry climate (TrD-Sh) have a Spearman's coefficient of 0.719, showing a strong association between lightning flashes and fire occurrence. The shrub-grass mosaic in that climate (TrD-SG) also shows high Rs values (= 0.566). These fuel types are widely present in Australia, in the Western and Eastern African savannas, in Southern Africa and in Northern Mexico and Southern USA. Previous studies have analyzed the association between lightning

Table 4 Spearman's coefficient (Rs) for each fuel type

Fuel type	Cell count	Lightning Rs	Population Rs	Fuel type	Cell count	Lightning Rs	Population Rs
Bo-Tr	5696	0.115	−0.071	TrD-Tr	987	0.399	0.296
Bo-MT	3603	0.227	0.100	TrD-MT	800	0.445	−0.185
Bo-Sh	92	0.289	0.287	TrD-Sh	485	0.719	0.128
Bo-SG	5960	0.363	0.327	TrD-SG	3187	0.566	−0.058
Bo-Gr	568	0.162	0.355	TrD-Gr	584	0.350	–
Bo-Cr	58	–	–	TrD-Cr	779	0.139	−0.158
Bo-MC	212	−0.163	0.087	TrD-MC	1305	0.334	−0.429
Bo-MM	4878	0.497	0.324	TrD-MM	1836	0.417	−0.119
Bo-BA	4439	0.286	0.205	TrD-BA	4949	0.094	0.271
TeD-Tr	179	–	–	TrW -Tr	3313	0.086	0.390
TeD-MT	275	–	–	TrW-MT	1308	0.312	−0.331
TeD-Sh	372	0.158	–	TrW-Sh	29	–	−0.522
TeD-SG	2073	–	0.162	TrW-SG	347	–	−0.308
TeD-Gr	278	0.534	0.217	TrW-Gr	63	–	−0.547
TeD-Cr	796	0.228	0.235	TrW -Cr	285	–	−0.615
TeD-MC	971	–	–	TrW-MC	1047	–	−0.260
TeD-MM	1547	−0.106	–	TrW-MM	1493	0.131	−0.462
TeD-BA	1837	0.190	–	TrW-BA	2	–	–
TeW-Tr	1433	0.196	0.140				
TeW-MT	1099	0.236	–				
TeW-Sh	26	0.686	–				
TeW-SG	286	0.543	–				
TeW -Gr	53	0.465	−0.448				
TeW-Cr	802	0.164	–				
TeW-MC	925	0.252	−0.202				
TeW-MM	1168	0.185	−0.150				
TeW-BA	24	0.749	0.417				

and fires in these areas. Lightning from summer thunderstorms have been identified as a frequent source of natural ignition in the chaparral regions of Baja California (Minnich et al. 1993), Manry and Knight (1986) have studied the relationship between lightning frequency and vegetation distribution in different biomes in South Africa, and proposed that the geographic expansion of certain plant communities could be restricted by their fire-sensitivity and lightning density. Lightning strikes have been stated as the main cause of fires at the Etosha National Park, in Namibia (Frost 1999).

The shrubs and shrub-grass mosaics in temperate wet climate also show a high correlation between lightning strikes and fire occurrence, with TeW-Sh's Rs = 0.686 and TeW-SG's Rs = 0.543. These fuel types are mainly located in the United Kingdom, central China, Turkey, France, southern Argentina and Uruguay. Although there is some evidence on the importance of lightning as a causative agent in Patagonia, Argentina (Veblen et al. 1999), fire density in most of those regions is relatively low, and their causes have not been thoroughly studied.

On the other hand, there is evidence of lightning as a main cause of forest fires in Northeast China (Zhao et al. 2007) and Canada (Stocks et al. 2003), but the correlation coefficients found were low. One probable reason for these results is the fact that these areas belong to the Boreal climatic region (fuel types Bo-Tr and Bo-MT), and the quality of the lightning database for the high latitudes is poor compared to the Tropical regions. Also, these fuel types comprise a wide geographical region mostly in the northern hemisphere, and other biophysical or human variables could have a relevant influence in these particular areas, such as topography, amount of precipitation, or fuel management policies.

A similar situation was found in the Pacific Northwest of the United States, where lightning flashes are the main cause of wildland fires (Rorig and Ferguson 1999), although the correlation coefficients for these fuel types are low (TeW-Tr's $Rs = 0.196$ and TeW-MT's $Rs = 0.236$) and show no clear association between the variables. Further research should be performed to analyze these findings; the use of monthly data to account for the relation between fire season and lightning season should be explored in the future.

In general, and as human activities have increased, the importance of lightning as a causative agent has decreased, and fire occurrence has departed from the natural fire regimes (Venevsky et al. 2002; Syphard et al. 2007). Nowadays, in most of the world human causes are the main sources of fire occurrence (Moreno et al. 1998; Frost 1999; Cardille et al. 2001). But humans influence fire patterns not only by adding ignition sources, but also by suppressing both anthropogenic and natural fires. Both effects increase with increasing population, to some extent cancelling each other (Pechony and Shindell 2009).

The results of the Spearman's coefficients between population density and fire occurrence show the highest associations in the tropical wet climate, and with a negative sign. The coefficients are -0.615 for the crops, -0.547 for the grass and -0.522 for the shrub fuel types. The TrW-Cr pixels are mostly located in Southern Brazil, Bangladesh, India and Thailand. The TrW-Sh belongs mainly to Eastern India and Guinea, while the TrW-Gr pixels are concentrated in Colombia, Madagascar and Uruguay.

Significant associations were also found in the TrW-MM fuel type ($Rs = -0.462$), with its pixels situated mainly in eastern South America (Brazil, Paraguay, Argentina's Litoral and Uruguay), Southeast Asia (Indonesia, Philippines, Malaysia, Thailand, Myanmar, Vietnam), Eastern India, Colombia, and the South-eastern US. Other moderate associations were found in TeW-Gr ($Rs = -0.448$) situated mostly in Ireland, Wales and France; and TrD-MC ($Rs = -0.429$), located mainly in India, Sub-Saharan Africa, Eastern Brazil, Colombia and Mexico.

All these Spearman coefficients are negative, showing an inverse correlation between fire occurrence and population density. This inverse correlation has been previously proposed by Venevsky et al. (2002), Pechony and Shindell (2009) and Kloster et al. (2010), amongst others. Venevsky et al. state that an average person is more likely to cause a fire in sparsely populated regions as they interact more with the natural ecosystems compared to persons living in densely populated areas. Furthermore, Kloster et al. suggest that fire suppression will more likely take place in densely populated areas compared to sparsely populated ones.

Archibald et al. (2010) found similar results for Southern Africa, with number of fires increasing as population density increases up to $\sim$25 people/km^2 and then declining, while the size of fires decreases steadily with increasing population density. These data also agree with other studies (Pechony and Shindell 2009), that proposed an increase in the number of potential anthropogenic ignition sources until a certain limit (in this case $\sim$10 people/km^2), at which point fire suppression activities decrease fire occurrence. These authors assume that in highly populated areas fires are detected earlier and suppressed more effectively than in scarcely populated areas, and the fraction of suppressed fires increases with increasing population density.

Land use also has an important role in fire occurrence. There is evidence that a small percentage of crops burn frequently in Southern Africa (Archibald et al. 2010), and that agriculture significantly reduces fire density in prairies and savannas in Southern America (Di Bella et al. 2006). These findings agree with the results obtained in this study, with the TrW-Cr coefficient of -0.615.

But on the other hand, Di Bella et al. also found the opposite behaviour in rain forests, where agriculture increases fire density, since fire is a cheap and effective tool for land clearing, nutrient recycling and plant disease or weed control. Other authors have also studied the association between human activities and fire occurrence in tropical forests, finding positive correlation between these variables (Uhl and Kauffman 1990; J. B. Kauffman and Cummings 1995; J. Boone Kauffman et al. 1998; Arima et al. 2007). We found that, although the Spearman's coefficient is not high (Rs $= 0.390$ for TrW-Tr), this fuel type is the only one for that climatic region that has a positive correlation with population density, which agrees with those previous results.

4 Conclusions

The analysis of the association between the global average fire density and its causative agents show diverse results depending on the fuel types present. In the case of lightning, the associations are positive, and a few fuel types show strong associations between the variables. Regarding the population density, its strongest associations are negatively correlated to the AFD, and were found mainly in the tropical regions. Nevertheless, many of the proposed fuel types, especially in the coldest climates, do not show clear association between the causative agents and fire density.

Although the findings in this work agree with previous studies, further research is needed to better understand the causative agents influencing fire ignition, with the goal of explaining global fire occurrence. Other variables should be considered, such as seasonality of fires and lightning strikes in the case of natural causes of fire. Future work will focus on these variables, and it will also take into account other anthropogenic factors, such as land use patterns, agricultural practices and fire management.

Acknowledgments This research has been funded by the Fireglobe project (CGL2008-01083/CLI) and the University of Alcala by means of the FPI grant program which supports M. Lucrecia Pettinari.

References

Archibald S, Scholes RJ, Roy DP, Roberts G, Boschetti L (2010) Southern African fire regimes as revealed by remote sensing. Int J Wildland Fire 19:861–878

Arima EY, Simmons CS, Walker RT, Cochrane MA (2007) Fire in the Brazilian Amazon: a spatially explicit model for policy impact analysis. J Reg Sci 47(3):541–567

Arino O, Gross D, Ranera F, Bourg L, Leroy M, Bicheron P, et al., (2007) GlobCover: ESA service for global land cover from MERIS. In: IEEE international geoscience and remote sensing symposium, Barcelona, Spain, pp 2412–2415 doi:10.1109/IGARSS.2007.4423328 (IEEE- Inst Electrical Electronics Engineer Inc.)

Arroyo LA, Pascual C, Manzanera JA (2008) Fire models and methods to map fuel types: the role of remote sensing. For Ecol Manage 256(6):1239–1252. doi:10.1016/j.foreco.2008.06.048

Barroso Ramos-Neto M, Pivello VR (2000) Lightning fires in a brazilian savanna National Park: rethinking management strategies. Environ Manage 26(6):675–684. doi:10.1007/s002670010124

Bartholomé E, Belward AS (2005) GLC2000: a new approach to global land cover mapping from Earth observation data. Int J Remote Sens 26(9):1959–1977. doi:10.1080/01431160412331291297

Bond WJ, Woodward FI, Midgley GF (2005) The global distribution of ecosystems in a world without fire. New Phytol 165:525–538. doi:10.1111/j.1469-8137.2004.01252.x

Burgan RE, Klaver RW, Klaver JM (1998) Fuel models and fire potential from satellite and surface observations. [Article]. Int J Wildland Fire 8(3):159–170

Cardille JA, Ventura SJ, Turner MG (2001) Environmental and social factors influencing wildfires in the upper midwest. U S Ecol Appl 11(1):111–127

Christian HJ, Driscoll K, Goodman S, Blakeslee R, Mach D, D., B. The optical transient detector (OTD). In: Proceedings of the 10th international conference on atmospheric electricity, Osaka, Japan, June 10-14 1996: 368–371

Chuvieco E, Giglio L, Justice C (2008) Global characterization of fire activity: toward defining fire regimes from Earth observation data. Glob Change Biol 14:1488–1502. doi:10.1111/j.1365-2486.2008.01585.x

Chuvieco E, Justice C (2010) Relations between human factors and global fire activity. In: Chuvieco E, Li J, Yang X (eds) Advances in Earth observation of global change. Springer, London, pp 187–199

Chuvieco E, Wagtendonk J, Riaño D, Yebra M, Ustin SL (2009) Estimation of fuel conditions for fire danger assessment. In: Chuvieco E (ed) Earth observation of wildland fires in Mediterranean ecosystems. Springer, Berlin, pp 83–96

Cochrane MA, Alencar A, Schulze MD, Souza CM Jr, Nepstad DC, Lefebvre P (1999) Positive feedbacks in the fire dynamic of closed canopy tropical forests. Science 284:1832–1835

Cohen JD, Deeming JE (1985) The national fire-danger rating system: basic equations. 23 Berkeley, CA: USDA Forest Service, Pacific Southwest Forest and Range Experiment Station

Collins TW (2005) Households, forests, and fire hazard vulnerability in the American west: a case study of a California community. Environ Hazards 6:23–37

Di Bella CM, Jobbágy EG, Paruelo JM, Pinnock S (2006) Continental fire density patterns in South America. Glob Ecol Biogeogr 15:192–199

Di Gregorio A, Jansen LJM (1998). Land cover classification system (LCCS): classification concepts and user manual. In: FAO (ed), Environment and Natural Resources Service, Rome, pp 157

FAO (2007) Fire management—global assessment 2006. FAO, Communication Division, Rome

Friedl MA, McIver DK, Hodges JCF, Zhang XY, Muchoney D, Strahler AH (2002) Global land cover mapping from MODIS: algorithms and early results. Remote Sens Environ 83:287–302

Frost PGH (1999) Fires in Southern African woodlands: origins, impacts, effects and control. In: FAO meeting on public policies affecting forest fires, Vol Forestry Paper 138., Rome, Italy, FAO, pp 181–205

Giglio L, Descloitres J, Justice CO, Kaufman YJ (2003) An enhanced contextual fire detection algorithm for MODIS. Remote Sens Environ 87:273–282. doi:10.1016/S0034-4257(03)00184-6

Herold M, Mayaux P, Woodcock CE, Baccini A, Schmullius C (2008) Some challenges in global land cover mapping: an assessment of agreement and accuracy in existing 1 km datasets. Remote Sens Environ 112(5):2538–2556. doi:10.1016/j.rse.2007.11.013

Holdridge LR (1987) *Ecología basada en zonas de vida* Vol. 83, Colección libros y materiales educativos. San José, Costa Rica, IICA

Kauffman JB, Cummings DL (1995) Fire in the Brazilian Amazon: 1. Biomass, nutrient pools, and looses in slashed primary forests. Oecologia 104:397–408

Kauffman JB, Cummings DL, Ward DE (1998) Fire in the Brazilian Amazon. 2. Biomass, nutrient pools and looses in cattle pastures. Oecologia 113(3):415–427

Kloster S, Mahowald NM, Randerson JT, Thornton PE, Hoffman FM, Levis S (2010) Fire dynamics during the 20th century simulated by the Community Land Model. Biogeosciences 7:1877–1902. doi:10.5194/bg-7-1877-2010

Krawchuk MA, Moritz MA, Parisien MA, Van Dorn J, Hayhoe K (2009) Global pyrogeography: the current and future distribution of wildfire. Plos One 4(4):e5102. doi:10.1371/journal.pone.0005102

Kummerow C, Barnes W, Kozu T, Shiue J, Simpson J (1998) The tropical rainfall measuring mission (TRMM) sensor package. J Atmos Oceanic Technol 15:809–817

Lasaponara R, Lanorte A (2007) Remotely sensed characterization of forest fuel types by using satellite ASTER data. Int J Appl Earth Obs Geoinf 9(3):225–234. doi:10.1016/j.jag.2006.08.001

Lohmann U, Sausen R, Bengtsson L, Cubasch U, Perlwitz J, Roeckner E (1993) The Köppen climate classification as a diagnostic tool for general circulation models. Climate Res 3:177–193

Loveland TR, Reed BC, Brown JF, Ohlen DO, Zhu Z, Yang L (2000) Development of a global land cover characteristics database and IGBP DISCover from 1 km AVHRR data. Int J Remote Sens 21(6 & 7):1303–1330

Manry DE, Knight RS (1986) Lightning density and burning frequency in South African vegetation. Vegetatio 66:67–76

McCallum I, Obersteiner M, Nilsson S, Shvidenko A (2006) A spatial comparison of four satellite derived 1 km global land cover datasets. Int J Appl Earth Obs Geoinf 8(4):246–255. doi:10.1016/j.jag.2005.12.002

Minnich RA, Vizcaino EF, Sosa-Ramirez J, Chou YH (1993) Lightning detection rates and wildland fire in the mountains of northern Baja California, Mexico. *Atmosfera 6*:235–253

Moreno JM, Vazquez A, Velez R (1998) Recent history of forest fires in Spain. In: Moreno JM (ed) Large forest fires. Backhuys Publishers, Leiden, pp 159–185

Pechony O, Shindell DT (2009) Fire parametrization on a global scale. J Geophys Res 114:D16115. doi:10.1029/2009JD011927

Prentice SA, Mackerras D (1977) The ratio of cloud to cloud-ground lightning flashes in thunderstorms. J Appl Meteorol 16:545–550

Riaño D, Chuvieco E, Salas J, Palacios-Orueta A, Bastarrika A (2002) Generation of fuel type maps from Landsat TM images and ancillary data in Mediterranean ecosystems. Can J For Res 32(8):15

Rorig ML, Ferguson SA (1999) Characteristics of lightning and wildland fire ignition in the Pacific Northwest. J Appl Meteorol 38:1565–1575

Stocks BJ, Mason JA, Todd JB, Bosch EM, Wotton BM, Amiro BD (2003) Large forest fires in Canada, 1959–1997. J Geophys Res 107:8149. doi:10.1029/2001JD000484

Syphard AD, Radeloff VC, Keeley JE, Hawbaker TJ, Clayton MK, Stewart SI et al (2007) Human influence on California fire regimes. Ecol Appl 17(5):1388–1402

Tian XR, McRae DJ, Shu LF, Wang MY (2005) Fuel classification and mapping from satellite imagines. J For Res 16(4):311–316

Uhl C, Kauffman JB (1990) Deforestation, fire susceptibility, and potential tree responses to fire in the eastern Amazon. Ecology 71(2):437–449

van der Werf GR, Randerson JT, Giglio L, Collatz GJ, Kasibhatla PS, Arellano AF Jr (2006) Interannual variability in global biomass burning emissions from 1997 to 2004. Atmos Chem Phys 6:3423–3441

Veblen TT, Kitzberger T, Villalba R, Donnegan J (1999) Fire history in northern Patagonia: the roles of humans and climatic variation. Ecol Monogr 69(1):47–67

Venevsky S, Thonicke K, Sitch S, Cramer W (2002) Simulating fire regimes in human-dominated ecosystems: Iberian Peninsula case study. Glob Change Biol 8:984–998

Zhao J, Sun L, Zhang, T, Zhang D, Guo G, Zhang Z, et al., (2007) Spatial and temporal distributions of lightning activities in Northeast China from satellite observation and analysis for lightning fire. In: Proceedings of the SPIE San Diego, Vol. 6679, USA, doi:10.1117/12.729349, pp 66790M

From Structural Health Monitoring to Geo-Hazard Early Warning: An Integrated Approach Using GNSS Positioning Technology

Xiaolin Meng

Abstract This paper summarises recent achievements in Global Navigation Satellite Systems (GNSS) based bridge structural health monitoring (SHM) research and development with a focus on our own contribution. During the last decade, the author of this paper has led the deformation monitoring studies of a few major suspension bridges in the UK and China and acquired a large amount of monitoring data sets. Since these slender bridges are very sensitive to small quakes and normally well equipped with a variety of monitoring sensors, such as accelerometers, weather stations, and rover GNSS stations, they can be treated as useful sensor nodes for the detection of earthquakes or other developing environmental phenomena. If used together with the continuously operating GNSS reference stations (CORSs) that cover wide regions they could play a significant role for the integrated monitoring and analysis of bridge deformation and geo-hazardous phenomena, such as earthquakes, tsunamis, flooding, high winds, etc. In this paper, the author introduces the fundamentals and concepts of integrated monitoring and processing for the formation of a regional geo-hazard early warning system using GNSS positioning technology. The architecture of such a system is presented with the findings drawn from analysing real-life data sets.

1 Introduction

Structural Health Monitoring (SHM) is an effective approach that is employed for the real-time assessment of the operational conditions of structures, origninating from aerospace and mechanics engineering (Meng 2002). It has been gradually

X. Meng (✉)
Department of Civil Engineering, The University of Nottingham, Nottingham, UK
e-mail: Xiaolin.Meng@nottingham.ac.uk

J. M. Krisp et al. (eds.), *Earth Observation of Global Changes (EOGC)*,
Lecture Notes in Geoinformation and Cartography, DOI: 10.1007/978-3-642-32714-8_19,

adopted for civil engineering applications, especially for the global monitoring of long bridges and high rise buildings in the past decade. In recent years due to the new inventions in construction materials and techniques, the high demands of road transport serviceability, and the breakthrough in bridge design theories, new bridges are built longer and longer and some of them have a bridge span of a few kilometres. Some of these long bridges are built in the earthquake prone areas, and need to operate under freak weather conditions. For example, the world record holding suspension bridge, Japanese Akashi Kaikyo Bridge was built in a location that is around 150 km away from an epicentre with potential earthquakes of Richter Scale 8.0 and has to face wind loading at a speed of up to 288 km/h (Kashima et al. 2001). This has posed a great challenge to the bridge authorities in maintaining safe and sound operation of these bridges. Sensor networks, whether they are wired or wireless, have been buried into the bridges during the construction phases or installed afterwards. These sensors have been playing an essential role in monitoring the health conditions but are limited to the detection of certain metrics (such as strain, cracking, acceleration etc) and to the constricted areas. Bridge engineers are looking for more universal and practical solutions to tackle the bridge management and maintenance problems.

In the past decade with the advancements of the Global Navigation Satellite Systems (GNSS), particularly the Global Positioning System (GPS), a few case studies have been implemented to investigate the feasibility of GNSS for bridge monitoring (Ashkenazi and Roberts 1997). It has been proven that GNSS could be a very capable alternative for globally monitoring static and dynamic movements of long bridges (Meng et al. 2007a, 2007b). However, GNSS-based SHM of bridges has some inherent drawbacks, such as the low system robustness, high initial implementation cost, inadequate accuracy, slow sampling rate, etc. The University of Nottingham in the UK initiated a GNSS based long bridge monitoring study from the early 1990s and the researchers at the Nottingham Geospatial Institute (former Institute of Engineering Surveying and Space Geodesy) of the University of Nottingham had carried out systematic studies to address these issues (Roberts et al. 2006; Meng and Huang 2009). For attaining high positioning performance, integrated sensor systems and advanced processing algorithms have been developed to improve real-time positionin accuracy, increase the measurement sampling rates and effectively mitigate the multipath signature. The developed prototype monitoring system is able to detect both the high structural dynamics and identify the subtle deformations that are normally buried by a high level of noise (Meng 2002). It demonstrated that under controlled testing environments a millimetre level of 3D positioning accuracy is possible (Meng et al. 2004, 2007a). For reducing the initial system implementation investment, low-cost GPS positioning platforms have also been tested and it proved that through using precise network-based real-time kinematic (NRTK) GNSS corrections it is highly possible to achieve continuous positioning accuracy of better than 1 centimetre (Meng et al. 2010). This has opened the door for the large scale adoption of GNSS for SHM of bridges at an affordable price in the near future.

This paper summarises recent achievements in GNSS based bridge SHM research and development with a focus on our own work. During the past decade, the author of this paper has led the monitoring work of a few major suspension bridges in the UK and China and accumulated a large amount of essential data sets and rich experience. Since long bridges and high rise buildings are susceptible to small trembling, structures equipped with multiple rover GNSS stations can be treated as useful sensor nodes within a regional geo-hazard monitoring system. If used together with those continuously operating GNSS reference stations (CORSs) they can form an effective approach for the integrated monitoring of bridge deformation and geo-hazardous phenomenon, such as earthquakes, tsunamis, flooding, high winds, etc. In this paper the author introduces the fundamentals and concepts of integrated monitoring and processing for the formation of a regional geo-hazard early warning system. The architecture of such a system is presented with the findings drawn from analysing real-life monitoring data sets.

2 GNSS for Monitoring Slender Structures

2.1 A Brief Introduction to the Previous Work

The research in using GPS for bridge deformation monitoring started in the middle of 1990s at the University of Nottingham (Ashkenazi et al. 1997) and the University of Nottingham was one of a very few institutions around the world that explored this new application field (Meng 2002). In the past decade, the Humber Bridge (Ashkenazi and Roberts 1997), the Forth Road Bridge (Meng et al. 2007a) and the London Millennium Bridge (Roberts et al. 2006a, b) were used for feasibility studies, testing equipment and algorithms and gathering critical deformation parameters. In addition to these trials, a small suspension footbridge over the River Trent in Nottingham was also used extensively as a testbed due to its access convenience (less than 4 km from the University's main campus) and unique deformation characteristics of up to a few centimeters even under normal pedestrian loading. However, these tests were all carried out in an episodic campaign manner and normally only lasted a maximum three days. Furthermore, in these tests only a few GPS and/or accelerometers were installed at limited locations where accessible. Data were processed in a postprocessing manner. Figure 1 shows a typical set up of a rover station (left) on the Forth Road Bridge and their reference stations (right) in a close vicinity.

Past research concludes: current GPS positioning can be used to monitor real-time deformations of large amplitudes at a 3D positioning accuracy of a few centimetres with high grade geodetic receivers; the sampling rate from current commercial off-the-shelf (COTS) receivers is fast enough for the identification of structural vibration frequencies; GPS can be effectively utilised to monitor the deformations caused by live traffic loading and changes of temperature; it is an

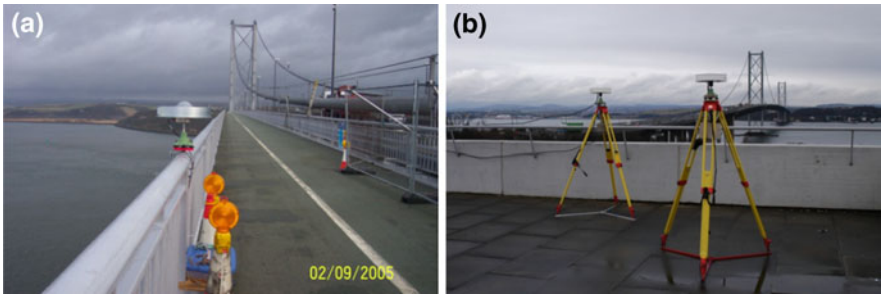

Fig. 1 A typical GPS receiver set up for **a** rover (*left*) and **b** reference stations (*right*)

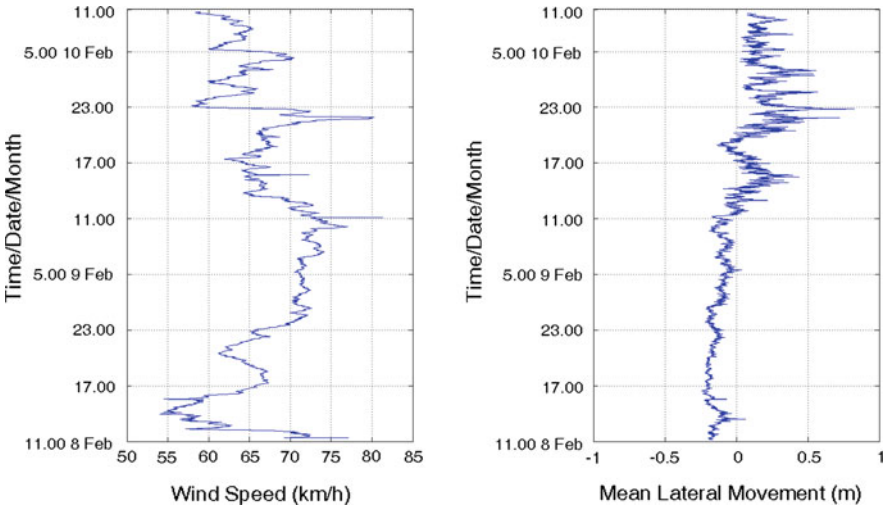

Fig. 2 Relationship between wind loading and a bridge's lateral response over 48 h

ideal tool for measuring a bridge's response to wind loading as shown Fig. 2. The final capacity is of civil engineers' great interest in understanding the relationship between wind loading and bridge response. From Fig. 2 it is evident that there exists a high correlation between wind loading speed/force and lateral bridge movements.

It is also apparent that from previous studies GPS positioning is not an accurate and cost-effective approach for the monitoring of the deformation at an accuracy of a few millimetres and this level of positioning accuracy is required by SHM of medium to small bridges. Furthermore, the GPS receivers used for these studies are very expensive, so the sensor density could never be met for the purpose. Single or dual reference stations based monitoring approach is not failure-free. The author experienced a complete system failure that lasted 1 h during the Forth Road Bridge monitoring in February 2005. Both reference stations stopped working at the same time but the real reason could not be identified. In these tests since

wireless communication links were not used the reasons must come from either receiver hardware failure or something related to GPS satellite health status.

In these tests, the collected data were normally post-processed in a kinematic manner to obtain 3D coordinate time series of each monitoring site on the bridge deck or supporting towers. A high level of multipath is another issue that has not been properly addressed and signal availability under a bridge deformation monitoring context is also problematic due to many affecting factors that attenuate and block GPS signal reception.

2.2 Recent Progress in Using NRTK GNSS Positioning for SHM of Bridges

Network Real-time Kinematic (NRTK) GNSS positioning represents the latest GNSS development trend (GPS 2009). Compared with traditional single reference station based RTK positioning, NRTK could bring the users a much improved performance in terms of overall positioning accuracy, reliability and productivity. For example, since an array of continuously operating reference stations (CORS) are used in the generation of NRTK corrections, it provides the capacity to precisely model distance dependent errors, such as orbital error, tropospheric and ionosperic delays, in a region. Due to this reason fewer reference stations are required to cover the same area as for traditional RTK positioning and the inter-station distances can be extended to at least 100 km rather than 10 km, representing a huge saving in the infrastructure construction and labour required for positioning activities. As for a rover receiver, the baseline between a rover and a nearest reference station could be up to 50 km which could significantly increase mobility and efficiency. NRTK replies on GSM/GPRS/3G links to transmit the instant corrections that have a better signal penetration capacity. As an example from a key service provider's recent action in promoting NRTK, Fig. 3 shows the coverage of Leica Geosystems's NRTK service—SmartEurope. Other correction service providers are developing their national, regional or even global NRTK networks (Leica 2012)

The real-time data sets gathered from CORSs could not only be used to generate precise NRTK corrections and provide useful satellite orbit and clock information for reducing convergence time of precise point positioning (PPP) as proposed by Geng et al. (2010), but also play a perfect role in sensing the development of atmospheric events through monitoring water vapour components and tectonic movements through processing the measurements of long-term site movement observations.

Fig. 3 Current coverage of SmartNet Europe by Leica geosystems's CORSs

3 An Integrated Approach for Monitoring Slender Structures

To effectively monitor earthquakes, seismometers have been installed not only on the ground but also on a variety of structures such as high rise buildings, long bridges, and dams (Apostolou et al. 2007; Nickitopouloua et al. 2006). Whilst GPS is used for monitoring bridge deformations induced by different forces such as traffic, temperature, water currents, wind, and earthquakes, GPS Seismology as a new science is emerging as an effective tool to be used together with motion-based seismometers (Xu and Chan 2009; Larson 2009). Recent studies by the author himself and his institute reveal that there are many advantages from combining GPS based regional geo-hazard monitoring with structural deformation monitoring (Meng et al. 2008). Figure 4 shows that the 2D movements of the GPS antenna of an IGS station caused by an earthquake of a magnitude 6.3 is evident from processing the measurements from a CORS station—MOSE station near Rome, Italy (Geng et al. 2009).

As described in Fig. 2, slender structures are more susceptible to external forces and thus it makes them ideal sensor nodes to detect surface and underground force movements caused by events such as hurricanes and earthquakes, to form an essential part of an integrated early warning system, whilst CORSs are continuously monitoring surface deformations and at the same time providing precise NRTK corrections. Measurements from some of these IGS CORSs are currently used for near real-time weather forecasting through computation of water vapour components. In considering the deformation characteristics of slender structures, and processing and analysis of real-time data sets gathered from both CORSs and rover stations, an integrated geo-hazard early warning system could be formed and further used to

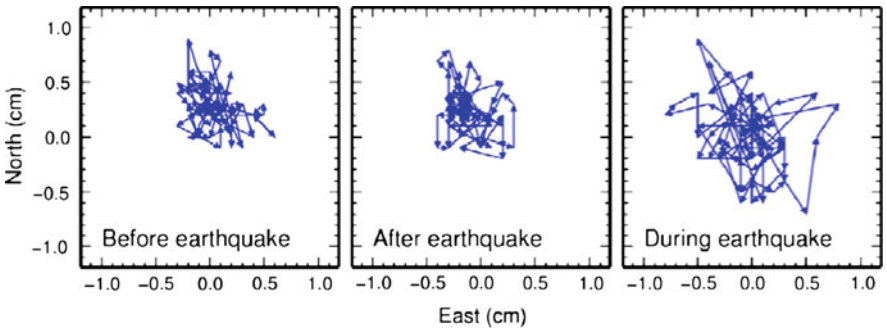

Fig. 4 2D antenna movements pre-, during and post-earthquake (Geng et al. 2009)

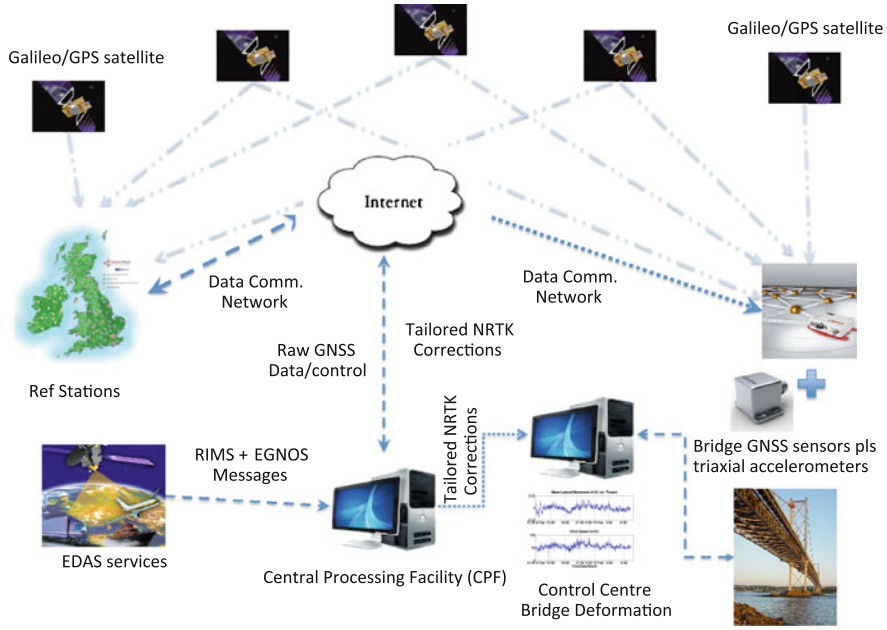

Fig. 5 Schematic of a proposed geo-hazard early warning system that includes GNSS receivers, EDAS service and triaxial accelerometers

verify or calibrate the data sets produced by other geo-hazard monitoring sensors such as those for remote sensing, weather forecasting, movement monitoring, etc. Following these considerations, an architecture design for a geo-hazard early warning system is illustrated in Fig. 5. Since high integrity information about the satellite health conditions is essential for avoiding the sending of false alarms due to poor measurement quality, in this design integrity information provided by EDAS (*EGNOS* Data Access Service) is used in the data processing and only the healthy satellites will be utilised to produce highly precise NRTK corrections. The other

characteristics of this system are the inclusion of the future Galileo system into the data processing and integration with triaxial accelerometers. By 2014, Galileo will approach its initial operational capacity stage. The addition of Galileo signals will significantly improves the 3D positioning performance (accuracy, reliability, and integrity) of GNSS based SHM of bridges.

4 Conclusions

In this paper the author proposed how to integrate the monitoring sensors installed on the slender structures such as long suspension bridges with GNSS continuously operational reference stations (CORSs) for geo-hazard monitoring and early warning purposes. It demonstrated that the data sets gathered from CORSs could serve two purposes, i.e. provision of highly accurate NRTK corrections for local structural deformation monitoring of slender structures and conducting continuous monitoring of both atmospheric events and ground forces as GNSS seismometers. At the same time, GNSS receivers on the structures could provide real-time structural deformation information and through correlating this deformation information with those obtained from CORSs a clearer picture about the development and detection of even a small geo-hazard event will be possible. However, how to distinguish deformations caused by an earthquake from those caused by wind and traffic loading need to be further investigated. It is anticipated that this could be resolved through establishing the relationship between loading and response of each individual geo-hazard event. Different loadings will cause different structural responses in terms of 3D vibration frequencies and displacements.

Acknowledgments The author would like to express his appreciations to those who involved in the bridge deformation monitoring exercises from different aspects in the past decade. The UK's Engineering and Physical Sciences Research Council, and the former Ministry of Construction of China are acknowledged for the provision of two dedicated research grants.

References

Apostolou M, Gazetas G, Garini E (2007) Seismic response of slender rigid structures with foundation uplifting. Soil Dyn Earthq Eng 27(7):642–654, 27

Ashkenazi V, Roberts GW (1997) Experimental monitoring of the Humber bridge using GPS. Civ Eng 120(4):177–182

Ashkenazi V, Dodson AH, Moore T, Roberts GW (1997) Monitoring the movements of bridges by GPS. In: Proceedings of the 10th international technical meeting of the satellite division of the US institute of navigation, Kansas City, USA, pp 1165–1172

Geng J, Tefeler FN, Meng X, Dodson AH (2009) Ambiguity resolution in precise point positioning: Enabling new applications in geosciences. In: British geophysical association 2009 postgraduate research in progress meeting, London

Geng J, Meng X, Dodson AH, Ge M, Teferle FN (2010) Rapid re-convergences to ambiguity-fixed solutions in precise point positioning. J Geodesy 84(12):705–714

GPS (2009) Technology to watch. GPS World 20(5):32–41
Kashima S, Yanaka Y, Mori K (2001) Monitoring the Akashi Kaikyo bridge: first experiences. Struct Eng Int 11(2):120–123
Larson KM (2009) GPS seismology. J Geodesy 83(3):227–233
Leica (2012). http://www.smartnet-eu.com. Accessed 3 Aug 2012
Meng X (2002) Real-time deformation monitoring of bridges using GPS/accelerometers. PhD thesis, The University of Nottingham, UK
Meng X, Huang W (2009) Global navigation satellite systems (GNSSs) for monitoring long bridges. In: Boller C, Chang F-K, Fujino Y (eds) Encyclopedia of structural health monitoring: sensors, Wiley, http://onlinelibrary.wiley.com/doi/10.1002/9780470061626.shm079/pdf
Meng X, Roberts GW, Dodson AH, Cosser E, Bames J, Rizos C (2004) Impact of GPS satellite and pseudolite geometry on structural deformation monitoring: analytical and empirical studies. J Geodesy 77(12):809–822
Meng X, Dodson AH, Roberts GW (2007a) Detecting bridge dynamics with GPS and triaxial accelerometers. Eng Struct 29(11):3178–3184
Meng X, Roberts GW, Dodson AH (2007b) Using GPS to measure the response of the forth road bridge to wind and temperature loading. J Geospatial Eng 9(1):1–11
Meng X, Teferle FN, Sowter A, Geng J, Bingley R, Dodson AH (2008) Satellite based geo-hazard monitoring activities and data interpretation at the University of Nottingham. In: Proceedings of international association of chinese professionals in global positioning systems' workshop on the Wenchuan earthquake, Wuhan University, China
Meng X, Tang W, Shi C, Sun F (2010) Using low-cost GPS receivers and network RTK positioning for high precision LBS and ITSS. In: Proceedings of ENC GNSS 2010, Braunschweig, Germany
Nickitopouloua A, Protopsaltia K, Stiros S (2006) Monitoring dynamic and quasi-static deformations of large flexible engineering structures with GPS: accuracy, limitations and promises. Eng Struct 28(10):1471–1482
Roberts GW, Brown CJ, Meng X (2006a) Bridge deflection monitoring—tracking millimeters across the firth of forth. GPS World 11(2):26–31
Roberts GW, Meng X, Brown CJ, Dallard P (2006b) GPS measurements on the London millennium bridge. ICE Bridge Eng J 159(BE4), pp 153–161
Xu YL, Chan WS (2009) Wind and structural monitoring of long span cable supported bridges with GPS. The seventh Asia-Pacific conference on wind engineering, Taiwan, http://www.iawe.org/Proceedings/7APCWE/IS1.pdf